



ATLAS Note

ATL-COM-PHYS-2017-673

13th April 2018



Draft version 4.1

¹ ² ³ Measurement of the $t\bar{t}\gamma$ production cross-section in pp collisions at $\sqrt{s} = 13$ TeV with ATLAS detector

⁴ The ATLAS Collaboration¹, Binish Batool^c, Julien Caudron^a, Markus
⁵ Cristinziani^a, Ivor Fleck^c, Sara Ghasemi^c, Mazuza M. A. Ghneimat^a, Yichen
⁶ Li^c, Maria Moreno Llacer^d, John Meshreki^c, Arnulf Quadt^b, Amartya Rej^c,
⁷ Elizaveta Shabalina^b, Joshua Wyatt Smith^b, Benedikt Völkel^b, Knut Zoch^b

⁸ ^a*University of Bonn*

⁹ ^d*CERN*

¹⁰ ^b*University of Göttingen*

¹¹ ^c*University of Siegen*

¹² The production of a top-quark pair in association with a photon is measured in proton-proton
¹³ collisions at a center-of-mass energy of 13 TeV. The integrated luminosity is 36.1 fb^{-1} ,
¹⁴ collected in 2015 and 2016. The measurement is performed in the single and dilepton
¹⁵ channels. In the single lepton channels, exactly one lepton and at least four jets are requested,
¹⁶ with at least one jet being b -tagged. In the dilepton channels, exactly two opposite charge
¹⁷ leptons, at least two jets with at least one jet being b -tagged, and a large missing transverse
¹⁸ momentum are requested. A veto is also imposed for events compatible with a Z boson
¹⁹ mass reconstruction. For all channels exactly one isolated photon with $p_T > 20 \text{ GeV}$ and
²⁰ $|\eta| < 2.37$ is required. This photon should not be too close to the selected leptons and
²¹ jets. In addition, an event-level multivariate analysis is performed using event-level variables
²² with the output variable distribution used in a profile likelihood fit, from which the final
²³ results are obtained. The fiducial cross-sections in the different channels are extracted
²⁴ as $\sigma_{\text{fid}}^{\text{SL}} = 528.30^{+44.90}_{-43.11}(\text{sys.})^{+9.23}_{-9.20}(\text{stat.}) \text{ fb}$ and $\sigma_{\text{fid}}^{\text{DL}} = 69.30^{+4.24}_{-3.71}(\text{sys.})^{+2.65}_{-2.59}(\text{stat.}) \text{ fb}$ for
²⁵ single lepton and dilepton, respectively, with a final combined fit to all 5 channels giving
²⁶ $\sigma_{\text{fid}}^{\text{Incl.}} = 597.53^{+34.88}_{-33.09}(\text{sys.})^{+9.67}_{-9.45}(\text{stat.}) \text{ fb}$. Several differential cross-sections are also extracted:
²⁷ as function of the photon p_T , the photon $|\eta|$ and the distance between the photon and closest
²⁸ lepton for both single lepton and dilepton channels and as function of the η and ϕ angle
²⁹ between the two leptons in the dilepton channel. All these measurements are in agreement
³⁰ with the theoretically computed numbers.

32 **Contents**

33 1 Introduction	11
34 2 ATLAS detector	14
35 3 Data and simulation samples	15
36 3.1 Samples description	15
37 3.2 Removal of the double counting of events in X+jets and X+ γ samples	16
38 4 Objects definition	17
39 4.1 Objects selection	17
40 4.2 Prompt photon tagger	19
41 4.2.1 PPT training	20
42 4.2.2 Systematic uncertainties for the PPT	22
43 5 Signal region definition	33
44 5.1 Event selection	33
45 5.2 Event level MVA	34
46 5.2.1 Discriminator for single lepton and dilepton channels	34
47 5.2.2 Variable selection and training	35
48 5.2.3 Application and evaluation	45
49 6 Background descriptions	53
50 6.1 Background due to mis-reconstructed electrons	53
51 6.1.1 Control regions	53
52 6.1.2 Fake sources	54
53 6.1.3 Fake rates	56
54 6.1.4 Signal region $e \rightarrow \gamma$ fake	60
55 6.1.5 PPT systematics	62
56 6.2 Background due to hadronic fakes	64
57 6.2.1 Estimation of hadronic fakes in single lepton channel	64
58 6.2.2 Estimation of hadronic fakes in dilepton channel	67
59 6.3 Background due to fake leptons	75
60 6.3.1 Fake leptons in single lepton channel	75
61 6.3.2 Fake leptons in dilepton channel	77
62 6.4 Prompt photons background	80
63 6.4.1 $Z\gamma$ validation region	80
64 6.4.2 $W\gamma$ validation region	81
65 7 Pre-fit distributions with scale factors applied to the single lepton channels	87
66 8 Systematic uncertainties	91
67 8.1 Smoothing, symmetrisation and pruning	91
68 8.2 Theoretical Uncertainties	93
69 8.2.1 Signal Modeling	93
70 8.2.2 Background Modelling	94
71 8.3 Experimental Uncertainties	95

72	8.3.1 Sources of experimental uncertainties	96
73	8.4 Propagation of the systematic uncertainties to the unfolding framework	99
74	9 Cross section definitions	101
75	9.1 Fiducial region	101
76	9.1.1 Particle definition for fiducial region	101
77	9.1.2 Event selection for fiducial region	101
78	9.1.3 Acceptance and correction factor	102
79	9.2 Fiducial cross section	103
80	9.3 Total cross section	103
81	9.4 Differential cross section	104
82	10 Fit strategy	110
83	10.1 Likelihood function	110
84	10.2 Signal strength	111
85	10.3 Fiducial cross section	111
86	10.4 Total cross section	111
87	10.5 Differential cross section	112
88	11 Unfolding	113
89	11.1 Iterative Bayesian method	113
90	11.1.1 The pseudo-data	114
91	11.1.2 Optimising the number of iterations	114
92	11.1.3 The closure test	115
93	11.1.4 Pull study	115
94	11.1.5 Stress tests	124
95	11.2 Cross-check methods	127
96	11.2.1 Bin-by-bin correction method	127
97	11.2.2 The singular value decomposition method	127
98	11.2.3 Comparison test	130
99	12 Theory prediction	133
100	12.1 NLO cross-section	133
101	12.2 LO cross-section	133
102	12.3 Kfactor and fiducial cross-section	134
103	13 Results	136
104	13.1 Fit model and results	136
105	13.1.1 μ , best-fit	136
106	13.1.2 Post-fit plots and yields	136
107	13.1.3 Nuisance parameters	136
108	13.2 Fiducial cross section	138
109	13.3 Differential cross section	144
110	14 Conclusion	149

111	Appendices	154
112	A Additional information for PPT	155
113	A.1 Comparison of different architectures of PPT	155
114	A.2 Further data/MC plots for PPT systematics	155
115	A.3 Derivations used for training	155
116	A.4 Shower shape comparisons in different p_T and η regions	158
117	A.5 Shower shape comparisons for training and test split	158
118	B Cuts optimization	161
119	B.1 Cuts optimization in the single lepton channel	161
120	B.1.1 Results in the single lepton channel	162
121	B.2 Cuts optimization in the dilepton channel	162
122	B.2.1 Results in the dilepton channel	165
123	C Radiative photon decay versus radiative production	170
124	D Photon isolation cut	171
125	E Hadronic-fake background appendix	173
126	E.1 Data-driven double ratio	173
127	F $Z\gamma$ light jet validation region	179
128	G $W\gamma$ light jet validation region	182
129	H Systematic uncertainty breakdown	185
130	I Unfolding using fine binning	187
131	I.1 Inputs	187
132	I.1.1 Optimising the number of iterations	190
133	I.1.2 The closure test	190
134	I.1.3 Pull study	190
135	I.1.4 Stress tests	192
136	I.2 Cross-check methods	193
137	I.2.1 Closure tests	193
138	J Pull study for unfolding with IBS	200
139	K Results appendix	202
140	K.1 Results for $e+jets$, $\mu+jets$, ee , $\mu\mu$ and $e\mu$	202
141	K.2 Asimov fit scenarios: $V\gamma$ floating or constrained	203
142	K.2.1 single lepton and dilepton combined pull plots	203
143	K.2.2 Individual channel pull plots	208
144	L New physics observations using Effective Field Theory	216
145	L.1 EFT samples	217
146	L.2 The study in the fiducial region	217
147	L.2.1 The fit	218

148	M First look at EFT	221
149	M.1 Cross check of first EFT results	221
150	M.2 The Monte Carlo study in the fiducial region in the single lepton channel	221
151	M.3 Further variables for the EFT in the fiducial region	224
152	N EFT validation	227
153	O Studying larger weights in the $W\gamma$ and $Z\gamma$ MC samples	229
154	P Estimation of a possible mis-modelling of prompt photons from Pile-Up	233
155	Q Monte Carlo Samples	235
156	Q.1 Nominal samples	235
157	Q.2 Samples for estimation of systematic uncertainties	239

Not reviewed, for internal circulation only

List of contributions

158	Binish Batool Julien Caudron Markus Cristinziani Ivor Fleck Sara Ghasemi Mazuza M. A. Ghneimat Yichen Li	Fiducial measurement Ntuples production, Analysis contact, Editor Supervision of M. Ghneimat Supervision of B. Batool, S. Ghasemi, J. Meshreki and A. Rej hadronic fakes estimation, Editor Theoretical cross-section prediction, Unfolding using IBS $e \rightarrow \gamma$ fake estimation, Unfolding using ML, Analysis contact
159	Maria Moreno Llacer John Meshreki Arnulf Quadt Amartya Rej Elizaveta Shabalina Joshua Wyatt Smith Benedikt Völkel Knut Zoch	Supervision of J. Smith, B. Völkel and K. Zoch Fake leptons estimation for single lepton channel Supervision of J. Smith, B. Völkel and K. Zoch Systematics uncertainties estimation Supervision of J. Smith, B. Völkel and K. Zoch Profile likelihood fit, PPT and ELD development, Systematics, Editor PPT development PPT development, Systematics
160		

Not reviewed, for internal circulation only

161 **Updates / History**

162 • **version 2.1, 18 August 2017**

- 163 – first draft being given to the EB

164 • **version 2.2, 04 August 2017**

- 165 – General: Changed the order of chapters
- 166 – Chapter 4, Object definition
- 167 * Chapter 4.2.1: PPT training: Included selection cuts and trigger information, added plots
168 for PPT applied to $t\bar{t}\gamma$ ntuples
 - 169 * Chapter 4.2.2: Systematic uncertainties for PPT from hadronic fake CR.
 - 170 – Chapter 5, Signal region definition
 - 171 * Included many more plots including ph_pt, jet_pt, nbjets, etc.
 - 172 * Included plots showing b-tags vs ELD output.
 - 173 – Chapter 6, Background description
 - 174 * 6.2 Background due to hadronic fakes: $e \rightarrow \gamma$ fake is also subtracted from data now, plots
175 and numbers are updated with new lumi syst and taking into account the $e \rightarrow \gamma$ fake SF.
 - 176 * 6.4.1 Prompt photons background, $Z\gamma$ Validation region. Redone with NLO samples.
 - 177 – Chapter 8, Cross section definitions
 - 178 * 8.4 Differential cross section: Added new potential for differential study.

179 • **version 3.0, 21 December 2017**

- 180 – Chapter 6, Background description

- 181 * 6.1 $p_T\text{-}\eta$ 2D SFs are provided as well as their systematics studied. $e \rightarrow \gamma$ fake PPT shape
182 systematics is also studied.
- 183 * 6.2 Double ratio factor to correct for photon's isolation and identification correlation is
184 added.
- 185 * 6.3.1 Different parameterisations for Multijet estimation for single lepton channel are
186 studied. Nominal and systematic variations of parameterisation are given.

- 187 – Chapter 7, Pre-fit distributions with SF's

- 188 * Added a chapter to show single lepton after the SF's from background section have been
189 applied.

- 190 – Chapter 8, Systematics

- 191 * 8.2.3 Further section added describing the methods used to prune and smooth nuisance
192 parameters.

- 193 * 8.3 Propagation of uncertainties into the unfolding framework.

- Chapter 9, Cross section definitions
 - * 9.4 The correction and acceptance values are updated with systematics.
 - * 9.4 The description of differential cross section is simplified. Inputs for unfolding (efficiencies and migration matrices) are updated.
- Chapter 10, Fit strategy
 - * 10.5 The description of fit strategy for differential cross section is simplified.
- Chapter 11, Unfolding
 - * 11.1 Closure/Pull/Stress tests of the iterative bayesian unfolding are added
- Chapter 11, Theory prediction
 - * 11.3 The NLO fiducial cross section values are updated with systematics.
- Chapter 13, Results
 - * 12.1 Final μ results have been added with previous studies moved to the appendix .
 - * Included Post fit plots, yields, and systematic studies.
 - * 12.3 Added differential cross section results.
- **version 4.0, 3rd April 2018**
 - Chapter 3, Data and simulation samples
 - * 3.2 Add more explanations on effect of the removal of double counting events and comparison with other methods
 - Chapter 4, Object definition
 - * 4.2 Prompt Photon Tagger (PPT):
 - Systematics now use slicing in η and p_T
 - Shape discrepancies from PPT prompt CR now not only used as systematics, but also as corrections for prompt contributions in the signal regions
 - Additional systematic for hadronic fake to account for isolation uncertainty
 - Chapter 6, Background descriptions
 - * 6.1 Background due to mis-reconstructed electrons:
 - Updated $e \rightarrow \gamma$ fake numbers/plots/tables to their latest version.
 - Added subsection 6.1.4 to explain an additional data-driven correction to $e \rightarrow \gamma$ fake.
 - * 6.2: Background due to hadronic fakes
 - 6.2.1: hadronic fake SF's are now separated for converted and unconverted photons and are provided in $\eta - p_T$ 2D bins.
 - 6.2.2: Added extrapolation uncertainty for using hadronic fake SF's of the single lepton channel to the dilepton channel.

- Chapter 8, Systematic uncertainties
 - * Added signal and $t\bar{t}$ modelling systematic + red/blue plots.
 - * Summarised all systematics and added many plots.
- Chapter 9, Cross section definitions
 - * 9.1: Fiducial region: Updated table of acceptance and correction factor
 - * 9.4: Differential cross section: Added a new variable (minimum $\Delta R(\text{lepton}, \gamma)$) for the inputs to the unfolding (efficiencies and migration matrices).
- Chapter 11, Unfolding
 - * Added new variables minimum $\Delta R(\text{lepton}, \gamma)$ in both channels, $\Delta\eta(\text{lepton}, \text{lepton})$ and $\Delta\phi(\text{lepton}, \text{lepton})$ in dilepton channel.
- Chapter 12, Theory prediction
 - * Rewrite almost the whole chapter
 - * Document the new k-factor approach and the final predicted fiducial cross-sections
- Chapter 13, Results
 - * 13.2 Fiducial cross section:
 - Updated cross section results
 - * 13.2 Differential cross section:
 - Updated differential cross section results, plotting and systematic tables.
 - Added missing signal modelling systematics.
- Chapter 14, EFT
 - * Moved the entire chapter to appendix (Appendix [L](#)).
 - Remove appendix B (Cut flow tables), since it was outdated and in general not useful
 - Remove the cut optimisations for met + mwt from appendix C.1 (Cut optimisation in the single lepton channel, now Appendix [B.1](#)), since it was outdated and buggy.
 - Added an appendix for extra material for hadronic fake background (Appendix [E](#))
 - Added an appendix for extra material for unfolding (Appendix [I](#)).
 - Added appendix [O](#): Studying large weights in $W\gamma$ and $Z\gamma$ MC samples
 - Added appendix [P](#): Checked for prompt photons from pile-up.
- **version 4.1, 13 April 2018**
 - The draft to be circulated in Top WG.
 - Chapter [6.4](#) Prompt photons background
 - * Updated $W\gamma$ and $Z\gamma$ background section to include some more plots and χ^2 values.

- 259 – Chapter 8, Systematic uncertainties
- 260 * Included information on the ROOT TH1:Smooth method which we now use for some
261 systematic sources.
- 262 – Chapter 13, Results
- 263 * Updated fits using custom jet flavour composition histograms.
- 264 * Added an “inclusive combined” fit result.

[Not reviewed, for internal circulation only]

265 1 Introduction

266 The study of the top quark particle is one of the major fields in modern particle physics. Due to its heavy
 267 mass and short life time, the top quark particle plays an important role in the Standard Model, and is
 268 a good candidate to interact with new physics in many Beyond Standard Model theories. The precise
 269 measurement of its properties is therefore an important topic, and has been the subject to a lot of analyses,
 270 as for example in [1]. The top quark coupling measurements can uncover new physics. In particular, the
 271 electroweak top quark coupling with the photon, $t\gamma$, can be affected through anomalous dipole moments
 272 of the top quark [2–7]. The top-photon coupling can be probed in the top quark pair production associated
 273 with a photon ($t\bar{t}\gamma$).

274 The first evidence of $t\bar{t}\gamma$ production was obtained at the Tevatron, and since then, several measurements
 275 have been realized at the LHC experiments. The previous results are summarized in Table 1.

Table 1: Previous measurements of the $t\bar{t}\gamma$ cross-section. If not splitted, the uncertainties is the combined uncertainties. Otherwise, the keywords *sy*, *st*, *lu*, *sc* and *pdf* stands for, respectively, the uncertainty due to systematical uncertainties, statistical uncertainties, luminosity, scale and PDF. The last-but-one column is the relative combined uncertainty of the observed result.

Luminosity	Measurement	p_T^γ cut [GeV]	Theory [fb]	Observed result [fb]	Obs. rel. uncert.	Ref.
Tevatron ($p\bar{p}$), CDF, 1.96 TeV						
6.0fb^{-1}	inclusive	10	170 ± 30	$180 \pm 70(\text{st}) \pm 40(\text{sy}) \pm 10(\text{lu})$	8.1%	[8]
LHC ($p\bar{p}$), ATLAS, 7 TeV						
1.04fb^{-1}	inclusive non-all-hadronic	8	2100 ± 400	$2000 \pm 500(\text{st}) \pm 700(\text{sy})$	43.0%	[9]
4.59fb^{-1}	fiducial $\ell+\text{jets}$	20	48000 ± 10000	$63000 \pm 8000(\text{st})^{+17000}_{-13000}(\text{sy})$	27.0%	[10]
LHC ($p\bar{p}$), CMS, 8 TeV						
19.7fb^{-1}	inclusive $\mu+\text{jets}$	20	1800 ± 500	$2400 \pm 200(\text{st}) \pm 600(\text{sy})$	26.3%	[11]
19.7fb^{-1}	inclusive $\ell+\text{jets}$	25	$591 \pm 71(\text{sc}) \pm 30(\text{pdF})$	515 ± 108	21.0%	[12]
19.7fb^{-1}	fiducial $\ell+\text{jets}$	25	-	127 ± 27	21.2%	[12]
LHC ($p\bar{p}$), ATLAS, 8 TeV						
20.2fb^{-1}	fiducial $\ell+\text{jets}$	15	151 ± 24	$139 \pm 7(\text{st}) \pm 17(\text{sy})$	13.2%	[13]
20.2fb^{-1}	differential $\ell+\text{jets}$	15	-	-	-	[13]

276 The final state of the $t\bar{t}\gamma$ process is similar to the final state of the usual top quark pair production, but
 277 contains an additional prompt energetic photon. In this final state, the photon can have different origin.
 278 It can be the result of Initial State Radiation (ISR) of the initial partons, which is mainly obtained when
 279 the top quark pair is produced by quark-antiquark annihilation. It can be the result of a radiation directly
 280 from the top quark, which is the relevant contribution for the study of the top-photon coupling. Finally, it
 281 can also be the result of Final State Radiation (FSR), radiated by the decay products of the top quark: the
 282 W -boson, the b -quark or the decay products of the W -boson. Theoretical NLO cross-section calculations
 283 have been performed considering the unstable top quark hypothesis, therefore including the latter case
 284 [14]. Some representative Feynman diagrams for the photon radiated during top production and radiated
 285 during top decay are shown in Figure 1 and Figure 2, respectively. The considered signal in this analysis is
 286 originating from any of these sources. However, some selections are intended to reduce the contribution
 287 of the photon radiated from the decay products of the top quark, enhancing the contribution originating
 288 from the top-photon coupling.

289 The strategy is to select a single lepton or dilepton final state of $t\bar{t}$, and request the presence of a photon.
 290 In previous $t\bar{t}\gamma$ ATLAS analyses, the dominant background was the contribution due to non-prompt
 291 photons, and a maximum-likelihood fit using templates on a discriminative variable (the photon isolation

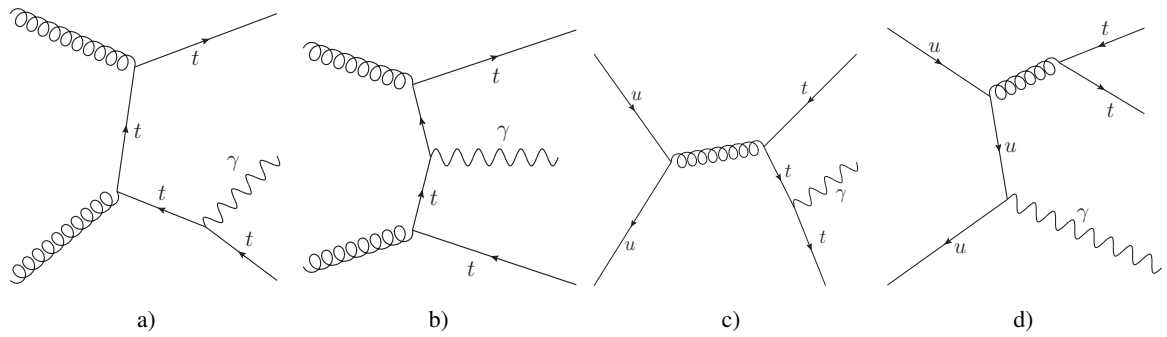


Figure 1: Some representative Feynman diagrams for the $t\bar{t}\gamma$ process where the photon is radiated during top-quark production (a,b,c) or radiated from initial partons (d).

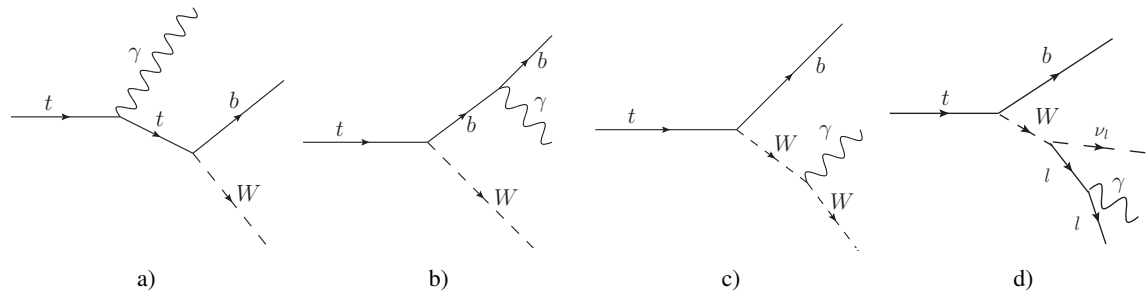


Figure 2: Some representative Feynman diagrams for the $t\bar{t}\gamma$ process where the photon is radiated during top-quark decay.

in the tracker) was performed. In this analysis, an analysis-independent multivariate analysis discriminant optimized to select prompt photons has been introduced. This discriminant enters in a second multivariate analysis discriminant, analysis-dependent and exploiting event-level variables, used as final variable on which the fit is performed. The final states considered are the single lepton channels ($e+\text{jets}$ and $\mu+\text{jets}$) and dilepton channels (ee , $e\mu$, $\mu\mu$), including electrons and muons from possible leptonic τ lepton decay. The inclusive and differential cross-sections for the different channels are extracted. The differential cross-sections are presented as a function of the photon transverse momentum and as a function of the photon pseudo-rapidity. An unfolding procedure is performed, and the results are compared with the theoretical prediction.

This note is organised as follows. Section 2 provides a brief introduction to the ATLAS detector. Section 3 contains the description of the data and simulated samples used in this analysis. Section 4 describes the object reconstruction and selection, including the description of the prompt-photon discriminant. Section 5 describes the event selection for the signal region, including the description of the event-level discriminant. Section 6 describes the background processes studies, detailing the estimation of the fake photon contribution due to mis-reconstructed hadrons and mis-reconstructed electrons, the estimation of the prompt photon background and the estimation of the contribution from fake leptons. Section 8 lists the systematic uncertainties taken into account in this analysis. Section 9 describes the method used to extract the total cross-section from the measured fiducial cross-section, followed by Section 10 which describes the fit procedure and a dedicated chapter, Section 11, explaining the intensive study of the unfolding procedure. Section 12 presents the theory prediction for the signal. Section 13 presents the final results. Finally, the conclusion is in Section 14.

313 The appendix includes additional information on the prompt photon tagger (Appendix A), the cuts optimiza-
314 tion study (Appendix B), the study of the signal contributions for photon radiated from top production
315 or radiated from top decay (Appendix C), a comparison of before and after applying the photon isolation
316 cut (Appendix D), the extra material for hadronic fake background (Appendix E), the additional validation
317 regions for $Z\gamma$ (Appendix F) and $W\gamma$ (Appendix G), the extra material for unfolding section (Appendix I),
318 some pull distributions (Appendix J), the extra material from result section (Appendix K), some discus-
319 sions about new constrains on Effective Field Theory operators and their validation ((Appendix L, M
320 and N), studies of issue of large weights in the $V + \gamma$ samples (Appendix O), the study of the modelling
321 of prompt photons from pile-up (Appendix P), and the detailed list of the MC samples (Appendix Q).

322 2 ATLAS detector

323 The ATLAS detector [15] consists of three main components. The innermost component is the Inner
 324 Detector (ID) which surrounds the beam pipe and is used for tracking charged particles. An additional
 325 silicon pixel layer, the insertable B-layer, was added between 3 and 4 cm from the beam line to improve
 326 b-hadron tagging [16, 17]. The ID is surrounded by a superconducting solenoid operating with a magnetic
 327 field of 2 T and the calorimeter which is divided into two subsystems. The first subsystem is the
 328 electromagnetic calorimeter (EMC) and the second is the hadronic calorimeter (HCAL). The outermost
 329 layer is the third main component of the ATLAS detector: the Muon Spectrometer (MS). The ID provides
 330 tracking information from pixel and silicon microstrip detectors in the pseudorapidity¹ range $|\eta| < 2.5$ and
 331 from a transition radiation tracker (TRT) covering $|\eta| < 2.0$. The 2 T magnetic field of the superconducting
 332 solenoid bends the charged particles for the momentum measurement. The EMC uses lead and liquid
 333 argon (LAr) and is divided into barrel ($|\eta| < 1.475$) and end-cap ($1.375 < |\eta| < 3.2$) regions. The HCAL
 334 is provided by a steel/scintillating-tile calorimeter, segmented into three barrel structures within $|\eta| < 1.7$,
 335 and two copper/LAr hadronic endcap calorimeters that cover the region $1.5 < |\eta| < 3.2$. The solid
 336 angle coverage is completed with forward copper/LAr and tungsten/LAr calorimeter modules, optimised
 337 for electromagnetic and hadronic measurements respectively, and covering the region $3.1 < |\eta| < 4.9$.
 338 The MS measures the deflection of muon tracks within $|\eta| < 2.7$ using multiple layers of high-precision
 339 tracking chambers located in toroidal fields of approximately 0.5 T and 1 T in the central and end-cap
 340 regions of the ATLAS, respectively. The MS is also instrumented with separate trigger chambers covering
 341 $|\eta| < 2.4$.

¹ ATLAS uses a right-handed coordinate system with its origin at the nominal interaction point (IP) in the centre of the detector and the z -axis along the beam pipe. The x -axis points from the IP to the centre of the LHC ring, and the y -axis points upward. Cylindrical coordinates (r, ϕ) are used in the transverse plane, ϕ being the azimuthal angle around the z -axis. The pseudorapidity is defined in terms of the polar angle θ as $\eta = -\ln \tan(\theta/2)$.

3 Data and simulation samples

3.1 Samples description

This analysis has been realized with proton-proton collision data harvested during 2015 and 2016, at a center-of-mass of energy of $\sqrt{s} = 13$ TeV. Only luminosity blocks of recorded data satisfying good quality criteria in the detector have been considered. This corresponds to a total integrated luminosity of 3212.96 pb⁻¹ in 2015 and 32884.6 pb⁻¹ in 2016.

The $t\bar{t}\gamma$ signal sample has been simulated for the semileptonic and dileptonic channels of $t\bar{t}$ decays at leading-order, with the MG5_aMC@NLO generator [18], using the NNPDF2.3LO parton distribution function (PDF) set [19]. The parton showering is simulated using PYTHIA 8 [20], and the A14 tune [21]. ATLAS recommendations for the SM and EW inputs are used with the particle masses listed in Table 2.

Table 2: Masses of quarks and leptons set for the simulation of the $t\bar{t}\gamma$ sample.

Particle	Quarks			Leptons		
	light-quarks (u, d, c, s)	t -quark	b -quark	electron	muon	tau
Mass [GeV]	0	172.5	4.7	0	0.105	1.777

352

In the simulation, the fine structure constant of 1/137 is used. The renormalisation and the factorization scales are dynamic and correspond to half the sum of the transverse masses. In order to avoid infrared and collinear singularities, a set of kinematic cuts listed below have been applied. The photon transverse momentum and pseudo-rapidity should be larger than 15 GeV and smaller than 5.0, respectively. A transverse momentum of the charged lepton is required to be larger than 15 GeV and their pseudo-rapidity should be smaller than 5.0. The ΔR distance between the photon and all other charged particles in the final state should be larger than 0.2. The total cross section calculated by MADGRAPH for the $t\bar{t}\gamma$ signal sample is found to be 4.623 pb, which is consistent with theoretical computations for the same phase-space.

The MC sample for the inclusive $t\bar{t}$ production is generated with POWHEG-BOX v2 [22] interfaced to PYTHIA8, using the A14 tune. This tune uses the NNPDF2.3LO set. The production of W -and Z -bosons + γ as well as the other vector boson production samples (W -and Z -bosons + jets) are simulated using SHERPA [23] 2.2.2 and 2.2.1, respectively, with the NNPDF30NNLO pdf set.

The single top-quark t -, s - and Wt -channel samples are produced by POWHEG-Box v1 generator. POWHEG matrix element events are generated with CT10 (NLO) PDF set [24], interfaced with PYTHIA 6 and using the Perugia2012 tune [25]. An additional photon radiation in the fragmentation process is simulated with PHOTOS [26]. The Wt -channel with inclusive diagram removal is used to estimate the background while the Wt -channel with inclusive diagram subtraction is used for uncertainties evaluation. The WW -, WZ - and ZZ -diboson samples are simulated using SHERPA 2.1 with the CT10(NLO) pdf set.

A full list of MC samples along with higher order cross-sections and k-factors can be found in Appendix Q.

374 3.2 Removal of the double counting of events in X+jets and X+ γ samples

375 Because the showering procedure will add photon radiations, the $t\bar{t}$ and V +jets samples can contain events
 376 already taking into account by the $t\bar{t}\gamma$ and $V\gamma$ samples. This overlap is removed by vetoing the events
 377 in $t\bar{t}$ and V +jets where the selected photon is originating from the hard interaction. This is done using a
 378 truth matching procedure, which identifies the origin and the type of the truth particle corresponding to
 379 the reconstructed photon. If the reconstructed photon is associated to a truth electron, or if a truth electron
 380 is present in a 0.2 cone around the reconstructed photon, the photon is considered as $e \rightarrow \gamma$ fake. If the
 381 reconstructed photon is associated with the type *BkgPhoton*², with an origin corresponding to a hadron,
 382 the photon is considered as hadronic fake. All other cases are considered as photon originating from
 383 the hard interaction. After this double counting removal, the $t\bar{t}$ and V +jets samples will only contribute
 384 to hadronic fake and $e \rightarrow \gamma$ fake backgrounds, while the dedicated $t\bar{t}\gamma$ and $V\gamma$ samples only provide
 385 the events containing prompt photons. Furthermore, this allows the classification of each event into the
 386 following categories: $t\bar{t}\gamma$ (contributions from only our signal sample), *hadronic fake*, $e \rightarrow \gamma$ *fake*, *Other*
 387 *prompt* and *Lep fake*. This procedure rejects less than 1% of events in $t\bar{t}\gamma$ and $V\gamma$ samples (with the
 388 exception of the $Z\gamma$ in the e +jets channel which can also contribute to the $e \rightarrow \gamma$ fake category when the
 389 prompt photon is not reconstructed/selected). For $t\bar{t}$ and V +jets samples, the prompt photon contribution
 390 is subject to large statistical uncertainty and its modelling is less trusted, it is why the $t\bar{t}\gamma$ and $V\gamma$ samples
 391 are used. But the yield of events rejected by this procedure in those samples is compatible with what is
 392 expected from $t\bar{t}\gamma$ and $V\gamma$.

393 Comparisons with other event double counting have been made. A method using the decay chain up to
 394 the truth particle photon has been used to identify the origin of the photon, and shows compatible results
 395 with the method used here. The method used in other analyses considers that a $t\bar{t}$ event is overlapping
 396 with $t\bar{t}\gamma$ when a truth particle photon with a transverse momentum higher than the value used during
 397 generation of $t\bar{t}\gamma$ not coming from a baryon or a meson exists. Tested in $t\bar{t}$, this alternative method
 398 agrees with the classification used in this analysis in 95% of the cases. The differences are mainly due to
 399 misclassifications, in this alternative method, of $e \rightarrow \gamma$ fake or prompt photons, where it has been found
 400 that the method used in this analysis is doing the correct classification (in one case, photons emitted by
 401 electrons were classified as prompt while they are accounted by the $e \rightarrow \gamma$ fake estimation method, in the
 402 other case, the algorithm was incorrectly considering generator-specific artifacts as baryons or mesons).

² This type *BkgPhoton* corresponds to a photon not originating from ISR/FSR, but from a boson or from a lepton.

4 Objects definition

4.1 Objects selection

The main physics objects considered in this analysis are electrons, muons, jets, b -jets, missing transverse energy and photons. The reconstruction of those objects follows the standard methods in the ATLAS Collaboration. Typical recommended corrections and calibrations are applied, using the top analysis group software AnalysisTop [27] in its version 2.4.33. The object definitions of leptons, jets, b -jets and missing transverse momentum are chosen to be as close as possible to the ones of the usual $t\bar{t}$ analyses. The photon reconstruction, identification and selection have been optimized for this analysis.

The electrons are reconstructed from energy deposits in the central region of the Electromagnetic Calorimeter associated with reconstructed tracks from the Inner Detector, and are required to satisfy the **TightLH** identification criteria and the **Gradient** isolation criteria. Scale factors based on comparison between data and MC are used to correct the simulation. Only electrons with calibrated $E_T > 25$ GeV and $|\eta_{\text{clus}}| < 2.47$, excluding the crack region $1.37 < |\eta_{\text{clus}}| < 1.52$, are considered (η_{clus} is the pseudo-rapidity of the calorimeter cluster associated to the electron). The recommended requirements on the impact parameter variables are also applied: the transverse impact parameter with respect to the beam line $|d_0|/\sigma(d_0)$ is required to be lower than 5 and the difference in the z -axis between the track origin and the primary vertex when expressed at the beam line $|\Delta z_0 \sin(\theta)|$ is required to be lower than 0.5 mm. The reconstruction, identification and scale factor extraction methods are described in [28], the isolation is described in [29], and the calibration is described in [30].

The muons are reconstructed with the combined algorithm, using the track segments in the various layers of the muon spectrometer and the tracks in the Inner Detector. They are required to have the **Medium** identification quality criteria and the **Gradient** isolation criteria. Scale factors based on comparison between data and MC are used to correct the simulation. Only muons with calibrated $p_T > 27.5$ GeV and $|\eta| < 2.5$ are considered.³ The recommended requirements on the impact parameter variables are also applied: the transverse impact parameter with respect to the beam line $|d_0|/\sigma(d_0)$ is required to be lower than 3 and the difference in the z -axis between the track origin and the primary vertex when expressed at the beam line $\Delta z_0 \sin(\theta)$ is required to be lower than 0.5 mm. The reconstruction, identification, calibrations and scale factor extraction methods are described in [31], the isolation is described in [29].

The photons are reconstructed from energy deposits in the central region of the Electromagnetic Calorimeter. If the cluster is considered not matched to any reconstructed tracks in the Inner Detector, an unconverted photon candidate is reconstructed. If the cluster is matched with reconstructed tracks that are consistent with originating from a photon conversion and if in addition a conversion vertex is reconstructed, a converted photon candidate is reconstructed. Both kind of photons are considered in this study. The photons are required to satisfy the **Tight** identification criteria. The photon is also required to be isolated, using the **FixedCutTight** working point defined as $p_T^{\text{topoetcone}40} < 0.022 p_T(\gamma) + 2.45$ GeV and $p_T^{\text{cone}20}/p_T(\gamma) < 0.05$. Scale factors based on comparison between data and MC are used to correct the simulation. Only photons with calibrated $p_T > 20$ GeV and $|\eta_{\text{clus}}| < 2.37$, excluding the crack region $1.37 < |\eta_{\text{clus}}| < 1.52$, are considered (η_{clus} is the pseudo-rapidity of the calorimeter cluster associated to the photon). The reconstruction, identification and scale factor extraction methods are described in [32], the isolation is described in [29], and the calibration is described in [30].

³ This is different to the electron p_T of 25 GeV due to the availability of scale factors which only start at 27.5 GeV.

443 The jets are reconstructed using the anti- k_t algorithm [33] with a distance parameter $R = 0.4$ (in $\eta - \phi$
 444 space) and are reconstructed from topological calorimeter clusters [34]. The jet energy scale and jet energy
 445 resolution are calibrated [35]. The jets are required to have $p_T > 25$ GeV and $|\eta| < 2.5$. In order to reject
 446 jets from pile-up or other primary vertices, jets are required to have a Jet Vertex Tagger discriminant [36]
 447 larger than 0.59 for jets with $p_T < 60$ GeV and $|\eta| < 2.4$. This Jet Vertex Tagger efficiency is corrected
 448 by a scale factor extracted from data and MC comparison.

449 The b -tagging algorithm to identify jets from b quark hadronisation is the MV2c10 algorithm [37],
 450 which is based on a boosted decision tree (BDT) using the output weights of the JetFitter, IP3D and SV1
 451 algorithms as input. The 77% working point is used, corresponding to a cut at 0.645925, with calibration as
 452 recommended for Summer 2017 conferences (`2016-20_7-13TeV-MC15-CDI-2017-06-07_v2.root`).
 453 A scale factor to correct the b -tagging efficiency in simulation is also used.

454 The energy carried by the neutrinos is accounted for in the reconstructed missing transverse energy E_T^{miss}
 455 [38]. The E_T^{miss} is computed as the vector sum over all topoclusters in the event (considered as a massless
 456 particle originating from the center of the detector), and is further refined by applying corrections for
 457 identified electrons, muons, photons and jets.

458 An overlap removal procedure is applied to avoid that a same deposit in the calorimeters or track is used to
 459 reconstruct two different objects. The followed overlap removal procedure corresponds to the procedure
 460 recommended for Moriond 2017. First electrons that are sharing their track with a muon candidate are
 461 removed. Then, all the jets that are close to an electron in the $\eta - \phi$ plane ($\Delta R < 0.2$) are removed. Then,
 462 all the electrons that are close ($\Delta R < 0.4$) to a remaining jet are removed. For muons and jets that are close
 463 ($\Delta R < 0.4$), the muon is removed if the jet has more than 2 associated tracks, otherwise the jet is removed.
 464 All the photons that are close ($\Delta R < 0.4$) to a remaining electron or muon are removed. Finally, all the
 465 jets that are close ($\Delta R < 0.4$) to a remaining photon are removed (for technical reason, these photons are
 466 slightly looser than the one considered in the analysis, with loose ID, loose isolation and $p_T > 15$ GeV,
 467 but tests have shown this has a negligible impact).

468 The object selections are summarised in Table 3.

Object	Definition	$p_T (E_T)$	$ \eta $	Removed
Electron	TightLH, Gradient, $ d_0 /\sigma(d_0) < 5$, $ \Delta z_0 \sin(\theta) < 0.5\text{mm}$	25 GeV	[0, 1.37] & [1.52, 2.47]	(1) if sharing track with muon (3) if $\Delta R < 0.4$ wrt jet
Muon	Medium, Gradient, $ d_0 /\sigma(d_0) < 3$, $ \Delta z_0 \sin(\theta) < 0.5\text{mm}$	27.5 GeV	[0, 2.5]	(4) if $\Delta R < 0.4$ wrt jet & jet has ≥ 2 tracks
Photon	Tight, FixedCutTight	20 GeV	[0, 1.37] & [1.52, 2.37]	(5) if $\Delta R < 0.4$ wrt electron/muon
Jet	anti- k_t , $R = 0.4$, JVT > 0.59 when $p_T < 60$ GeV and $ \eta < 2.4$, b -jets: 77% WP	25 GeV	[0, 2.5]	(2) if $\Delta R < 0.2$ wrt electron (4) if $\Delta R < 0.4$ wrt muon & jet has < 2 tracks (6) if $\Delta R < 0.4$ wrt loose photon

Table 3: Summary of the object selection for electrons, muons, photons and jets, and their overlap removal (last column), with their removal order marked by numbers.

469 4.2 Prompt photon tagger

470 Photons originating from hadronic decays are uncorrelated to the initial hard interaction and are therefore
 471 considered background. Another important background contribution in this analysis are jets/hadrons
 472 misidentified as Tight photons. Both contributions are called *hadronic fakes* and are further discussed in
 473 Section 6. Photons from the hard interaction, on the other hand, are called *prompt photons*. To increase
 474 the purity of prompt photons in the set of Tight photon candidates and to suppress the contamination
 475 of hadronic fakes, an analysis-independent neural network (NN) was developed to classify photons, called
 476 *prompt-photon-tagger* (PPT).

477 The NN's architecture was developed and trained using Keras [39]. For reconstruction and application
 478 of the NN, the LightWeight Trained Neural Network library or LWTNN [40] is used. The input variables
 479 are chosen to be a subset of shower shape variables also used for photon identification, summarised in
 480 Table 4 [41]. The PPT classifies photon candidates in such a way that values towards 1 indicate prompt
 481 photons, whereas values towards 0 indicate hadronic fakes. Hence, the PPT is a binary classification tool.
 482 In this analysis, the full continuous PPT discriminant variable is used as an input to another event-level
 483 NN, further described in Section 5.2.

484 In Section 4.2.1 the NN training and results for the PPT are presented, and in Section 4.2.2 the procedure
 485 to estimate systematic uncertainties of the PPT is described.

name	description
Hadronic leakage	
R_{had} or $R_{\text{had}1}$	Transverse energy leakage in the hadronic calorimeter normalised to transverse energy of the photon candidate in the electromagnetic calorimeter. In the region $0.8 \leq \eta \leq 1.37$ the entire energy of the photon candidate in the hadronic calorimeter is used (R_{had}), while in the region $ \eta < 0.8$ and $ \eta > 1.37$ the energy of the first layer of the hadronic calorimeter is used ($R_{\text{had}1}$)
Energy ratios and width in the second layer of electromagnetic calorimeter	
R_η	Energy ratio of 3×7 to 7×7 cells in the $\eta \times \phi$ plane.
R_ϕ	Energy ratio of 3×3 to 3×7 cells in the $\eta \times \phi$ plane.
$w_{\eta 2}$	Lateral width of cluster in $\eta \times \phi = 3 \times 5$: $\sqrt{\frac{\sum_i E_i \eta_i^2}{\sum_i E_i} - \left(\frac{\sum_i E_i \eta_i}{\sum_i E_i}\right)^2}$
Energy ratios and widths in the first (strip) layer of electromagnetic calorimeter	
$w_{\eta 1}(w_{s3})$	Energy weighted width using 3 strips around the maximum: $\sqrt{\frac{\sum_i E_i (i - i_{\max})^2}{\sum_i E_i}}$
$w_{\text{tot},s1}(w_s)$	Energy weighted width using 20 strips around the maximum, see $w_{\eta,1}$.
f_{side}	Energy within 7 strips without 3 central strips normalised to energy in 3 central strips.
E_{ratio}	Ratio between difference of first 2 energy maxima divided by their sum ($E_{\text{ratio}} = 1$ if there is no second maximum).
ΔE	Difference between the second energy maximum and the minimum between first and second maximum ($\Delta E = 1$ if there is no second maximum).

Table 4: Summary of shower shape variables used for cut-based photon tight identification.

trigger name
HLT_g10_loose
HLT_g15_loose_L1EM7
HLT_g20_loose_L1EM12
HLT_g25_loose_L1EM15
HLT_g35_loose_L1EM15
HLT_g40_loose_L1EM15
HLT_g45_loose_L1EM15
HLT_g50_loose_L1EM15
HLT_g60_loose
HLT_g70_loose
HLT_g80_loose
HLT_g100_loose
HLT_g120_loose
HLT_g140_loose

Table 5: List of triggers to be passed for event selection in the PPT training.

486 **4.2.1 PPT training**

487 The photon candidates used to train the PPT are required to pass $p_T > 25$ GeV and $|\eta| < 2.37$, excluding
 488 the crack region where $1.37 < |\eta| < 1.52$. In addition, the candidates must fulfil the Tight photon
 489 identification criteria.⁴ To distinguish prompt photons and hadronic fakes, truth information is taken into
 490 account using `MCTruthClassifier` information. Prompt photons are required to originate from the hard
 491 interaction, that is, from either the matrix element calculation or the showering, as these types cannot be
 492 distinguished in the experiment. Objects identified as photons, but originating from hadronic decays or
 493 misidentified hadrons/jets are classified as hadronic fakes. Photons radiated by charged final-state leptons
 494 after hadronisation are not taken into account. The MC-generated events used for training the PPT are
 495 QCD-Compton processes containing prompt photons, as well as di-jet events with hadronic fakes. These
 496 samples are independent of those of the $t\bar{t}\gamma$ analysis and are listed in Table 40. Selected events have to
 497 pass triggers listed in Table 5. Good quality criteria in the detector are required and at least one photon
 498 has to be present according to the object definitions given above.

Variables were chosen as an input to the PPT based on their separation powers between prompt photons and hadronic fakes in MC events. The separation \mathcal{S} is calculated according to

$$\mathcal{S} = \frac{1}{2} \sum_{i \in \text{bins}} \frac{(s_i - b_i)^2}{(s_i + b_i)}, \quad (1)$$

499 where s_i and b_i are the number of prompt photons and hadronic fakes in bin i of the variable, respectively.

500 The calculated separation powers for all shower shape variables used as features, namely R_{had} , R_η , R_ϕ ,
 501 $w_{\eta,2}$, $w_{\eta,1}$ and f_{side} , are listed in Table 6. These variables were found to have the largest separation powers.
 502 Separation plots are shown in Figure 3. One key separation feature, reflected in the chosen input variables,

⁴ It is worth noting that, due to the analysis independence of the PPT, photon definitions do not have to match those used in the analysis exactly.

variable	separation
R_{had}	3.33 %
R_η	4.83 %
R_ϕ	7.01 %
$w_{\eta 2}$	2.01 %
$w_{\eta 1}$	4.14 %
f_{side}	7.21 %

Table 6: Separation power of shower shape variables calculated according to Eq. (1).

503 is the additional hadronic activity around hadronic fakes which leads to broader energy deposits in the
 504 electromagnetic calorimeter and larger hadronic leakage.

505 Figure 4 shows correlation matrices for the input variables and the other shower-shape variables, both
 506 for prompt photons and hadronic fakes. Between some of the input variables, for instance between R_η ,
 507 and $w_{\eta 2}$, correlations are as strong as -59.77% and -53.89% for prompt photons and hadronic fakes,
 508 respectively. Strong correlations are one of the reasons why simpler techniques, such as rectangular cuts on
 509 shower-shape variables, cannot be used to increase the separation between prompt photons and hadronic
 510 fakes efficiently. MVA techniques, on the contrary, take correlations between variables into account and
 511 are therefore applicable in this case.

512 Optimisations were done to determine the best NN architecture: the current PPT consists of 6 layers. The
 513 first, third and fifth layer contain 64, 40 and 52 neurons, respectively, of which the first uses a *rectified*
 514 *linear unit* activation function while the other two use a *softmax* activation function. The second and
 515 fourth layers are *batch normalisation* layers [42]. The final output layer comprises one single neuron with
 516 a *sigmoid* activation function.

517 About one million prompt photons and 200k hadronic fakes were used for training and testing the PPT,
 518 splitting the full set of samples into a training set with 80% and a test set with 20% of all samples. Figure 5
 519 shows the visualisation of the receiver operating characteristic (ROC) curves for both training and test
 520 samples. The ROC curves show the background rejection and the signal efficiency for different working
 521 points of the PPT. The two curves for training and test set overlay, therefore, the PPT can be generalised
 522 and applied to unseen data, that is, data that was not used within the training process.⁵ Both under- and
 523 overtraining could be avoided. The overall classification performance measure is given by the *Area Under*
 524 *Curve* (AUC) which is 0.8693 and 0.8690 for the training and test sets, respectively. The ROC curves and
 525 therefore the classification performances for the two sets are very similar. AUC values for different NN
 526 architectures and feature sets, all showing poorer performances, can be found in Appendix A.1.

527 In addition, the stability of the PPT training and the dependence of its performance on the training and
 528 test sets were evaluated by applying a 5-fold cross-validation. All samples were split into five orthogonal
 529 subsets. Each subset i was then once used as test set after the classifier had been trained on the remaining
 530 four subsets. Figure 5 shows the five ROC curves of the cross-validation. The largest obtained deviation is
 531 ≈ 0.0090 , which is small compared to the nominal performance. Hence, the trained PPT can be assumed
 532 to be stable with a reliable classification performance.

⁵ A necessary condition to draw this conclusion from overlaying training and test ROC curves is that the feature distributions in the training and test set agree with each other. That is the case within statistical uncertainties. The corresponding plots can be found in Appendix A.5.

533 In addition, the NN can be applied to the $t\bar{t}\gamma$ analysis MC samples described in Section 3 before event-level
 534 cuts. Figure 6 shows the PPT output values for different photon truth particle types. Truth type 20
 535 corresponds to $e \rightarrow \gamma$ fake photons. A value of 10 means the photon is classified as hadronic fake. For
 536 any value below 10, the photon is classified as signal-like, the exact source of which cannot be determined
 537 experimentally. For those signal-like photons a clear trend towards the signal-like region can be seen.
 538 The distribution for hadronic fake photons is flatter, with an increasing slope towards the background-like
 539 region. $e \rightarrow \gamma$ fake photons are classified to be more signal-like than background-like. This is expected
 540 as $e \rightarrow \gamma$ fake photons were not considered at any point in the PPT training.

541 4.2.2 Systematic uncertainties for the PPT

542 Systematics for the PPT within the $t\bar{t}\gamma$ analysis are derived conservatively from three dedicated PPT control
 543 regions. For all three regions, the analysis MC samples and experimental data introduced in Section 3
 544 as well as the data-driven fake lepton background derived in Section 6.3.1 are used. Scale factors for the
 545 $e \rightarrow \gamma$ fake and hadronic fake backgrounds derived in Sections 6.1 and 6.2 are not applied, as those were
 546 derived for the signal region only. The observed shape discrepancies between MC and data in the three
 547 regions are used as systematic variations.

548 In a dedicated hadronic fake control region, the PPT shape uncertainty with respect to hadronic fakes
 549 is estimated. The selection requirements are identical to those of the $e+\text{jets}$ and $\mu+\text{jets}$ signal regions
 550 described in Section 5.1, except for the reversed photon isolation requirements, that is, hadronic fake
 551 candidates must fail the `FixedCutTight` isolation working point. To further reduce signal contamination
 552 of the control region, track isolations of the photons are required to fulfil $p_T^{\text{cone}20} > 3$ GeV. A conservative
 553 method, comparing only shapes of the hadronic fake distributions, would be to remove the remaining
 554 signal contribution entirely. Another approach to avoid any sensitivity to the shape of the $t\bar{t}\gamma$ signal is to
 555 vary the signal contribution and choose the scenario that maximises shape differences between MC and
 556 data. To be conservative, scenarios with up and down variations of the signal of $\pm 50\%$ are tested. The
 557 shape differences between MC and data are found to be maximal with the $t\bar{t}\gamma$ signal scaled to 50%, hence,
 558 this scenario is chosen for the estimation of the shape systematics. After applying the $t\bar{t}\gamma$ signal scaling,
 559 all MC are scaled to data for shape comparison.

560 Good agreement between MC and data in the combined $e+\text{jets}$ and $\mu+\text{jets}$ control region can be seen for
 561 various observables in Figure 7. The histograms show an enhanced contribution of hadronic fakes due to
 562 the reversed photon isolation requirements. In Figure 9(a), the data/MC comparison plot of the PPT output
 563 is displayed.⁶ As the observed disagreement between data and MC shape is not covered by statistical
 564 uncertainties and because of expected dependencies of the PPT performance on η and p_T of the photon,
 565 the hadronic fake control region is further divided into three η and five p_T slices, the PPT distributions of
 566 which can be found in Figure 10. The discrepancies in the data/MC ratios are extracted from all individual
 567 slices and then applied as η and p_T -dependent systematic variations of the hadronic fake contributions in
 568 the signal regions.

569 As the hadronic fake systematic variations are extracted from a control region with orthogonal isolation
 570 requirements compared to the signal regions, an additional hadronic fake isolation control region is defined
 571 to extract a second systematic variation for hadronic fake contributions. The selection requirements follow
 572 those of the $e+\text{jets}$ and $\mu+\text{jets}$ signal regions, except for the reversed photon ID requirements, that is,
 573 hadronic fake candidates must fail the `Tight ID` cuts. In Figure 9(b), the data/MC comparison plot of the

⁶ Plots, where the $t\bar{t}\gamma$ signal contribution is increased to 150% can be found in Figures 100 and 101 in Appendix A.2.

574 PPT output is displayed. The hadronic fake isolation control region is divided into three η and three p_T
575 slices, for which the PPT output distributions can be found in Figure 11. The discrepancies in the data/MC
576 are extracted from the individual slices and are also applied as systematic variations of the hadronic fake
577 contributions in the signal regions.

578 In a third PPT control region, where prompt photons from processes other than $t\bar{t}\gamma$ are enhanced, the PPT
579 shape uncertainty for prompt photons is estimated. The selection requirements are identical to those of the
580 ee and $\mu\mu$ signal regions described in Section 5.1, with removed cuts on the number of jets and b -jets to
581 increase statistics. Additionally, to suppress signal contamination, the invariant mass of the dilepton pair
582 is required to be within [60, 100] GeV. Again, the MC distribution is scaled to data to extract the shape
583 differences. Control plots with ee and $\mu\mu$ combined are shown in Figure 8 with good agreement between
584 MC and data. The PPT output distribution in the prompt-photon control region in Figure 9(c) shows a
585 clear slope in the data/MC ratio. Again, the control region is divided into three η and five p_T slices to
586 account for different PPT behaviour for different photon kinematics. The PPT distributions of all slices
587 are shown in Figure 12. As the PPT prompt control region covers photons that are identical to those in the
588 signal regions in terms of ID and isolation requirements, the observed shape discrepancies in the data/MC
589 ratio are extracted and applied as a correction to the PPT values of the prompt contributions in the signal
590 regions. On top of that, the extracted shape discrepancies are additionally applied as η and p_T -dependent
591 systematic variations to the prompt contributions in the signal regions.

Not reviewed, for internal circulation only

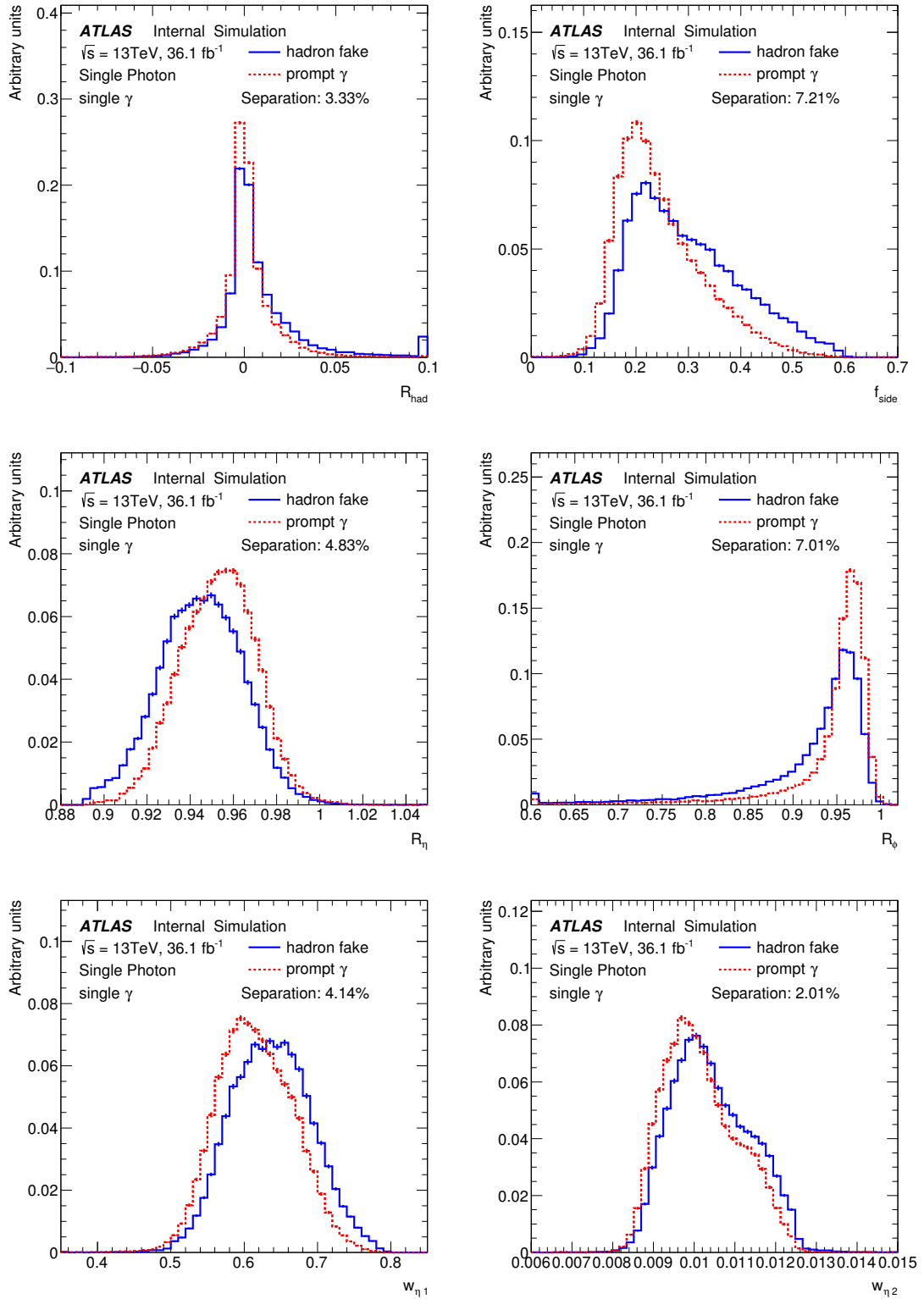


Figure 3: Distribution of shower-shape variables R_η , R_ϕ , R_{had} , f_{side} , $w_{\eta,1}$ and $w_{\eta,2}$ for prompt photons (red) and hadronic fakes (blue), both normalised to unity.

Not reviewed, for internal circulation only



(a) Shower-shape correlations for prompt photons.



(b) Shower-shape correlations for hadronic fakes.

Figure 4: Correlations between shower shape variables as described in Table 4.

Not reviewed, for internal circulation only

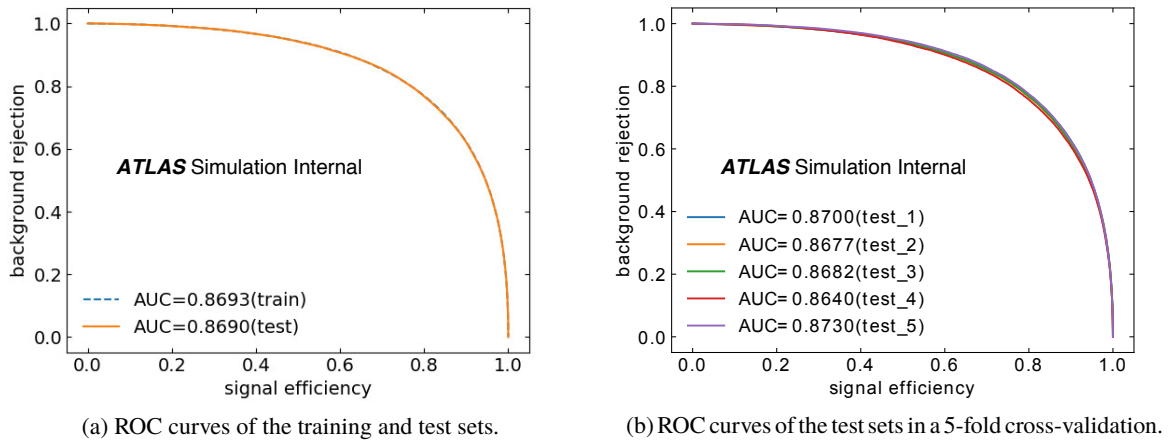


Figure 5: ROC curves of training and test sets as well as those obtained in a 5-fold cross-validation.

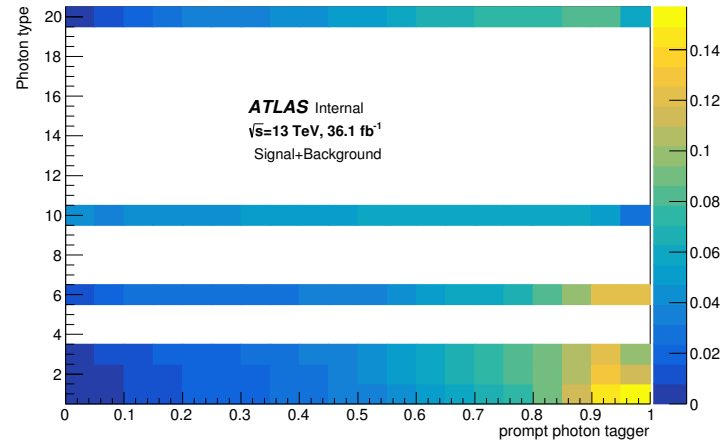


Figure 6: PPT output distributions for different photon truth particle types. The distributions are obtained by applying the PPT to the $t\bar{t}\gamma$ analysis MC samples before event-level cuts. Truth type 20 corresponds to $e \rightarrow \gamma$ fake photons. 10 means the photon is classified as an hadronic fake. Anything below 10 is a signal-like photon. All rows were normalised to unity individually.

Not reviewed, for internal circulation only

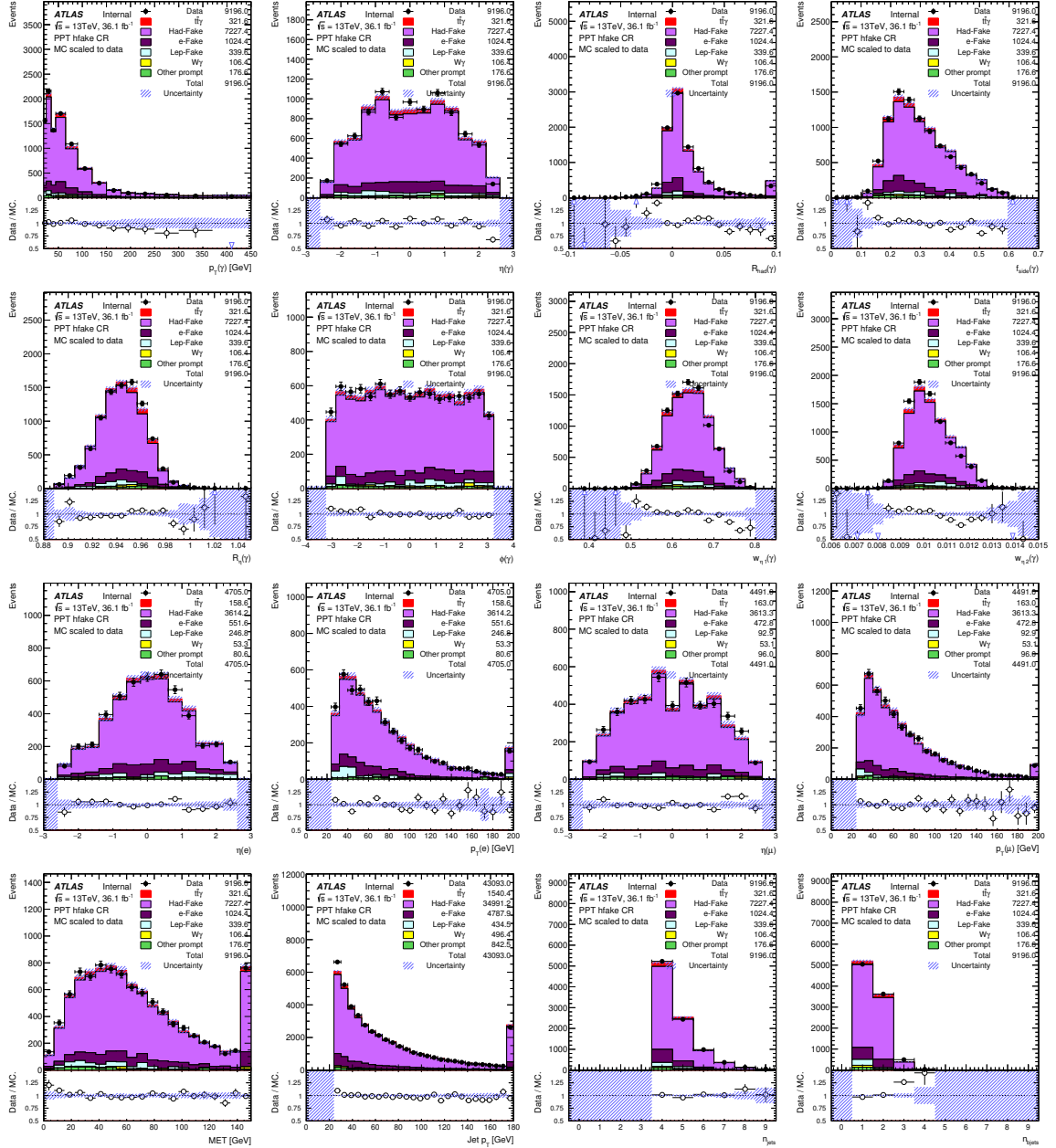


Figure 7: Control plots in the PPT hadronic fake control region, including distributions of the photon shower shape variables R_{had} , f_{side} , R_η , R_ϕ , $w_{\eta 1}$ and $w_{\eta 2}$ used as input to the NN. The $t\bar{t}\gamma$ signal is decreased to 50% and the total MC is scaled to data for shape comparisons. The displayed uncertainties are statistical only.

Not reviewed, for internal circulation only

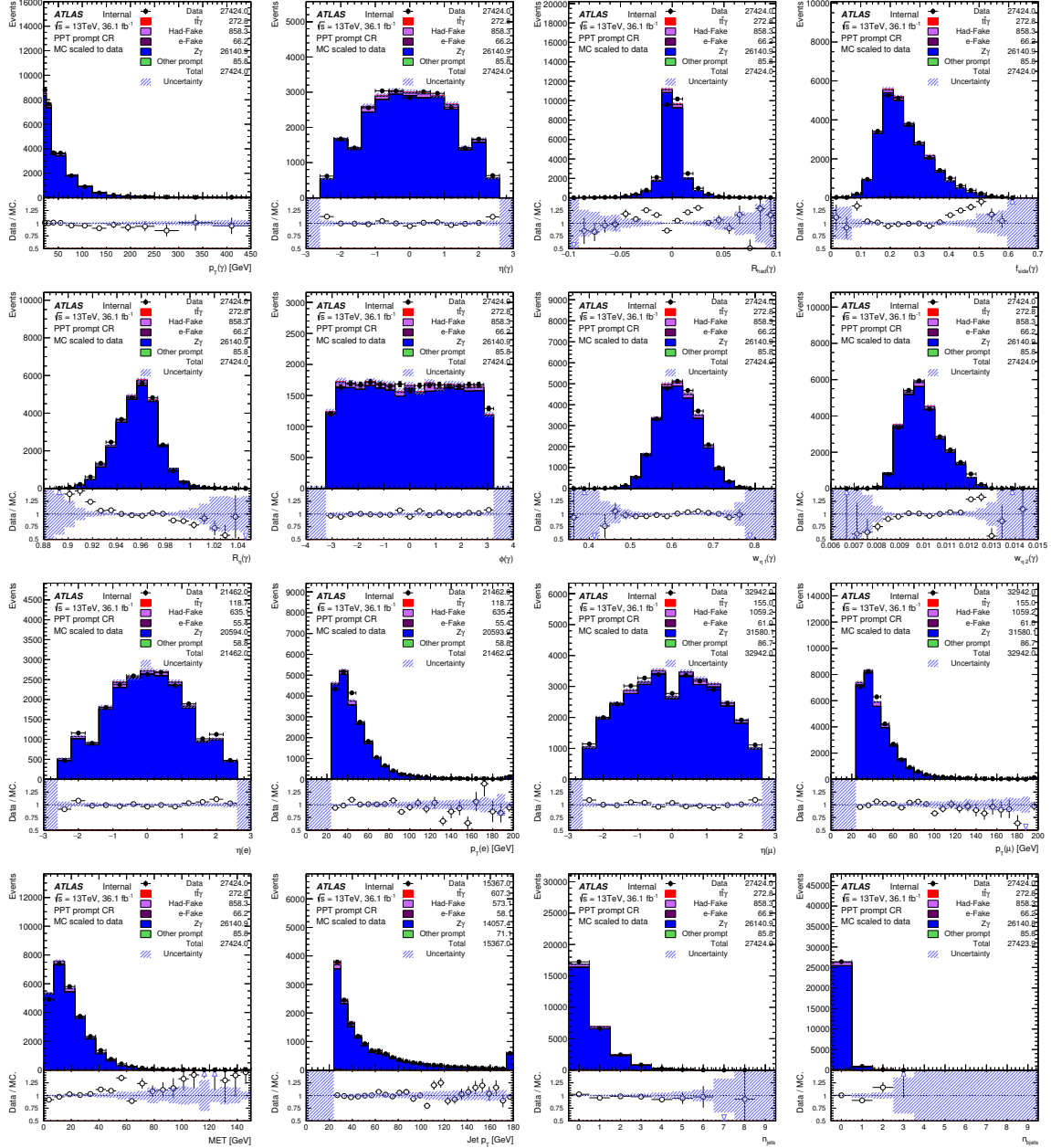


Figure 8: Control plots in the PPT prompt-photon control region, including distributions of the photon shower shape variables R_{had} , f_{side} , R_{η} , R_{ϕ} , $w_{\eta 1}$ and $w_{\eta 2}$ used as input to the NN. MC is scaled to data for shape comparisons. The displayed uncertainties are statistical only.

Not reviewed, for internal circulation only

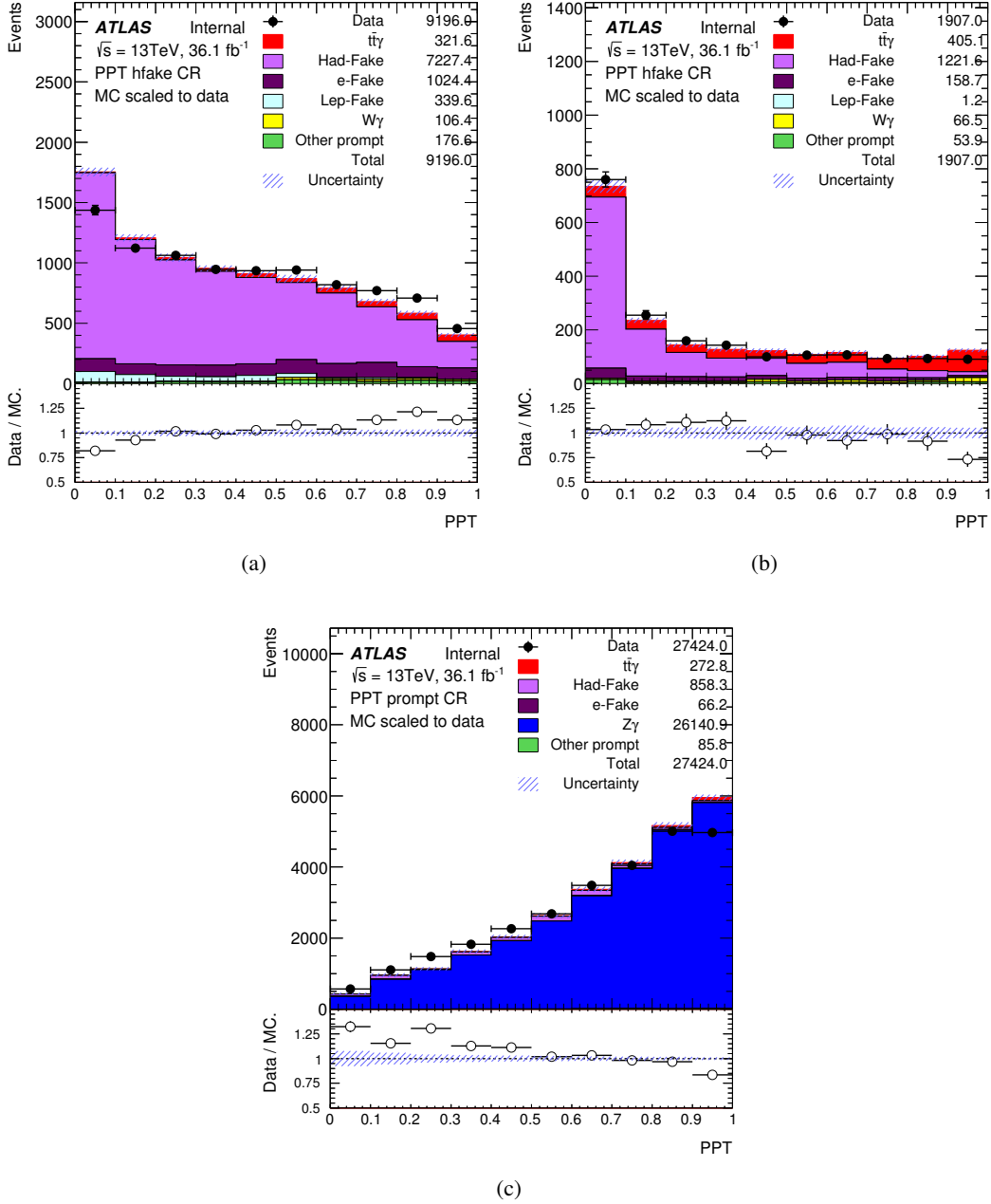


Figure 9: PPT distributions for (a) the hadronic fake control region, (b) the additional hadronic fake isolation control region and (c) the prompt photon control regions. For the hadronic fake control region shown in (a), the signal contribution is decreased to 50% to maximise shape differences. MC is scaled to data for shape comparison and only statistical uncertainties are included. The observed shape differences in the MC/data ratios of the three control regions are used as systematic variations of the PPT shape.

Not reviewed, for internal circulation only

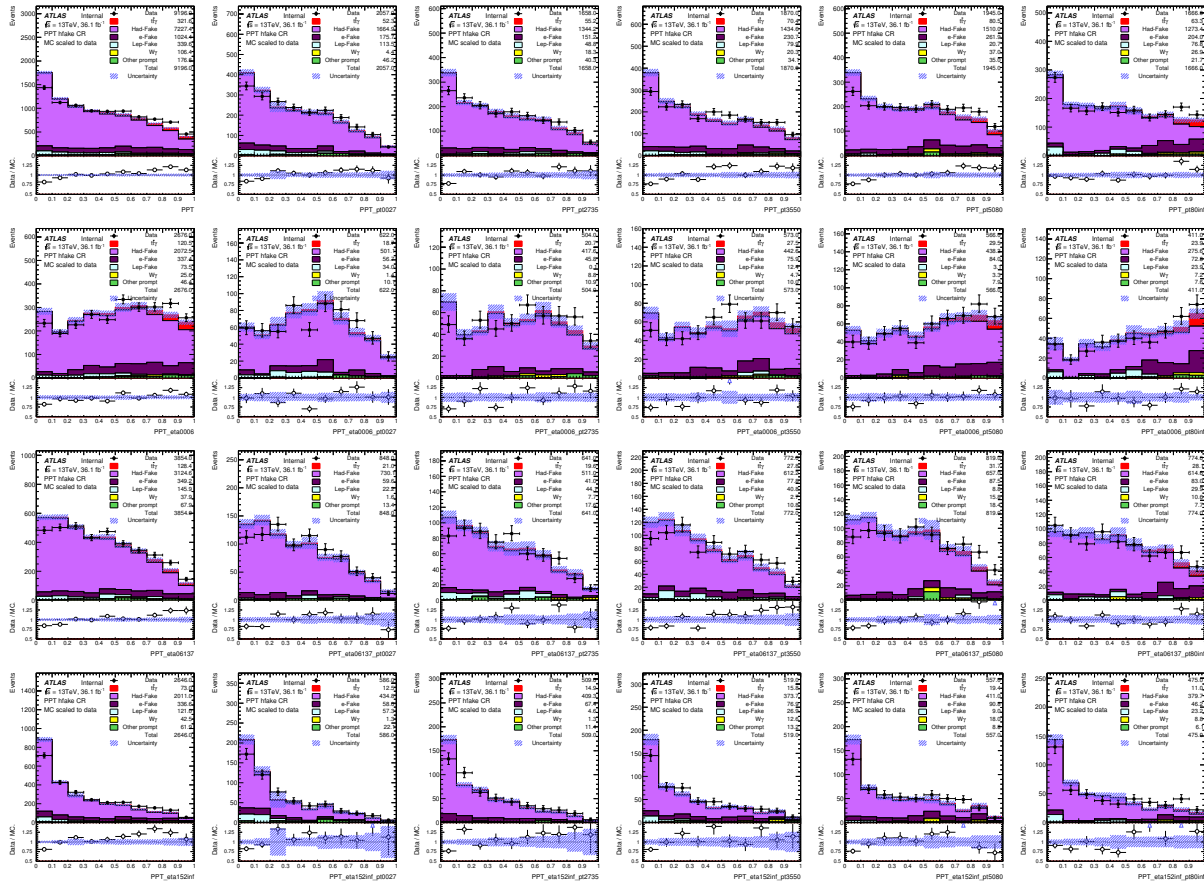


Figure 10: PPT output distributions for η and p_T slices in the PPT hadronic fake control region. While the top left distribution shows the full inclusive PPT distribution (identical to Figure 9(a)), the rows correspond to slices of η and the columns to slices of p_T . MC is scaled to data for shape comparisons. The displayed uncertainties are statistical only. The observed shape discrepancies in the data/MC ratio are extracted individually and used as systematic variations of the hadronic fake contributions in the signal regions.

Not reviewed, for internal circulation only

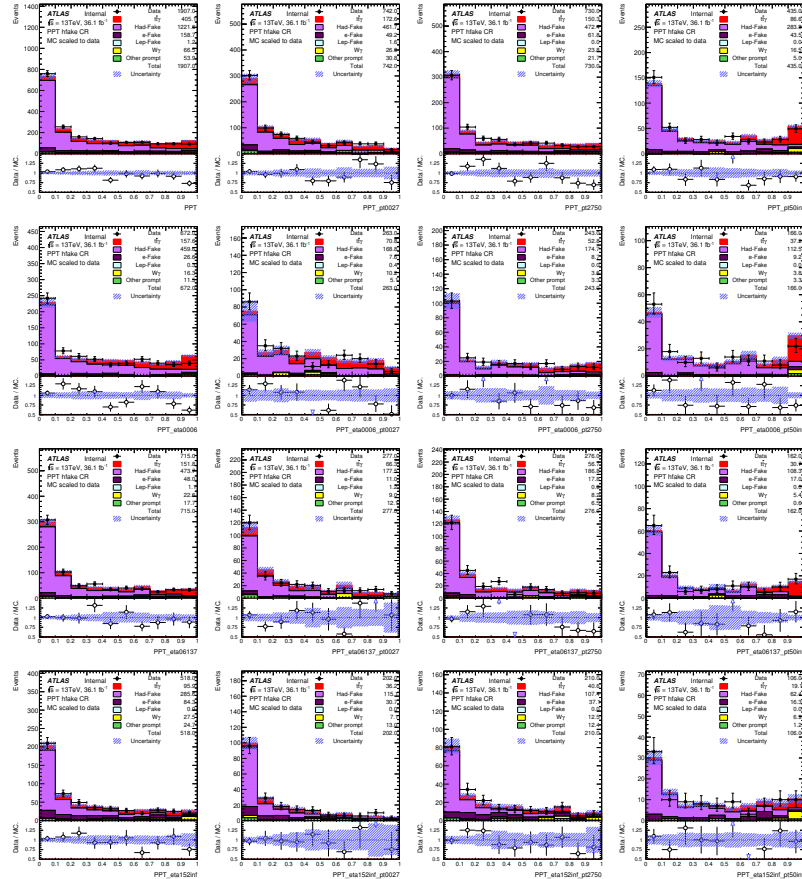


Figure 11: PPT output distributions for η and p_T slices in the additional PPT hadronic fake isolation control region. While the top left distribution shows the full inclusive PPT distribution (identical to Figure 9(b)), the rows correspond to slices of η and the columns to slices of p_T . MC is scaled to data for shape comparisons. The displayed uncertainties are statistical only. The observed shape discrepancies in the data/MC ratio are extracted individually and used as systematic variations of the hadronic fake contributions in the signal regions.

Not reviewed, for internal circulation only

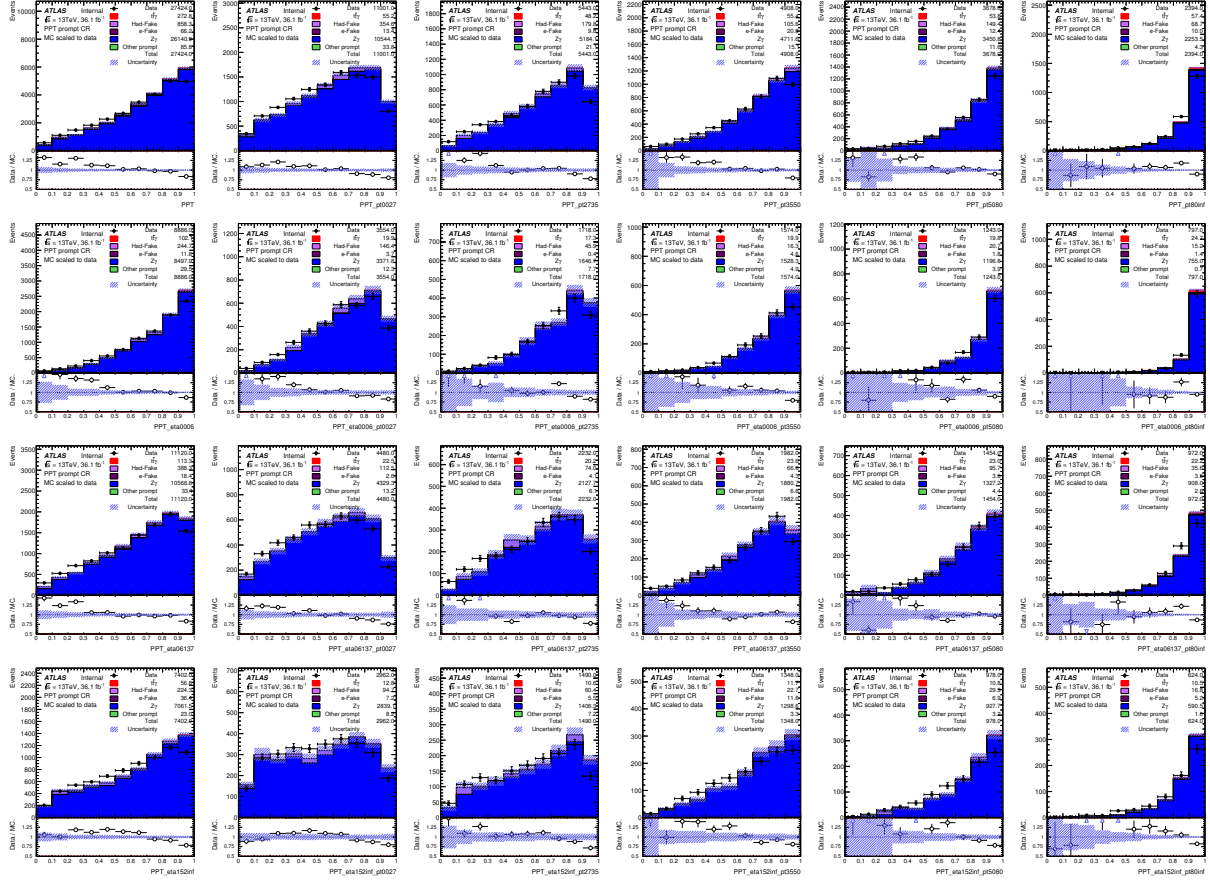


Figure 12: PPT output distributions for η and p_T slices in the PPT prompt control region. While the top left distribution shows the full inclusive PPT distribution (identical to Figure 9(c)), the rows correspond to slices of η and the columns to slices of p_T . MC is scaled to data for shape comparisons. The displayed uncertainties are statistical only. The observed shape discrepancies in the data/MC ratio are extracted and applied as a correction to the PPT values of the prompt contributions in the signal regions. In addition, the extracted shape discrepancies are applied as systematic variations.

592 5 Signal region definition

593 5.1 Event selection

594 This analysis has been realized with data harvested during 2015 and 2016, at a center-of-mass of energy
 595 of $\sqrt{s} = 13$ TeV. Only luminosity blocks of recorded data satisfying good quality criteria in the detector
 596 have been considered. This corresponds to a total integrated luminosity of 3212.96 pb^{-1} in 2015 and
 597 32884.6 pb^{-1} in 2016. The uncertainty for the combined integrated luminosity is 2.1%. It is derived,
 598 following a methodology similar to that detailed in [43], from a calibration of the luminosity scale using
 599 x-y beam-separation scans performed in August 2015 and May 2016.

600 Each event is required to have at least one reconstructed primary vertex, obtained from at least two
 601 tracks.

602 Each event is required to have fired at least one lepton trigger. The considered triggers are summarised in
 603 Table 7. The lepton triggers definition and associated scale factors are described in [28] and [44].

Year	electron trigger	muon trigger
2015	HLT_e24_lhmedium_L1EM20VH or HLT_e60_lhmedium or HLT_e120_lhloose	HLT_mu20_iloose_L1MU15 or HLT_mu50
2016	HLT_e26_lhtight_nod0_ivarloose or HLT_e60_lhmedium_nod0 or HLT_e140_lhloose_nod0	HLT_mu26_ivarmedium or HLT_mu50

Table 7: The lepton triggers considered in the event selections.

604 The rest of the selection depends on the considered decay channel:

- 605 • The single lepton channels are characterized by the presence of only one reconstructed lepton, while
 606 the dilepton channels are characterized by the presence of exactly two leptons. For $e+jets$ and ee
 607 channels, at least one electron trigger amongst the ones described previously should be fired, while
 608 for $\mu+jets$ and $\mu\mu$ channels, at least one muon trigger should be fired. For the $e\mu$ channel, at least
 609 one trigger should be fired which can be an electron trigger or a muon trigger. In order to be
 610 consistent with the trigger requirement, in addition to satisfying the lepton requirements described
 611 in Section 4.1, the minimum p_T of the highest p_T lepton is required to be 27 GeV (27.5 GeV) in
 612 the 2016 selection for electron (muon). At least one of the selected leptons in the event should be
 613 matched to a fired trigger.
- 614 • If the event appears to have badly reconstructed jets (based on criteria on energy fraction variables,
 615 using the LooseBad working point [45]) or badly reconstructed muons (inconsistency of the q/p
 616 uncertainty between the combined and the local tracks), this event is rejected.
- 617 • In the single lepton channels, at least four reconstructed jets are required. In the dilepton channels,
 618 at least two reconstructed jets are required.
- 619 • In the dilepton channels, the leptons are required to be of opposite charges, and to have an invariant
 620 mass larger than 15 GeV.
- 621 • For all channels, exactly one reconstructed photon in the event is required, satisfying the requirements
 622 described in Section 4.1.

- Event double counting removal: In the $W+\text{jets}$, $Z+\text{jets}$ and $t\bar{t}$ MC samples, the events with a prompt photon are removed based on the truth information, to avoid a double counting with the dedicated $W\gamma$, $Z\gamma$ and $t\bar{t}\gamma$ MC samples (more detail in Section 3.2).
- At least one b-tagged jet at a working point of 77% [37] is required for all the channels.
- E_T^{miss} : For the ee and $\mu\mu$ dilepton channels, $E_T^{\text{miss}} > 30 \text{ GeV}$.
- $m(\ell, \ell)$: For the ee and $\mu\mu$ dilepton channels, an invariant mass veto between the two leptons in the window [85,95] GeV.
- $m(\ell, \ell, \gamma)$: For the ee and $\mu\mu$ dilepton channels, an invariant mass veto between the two leptons and the photon in the [85,95] GeV.
- $m(\gamma, e)$: For the $e+\text{jets}$ channel, an invariant mass veto between the photon and the electron in the window $[m(Z)-5, m(Z)+5] \text{ GeV}$, where $m(Z)$ is the invariant mass of the Z boson.
- $\Delta R(\gamma, \ell)$: In all channels, the distance between the prompt photon and the lepton must be greater than 1.0. This is to limit the contribution from the photons originating from radiative decay. Further studies on this have been done and can be found in Appendix C.

The event selection for all channels are summarised in Table 8.

Channel	$e+\text{jets}$	$\mu+\text{jets}$	ee	$\mu\mu$	$e\mu$	
Primary vertex, Event cleaning, Run number, etc.						
Common	1 e	1 μ	2 e , OS	2 μ , OS	1 $e + 1 \mu$, OS	
	Trigger match					
	-		$m(\ell, \ell) > 15 \text{ GeV}$			
	1 γ with $p_T > 20 \text{ GeV}$					
Photon	≥ 4		≥ 2			
Jet	≥ 4		≥ 2			
b -jet			≥ 1			
$m(\ell, \ell)$	-		not in [85,95] GeV		-	
$m(\ell, \ell, \gamma)$	-		not in [85,95] GeV		-	
E_T^{miss}	-		$> 30 \text{ GeV}$		-	
$m(\gamma, e)$	not in [85,95] GeV		-			
$\Delta R(\gamma, \ell)$	> 1.0					

Table 8: Summary of the event selections.

Yields for the above mentioned cuts can be found in Table 9. A selection of pre-fit plots for each channel can be found in Figures 13, 14, 15, 16 and 17. In these plots, only statistical uncertainties are shown. For the $\mu\mu$ and ee channels larger statistical error bars can be seen for the $Z\gamma$ background. This is due to slightly larger than normal weights and is addressed in Appendix O.

5.2 Event level MVA

5.2.1 Discriminator for single lepton and dilepton channels

After the event selection, a multivariate discriminator at event level (ELD) has been developed separately for the single lepton and dilepton channels, and takes the form of neural networks.

	$e+jets$	$\mu+jets$	ee	$\mu\mu$	$e\mu$
$t\bar{t}\gamma$	3207 ± 14	3200 ± 13	145 ± 3.0	174 ± 3.1	401 ± 5.2
hadronic fake	440.6 ± 13	457.2 ± 14	7.2 ± 1.5	5.7 ± 2.2	17.6 ± 2.5
$e \rightarrow \gamma$ fake	773.68 ± 21	603.84 ± 16	0.46 ± 0.27	0.24 ± 0.54	1.07 ± 0.71
Lep fake	293 ± 35	63 ± 22	-	-	-
$W\gamma$	541 ± 29	579 ± 34	-	-	-
$Z\gamma$	-	-	21 ± 3.8	54 ± 14	-
Other prompt	410.5 ± 47	274.6 ± 15	5.1 ± 1.2	4.4 ± 0.84	8.3 ± 1.2
Total	5665 ± 71	5178 ± 50	179 ± 5.2	238 ± 14	428 ± 5.9
Data	6002	5660	196	233	473

Table 9: Pre-fit yields for each background and channel. Only statistical uncertainties are included. Scale factors for the different backgrounds are not included.

Not reviewed, for internal circulation only

646 Training was carried out on the full set of MC samples described in Section 3 and the data-driven fake
 647 lepton sample described in Section 6.3.1. Keras was used to train the neural networks and LWTNN was
 648 used to reconstruct them within analysis code.

649 For the single lepton training, the full set of selection cuts defined in Section 5.1 were applied. Looser
 650 cuts were used to train the dilepton NN. This includes dropping the two mass window cuts between the two
 651 leptons and the two leptons and the photon, neglecting the E_T^{miss} cut and not requiring a cut on the number
 652 of jets. This allows for more background contamination, enhances statistics and thus makes training more
 653 stable. Training only in the signal region (or close to the signal region) on events that are either signal
 654 or background in the final selection means the weights reach optimal values in a shorter amount of time.
 655 Each feature (or input variable) has been normalized to give a standard deviation of 1 and a mean of 0.

656 5.2.2 Variable selection and training

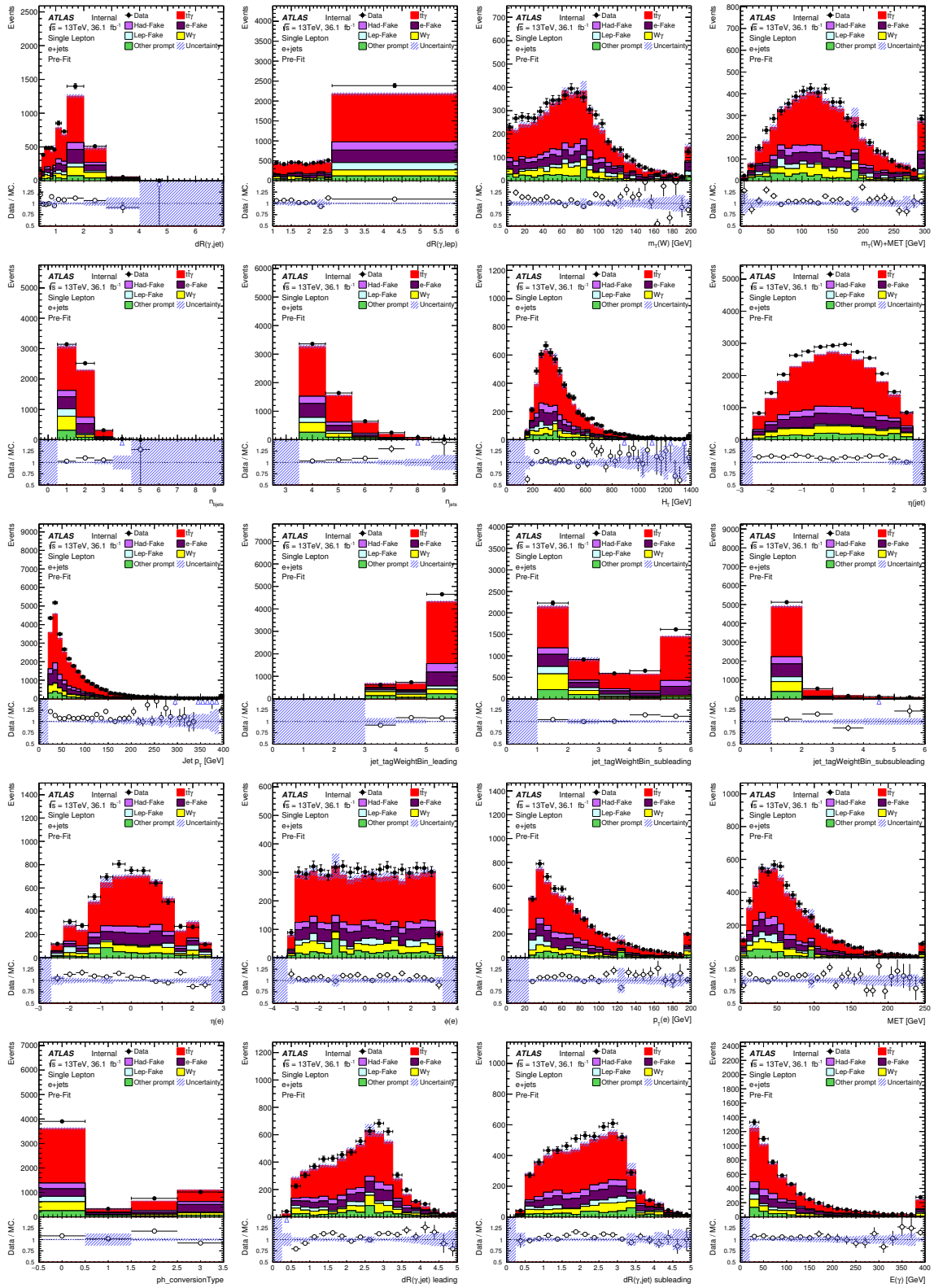
657 Each of the neural networks had hyper-parameter grid searches performed to achieve the best architecture
 658 and thus maximum separation.

659 The NN final topology is the same for single lepton and dilepton channels: 1 input dense layer consisting
 660 of 30 nodes is followed by a dropout layer then a batch normalization layer. A dense layer of 20 nodes
 661 follows with a final dense output layer consisting of 1 node with a sigmoid activation function to reduce
 662 outputs to values between 0 and 1. All layers' weights are initialized with uniform distributions and input
 663 and hidden layers receive a rectified linear unit (ReLU) activation function.

664 The dropout layer has a 30% chance that any node and its weights will randomly be removed from the
 665 epoch. This ensures that the network does not become too dependent on a node, which results in over-
 666 training. The batch normalization layer helps limit internal covariate shift in the weights that can occur
 667 due to fluctuations in the training set, and as a side effect, speeds up training.

668 The single lepton NN uses 75% of the raw input events for training with 25% used for testing. This
 669 equates to 144491 events used for training and 48164 events used for testing. Accumulatively, there are
 670 160679 signal and 31976 background events. The dilepton NN uses 67% of the raw input events for
 671 training with 33% used for testing. This equates to 20258 events used for training and 10160 events
 672 used for testing. Accumulatively, there are 21591 signal and 8827 background events. The ratio of the
 673 split between training and testing is done to ensure that when separate K-Fold validation is performed the

Not reviewed, for internal circulation only



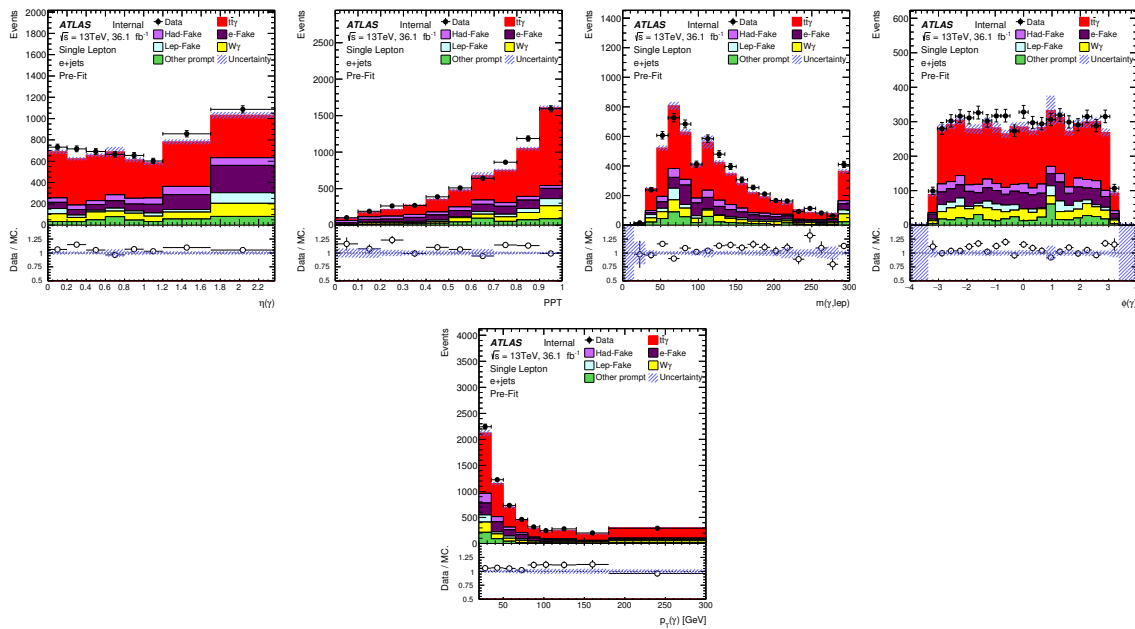


Figure 13: A selection of pre-fit distributions for the $e+jets$ channel. Only statistical uncertainties are included.

674 training and test samples can be split consistently into 4 and 3 different tests for single lepton and dilepton,
675 respectively.

676 The single lepton NN is trained using a batch size of 150 events while the dilepton NN uses 300 events. This
677 describes the number of events used for each gradient update. Optimisation for batch size was performed
678 using a grid search. Event weights are accounted for by scaling the *binary cross-entropy* loss function
679 during training, with negative event weights set to 0.

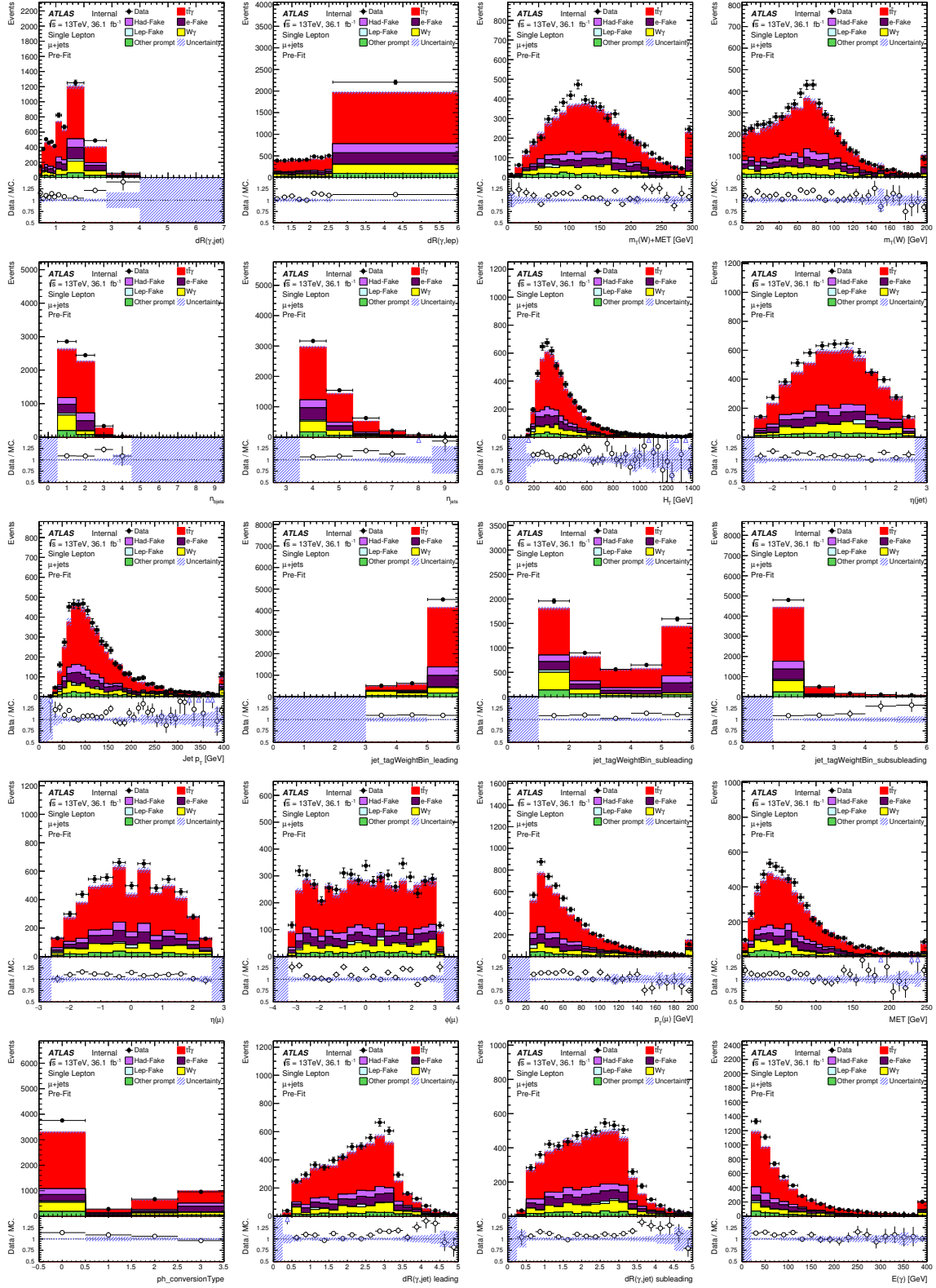
680 A range of potentially interesting variables were ranked by their signal/background separation (Equation 1)
681 to determine the priority in which different trainings were performed. The rankings for each channel are
682 shown in Table 10. A check mark means it was used in the final NN configuration. Of note, the variables
683 $p_T(\gamma)$, $\eta(\gamma)$, $dR(\gamma, \ell)$ and $dR(\gamma, jet)$ were neglected from this optimisation due to being considered for
684 differential measurements. Tables 11 and 12 show the ROC curve results for the training and test batches
685 when performed on an increasing number of variables (added according to separation rank).

686 In both cases, the NN performs the best with the most number of variables considered. However, for the
687 dilepton NN with more than 7 variables we see larger variations between multiple trainings and testings
688 and so with the limited statistics it's deemed more unstable with over training likely to occur. As a results
689 the network using 7 variables was selected. The distributions for the chosen variables in the combined
690 single lepton and dilepton channels are shown in Figures 18 and 19. These plots show the distributions
691 with the respective full signal region cuts applied.

692 Figure 20 shows the single lepton and dileptonNN's' response as well as the ROC curves for training on
693 seen and unseen training data.

694 A further check to ensure over-training has not occurred is to perform k-fold cross-validation on training
695 data. In this test, the data has been split into 4 separate batches for the single lepton case and 3 separate
696 batches for the dilepton case. One batch is used as a validation or test set, the other two or three are used

Not reviewed, for internal circulation only



Not reviewed, for internal circulation only

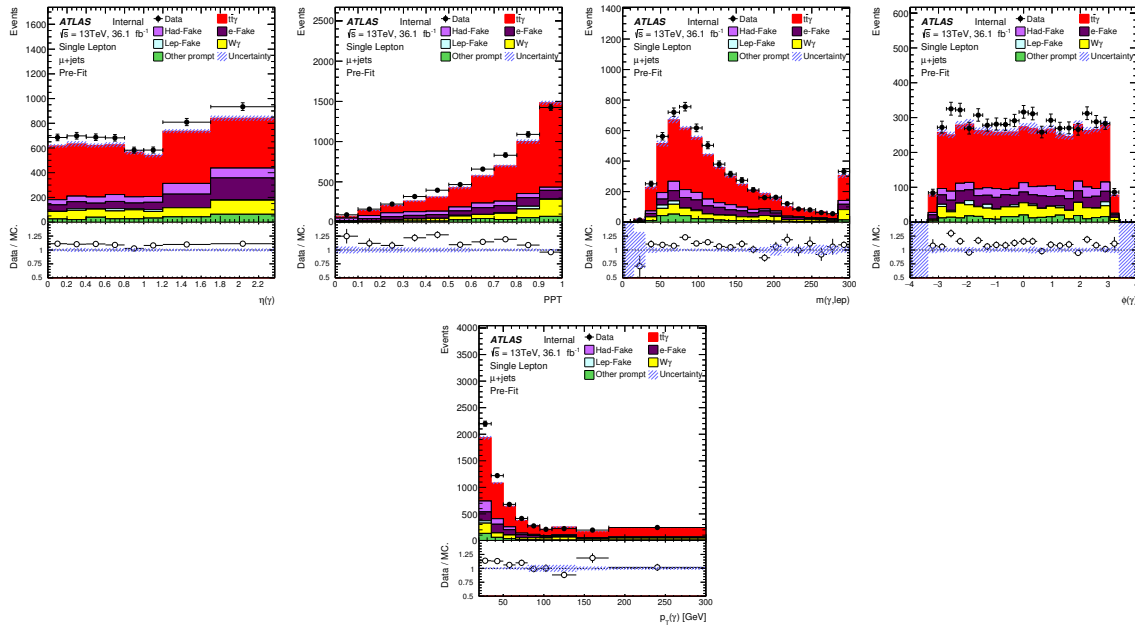
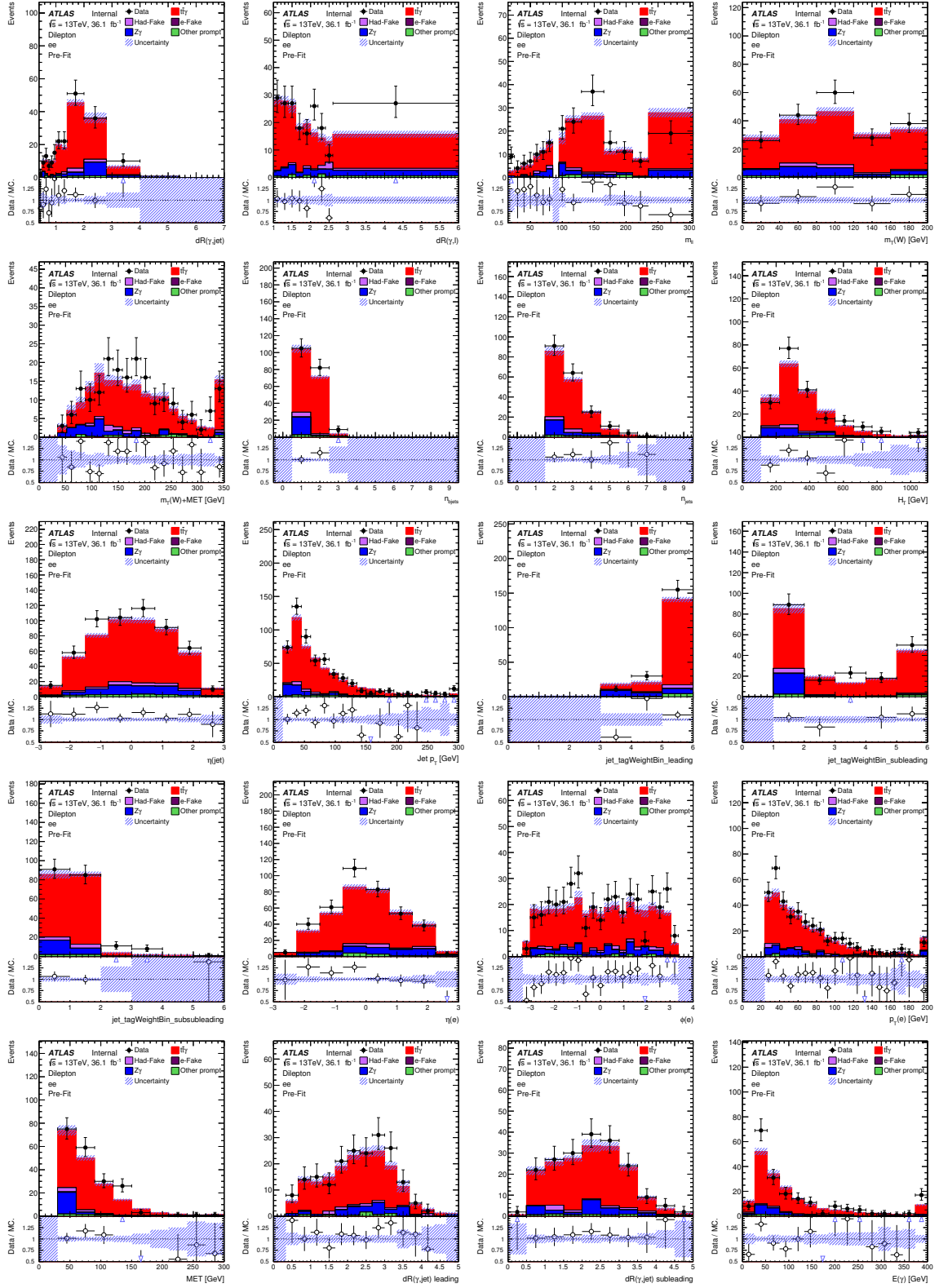


Figure 14: A selection of pre-fit distributions for the μ +jets channel. Only statistical uncertainties are included.

Table 10: Separation of each variable used in the training of the single lepton and dilepton NN’s. A check mark indicates that the variable was used in that NN.

Variable	single lepton separation (%)	dilepton separation (%)
Prompt Photon Tagger	3.46 ✓	6.76
H_T	1.79 ✓	1.32
number of jets	0.71 ✓	1.41
number of bjets	3.48 ✓	11.00 ✓
E_T^{miss}	0.78 ✓	12.8 ✓
$m_T(W)$	0.86 ✓	1.99
p_T of first jet	2.05 ✓	11.4 ✓
p_T of second jet	1.77 ✓	7.72 ✓
p_T of third jet	1.72 ✓	3.29
p_T of fourth jet	1.30 ✓	1.13
p_T of fifth jet	0.92 ✓	0.262
jet with first highest MV2C10 tag weight	8.96 ✓	10.5 ✓
jet with second highest MV2C10 tag weight	7.23 ✓	13.6 ✓
jet with third highest MV2C10 tag weight	5.4 ✓	-
$m(\ell, \ell)$	-	13.4 ✓
$m(\gamma, \ell)$	0.32 ✓	5.79
$m(\gamma, \ell, \ell)$	-	2.32
$dR(\gamma, \ell)$	0.45	13.4
$dR(\gamma, \text{jet})_{\text{leading}}$	1.80	3.07
$dR(\gamma, \text{jet})_{\text{subleading}}$	1.71	4.3

Not reviewed, for internal circulation only



Not reviewed, for internal circulation only

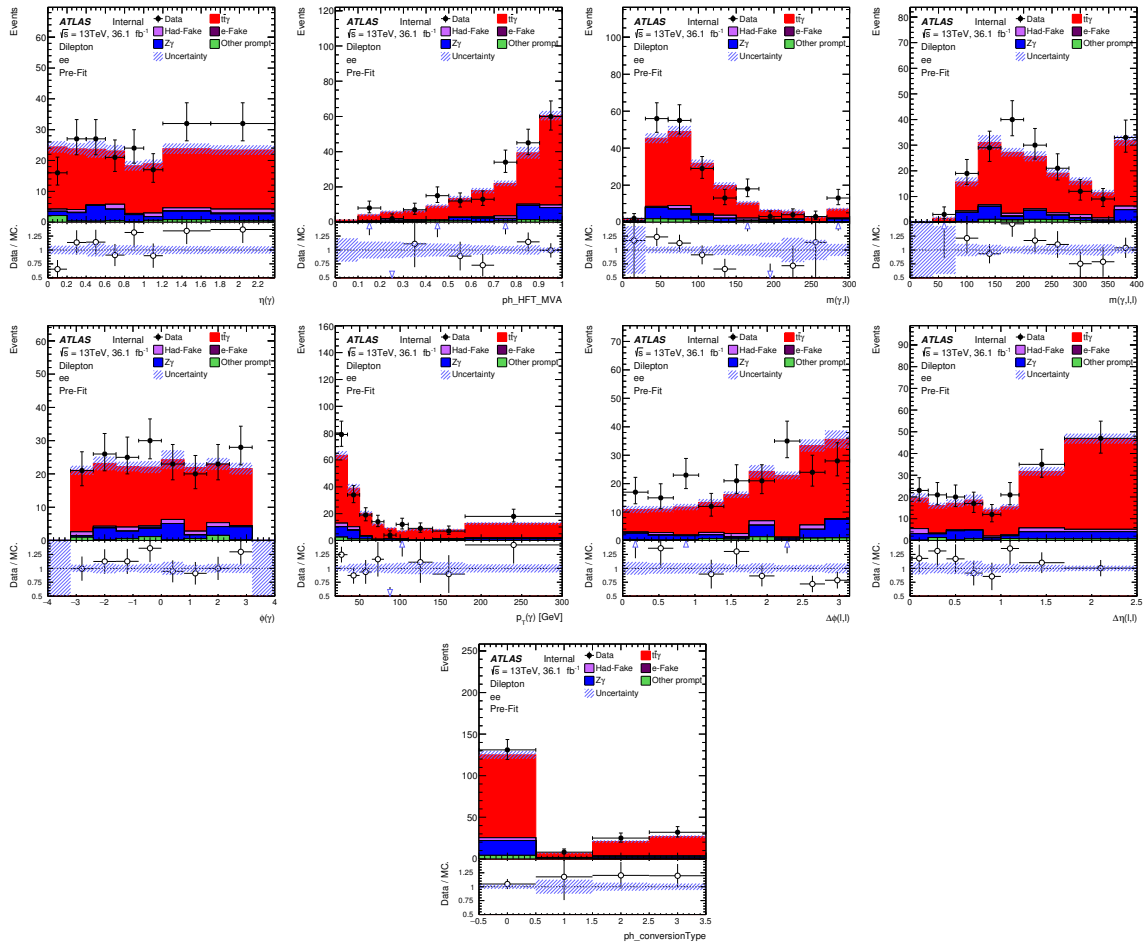


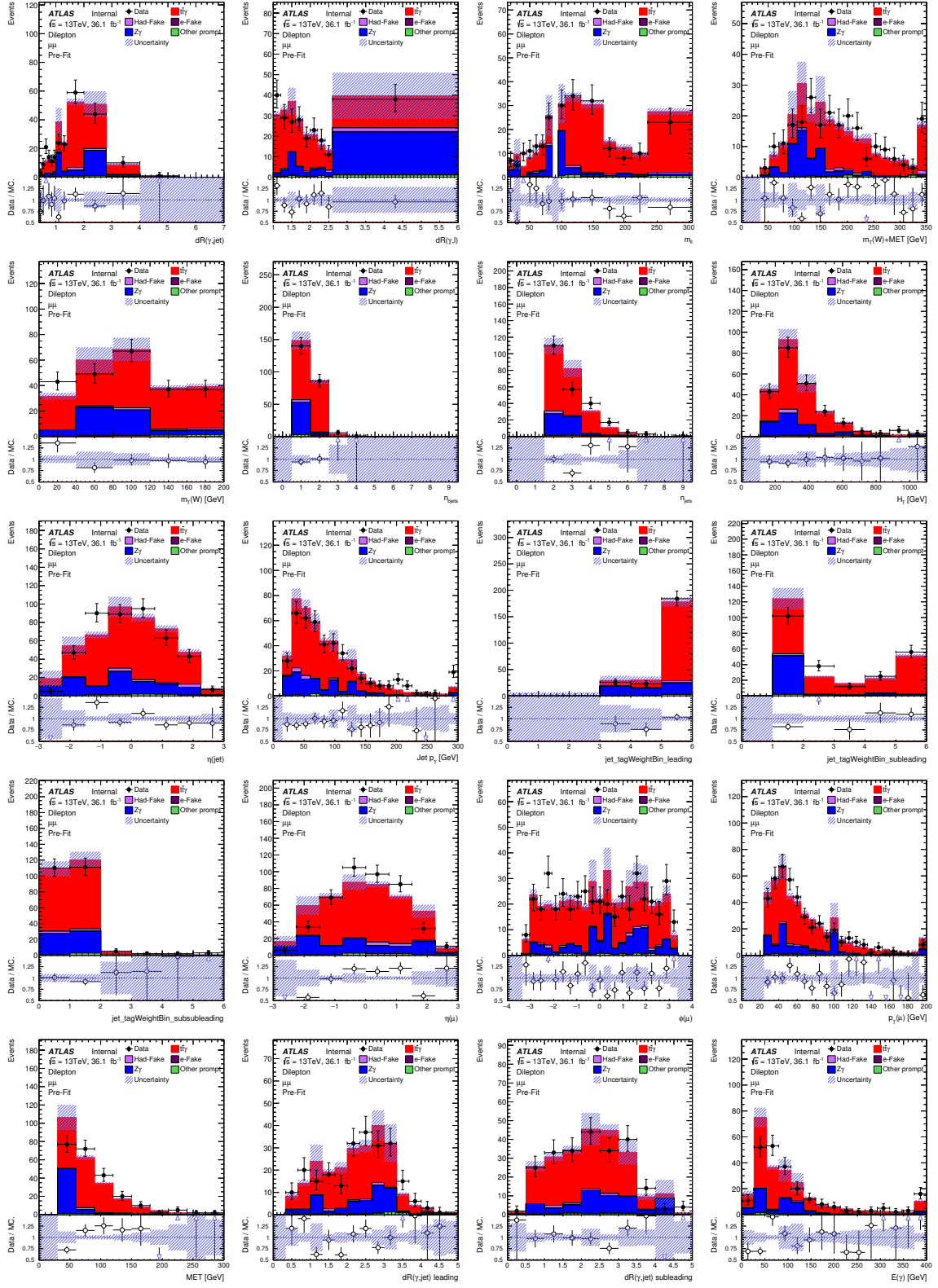
Figure 15: A selection of pre-fit distributions for the ee channel. Only statistical uncertainties are included.

Table 11: Variable optimisation for the single lepton NN. The starting point is the first row. Each subsequent row includes more variables described on top of the previous row. Variables are chosen according to separation rank.

Variables	ROC (train)	ROC (test)	Selected NN
(5) jet btag weight leading, jet btag weight subleading, jet btag weight subsubleading, PPT, number of bjets	0.6483	0.6474	
(10) +, p_T of first jet, H_T , p_T of second jet, p_T of third jet, p_T of fourth jet	0.6744	0.6736	
(14) +, p_T of fifth jet, $m_T(W)$, E_T^{miss} , number of jets,	0.6996	0.6906	
(15) +, $m(\gamma, \ell)$	0.7017	0.6929	✓

for training the NN. Each batch has a turn to be the test set. All ROC curves should be comparable with each other and only deviate slightly from the initial ROC curve (due to statistical fluctuations). The k-fold

Not reviewed, for internal circulation only



Not reviewed, for internal circulation only

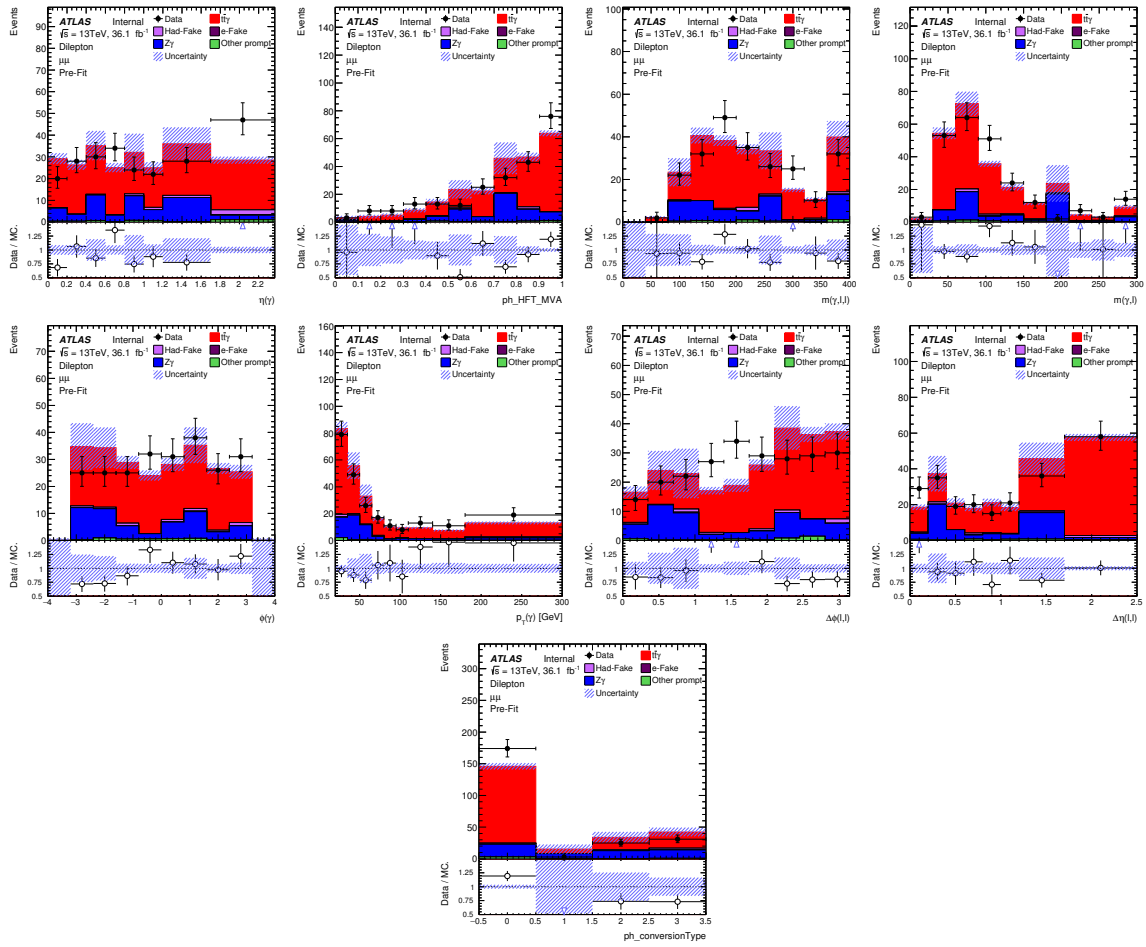


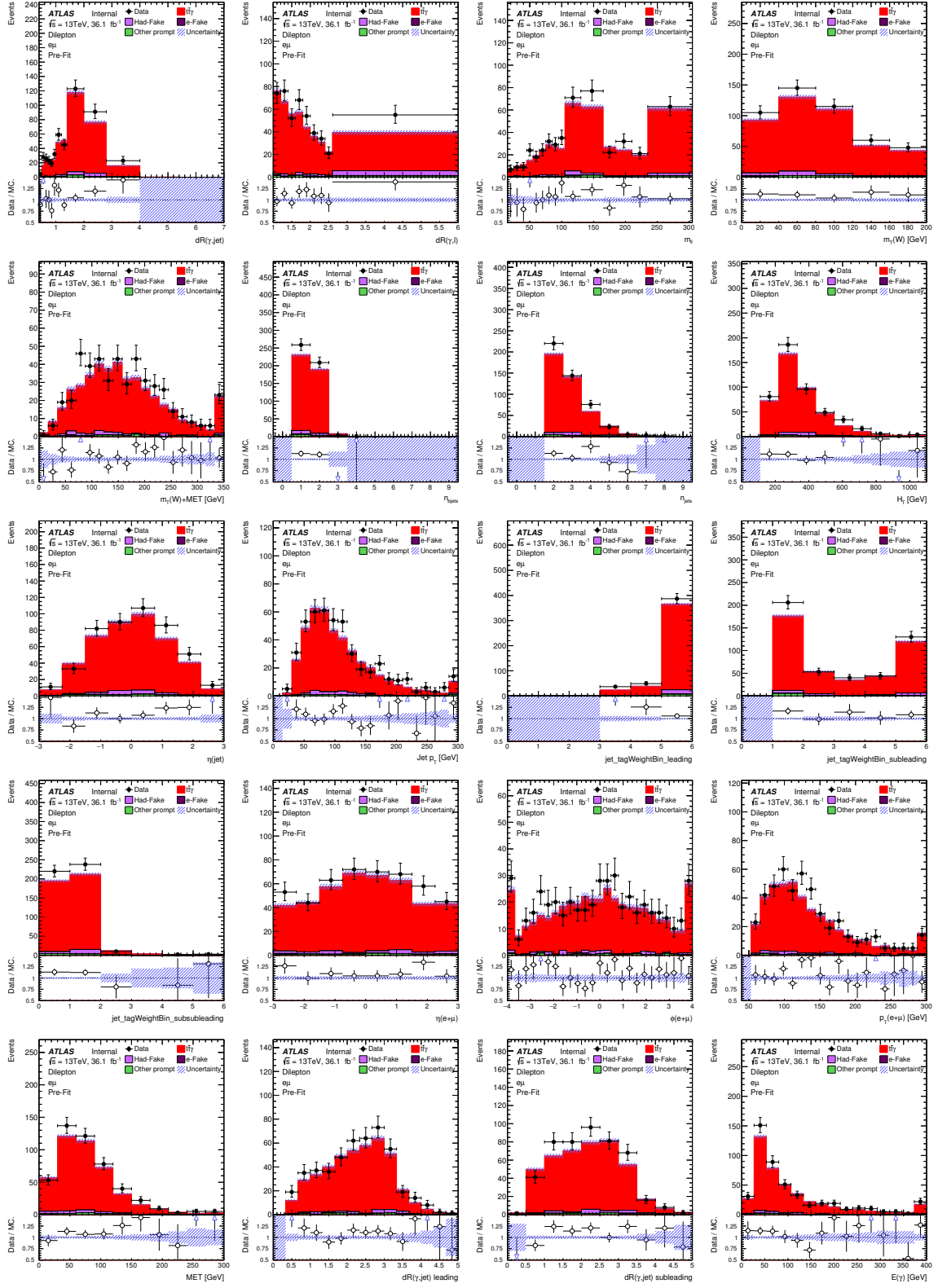
Figure 16: A selection of pre-fit distributions for the $\mu\mu$ channel. Only statistical uncertainties are included.

Table 12: Variable optimisation for the dilepton NN. The starting point is the first row. Each subsequent row includes more variables described on top of the previous row. Variables are chosen according to separation rank.

Variables	ROC (train)	ROC (test)	Selected NN
(3) jet btag weight subleading, $m(\ell, \ell), E_T^{\text{miss}}$	0.9289	0.9233	
(7) +, p_T of first jet, number of bjets, jet btag weight leading, p_T of second jet	0.9313	0.9258	✓
(8) +, PPT	0.9329	0.9261	
(10) +, p_T of third jet, $m(\gamma, \ell, \ell)$	0.9365	0.9313	
(13) +, $m_T(W)$, number of jets, H_T	0.9428	0.9393	

699 cross-validation plots are shown in Figure 21 for the single lepton and dilepton NN's. The agreement is
700 good for both channels and over-training has not occurred.

Not reviewed, for internal circulation only



Not reviewed, for internal circulation only

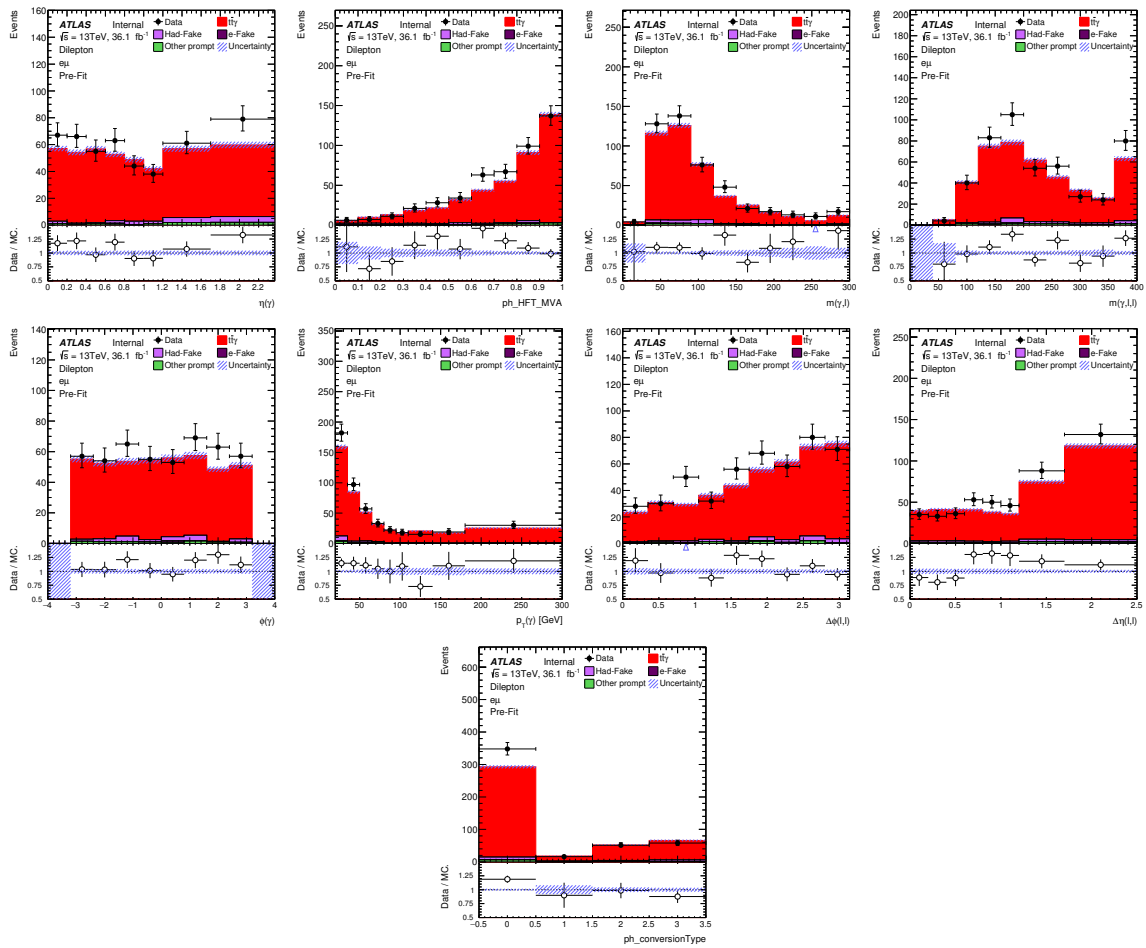


Figure 17: A selection of pre-fit distributions for the $e\mu$ channel. Only statistical uncertainties are included.

701 5.2.3 Application and evaluation

702 The output from the neural networks for each channel is shown in Figures 22, 23 and 24. Due to the smaller
 703 contribution of background in the dilepton channels, only the separation between the signal and the total
 704 background is shown. Only statistical uncertainties are included. For the single lepton channels the ELD
 705 struggles to separate out the hadronic fake and $e \rightarrow \gamma$ fake background. These have the smallest separation
 706 at 13.4% and 15.7% for the $e+jets$ channel, 11.9% and 10.2% for the $\mu+jets$ channel, respectively. The
 707 dilepton NN performs well where there is a background to separate, while for the $e\mu$ channel it is completely
 708 signal dominated in any case. These distributions are used to perform a binned maximum likelihood fit,
 709 as described in Section 10.

710 Since the b-tagged variables play such an import role in the ELD, we can examine the relationship
 711 between the b-jet dependence and the ELD output. Figure 25 shows this correlation for the single lepton
 712 and dilepton channel NN's, where each row of each plot has been normalised. In general, as more b-tagged
 713 jets enter into the event, the more signal-like it is. Background processes with a higher number of b-tagged
 714 jets in the event have an increased chance of being tagged as signal by the ELD.

715 Correlation plots for the ELD and the training input variables are shown in Figure 26. As expected the

Not reviewed, for internal circulation only

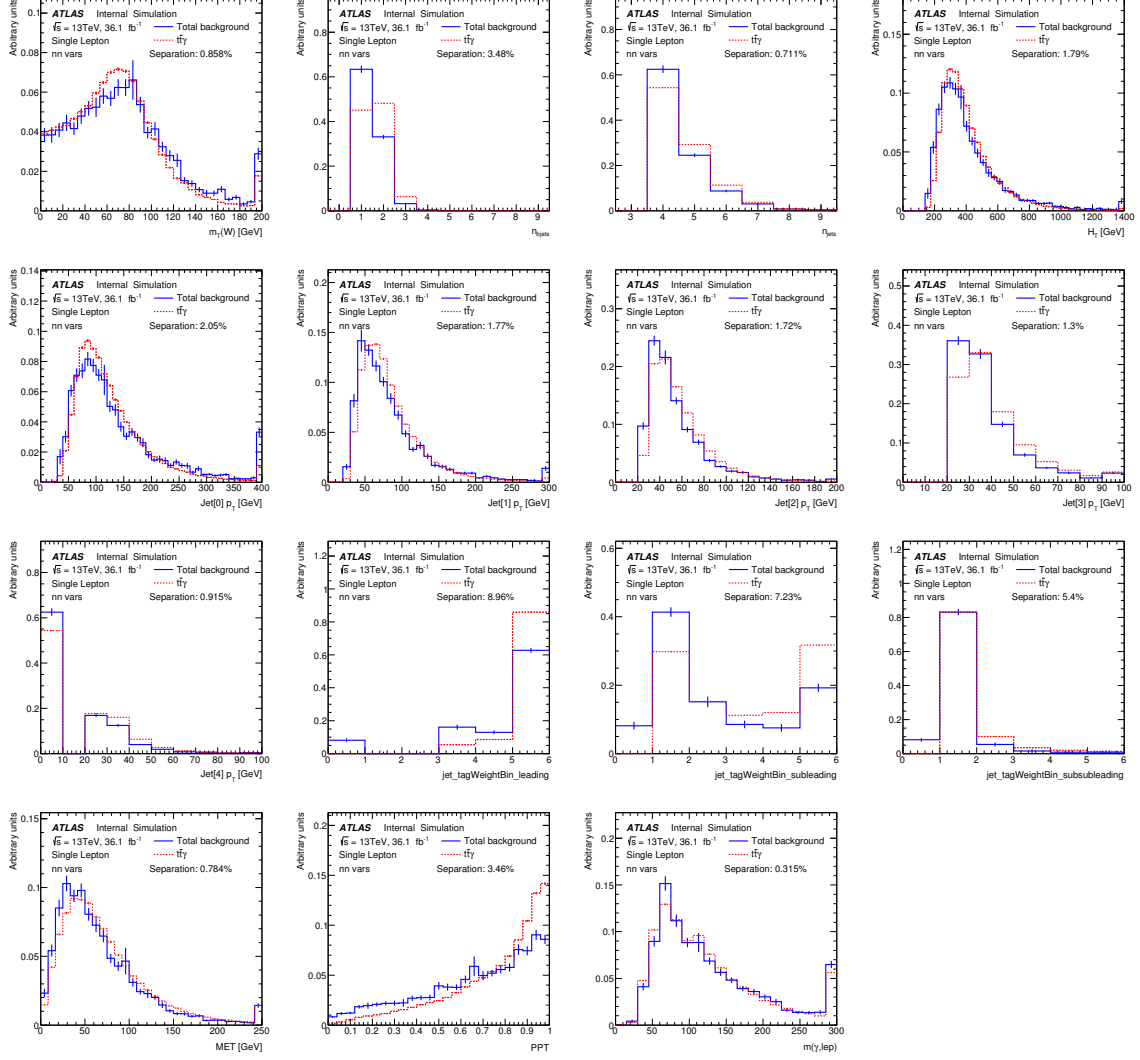


Figure 18: Variables used in training for the single lepton ELD neural network.

Not reviewed, for internal circulation only

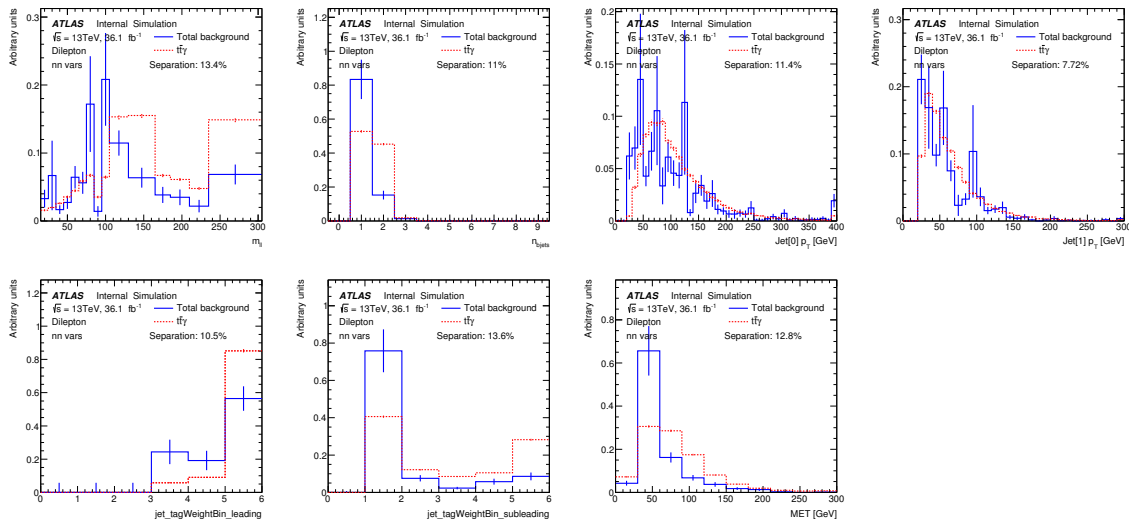


Figure 19: Variables used in training for the dilepton ELD neural network.

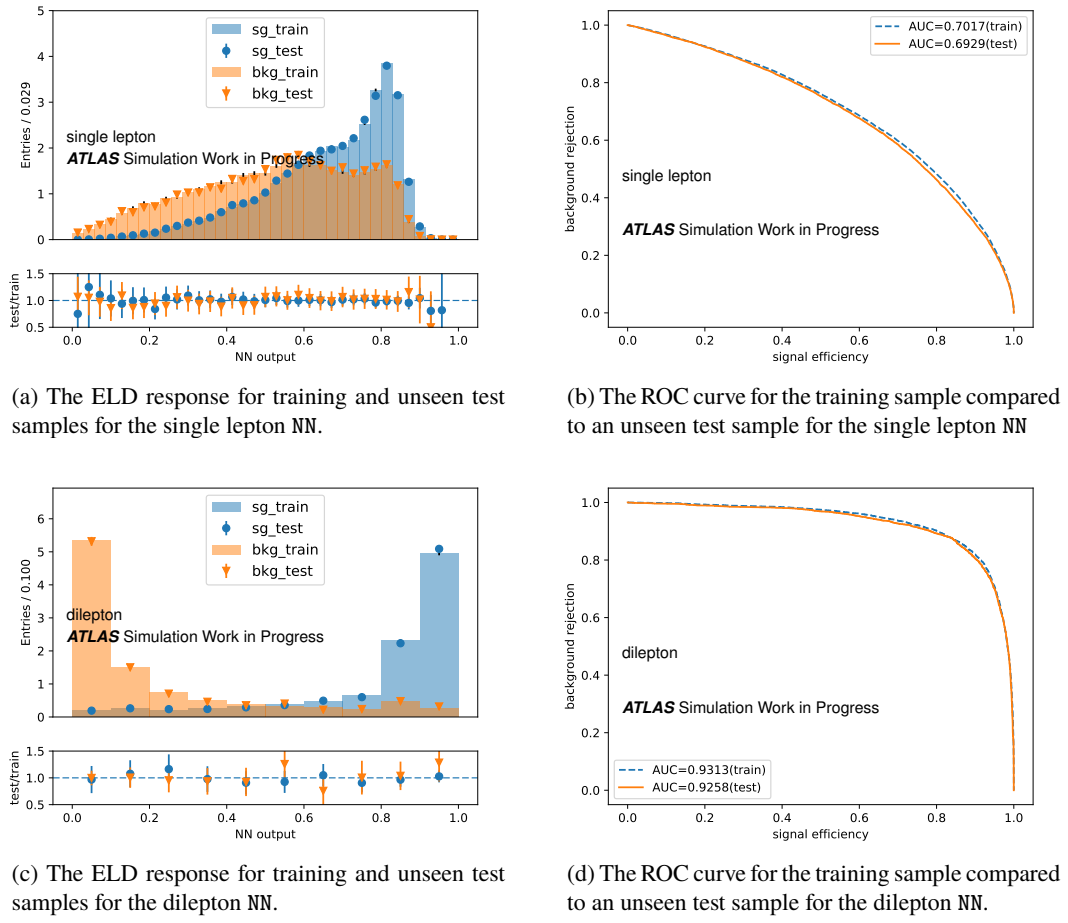


Figure 20: Event Level Discriminator training output.

Not reviewed, for internal circulation only

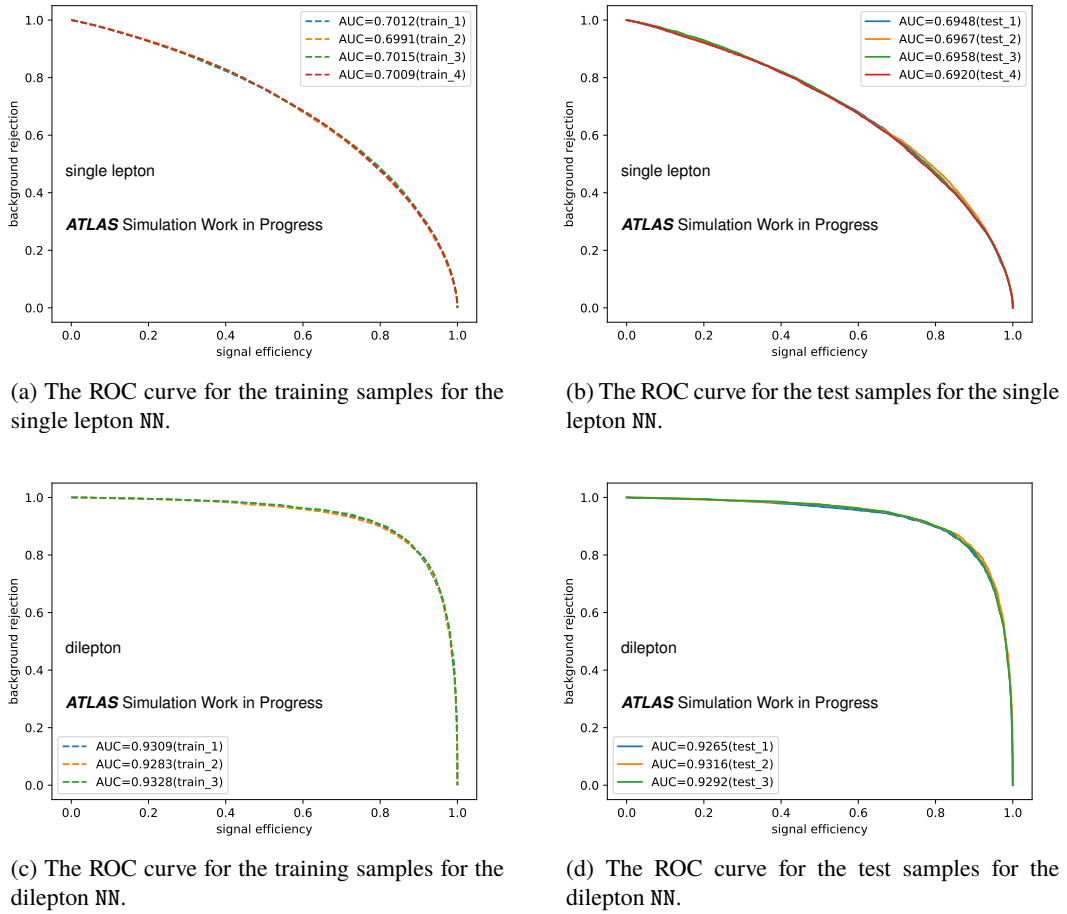


Figure 21: The k-fold cross validation plots is performed for each NN.

716 highest correlations for the ELD are with respect to the b-tagged variables in both signal and background
 717 for both channels.

Not reviewed, for internal circulation only

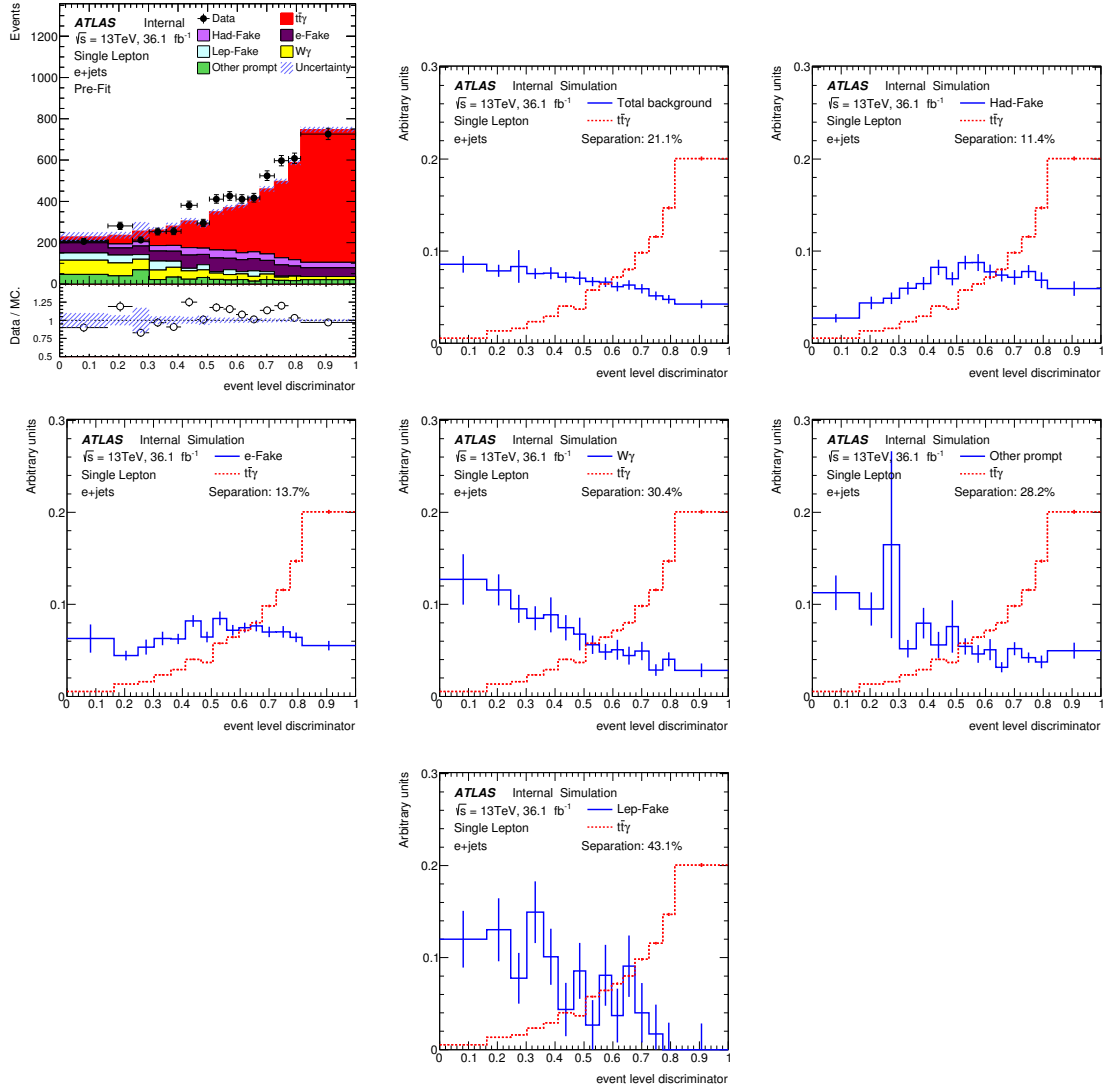


Figure 22: Event Level Discriminator variable for the $e+jets$ channel with separation plots shown for signal and the different background components.

Not reviewed, for internal circulation only

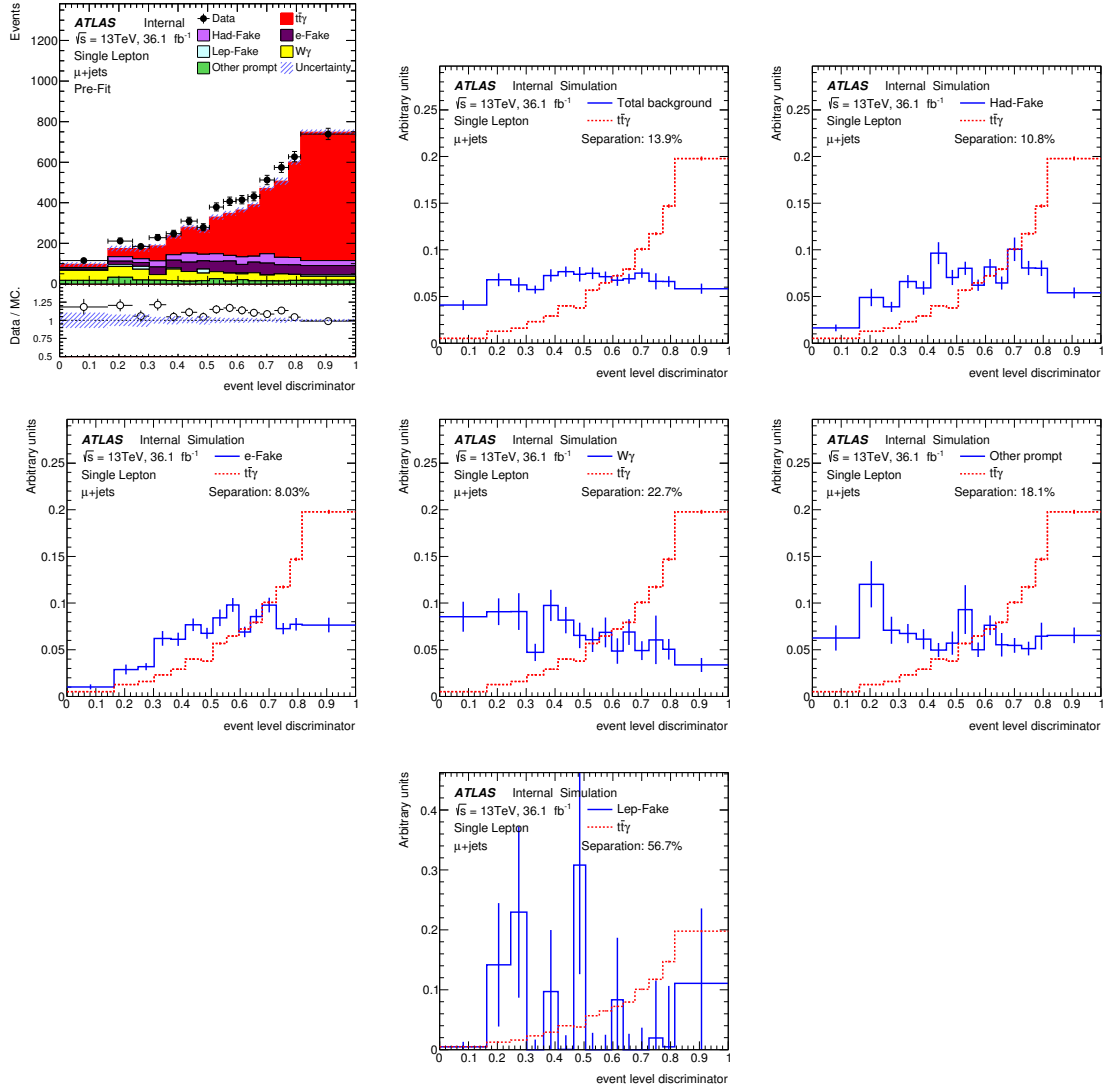


Figure 23: Event Level Discriminator variable for the μ +jets channel with separation plots shown for signal and the different background components.

Not reviewed, for internal circulation only

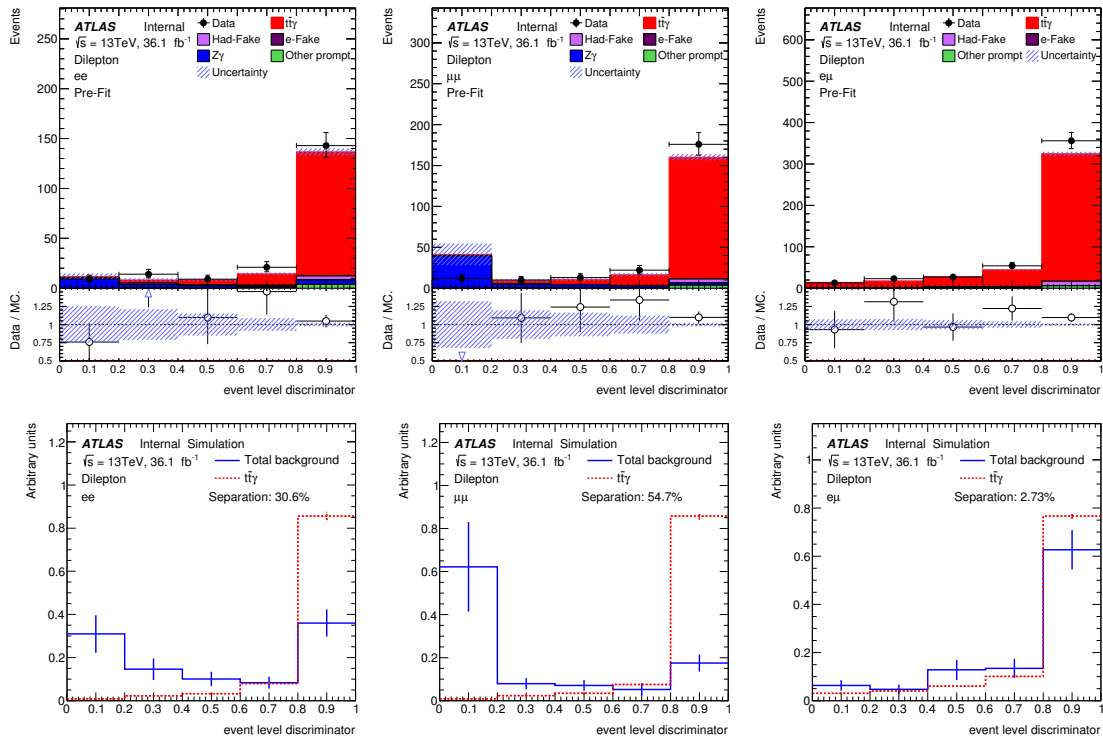


Figure 24: Event Level Discriminator variable for the dilepton channels with the corresponding separation plots for all summed backgrounds.

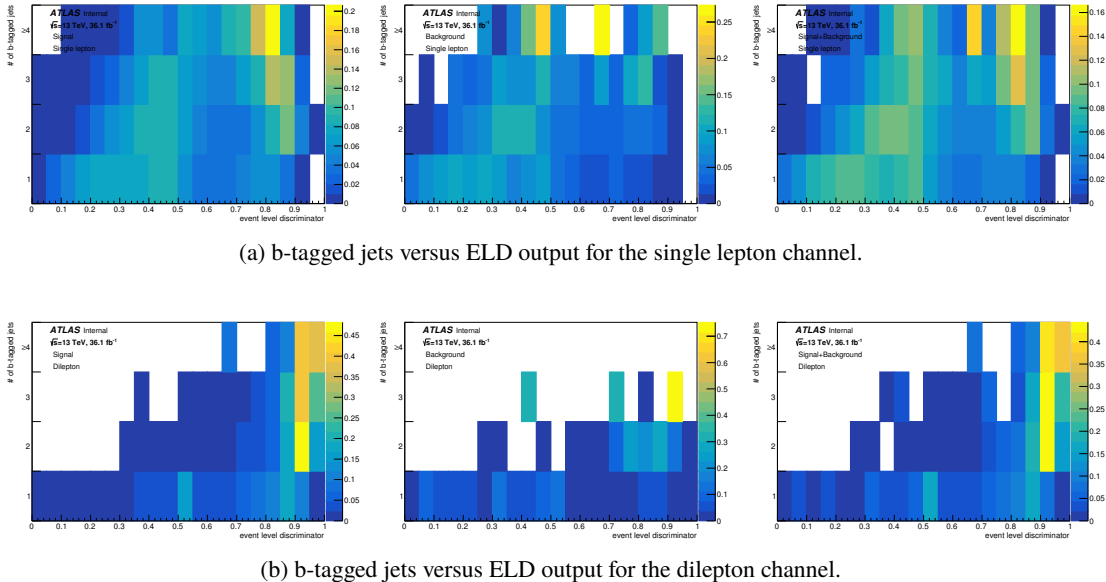


Figure 25: The number of b-tagged jets versus the ELD output for the signal, the background and the combination of both for each of the NN's. Each row of each plot is normalised.

Not reviewed, for internal circulation only

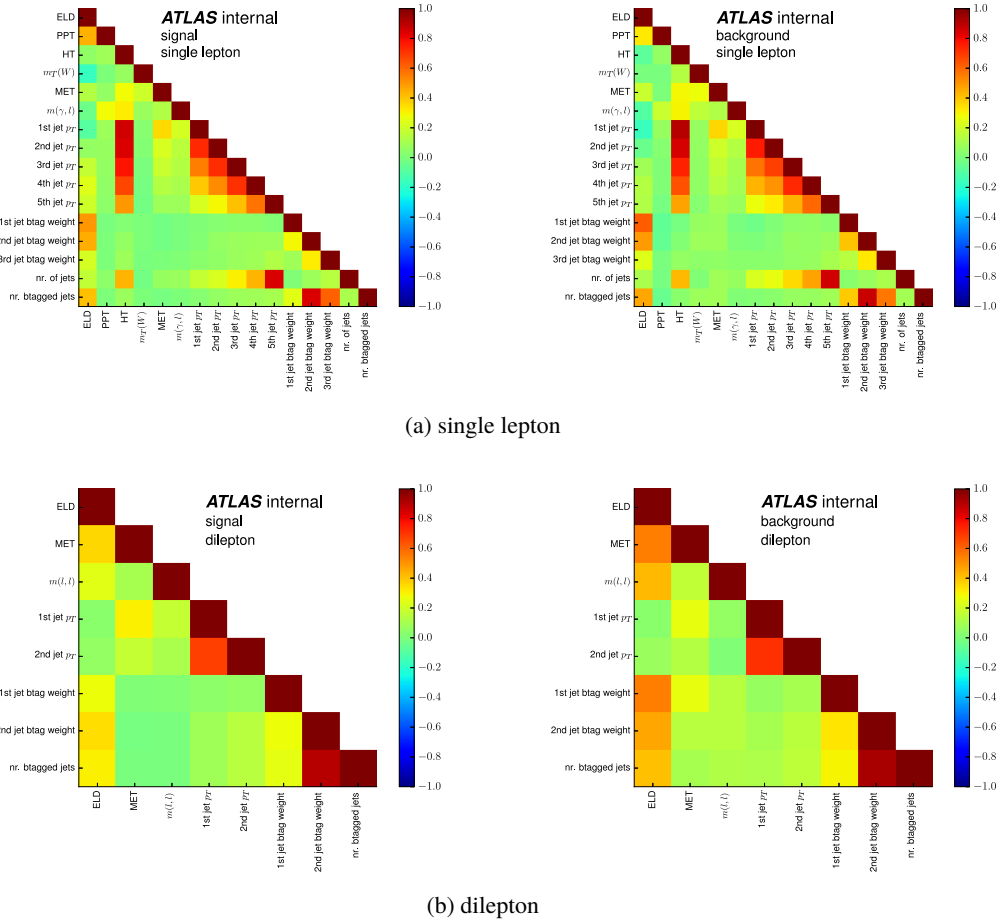


Figure 26: Correlation plots for the signal and background for each channel comparing the ELD and training variables. Full event selection and event weights have been applied.

718 6 Background descriptions

719 Several background processes mimic the $t\bar{t}\gamma$ signature. They can be events with a fake photon, either a
 720 hadronic fake (introduced in Section 4.2) or a fake due to an electron misidentification (a.k.a. $e \rightarrow \gamma$ fake),
 721 or they can be non- $t\bar{t}$ events with a prompt photon. This section describes the studies on the background
 722 processes and the detail of their estimation.

723 6.1 Background due to mis-reconstructed electrons

724 One of the important background contributions in $t\bar{t}\gamma$ originates from events in which one electron is
 725 misidentified as a photon, denoted as $e \rightarrow \gamma$ fake. It is an important background source in the single
 726 lepton channel. The main processes contributing to this background are the $t\bar{t}$ dileptonic decays (ee and
 727 $e\mu$ channels) and $Z \rightarrow ee$ decay, where one electron fakes a photon. The strategy of estimating this
 728 background is to use a fake rate scale factor, which is the ratio between the data-driven fake rate and the
 729 MC predicted fake rate, to correct for the number of fake photons predicted by MC in the signal region.
 730 Section 6.1.1 defines the control regions used for the study. Section 6.1.2 describes the studies on the
 731 source of $e \rightarrow \gamma$ fakes by matching them to the truth level particles. Section 6.1.3 defines the fake rate
 732 and contains the calculation of the fake rate scale factor.

733 6.1.1 Control regions

734 To study the $e \rightarrow \gamma$ fake rate, a fake enriched control region is defined by selecting events having a
 735 pair of back-to-back electron and photon, which will be called $e\gamma$ control region. More specifically, the
 736 requirements include:

- 737 • Exactly one electron which is trigger matched.
- 738 • At least one photon. The leading p_T photon is referred simply as photon in the following.
- 739 • The opening angle between the electron and the photon to be larger than 150 degrees.
- 740 • The invariant mass of the electron and the photon to be within 50 GeV around the Z mass.
- 741 • To avoid a trigger bias later when studying the fake rate, the p_T of the electron should be larger than
 742 the p_T of the photon.

743 In the selected events, the electron is called *tag electron* and the photon is called *probe photon*.

744 Another control region, that will be called *ee* control region, is defined in exactly the same way as above,
 745 but by replacing the photon in the requirements with an electron which should have opposite charge sign
 746 with respect to the tag electron. Thus, this electron is called *probe electron* and is used as a reference to
 747 be compared with the probe photon to define the fake rate later.

748 6.1.2 Fake sources

749 The $Z \rightarrow ee$ MC events selected in the above described $e\gamma$ control region can be used to study the source
 750 of $e \rightarrow \gamma$ fakes, by matching the probe photon with a truth particle before the detector simulation. The
 751 matching is done by extrapolating the track of the truth particle to the calorimeter layer and calculating the
 752 angular distance between the truth particle and the EM cluster, from which the photon is reconstructed. If
 753 the distance is smaller than a reference value ($\Delta R < 0.3$), the truth particle is considered to be the source
 754 of the photon.

755 After truth matching, the photon can be categorised into four classes (in the order of decreasing popula-
 756 tion):

- 757 • Type (a): denoted as "mis-reco.", where the photon is matched to a true electron. 59% of the
 758 selected photons belong to this class.
- 759 • Type (b): denoted as "mis-match", where the photon is matched to a true photon, but the photon's
 760 p_T is larger than that of the true photon by more than 10%, and at the same time, there is a nearby
 761 true electron with $\Delta R < 0.05$ w.r.t. the photon. 26% of the selected photons belong to this class.
- 762 • Type (c): denoted as "prompt QED", where the photon is matched to a true photon, and there is no
 763 nearby true electron with $\Delta R < 0.05$ w.r.t. the photon. 12% of the selected photons belong to this
 764 class.
- 765 • Type (d): denoted as "non-prompt QED", where the photon is matched to a true photon, and their
 766 relative p_T difference is smaller than 10%, although there is a nearby true electron with $\Delta R < 0.05$
 767 w.r.t. the probe photon. 3% of the selected photons belong to this class.

768 The categorization is summarized in Fig. 27.

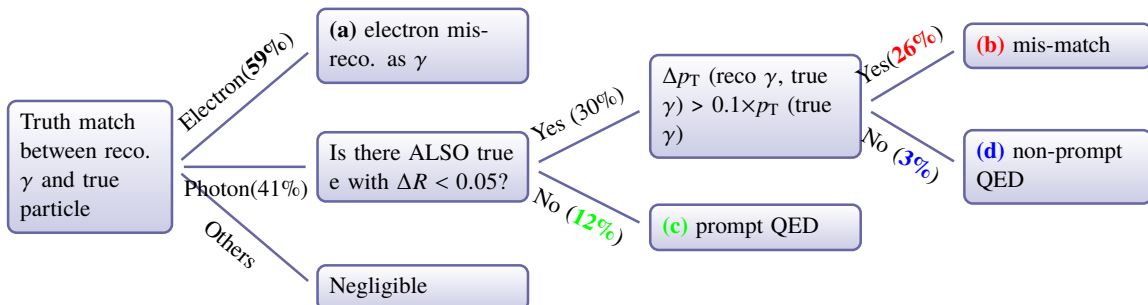


Figure 27: The categorisation of the selected probe photons in the $e\gamma$ control region via truth particle matching.

769 In the following, to better understand these four types of photons, their kinematics are shown and compared
 770 to that of the probe electron, when available.

771 The p_T and η of the probe photons are compared to those of the probe electron in Fig. 28. It can be seen
 772 that the p_T spectrum is rather similar between photon type (a), (b), and (d) and the probe electron, which
 773 indicates that they are truly $e \rightarrow \gamma$ fakes. For the η distribution, type (a) and (b) peak at high absolute
 774 η region. Connecting to the fact that there is also larger upstream material in high absolute η region, it
 775 implies (a) and (b) are likely to be bremsstrahlung induced fake photons. For type (d), its η spectrum is
 776 very similar to that of the probe electron. This could be explained by a very hard non-prompt QED that
 777 takes away almost all kinematics of its mother electron.

778 The p_T of tag electrons in the two control regions and the invariant mass between the tag and probe are
 779 compared in Fig. 29. The lower-shifted p_T and mass spectrum for type (c) indicates that it is a true prompt
 780 photon from the three body decay of $Z \rightarrow ee + \gamma$. Therefore, type (c) is not to be counted as fake.

Not reviewed, for internal circulation only

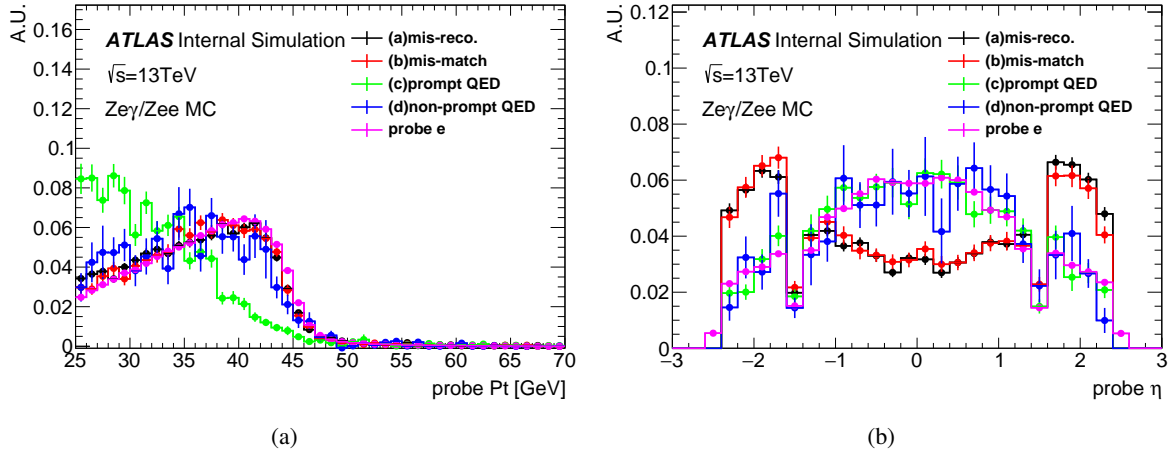


Figure 28: The p_T (a) and η (b) distributions of the probe photon, shown for different classes and compared to those of the probe electron.

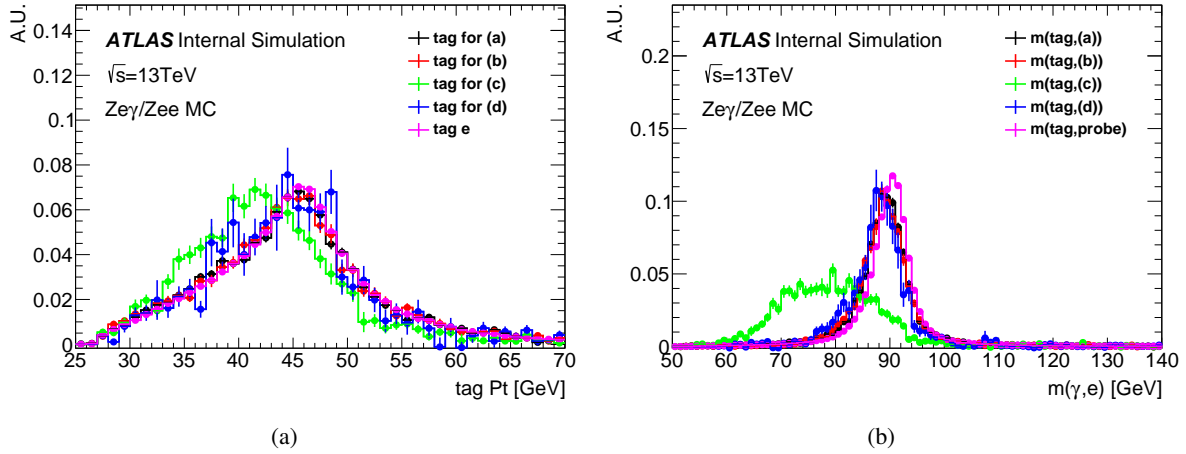


Figure 29: The p_T of the tag electron in the two control regions (a) and the invariant mass between the tag and probe (b).

781 The invariant mass distribution of tag electron and probe photon is shown in Fig. 30, with each type of
 782 photons being normalized to their expected yields. It can be seen that the fake is dominated by the type
 783 (a) and (b).

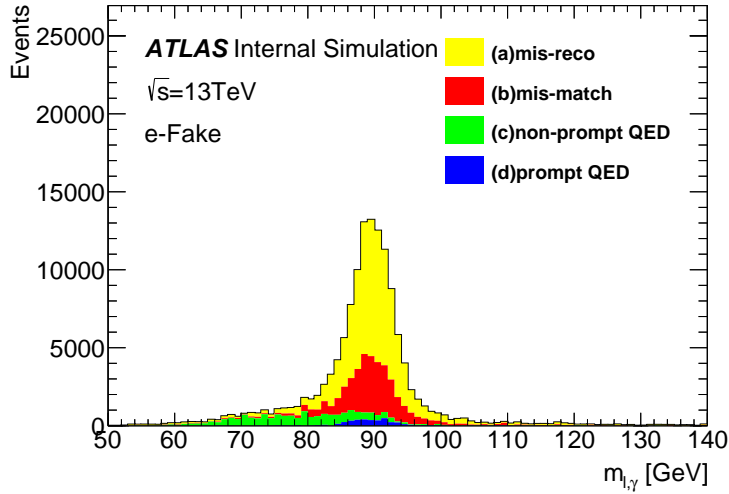


Figure 30: The invariant mass between the tag and probe.

784 6.1.3 Fake rates

785 Using the $Z \rightarrow ee$ MC, the number of $Z \rightarrow ee$ events observed with a tag electron and a fake photon can
 786 be expressed as follows:

$$N_{e,\gamma} = N_{true} \times \epsilon_e^{reco} \times \epsilon_e^{\text{others}} \times p_{e \rightarrow \gamma} \times \epsilon_{\gamma(F)} \quad (2)$$

787 where

- 788 • N_{true} : true number of generated $Z \rightarrow ee$ events
- 789 • ϵ_e^{reco} and $\epsilon_e^{\text{others}}$: reconstruction and other selection efficiencies of tag electron
- 790 • $p_{e \rightarrow \gamma}$: probability of misidentifying an electron as photon
- 791 • $\epsilon_{\gamma(F)}$: selection efficiency of the fake photon ("F" denotes the fact that it's a fake photon so that the
 792 efficiency can be different from the true photon)

793 Also, the number of $Z \rightarrow ee$ events observed with two electrons can be expressed as follows:

$$N_{e,e} = N_{true} \times \epsilon_{e1}^{reco} \times \epsilon_{e1}^{\text{others}} \times \epsilon_{e2}^{reco} \times \epsilon_{e2}^{\text{others}} \quad (3)$$

794 where

- 795 • ϵ_{e1}^{reco} and $\epsilon_{e1}^{\text{others}}$: reconstruction and other selection efficiencies of tag electron
- 796 • ϵ_{e2}^{reco} and $\epsilon_{e2}^{\text{others}}$: reconstruction and other selection efficiencies of probe electron

797 The fake rate (FR) is then defined as the ratio between $N_{e,\gamma}$ and $N_{e,e}$:

$$\text{FR} \equiv \frac{N_{e,\gamma}}{N_{e,e}} = p_{e \rightarrow \gamma} \times \frac{\epsilon_{\gamma(F)}}{\epsilon_{e2}^{reco} \cdot \epsilon_{e2}^{\text{others}}} = p_{e \rightarrow \gamma} \times C \quad (4)$$

Not reviewed, for internal circulation only

From the above formula, it is known that FR is proportional to the $e \rightarrow \gamma$ faking probability. But the proportion coefficient C could vary according to the p_T and η of the fake candidate, due to the p_T and η dependency of those efficiencies.

The overall fake rate calculated by using $Z \rightarrow ee$ MC are shown in Table 13. In Fig. 31, the p_T and η dependencies of the fake rate are shown. In both Table 13 and Fig. 31, the type (c), which is not really a fake photon, is shown for completeness.

Table 13: The overall fake rate calculated from $Z \rightarrow ee$ MC for different types of photon. Type (c) is not counted as fake photon and its value is just for shown. Only statistical uncertainties are shown.

	N(probe γ)	N(probe e)	FR _{MC} (%)
Type(a)	78240.80 ± 1096.92	4551436.50 ± 8419.50	1.72 ± 0.02
Type(b)	34156.20 ± 760.62	4551436.50 ± 8419.50	0.75 ± 0.02
Type(c)	16534.88 ± 493.96	4551436.50 ± 8419.50	0.36 ± 0.01
Type(d)	3786.88 ± 248.38	4551436.50 ± 8419.50	0.08 ± 0.01
All	132718.77 ± 1444.81	4551436.50 ± 8419.50	2.92 ± 0.03

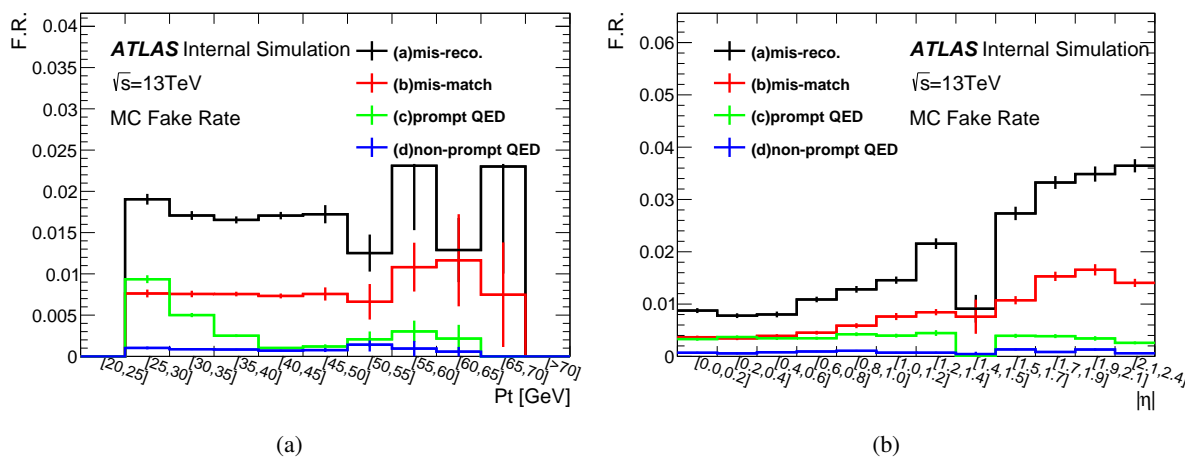


Figure 31: The p_T (a) and η (b) dependency of the fake rates

In order to calculate the data-driven fake rate, the only difference with respect to the above MC-based fake rate is that:

$$\text{FR}_{dd} = \frac{N_{e,\gamma}^{\text{data}} - N_{e,\gamma}^{\text{non-Z}}}{N_{e,e}^{\text{data}} - N_{e,e}^{\text{non-Z}}} \quad (5)$$

which means the denominator and numerator are replaced by their data-driven ones.

The subtraction of non-Z events from data in these control regions can't be done with MC samples since from MC study the non-Z background are negligible. Instead, it be done by side band fit, as shown in Figure 32, where the $Z \rightarrow ee$ signal is modelled by double-sided Crystal-ball function and the non-Z background by a Bernstein 4th order polynomial.

After that the data-driven fake rate is divided by the MC fake rate to derive a set of fake rate scale factors:

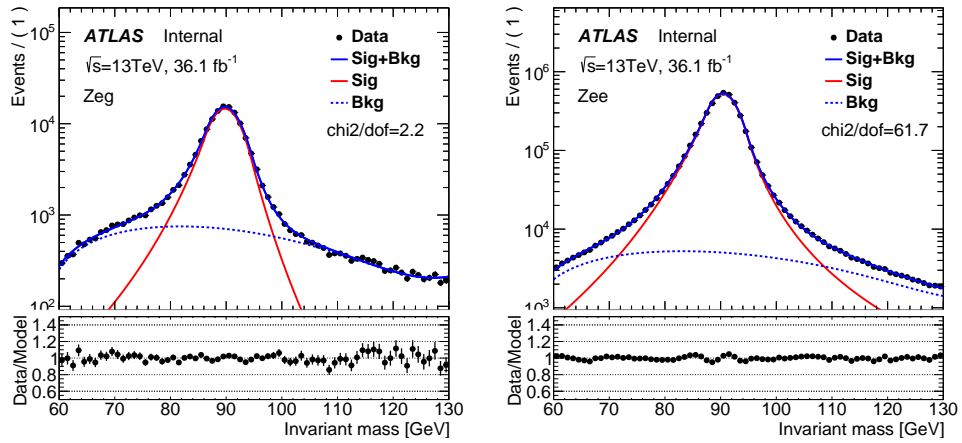


Figure 32: The side band fit in the two control regions to subtract non-Z events.

812

$$\text{SF}_{\text{FR}} = \frac{\text{FR}_{dd}}{\text{FR}_{MC}} \quad (6)$$

813 these scale factors will be applied to the $e \rightarrow \gamma$ MC samples as a data-driven correction.

814 The overall scale factor is calculated to be 0.97 ± 0.02 , with the error being statistical only. To estimate
815 the systematic uncertainty of the scale factor, the following variations are considered:

- 816 • signal function shape is changed from double sided Crystal-ball to MC predicted template (if
817 necessary with smoothing to reduce fluctuation), the result of which is shown in Figure 33 (a). The
818 scale factor is calculated to be 1.14, with a difference of 17% with respect to the nominal SF.
- 819 • fitting mass range shrunk by 5 or 10 GeV in the low end and 10 GeV in the high end, the result of
820 which is shown in Figure 33 (b). The scale factor is calculated to be 1.08, with a difference of 11%
821 with respect to the nominal SF.
- 822 • background function shape is changed from Bernstein to Gaussian, the result of which is shown in
823 Figure 33 (c). The scale factor is calculated to be 1.04, with a difference of 7% with respect to the
824 nominal SF.
- 825 • the MC model for the subtraction of prompt QED contribution is changed from $Z \rightarrow ee$ sample to
826 a $Z \rightarrow eey$ sample. The scale factor is calculated to be 0.99, with a difference of 2% with respect
827 to the nominal SF.

828 The total uncertainty is derived from their quadratic sum (including the statistical uncertainty), which
829 results in the final overall SF to be 0.97 ± 0.21 .

830 The SF can also be derived differentially with respect to the photon p_T and η . The choice of binning for
831 p_T is $[25, 35, 45, 60, \text{infinity}]$ (in GeV) and for η is $[0, 0.5, 1.0, 1.37]$ and $[1.52, 2.0, 2.37]$. So in the end,
832 there will be $4 \times 5 = 20$ bins. The nominal mass peak fits for each of these bins are shown in Figure 34 and
833 Figure 35. The final 2D scale factors are summarized in Figure 36, including statistical uncertainties as
834 well as the above systematic uncertainties. The scale factors are also shown as a function of η in different
835 p_T bins in Figure 37, where the total uncertainties are decomposed. To be noted: starting from the 2nd p_T
836 bin, which means from 45 GeV, the role of tag/probe is switched to gain statistics in high p_T region.

Not reviewed, for internal circulation only

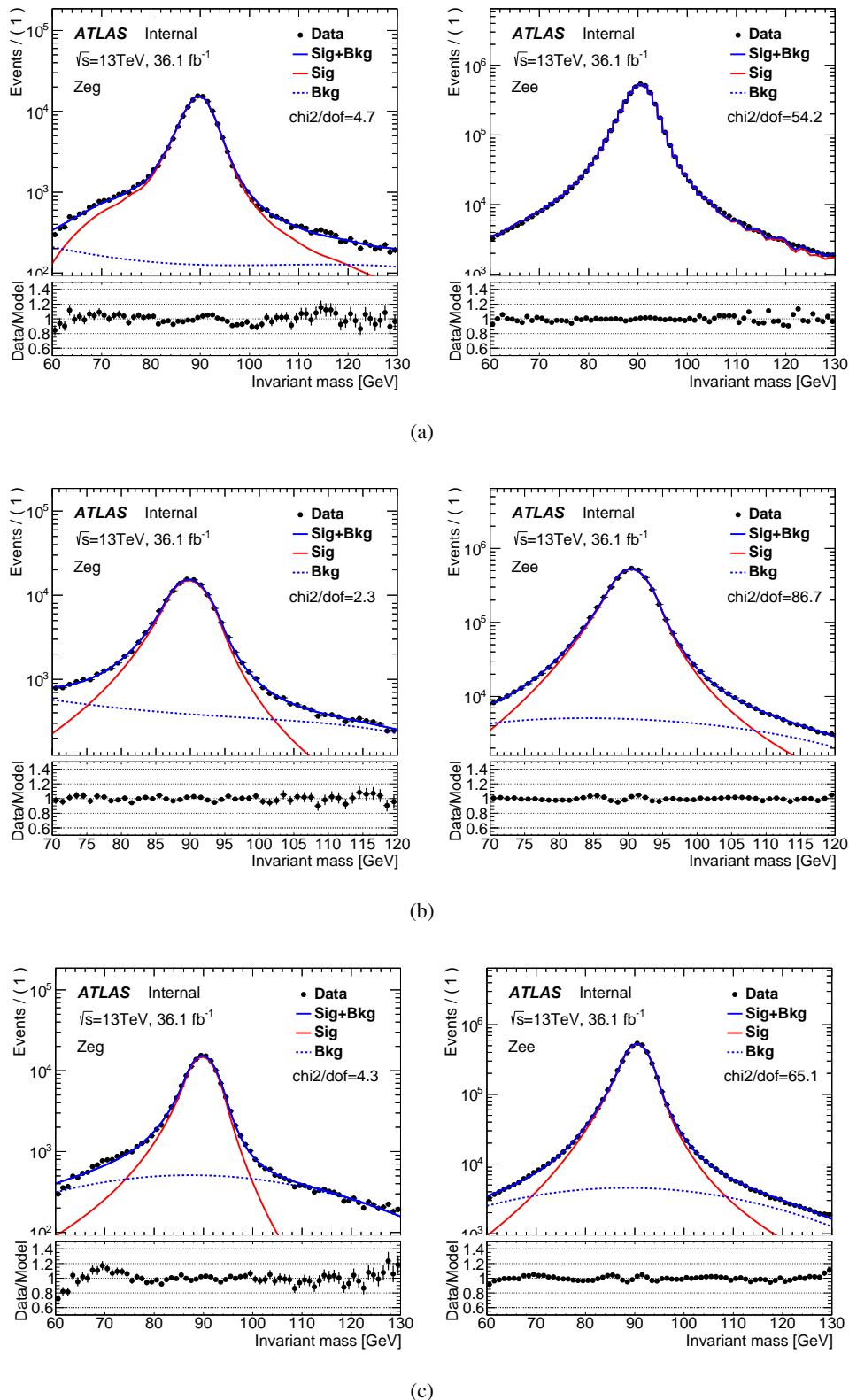


Figure 33: The side band fit in the two control regions to subtract non-Z events, where the signal function is switched from double-sided crystal ball to MC template (a), the fit range is shortened by 10 GeV(b), or the background function is switched from 4th order Bernstein polynomial to Gaussian (c).

Not reviewed, for internal circulation only

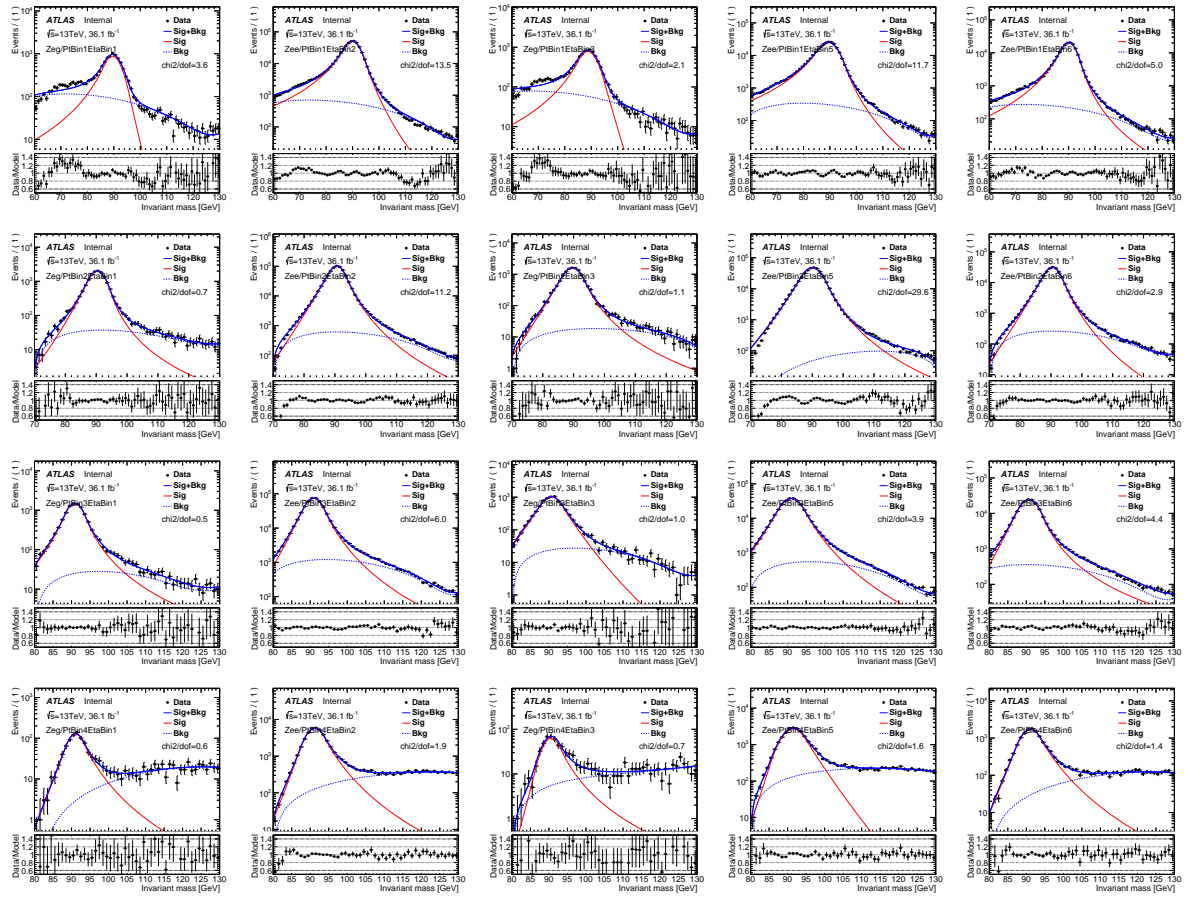


Figure 34: The postfit of the (e, γ) invariant mass distribution in different photon (p_T, η) bins.

837 6.1.4 Signal region $e \rightarrow \gamma$ fake

838 The $e \rightarrow \gamma$ fake in the signal region could be expressed as following:

$$N_{\ell,\gamma} = N_{\ell,e} \times \text{FR} \quad (7)$$

839 ℓ could be an electron or a muon, and when it's electron, the formula should be applied twice: one for the
 840 case of the leading electron faking the photon and the other for the subleading electron. $N_{\ell,e}$ is the number
 841 of events in a modified signal region by replacing all the photon related cuts with those on an electron. It
 842 plays the role of a pool of $e \rightarrow \gamma$ fake candidate. The above section corrected the FR with data-driven
 843 method. Here we try to correct $N_{\ell,e}$ in this modified signal region.

844 The p_T distributions of the leading lepton and subleading lepton when it's the modified $e+jets$ signal
 845 region and when it's the modified $\mu+jets$ signal region are shown in Figure 38, where a good data/MC
 846 agreement can be found. The resulting data-over-MC SFs are 0.97 ± 0.01 and 0.98 ± 0.01 for the modified
 847 $e+jets$ and $\mu+jets$ channels, respectively, with the error being statistical uncertainties. These SFs are used
 848 as an additional correction, on top of the FR SFs, to the $e \rightarrow \gamma$ fake MC samples. To this step, we have
 849 corrected all components of the $e \rightarrow \gamma$ sample with data.

Not reviewed, for internal circulation only

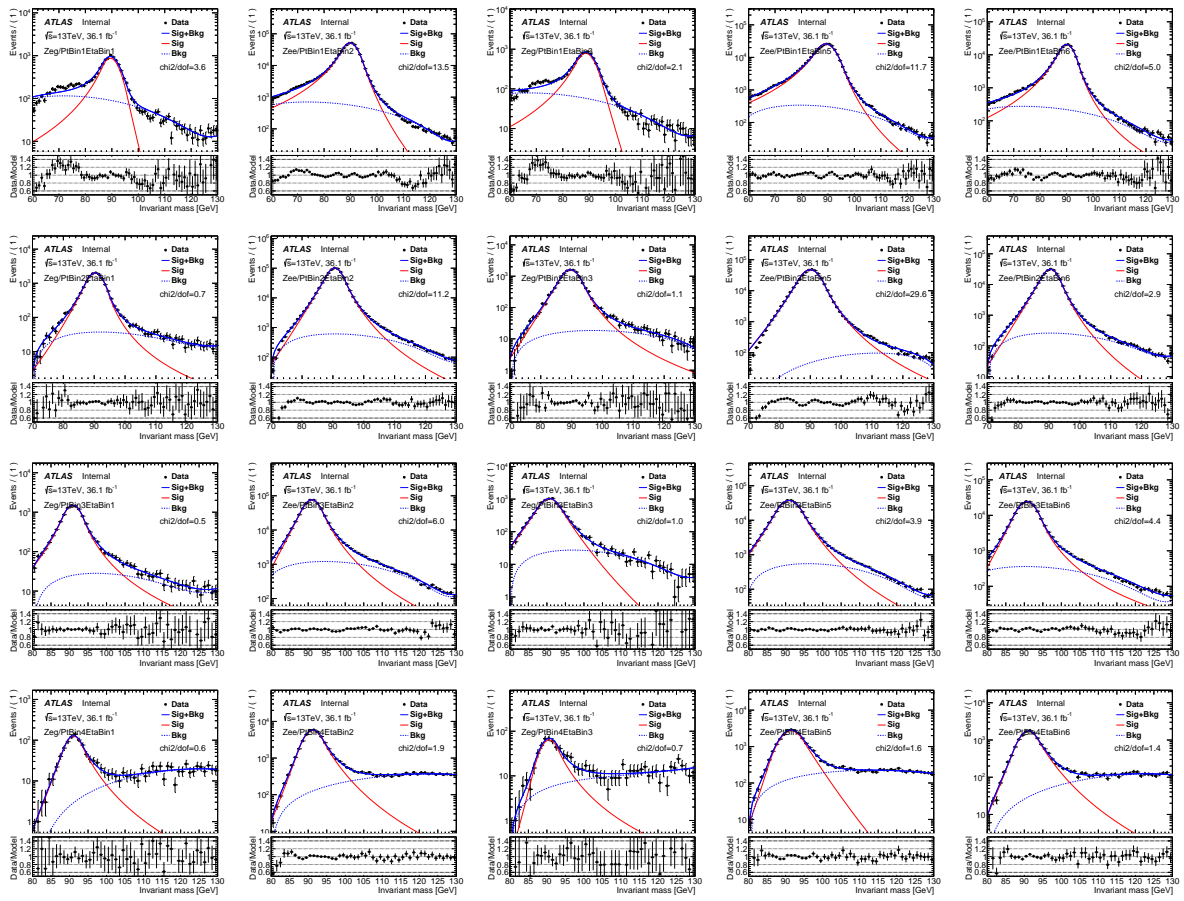


Figure 35: The postfit of the (e, e) invariant mass distribution in different photon (p_T, η) bins.

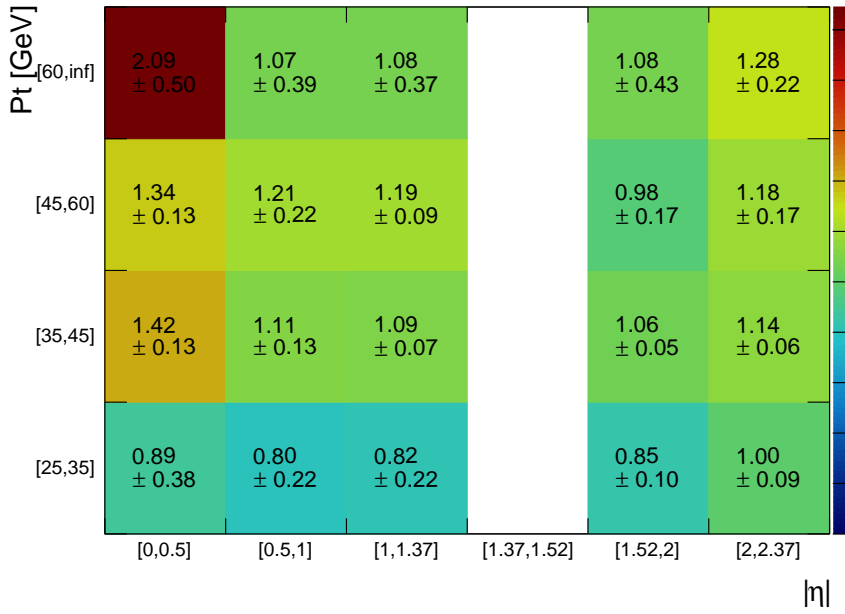


Figure 36: The final 2D fake rate scale factors with all uncertainties included.

Not reviewed, for internal circulation only

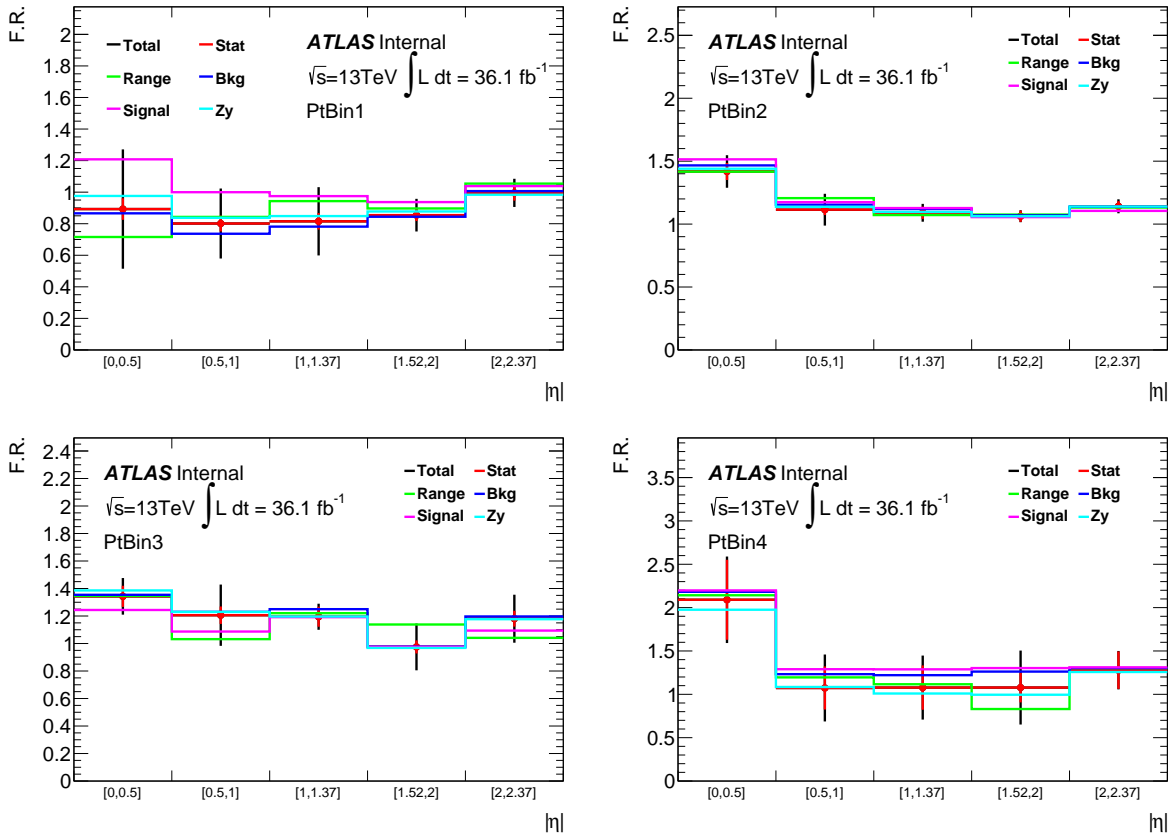


Figure 37: The final 2D fake rate scale factors illustrated in the form of 1D η distribution in each p_T bins. The total uncertainties are decomposed.

850 6.1.5 PPT systematics

851 Since in the end we do an ELD fit and the ELD takes as input the PPT, it is necessary to estimate the PPT
 852 systematics of the $e \rightarrow \gamma$ fake. This is done by comparing the PPT shape in the $Z \rightarrow e\gamma$ fake photon
 853 control region defined as above.

854 To subtract the non- Z background in the PPT distribution, a set of event weights are derived from the
 855 invariant mass distribution:

$$w_i = \frac{m_{i,Z}}{m_{i,\text{all}}}$$

856 where $m_{i,Z}$ is the number of estimated $Z \rightarrow ee$ event in the i th bin of the invariant mass distribution, and
 857 $m_{i,\text{all}}$ is the total number of event in that bin. Then this set of weights are applied to the data and the
 858 resulting data PPT distribution is compared with its MC correspondent.

859 In Figure 39, this PPT shape comparison is shown. The data/MC shape discrepancy looks very similar to
 860 that of the prompt photon, thus the prompt photon's PPT systematics are applied to the $e \rightarrow \gamma$ fake. This
 861 is not coincidence, as from Section 4.2 it is observed that the PPT shape is very similar between prompt
 862 photon and $e \rightarrow \gamma$ fake.

Not reviewed, for internal circulation only

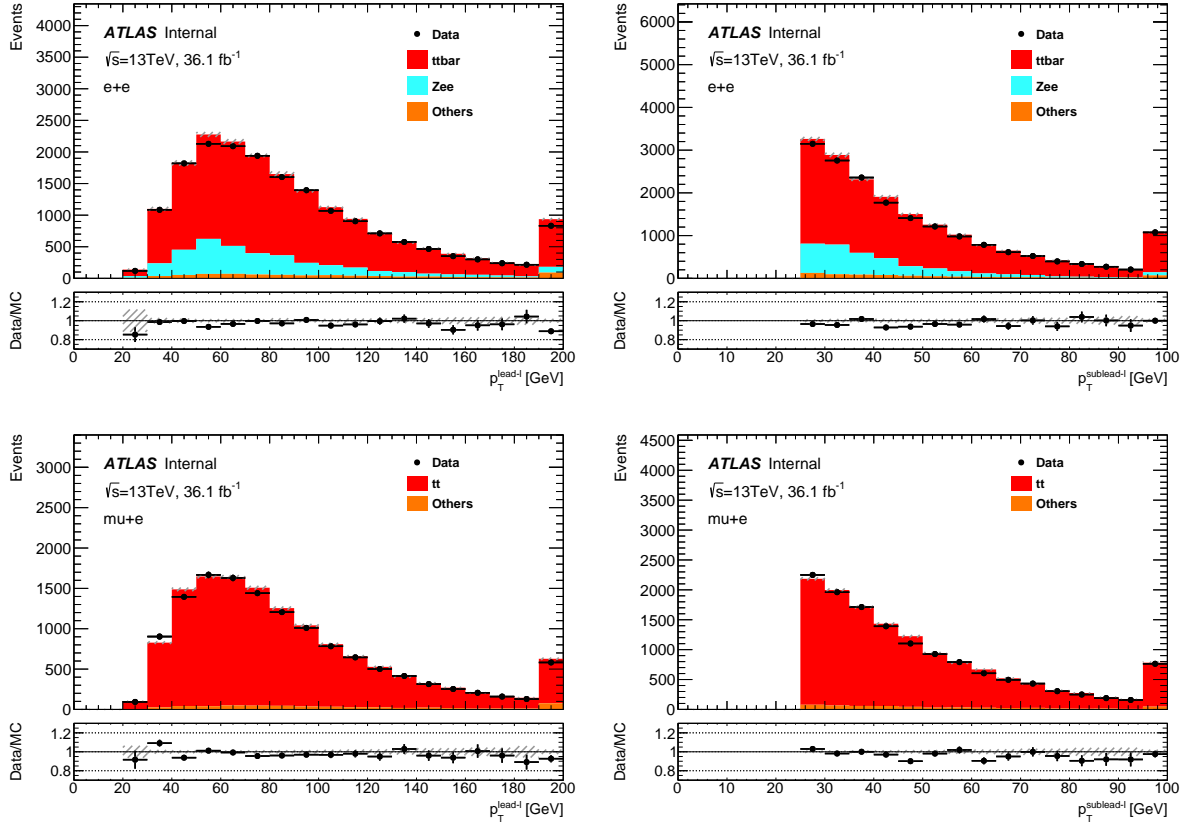


Figure 38: The p_T distributions of the leading lepton and subleading lepton of the modified $e+\text{jets}$ signal region (top) and of the modified $\mu+\text{jets}$ signal region (bottom). Only statistical uncertainties are shown in the error band.

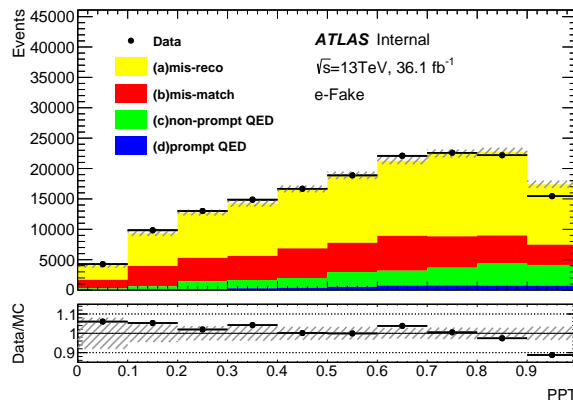


Figure 39: The PPT shape comparison between data and MC in the $Z \rightarrow e\gamma$ fake photon control region. The ratio is very similar to that of the prompt photon PPT.

863 6.2 Background due to hadronic fakes

864 The hadronic fakes are the photons originated from hadronic decays, or the hadrons that are misidentified as
 865 photons, as mentioned before in Section 4.2. The background contribution due to hadronic fakes is largely
 866 reduced by applying the photon isolation requirement, but still is one of the important backgrounds.

867 To estimate the hadronic fake background, first a data-driven two-dimensional sidebands method (ABCD
 868 method) is used. Then, the ratio of the data-driven estimate to the MC prediction of hadronic fake events is
 869 considered as the hadronic fake scale factor, and is used to scale the MC derived hadronic fake background
 870 in the final fit.

871 6.2.1 Estimation of hadronic fakes in single lepton channel

872 Four different regions in data are defined by dividing the photons into four categories based on their
 873 isolation and identification. The rest of the object and event selections remain the same as for the signal
 874 region (Sections 4.1 and 5.1). These four regions are illustrated in Figure 40. Region D is identical to the
 875 signal region, while regions A, B and C are dominated by hadronic fakes.

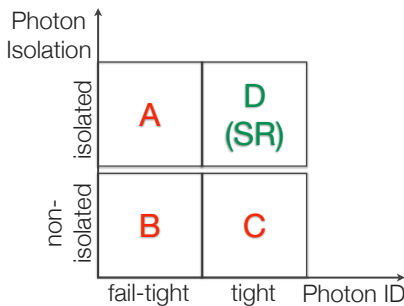


Figure 40: An illustration of ABCD method to estimate the hadronic fake background, using four category photons based on their identification and isolation.

876 Photons in regions B and C are required to be non-isolated. For this, they must fail the isolation working
 877 point (`FixedCutTight`, see Section 4.1) and in addition have $p_T^{\text{cone}20} > 3 \text{ GeV}$. The choice for the extra
 878 cut on the photon track isolation at 3 GeV, which is called *isolation gap* hereafter, is to reduce the prompt
 879 photon contamination, specially in region C.

880 Photons in regions A and B are required to be identified as *fail-tight*. The fail-tight identification requires
 881 the photon to pass all the tight identification cuts except for the cuts on the shower-shape variables f_{side} ,
 882 w_{s_3} , ΔE and E_{ratio} (see Table 4 for the description of the variables): at least two of these four cuts
 883 are explicitly asked to be failed. These four shower-shape variables contain information from the first
 884 layer of the electromagnetic calorimeter (strip layer). The strip layer is finely granulated in η , with the
 885 purpose of suppressing the background photons which typically have a broader shower profile. While
 886 these four variables have strong discrimination power between the prompt and hadronic fake photons,
 887 their correlation with photon isolation is very small [46]. The choice of the least number of cuts to fail, is
 888 based on a compromise between reducing the prompt photon contamination and keeping enough statistics,
 889 specifically in region A.

890 Control plots for regions A, B and C for $e+jets$ and $\mu+jets$ are shown in Figures 44, 45, 46, 47, 48 and 49
 891 . In these plots only the statistical uncertainties are shown.

892 Assuming no correlation between photon isolation and photon identification, the following relation
 893 holds:

$$\frac{N_A^{\text{h-fake}}}{N_B^{\text{h-fake}}} = \frac{N_D^{\text{h-fake}}}{N_C^{\text{h-fake}}} \quad (8)$$

894 Although regions A, B and C are dominated by hadronic fakes, as it can be seen from the control plots,
 895 there are contaminations from events with prompt photons and $e \rightarrow \gamma$ fakes. Therefore, the data numbers
 896 in regions A, B and C are corrected for prompt photons, using the MC numbers, and for $e \rightarrow \gamma$ fake
 897 leakage, using the MC number scaled by the $e \rightarrow \gamma$ fake scale factor (Section 6.1). Also, since in the
 898 data-driven fake lepton background estimation (Section 6.3.1), the fake lepton events with prompt and fake
 899 photons are not distinguished and the estimated fake lepton background is entering the final fit directly,
 900 the lepton fake background is subtracted from data:

$$N_{i,\text{data}}^{\text{h-fake}} = N_{i,\text{data}} - N_{i,\text{MC}}^{\text{prompt-}\gamma} - \text{SF}^{e \rightarrow \gamma} \times N_{i,\text{MC}}^{e \rightarrow \gamma} - N_{i,\text{d.d.}}^{\text{fake-lepton}}, \quad i \in \text{A, B, C} \quad (9)$$

901 The ABCD method assumes that the two discriminating variables are independent for the background.
 902 Although the isolation and identification criteria are chosen to minimise any such dependency, but any
 903 deviation from this assumption can be quantified by the following double ratio, using MC:

$$\theta_{\text{MC}} = \frac{N_{\text{D,MC}}^{\text{h-fake}} / N_{\text{C,MC}}^{\text{h-fake}}}{N_{\text{A,MC}}^{\text{h-fake}} / N_{\text{B,MC}}^{\text{h-fake}}} \quad (10)$$

904 The measured θ_{MC} (here for inclusive photon p_T , η and conversion type) are summarised in Table 14,
 905 with their uncertainties. Since the $N_{i,\text{MC}}^{\text{h-fake}}$ ($i \in \text{A, B, C, D}$) is dominated by the $t\bar{t}$ process, the modelling
 906 systematics for $t\bar{t}$ MC sample are considered. The uncertainty on hard scattering modelling (generat.)
 907 and parton shower and hadronisation (PS) are estimated by comparing the $t\bar{t}$ nominal sample produced
 908 by Powheg and interfaced by Pythia8, with the $t\bar{t}$ sample produced by Sherpa. The uncertainty on
 909 modelling of extra radiation (rad.-up/-down) is estimated by comparing the $t\bar{t}$ nominal sample, with the
 910 two samples that are produced with different tunes for higher or lower QCD radiation activity.

Channel	conv. type	$p_T - \eta$ bin	θ_{MC}	stat.	rad.-up	rad.-down	PS and generator
$e + \text{jets}$	all	inclusive	1.41	± 0.07	+0.08	-0.15	± 0.07
$\mu + \text{jets}$	all	inclusive	1.47	± 0.08	+0.07	-0.12	± 0.38
combined	all	inclusive	1.44	± 0.06	+0.08	-0.03	± 0.22

Table 14: Inclusive MC-based double ratio correction factor for $e + \text{jets}$ and $\mu + \text{jets}$ channels separately and combined.

911 The deviation of measured θ_{MC} from unity indicates to a residual correlation, and should be taken into
 912 account. Therefore, the hadronic fake background is estimated as:

$$N_{\text{est.}}^{\text{h-fake}} = \frac{N_{\text{A, data}}^{\text{h-fake}} \cdot N_{\text{C,data}}^{\text{h-fake}}}{N_{\text{B,data}}^{\text{h-fake}}} \times \theta_{\text{MC}} \quad (11)$$

913 The double ratio is also calculated from a data-driven method as a cross check, the detail of which can be
 914 find in Appendix E.

915 Finally, the hadronic fake scale factor is calculated as:

$$\text{SF}^{\text{h-fake}} = \frac{N_{\text{est.}}^{\text{h-fake}}}{N_{\text{MC}}^{\text{h-fake}}} \quad (12)$$

916 The resulting scale factor for inclusive photon p_T , η and conversion type, are summarised in Table 15. The
 917 systematics uncertainty of $\text{SF}^{\text{h-fake}}$ includes the uncertainties of the subtraction of the non-hadronic-fakes
 918 from data (see Equation 9), where 100% is considered for $t\bar{t}\gamma$, 50% for the rest of the prompts, 50% for
 919 $e \rightarrow \gamma$ fakes and the uncertainty of the data-driven fake-leptons as explained in Section 6.3.1. The rest of
 920 systematics uncertainty of $\text{SF}^{\text{h-fake}}$ comes from the uncertainty of θ_{MC} , due to its statistics and $t\bar{t}$ modelling
 921 systematics.

Channel	conv. type	$p_T - \eta$ bin	$\text{SF}^{\text{h-fake}}$	stat.	syst.				
					$t\bar{t}\gamma$ subtract.	rest subtract.	θ_{MC} stat.	θ_{MC} rad.-up/-down	θ_{MC} PS and gen.
$e + \text{jets}$	all	inclusive	1.63	± 0.11	± 0.18	± 0.15	± 0.08	$+0.09/-0.17$	± 0.08
$\mu + \text{jets}$	all	inclusive	1.57	± 0.10	± 0.19	± 0.10	± 0.09	$+0.07/-0.13$	± 0.41
combined	all	inclusive	1.60	± 0.07	± 0.19	± 0.12	± 0.07	$+0.09/-0.03$	± 0.24

Table 15: Inclusive hadronic fake scale factor for $e + \text{jets}$ and $\mu + \text{jets}$ channels separately and combined.

922 Furthermore, $\text{SF}^{\text{h-fake}}$ is calculated for bins of photon p_T and η , separately for converted and unconverted
 923 photons. This is done by using the θ_{MC} that is measured for the same kinematic range and conversion
 924 type. The resulting $\text{SF}^{\text{h-fake}}$ are shown in Figure 41 and 42 for combined single lepton. The choice of
 925 binning for p_T is based on the statistics and the $|\eta|$ bins are chosen according to the detector geometry. A
 926 clear dependency on p_T , η and conversion type can be seen.

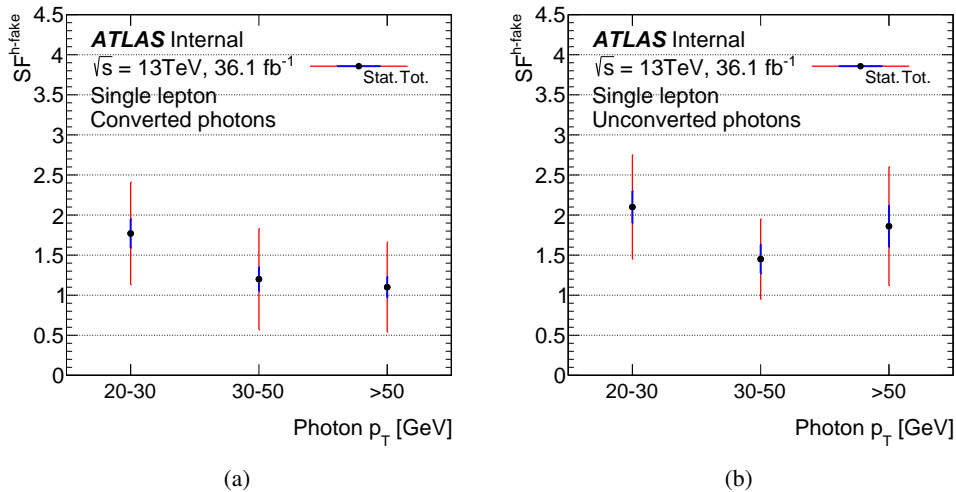


Figure 41: $\text{SF}^{\text{h-fake}}$ in photon p_T bins for (a) converted and (b) unconverted photons.

927 The final $\text{SF}^{\text{h-fake}}$ used in the analysis are the scale factors that are calculated in 2D bins of $p_T - \eta$ and
 928 separated for converted and unconverted photons, using the θ_{MC} derived for the same kinematic 2D bin

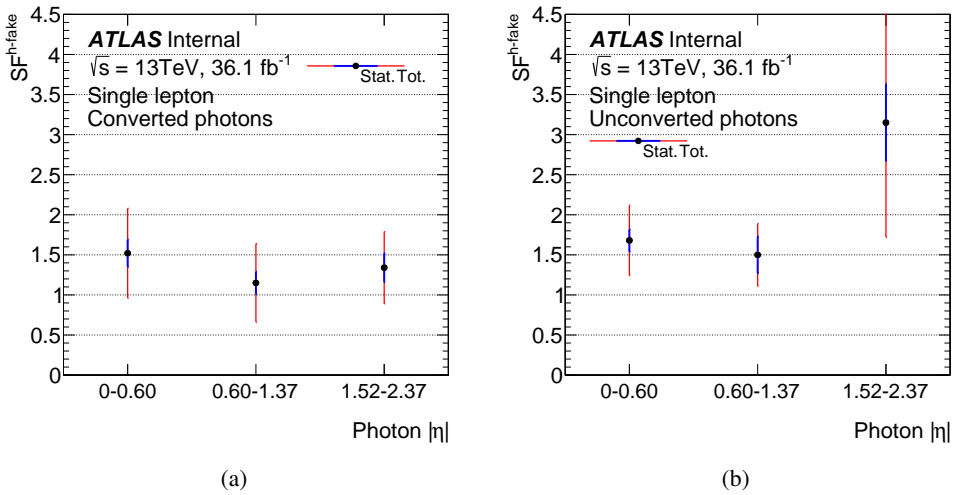


Figure 42: $SF^{h\text{-fake}}$ in photon $|\eta|$ bins for (a) converted and (b) unconverted photons.

and conversion type. The neighbouring kinematic bins that resulted to $SF^{h\text{-fake}}$ consistent within statistical uncertainties are merged together. This leads to five 2D bins for each of the converted and unconverted category. Figure 43 and Table 16 show the resulting $SF^{h\text{-fake}}$ for the combined single lepton channel.

In the final fit, the systematics uncertainties of $SF^{h\text{-fake}}$ due the $t\bar{t}$ modelling are correlated to the relevant same systematics source.

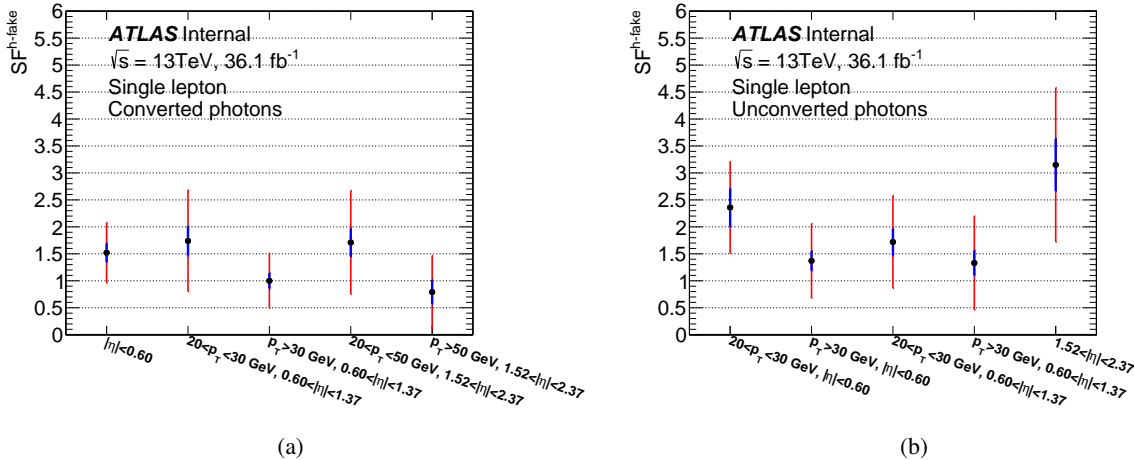


Figure 43: Final $SF^{h\text{-fake}}$, derived for 2D $p_T - \eta$ bins separately for (a) converted and (b) unconverted photons.

6.2.2 Estimation of hadronic fakes in dilepton channel

For the dilepton channel, there are not enough statistics in the regions A and C to use the ABCD method. The contribution of hadronic fake background is much smaller in this channel, the MC estimate shows 3-5% contribution for different dilepton channels (Table 9).

Not reviewed, for internal circulation only

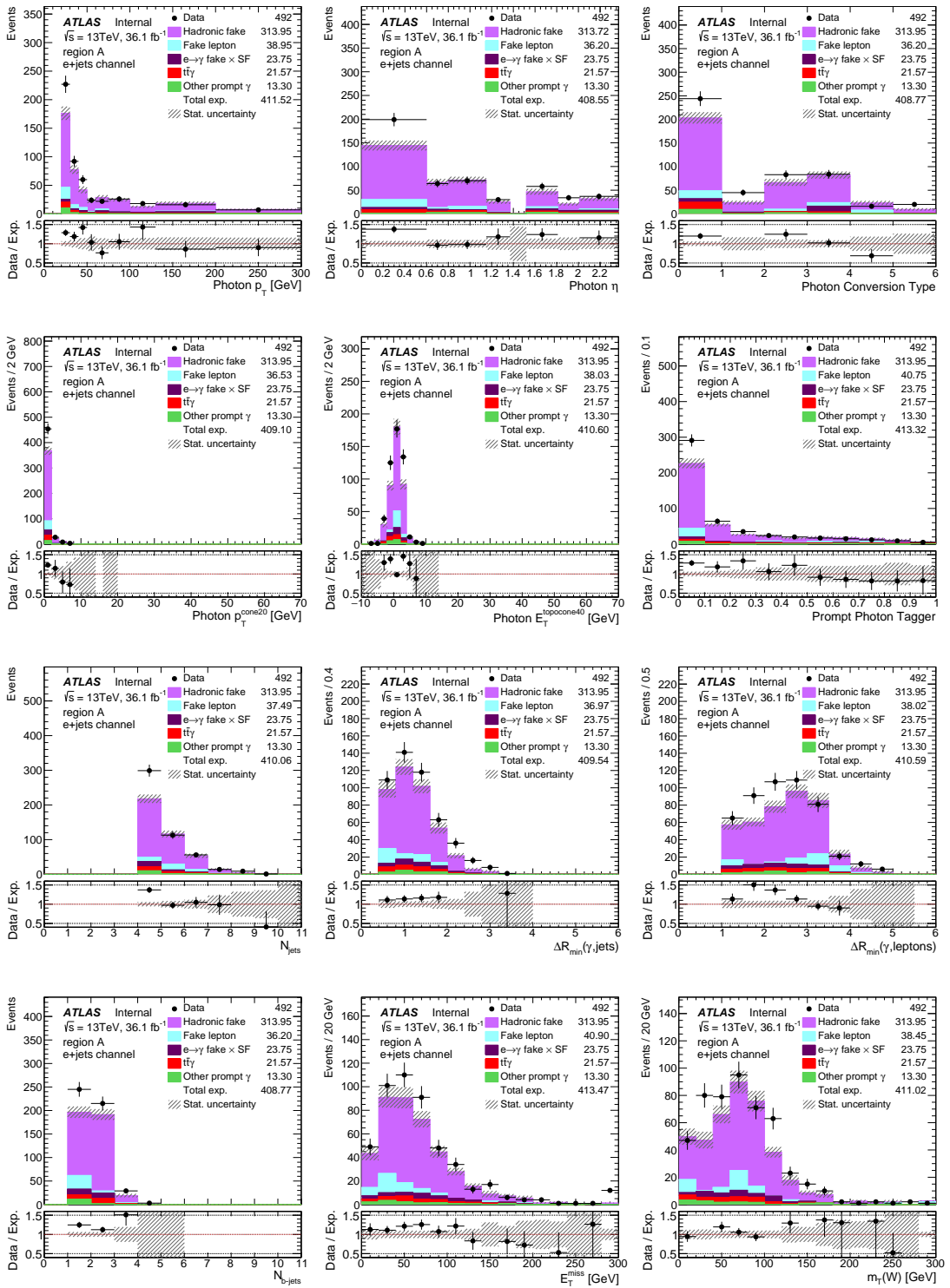


Figure 44: Plots of region A in $e+jets$ channel, where photons are identified as fail-tight and are isolated.

Not reviewed, for internal circulation only

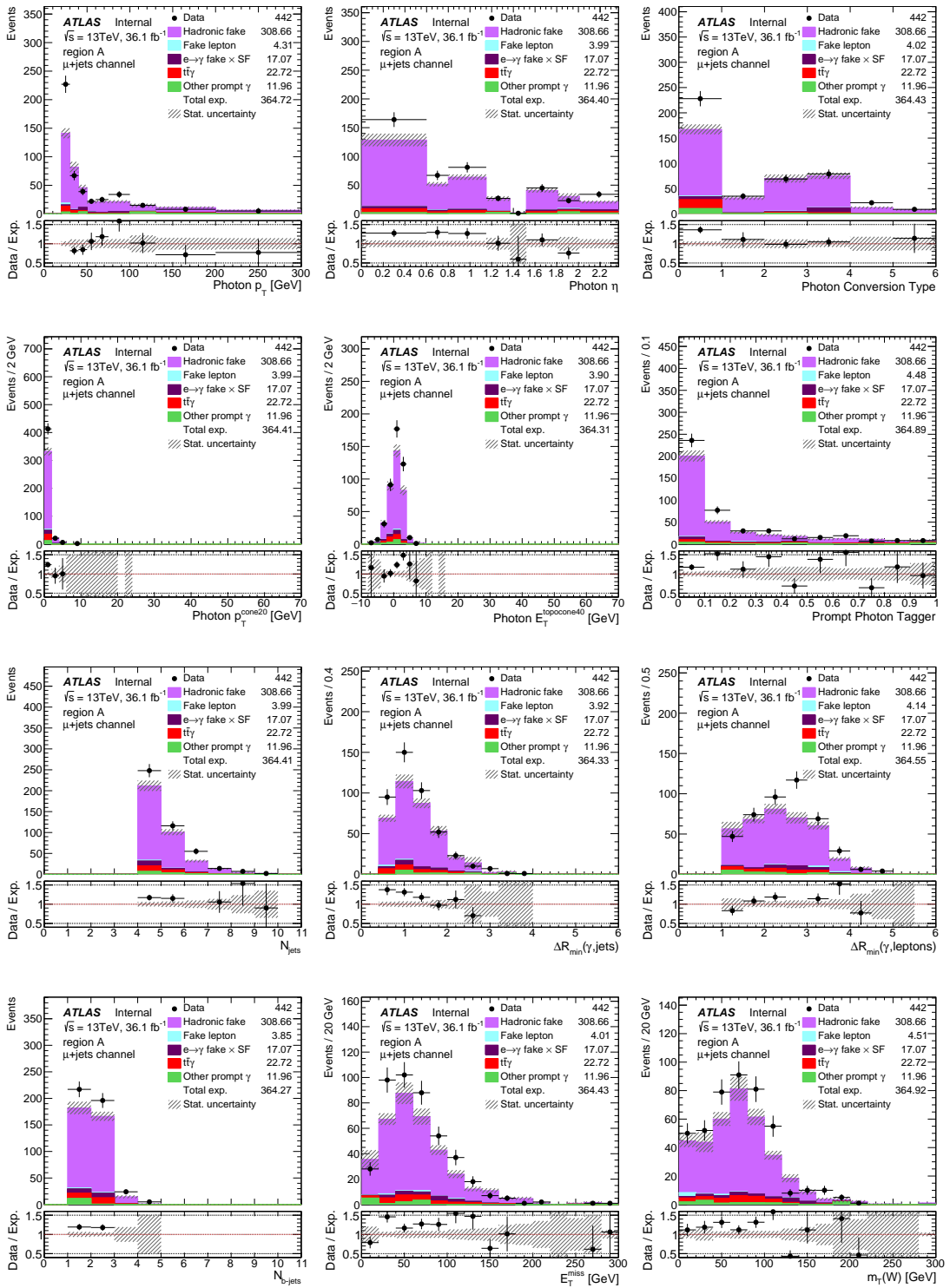


Figure 45: Plots of region A in $\mu+\text{jets}$ channel, where photons are identified as fail-tight and are isolated.

Not reviewed, for internal circulation only

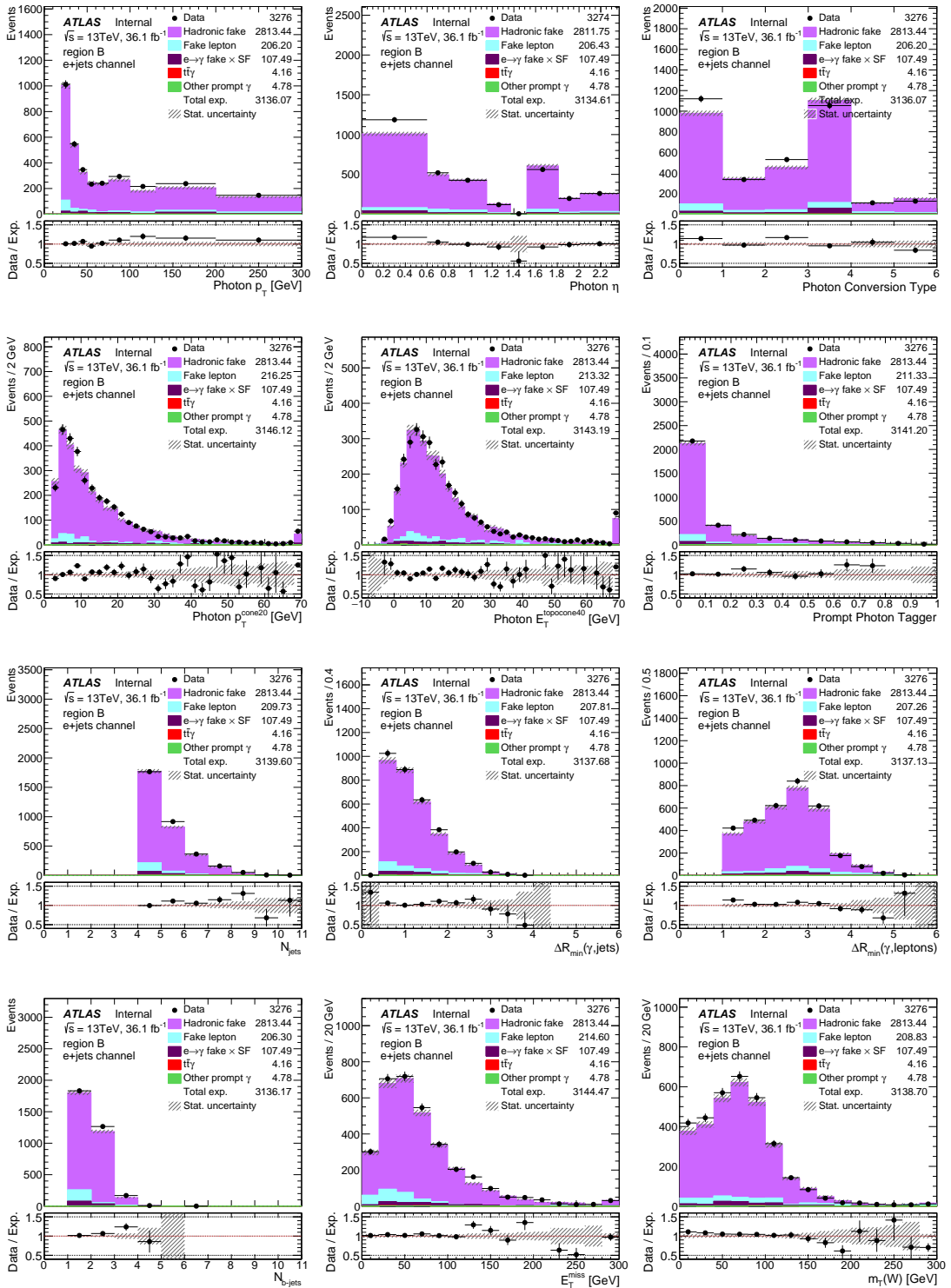


Figure 46: Plots of region B in $e+\text{jets}$ channel, where photons are identified as fail-tight and are non-isolated.

Not reviewed, for internal circulation only

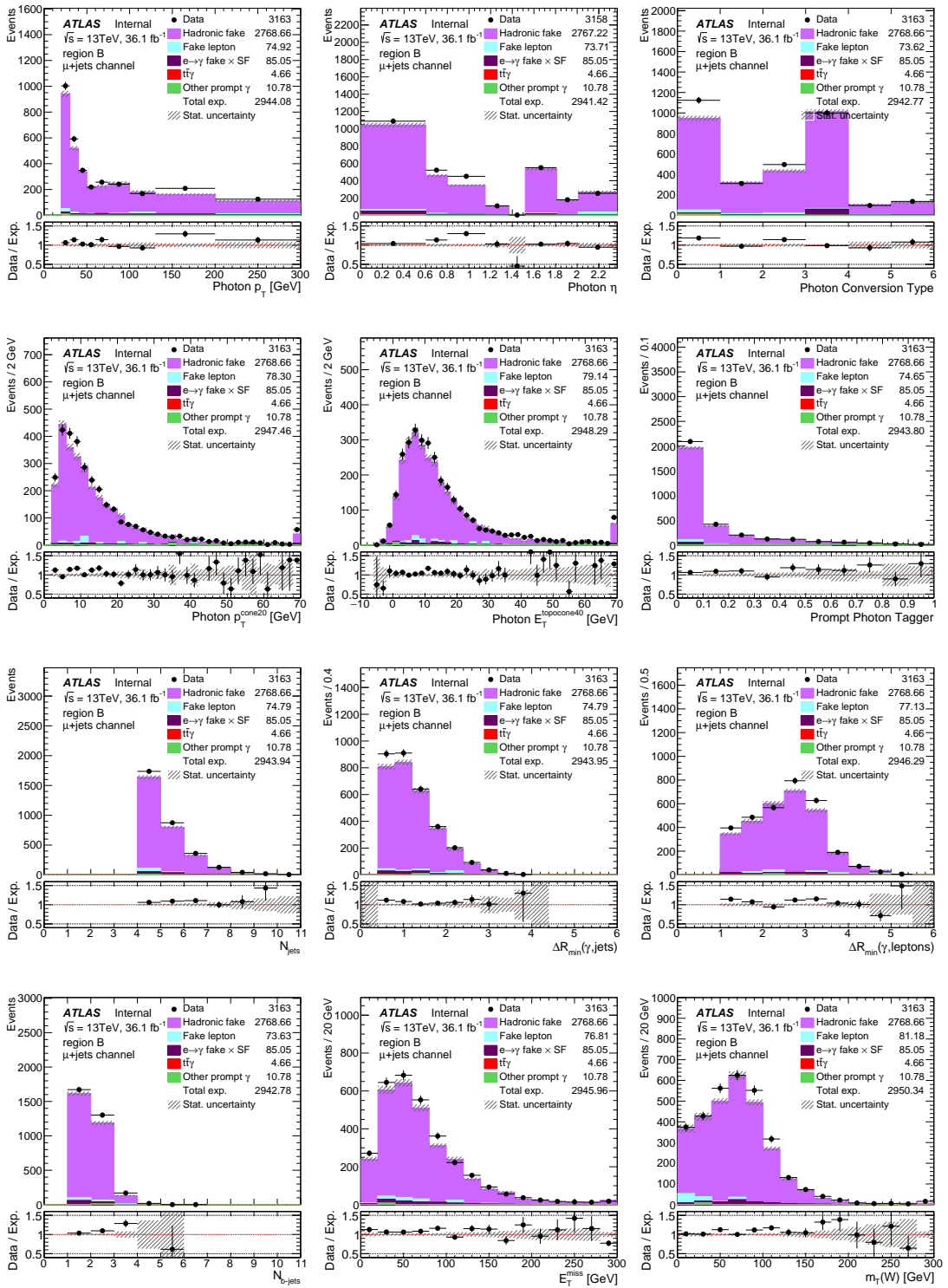


Figure 47: Plots of region B in $\mu + \text{jets}$ channel, where photons are identified as fail-tight and are non-isolated.

Not reviewed, for internal circulation only

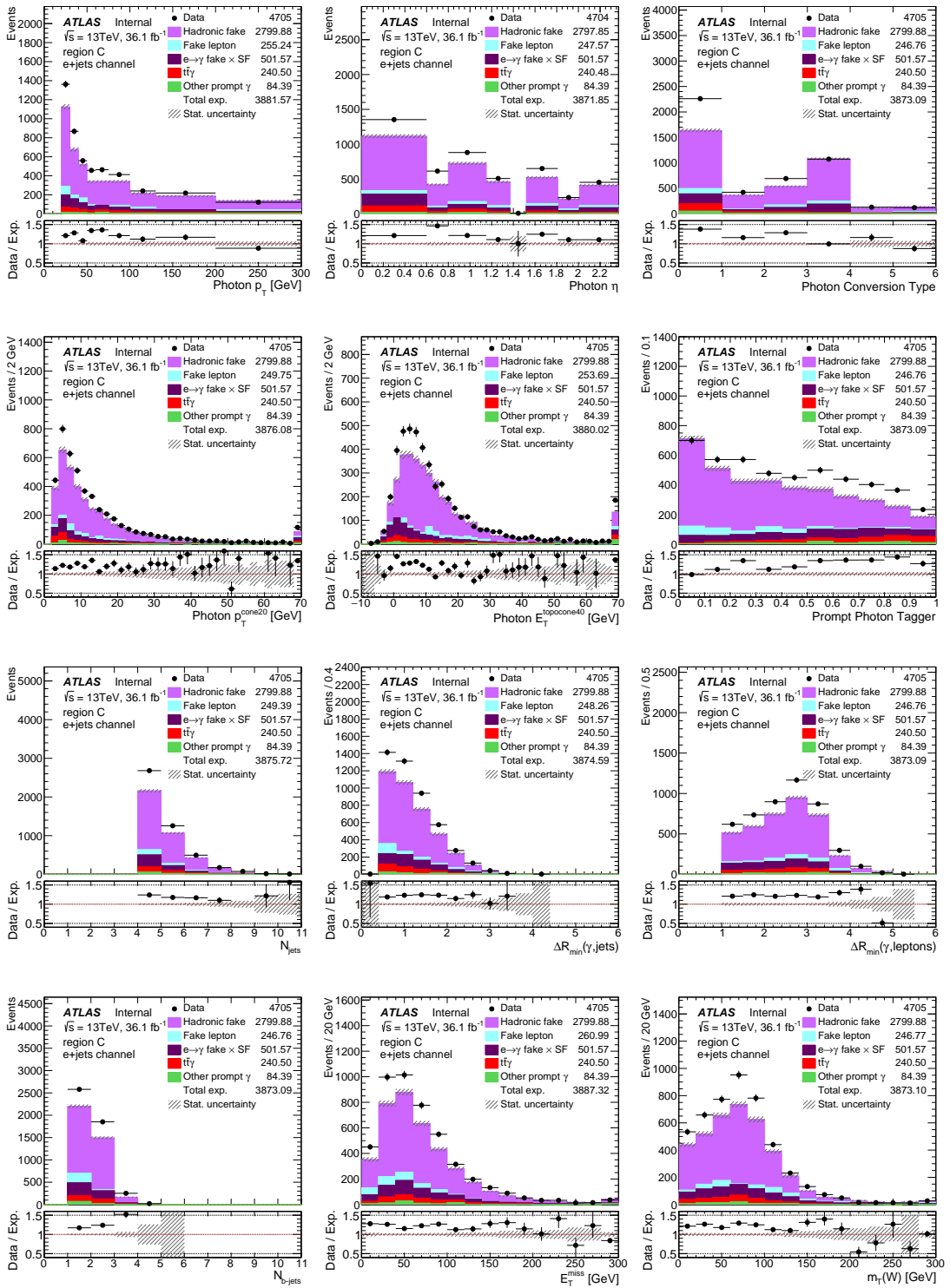


Figure 48: Plots of region C in $e+jets$ channel, where photons are identified as tight and are non-isolated.

Not reviewed, for internal circulation only

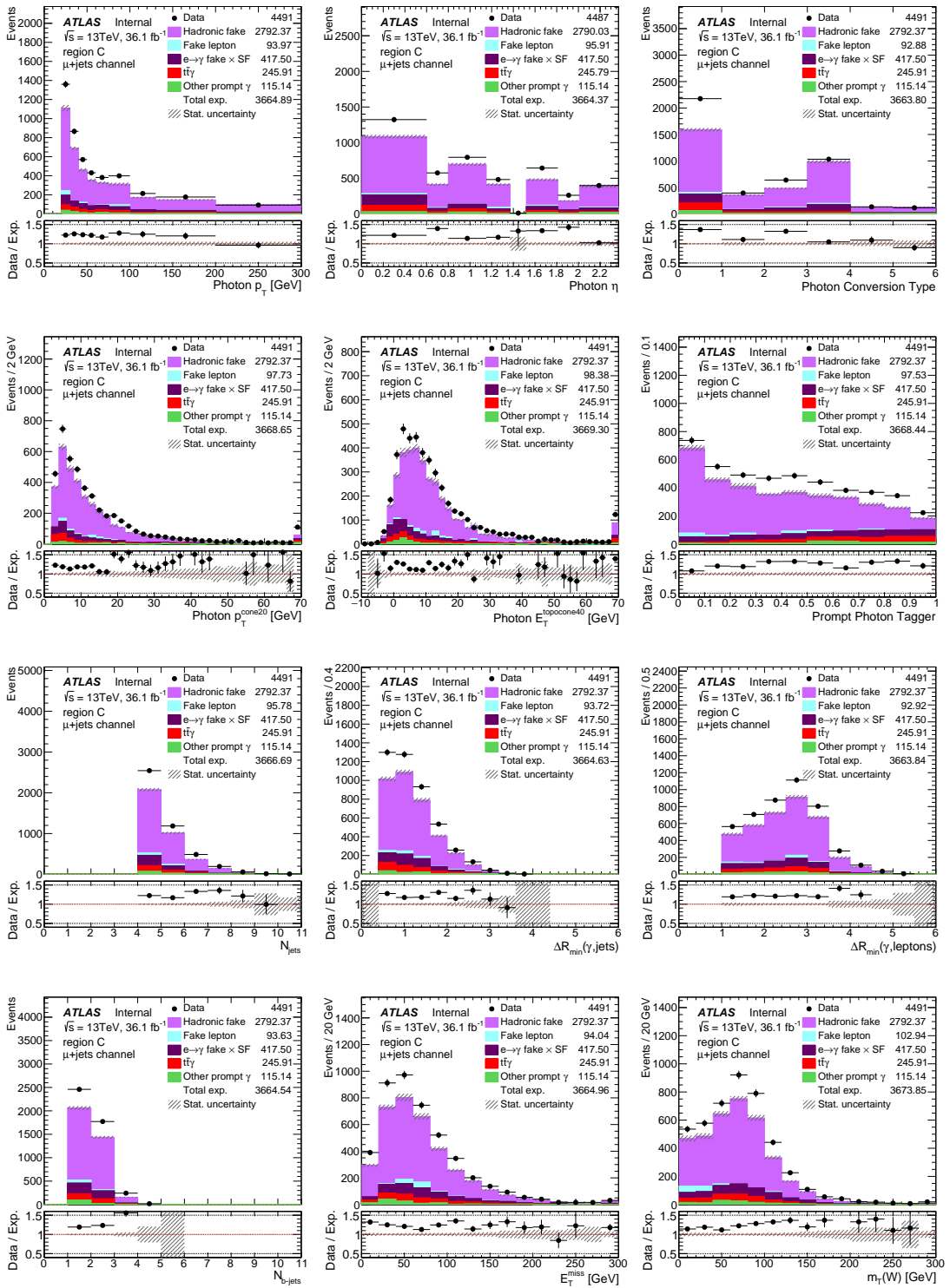


Figure 49: Plots of region C in $\mu+\text{jets}$ channel, where photons are identified as tight and are non-isolated.

Channel	conv. type	$p_T - \eta$ bin	SF-fake	stat.	syst.				
					$t\bar{t}\gamma$ subtract.	rest subtract.	θ_{MC} stat.	θ_{MC} rad.-up/-down	θ_{MC} PS and gen.
single lepton	conv.	$ \eta < 0.60$	1.52	± 0.17	± 0.13	± 0.15	± 0.18	$+0.26/-0.18$	± 0.38
		$0.60 < \eta < 1.37, 20 < p_T < 30$	1.74	± 0.27	± 0.14	± 0.09	± 0.23	$+0.16/-0.47$	± 0.71
		$0.60 < \eta < 1.37, p_T > 30$	1.00	± 0.14	± 0.07	± 0.09	± 0.08	$+0.00/-0.09$	± 0.46
		$1.52 < \eta < 2.37, 20 < p_T < 50$	1.71	± 0.26	± 0.15	± 0.23	± 0.23	$+0.05/-0.59$	± 0.60
		$1.52 < \eta < 2.37, p_T > 50$	0.79	± 0.22	± 0.06	± 0.12	± 0.12	$+0.59/-0.26$	± 0.17
	unconv.	$ \eta < 0.60, 20 < p_T < 30$	2.36	± 0.35	± 0.25	± 0.13	± 0.42	$-0.49/-0.39$	± 0.36
		$ \eta < 0.60, p_T > 30$	1.37	± 0.18	± 0.24	± 0.12	± 0.15	$-0.13/-0.08$	± 0.58
		$0.60 < \eta < 1.37, 20 < p_T < 30$	1.72	± 0.25	± 0.18	± 0.05	± 0.22	$-0.19/-0.48$	± 0.60
		$0.60 < \eta < 1.37, p_T > 30$	1.33	± 0.23	± 0.23	± 0.14	± 0.14	$-0.08/-0.72$	± 0.31
		$1.52 < \eta < 2.37$	3.15	± 0.48	± 0.57	± 0.27	± 0.37	$+0.95/-0.98$	± 0.61

Table 16: hadronic fake scale factor for single lepton channel derived for 2D photon $p_T - \eta$ bins separately for converted and unconverted photons.

938 Since the source of hadronic fakes are not depending on the number of leptons, the same scale factor of
 939 single lepton channel are used, with additional extrapolation systematics.

940 The extrapolation systematics are studied by varying the ratio between MC predicted hadronic fakes in the
 941 dilepton channel over that of the single lepton channel, since the dilepton hadronic fakes can be expressed
 942 as:

$$N_{dilepton} = \text{SF} \times N_{dilepton}^{MC} = N_{singlelepton}^{data} \times \frac{N_{dilepton}^{MC}}{N_{singlelepton}^{MC}} \quad (13)$$

943 where systematics enter mainly through the ratio term.

944 The considered systematic variations include: the $t\bar{t}$ modelling uncertainties discussed above, which
 945 amounts to 10%, dominated by the Sherpa variation. all the experimental uncertainties, which are 8%,
 946 dominated by pile-up uncertainty.

947 6.3 Background due to fake leptons

948 Another background contribution to $t\bar{t}\gamma$ SR comes from the so called *fake leptons*. They are the non-prompt
 949 leptons misidentified as prompt leptons, or jets that are mis-reconstructed as leptons. The non-prompt
 950 leptons could be coming from the decay of a heavy hadron (bottom or charm hadrons), or from a photon
 951 conversion, or they can be produced from the decay of a pion or a kaon.

952 The fake lepton background contribution to the single lepton channel is typically from QCD multijets
 953 events with associated photon production, and the contribution to the dilepton channel is typically from
 954 single lepton $t\bar{t}\gamma$ events or $W+jets$ events with associated photon production, with a fake lepton in addition
 955 to the real lepton (events with two fake leptons very rarely happen).

956 6.3.1 Fake leptons in single lepton channel

957 The estimation of this background in the single lepton channel is done in two steps: firstly, the *matrix*
 958 *method* in the standard $t\bar{t}$ analysis is applied to estimate fake lepton events satisfying all the signal region
 959 cuts, except for the photon related ones; then, the photon cuts are reapplied to the above fake lepton sample
 960 to estimate the background of fake lepton plus photon. More details are given below.

961 **The Matrix Method for fake lepton estimation:** The method is based on classifying leptons into two
 962 categories: *loose* and *tight*. The loose and tight definitions are as follow:

963

- 964 • Tight definition (same as nominal lepton definition in section 4.1):

965 For electrons: Tight LH, $p_T > 25$ GeV and gradient isolation.

966 For muons: Medium ID, $p_T > 25$ GeV and gradient isolation.

- 967 • Loose definition:

968 For electrons: Medium LH and no isolation.

969 For muons: Medium ID and no isolation. Besides, the low p_T muon trigger (below 51 GeV) for
 970 data of year 2016 is replaced from the nominal one as mentioned in Section 5.1 to the pre-scaled
 971 trigger of *HLT_mu24*, with a pre-scale of 50 to avoid possible trigger bias.

972 Based on these two lepton identification categories, two $t\bar{t}$ data samples are defined, differing only in the
 973 lepton identification while keeping the rest of the selection same as the signal region selection described
 974 in Section 5, but neglecting the photon related cuts.

975 The tight sample contains mostly events with real leptons, while the loose sample is enriched in events
 976 with fake leptons. The number of events in loose and tight samples is a linear combination of real and
 977 fake leptons:

$$N^{\text{loose}} = N_{\text{real}}^{\text{loose}} + N_{\text{fake}}^{\text{loose}} \quad (14)$$

978

$$N^{\text{tight}} = N_{\text{real}}^{\text{tight}} + N_{\text{fake}}^{\text{tight}} \quad (15)$$

979 By defining ϵ_{real} (ϵ_{fake}) as the probability of real (fake) leptons in the loose sample to pass the tight
 980 selection, one can write:

$$N^{\text{tight}} = \epsilon_{\text{real}} N_{\text{real}}^{\text{loose}} + \epsilon_{\text{fake}} N_{\text{fake}}^{\text{loose}} \quad (16)$$

981 From equations 14-16, the number of tight events in data with fakes leptons can be written as:

$$N_{\text{fake}}^{\text{tight}} = \frac{\epsilon_{\text{fake}}}{\epsilon_{\text{real}} - \epsilon_{\text{fake}}} (\epsilon_{\text{real}} N_{\text{real}}^{\text{loose}} - N^{\text{tight}}) \quad (17)$$

982 Both ϵ_{real} and ϵ_{fake} have dependency on lepton kinematics and event topology (e.g. number of jets or
 983 b -jets) and they are estimated as described in [47]. To estimate the fake lepton background, an event
 984 weight could be computed using these real and fake efficiencies, where the efficiencies would be functions
 985 of various object and event properties:

$$w_i = \frac{\epsilon_{\text{fake}}}{\epsilon_{\text{real}} - \epsilon_{\text{fake}}} (\epsilon_{\text{real}} - \delta_i) \quad (18)$$

986 where δ_i is unity if loose event i pass the tight selection and 0 otherwise. The sample of N^{loose} together
 987 with this set of weights constitute a fake lepton sample in the signal region with the photon related cuts
 988 stripped away. What's left to do is just to reapply the photon cuts to this sample, which is trivial.

989 **The parametrisation of the efficiencies:** The real and fake efficiencies are measured in a fake lepton
 990 control region with respect to different variables, which are called different parametrisation of the effi-
 991 ciencies. They are all centrally measured in the top group and distributed to each analyses. The variables
 992 or parametrisations tested in this analysis include:

- 993 • “pt”: p_T of the lepton
- 994 • “eta”: $|\eta|$ of the lepton
- 995 • “jetpt”: p_T of the leading jet
- 996 • “dR”: minimum ΔR between the lepton and the closest jet
- 997 • “dPhi”: $\Delta\phi$ between the lepton and E_T^{miss}
- 998 • “nbtag”: number of b -jets
- 999 • “mtw”: transverse mass of W boson candidate ⁷

1000 Besides, the double combination and triple combination of the above choices are also tested. Thus
 1001 in total $7 + C_7^2 + C_7^3 = 63$ parametrisations are studied. From the distribution of event yield of all
 1002 these parameterisations, some give negative values or values that are very far way from the peak of the
 1003 distribution, so they are removed in the following. In practise, all “pt” related parametrisations in $e+jets$
 1004 channel and all “dPhi” related parametrisations in $\mu+jets$ channel are removed.

⁷ $m_T(W) = \sqrt{2p_T(l) \times E_T^{\text{miss}}(1 - \cos\phi)}$, where ϕ is the azimuthal angle between the lepton direction and the E_T^{miss} .

Not reviewed, for internal circulation only

1005 For the $e+jets$ channel, the remaining parametrisations are shown in the left plot of Figure 50. This
 1006 distribution is projected onto its y axis, as shown in the right plot of Figure 50. It shows a peak with
 1007 certain width. Thus it is decided to use the parametrisation that is most close to the peak of the distribution
 1008 as the nominal and the two parametrisations corresponding to the lower and upper edge of this peak as up
 1009 and down systematic variations.

1010 The same procedure can be performed for the $\mu+jets$ channel and the results are summarized in Figure 51.
 1011 And the finally predicted lepton fake backgrounds, together with its systematic variations, are summarized
 1012 in table 17.

1013 In Figure 52 and Figure 53, some kinematic distributions are compared between the nominal and the
 1014 up and down variations for the $e+jets$ and $\mu+jets$ channels respectively. We can see the up and down
 1015 variations enclose the nominal very well. Besides, since the up and down variation already cover a wide
 1016 range and the fake lepton is a small background, no additional systematics will be considered.

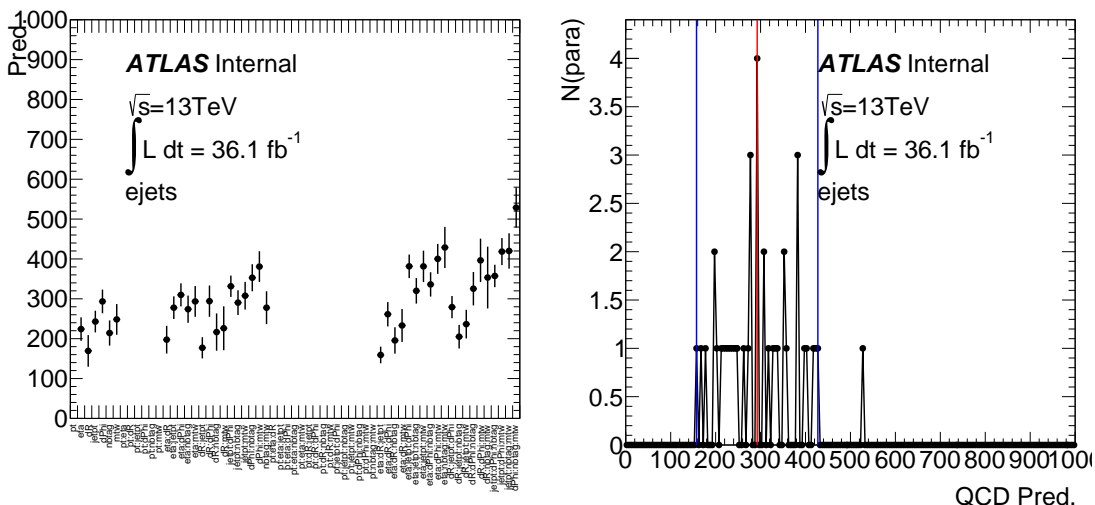


Figure 50: Left: the distribution of predicted lepton fake for different parameterisations in the $e+jets$ channel. Right: the projection of the distribution in the left onto its y axis.

Table 17: The nominal and up and down variation of the fake lepton in the single lepton channel.

Variation	Down	Nominal	Up
$e+jets$ para.	eta:dR:jpt	eta:mtw	eta:nbtags:mtw
$e+jets$ N	159.1 ± 20.9	293.5 ± 38.6	428.8 ± 51.6
$\mu+jets$ para.	pt:eta:dR	pt:mtw	jetpt:nbtags
$\mu+jets$ N	9.8 ± 25.0	72.1 ± 26.8	135.8 ± 38.4

1017 6.3.2 Fake leptons in dilepton channel

1018 Events with one prompt lepton and one fake lepton are calculated in a control region, defined in the same
 1019 way as the signal region described in Section 5 except for the opposite-sign two leptons are replaced by

Not reviewed, for internal circulation only

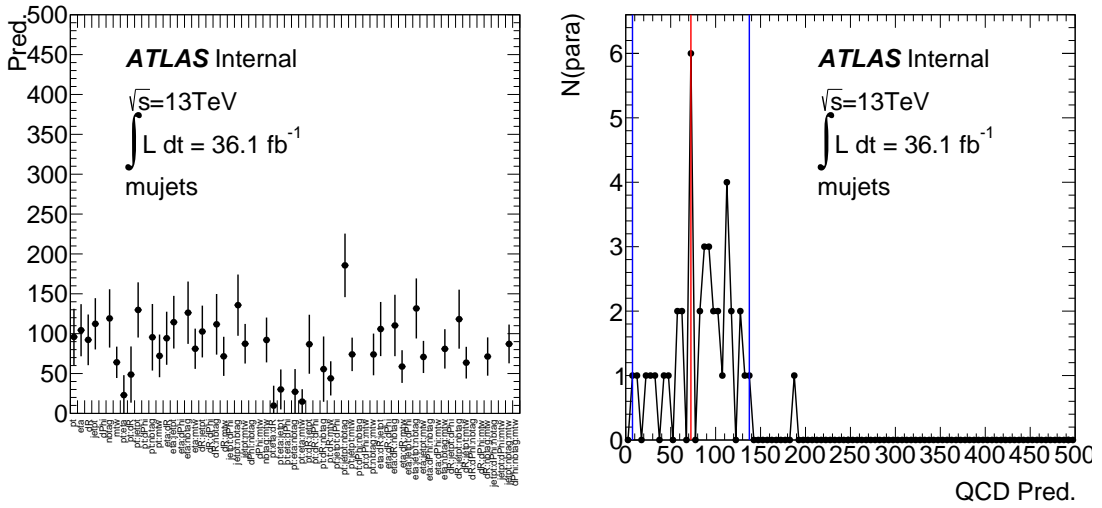


Figure 51: Left: the distribution of predicted lepton fake for different parameterisations in the μ +jets channel. Right: the projection of the distribution in the left onto its y axis.

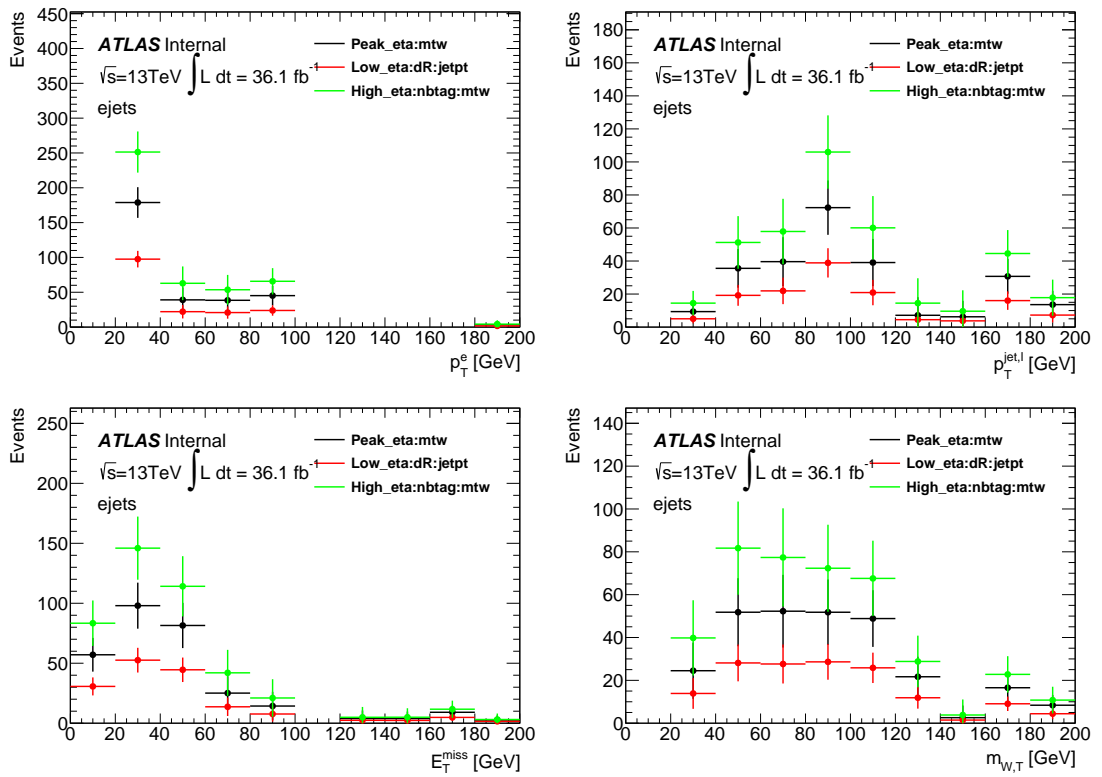


Figure 52: The lepton p_T , leading jet p_T , MET, and MWT distributions for the nominal (black), up variation (blue) and down variation (red) of the fake lepton background in the e +jets channel.

Not reviewed, for internal circulation only

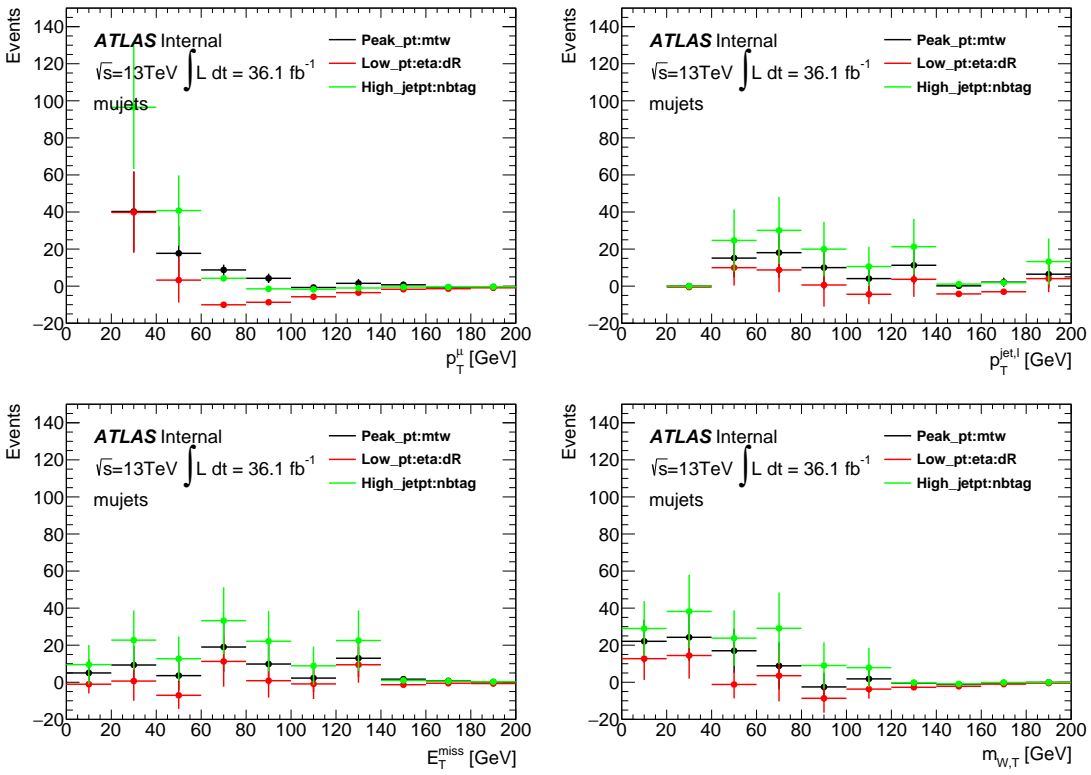


Figure 53: The lepton p_T , leading jet p_T , MET, and MWT distributions for the nominal (black), up variation (blue), and down variation (red) of the fake lepton background in the $e+jets$ channel.

1020 same-sign two leptons. The non-prompt (i.e. fake) leptons are identified using the truth MC record.

1021 The same MC samples described in Section 3 are used to estimate this background. It was found that the
 1022 majority is coming from $t\bar{t}$ single lepton events, with an extra fake lepton. While the most leptons in the
 1023 same sign regions are from prompt sources as described in Table 18. Other is a lepton coming from the
 1024 decay of a pion or a kaon or a misidentified lepton.

1025 The final number of fakes can be considered as the same sign data events after subtracting the prompt MC
 1026 events, which is found to be very small and negligible in the same flavour channel (ee and $\mu\mu$) compared
 1027 to the opposite sign signal region. Thus, a 100% uncertainty is assigned.

Table 18: The number of events in the same sign region in data, and the expected number of events with two prompt leptons or events with at least one fake lepton estimated from MC. The numbers are normalized to the total integrated luminosity of 36.47 fb^{-1} and statistical uncertainties are given.

Component	$e\mu$	ee	$\mu\mu$
Prompt lepton	5.8 ± 1.3	7.6 ± 1.5	0.1 ± 0.1
Heavy flavour	1.9 ± 1.0	0	0.5 ± 0.4
Other	0.5 ± 0.3	0	0
Data	17	3	2

1028 **6.4 Prompt photons background**

1029 All backgrounds to the $t\bar{t}$ process are also considered when accompanied by prompt photon radiation.
 1030 More specifically, it includes $W\gamma + \text{jets}$ ($W\gamma$), $Z\gamma + \text{jets}$ ($Z\gamma$), single top, diboson and $t\bar{t}V$ production with
 1031 an additional prompt photon.

1032 These backgrounds are estimated from MC simulations with the corresponding MC generator described
 1033 in Section 3. Events are selected using the $t\bar{t}\gamma$ event selections as described in Section 5. The $W\gamma$ and $Z\gamma$
 1034 samples are normalised to the NLO cross sections.

1035 For the single top and diboson samples, the QED radiation is simulated either internally in the parton
 1036 shower or with PHOTOS [26].

1037 Since the contributions from $W\gamma$ and $Z\gamma$ processes are the dominant ones in this prompt photon background
 1038 dedicated validation regions are defined to check how well our MC is modelling these processes. The
 1039 $Z\gamma$ background is modelled in the ee and $\mu\mu$ channels which can be found in Section 6.4.1, while the
 1040 modelling of the $W\gamma$ background in the $e+\text{jets}$ and $\mu+\text{jets}$ channels is described in Section 6.4.2.

1041 Table 19 summarises the contributions of backgrounds with an emission of a prompt photon after the full
 1042 selections in the dilepton and single lepton channels. The associated errors are the statistical uncertainties.
 1043 From here-on, the prompt photon contributions from the single top, diboson and $t\bar{t}V$ samples are grouped
 1044 into the Other prompt background category. In addition, depending on the channel, the $V\gamma$ process will
 1045 also be included in Other prompt. I.e., Other prompt will also contain $Z\gamma$ prompt photons for the single
 1046 lepton channels, and $W\gamma$ prompt photons for the dilepton channels.

Table 19: The expected yields of prompt photon background events from MC. The numbers are normalised to the total integrated luminosity of 36.1 fb^{-1} . Only statistical uncertainties are included.

Process	$e\mu$	$\mu\mu$	ee	$e+\text{jets}$	$\mu+\text{jets}$
$W\gamma$	-	-	-	540.80 ± 29.36	579.36 ± 33.57
$Z\gamma$	-	53.66 ± 13.65	21.40 ± 3.85	295.23 ± 46.27	151.98 ± 13.21
Single top	5.81 ± 1.14	2.64 ± 0.83	3.66 ± 1.21	84.61 ± 5.45	92.17 ± 6.20
Diboson	-	0.19 ± 0.30	0.16 ± 0.31	4.02 ± 0.96	5.60 ± 1.21
$t\bar{t}V$	2.50 ± 0.20	1.52 ± 0.14	1.31 ± 0.13	26.54 ± 0.76	24.80 ± 0.71

1047 **6.4.1 $Z\gamma$ validation region**

1048 The $Z\gamma$ background modeling was checked in different validation regions, orthogonal to the SR, i.e.
 1049 exactly two leptons and one photon as defined in Section 4.1 is required. The non- $Z\gamma$ contributions are
 1050 estimated from MC in the same way as in the signal region. Some selections are different with respect
 1051 to the signal region to have an enriched $Z\gamma$ VR. For the chosen VR the selections are defined as the
 1052 following: jets ≥ 0 , number of b-tagged jets = 1 and finally the invariant mass of the two leptons is
 1053 required to be in a mass window of [60, 100] GeV. With the requirement of b-tagged jets = 1 we enter the
 1054 heavy flavour jet modeling which is close to our signal region. A requirement asking for more than one
 1055 b-tagged jet introduces more $t\bar{t}\gamma$ signal into the region and so will not be considered.

Only statistical errors are included for these fits. Scale factors derived in the previous sections for hadronic fake and $e \rightarrow \gamma$ fake backgrounds have been applied. After performing a binned likelihood fit to the n_{jets} distribution we obtain scale factors of

$$SF_{ee} = 0.971 \pm 0.105$$

$$SF_{\mu\mu} = 1.035 \pm 0.090$$

1056 Pre- and post-fit distributions can be found in Figure 54 and 55. While difficult to see in these plots, the
 1057 $Z\gamma$ SHERPA samples are prone to slightly higher weights in very few events. Further studies have been
 1058 done to see if this impacts the result. This can be seen in Appendix O, which shows this not to be the
 1059 case.

1060 A further cross-check can be performed to assess the performance of the VR in the b-tagged jets = 0 region,
 1061 i.e., the light flavour region. The requirement on the cuts is identical to the above with the exception of the
 1062 b-tagged jet cut. From this fit we obtain scale factors of $SF_{ee} = 1.119 + 0.022$ and $SF_{\mu\mu} = 1.149 \pm 0.017$.
 1063 These plots can be seen in Section F.

1064 It can be concluded that we achieve decent modelling of the $Z\gamma$ background in the light and heavy flavour
 1065 jet region

1066 6.4.2 $W\gamma$ validation region

1067 Prompt photons in addition to $W \rightarrow l\nu$ form a non-negligible part of the single lepton background
 1068 contribution in the signal region. This validation region is used as a cross-check as the $W\gamma$ background
 1069 will be a free parameter in the final fit.

1070 For our chosen validation region, the difference in cuts with respect to the SR are the following: $2 \leq$
 1071 number of jets ≤ 3 , number of b-tagged jets = 1, $E_T^{\text{miss}} > 40$ GeV and $m_T(W) > 40$ GeV. In addition,
 1072 there is a further cut on the ELD distribution of < 0.04 to further reduce signal contamination. These cuts
 1073 select an orthogonal phase space to our SR with the E_T^{miss} and $m_T(W)$ cuts reducing contributions from
 1074 hadronic fake and $e \rightarrow \gamma$ fake backgrounds. For $e+jets$ we include a cut of $m(\gamma, lep) < 80$ GeV to further
 1075 reduce the contribution from $e \rightarrow \gamma$ fake.

Only statistical errors are included for these fits. Scale factors derived in the previous sections for hadronic fake and $e \rightarrow \gamma$ fake backgrounds have been applied. After performing a binned likelihood fit to the n_{jets} distribution (essentially making this a basic “cut-and-count”) we obtain scale factors of

$$SF_{e+jets} = 0.970 \pm 0.353$$

$$SF_{\mu+jets} = 1.138 \pm 0.108.$$

1076 Pre- and post-fit distributions can be found in Figure 56 and 57. Due to slightly larger weights found in
 1077 SHERPA samples a larger uncertainty band can be see in some bins of various distributions. Appendix O
 1078 goes into more detail about this type of issue and shows that no concern is needed for these events.

1079 As a cross-check, a second VR is defined to encapsulate the data/MC agreement specifically for light jets.
 1080 The difference in cuts from our SR are as follows: $1 \leq$ number of jets ≤ 3 , number of b-tagged jets =
 1081 0, $E_T^{\text{miss}} > 40$ GeV, and $dR(\gamma, lep) < 2.8$. For the $e+jets$ we additionally ask for $m_T(W) > 40$ GeV and
 1082 exclude events where the mass between the photon and the lepton falls in a window of [60, 100] GeV.

Not reviewed, for internal circulation only

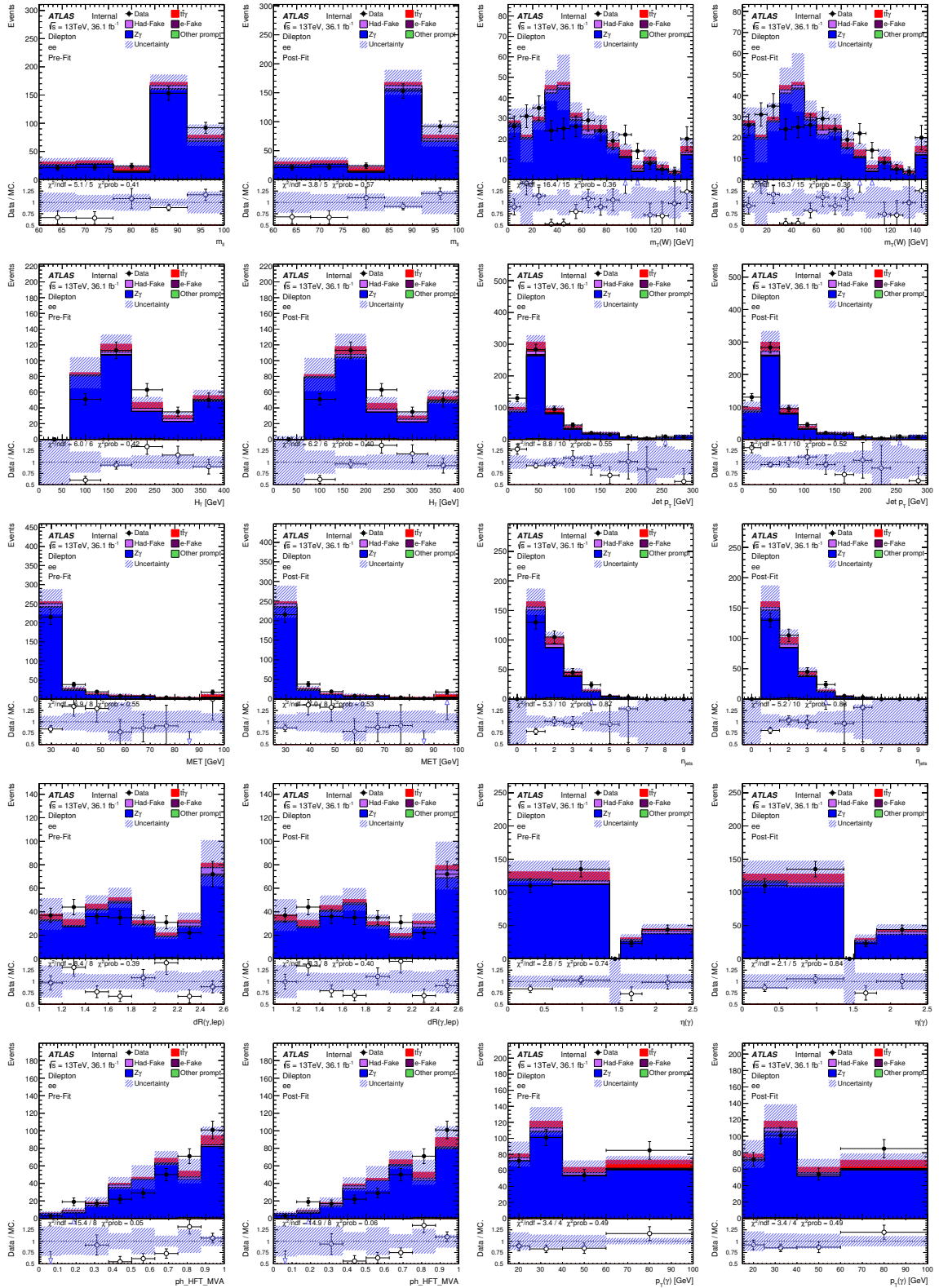


Figure 54: Pre and post-fit distributions for the ee $Z\gamma$ validation region, where number of b-tagged jets is 1.

Not reviewed, for internal circulation only

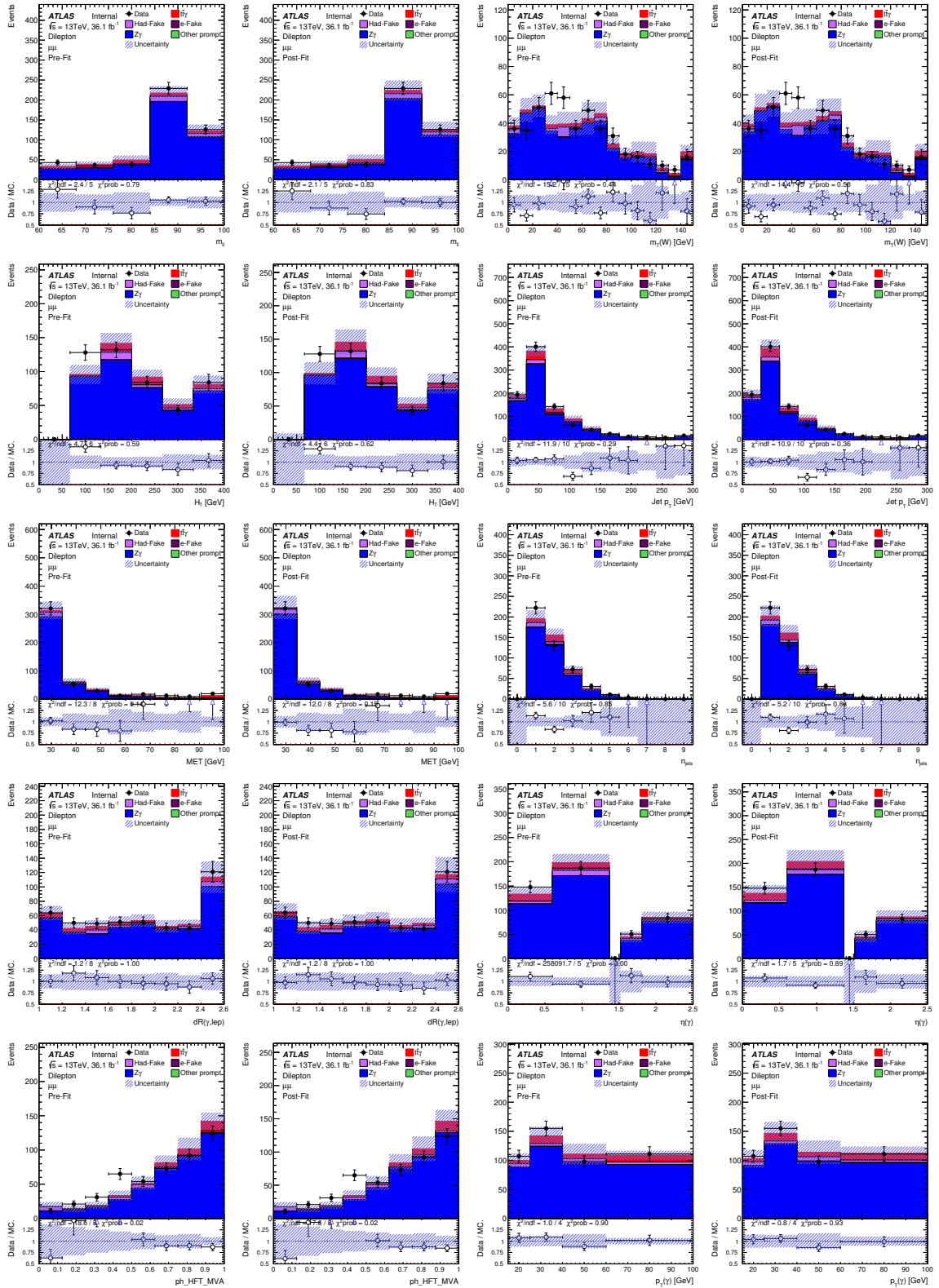


Figure 55: Pre and post-fit distributions for the $\mu\mu Z\gamma$ validation region, where number of b-tagged jets is 1.

¹⁰⁸³ The scale factors for e +jets and μ +jets fits are $SF_{e+\text{jets}} = 1.017 \pm 0.031$ and $SF_{\mu+\text{jets}} = 1.120 \pm 0.024$,
¹⁰⁸⁴ respectively. This shows that the normalisation in data and MC are in good agreement for the light and
¹⁰⁸⁵ heavy jet flavour phase space. These plots can be seen in Section G.

[Not reviewed, for internal circulation only]

Not reviewed, for internal circulation only

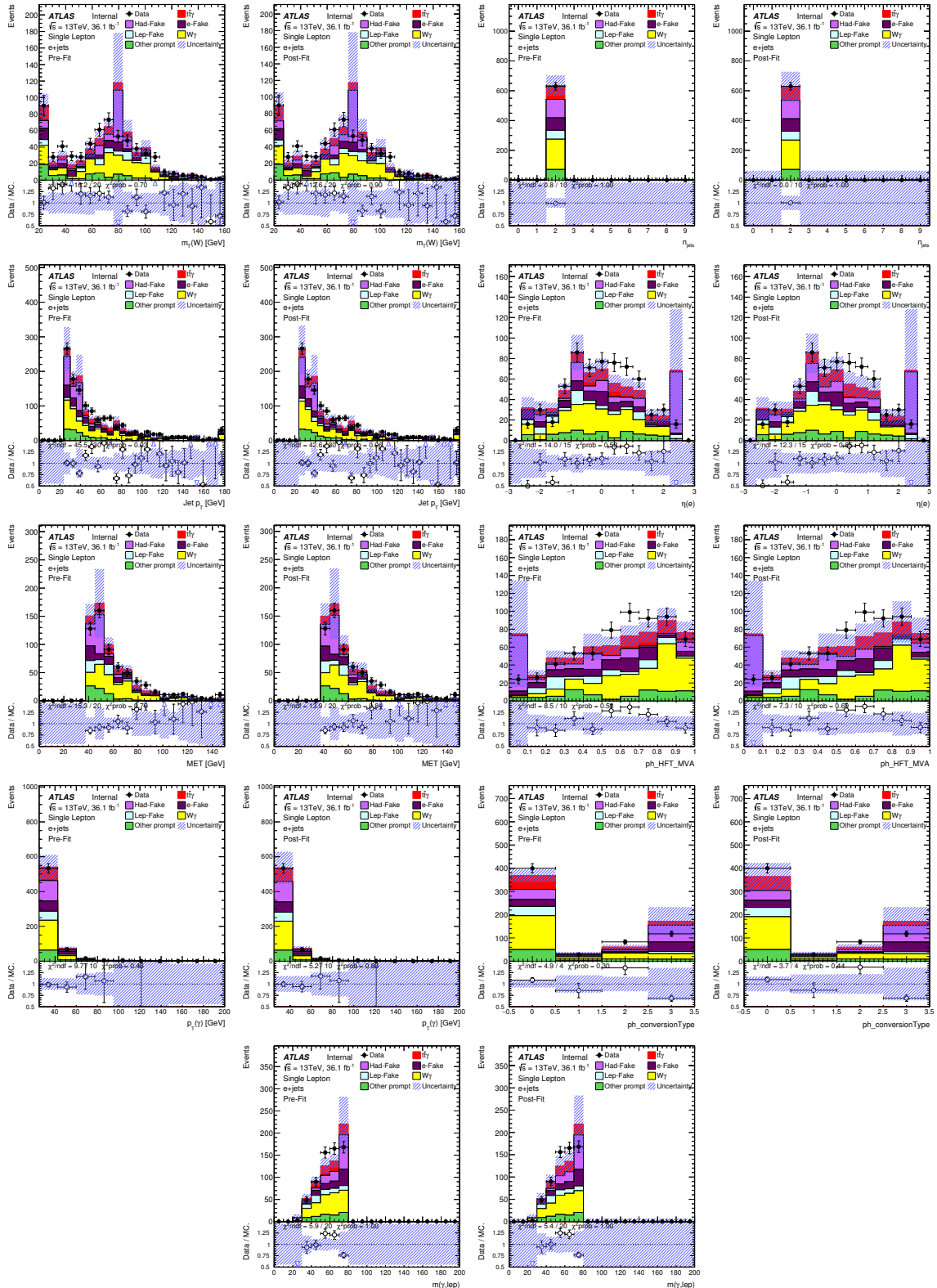


Figure 56: Pre and post-fit distributions for the $e + \text{jets}$ $W\gamma$ validation region, where number of b-tagged jets is 1.

Not reviewed, for internal circulation only

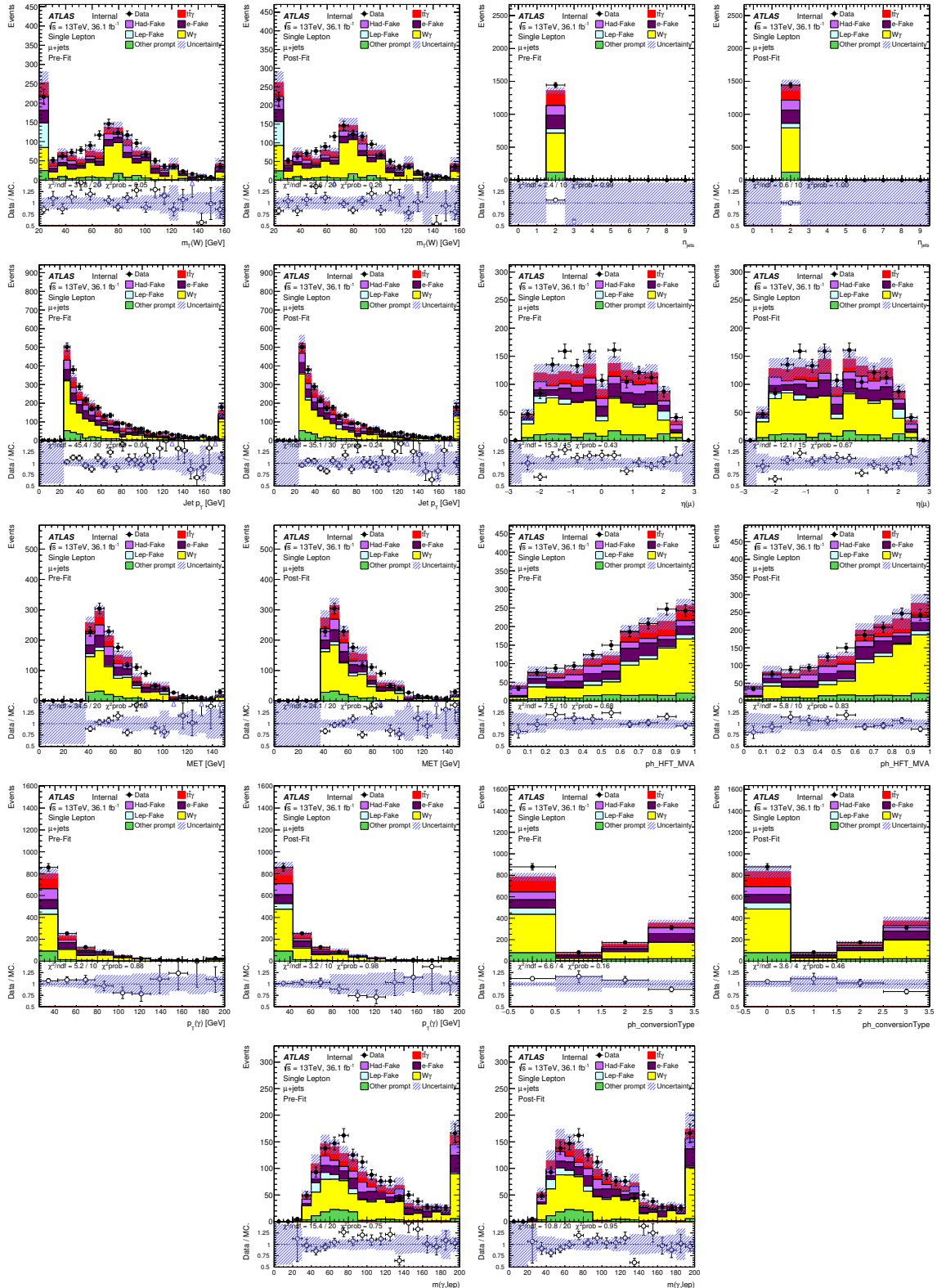
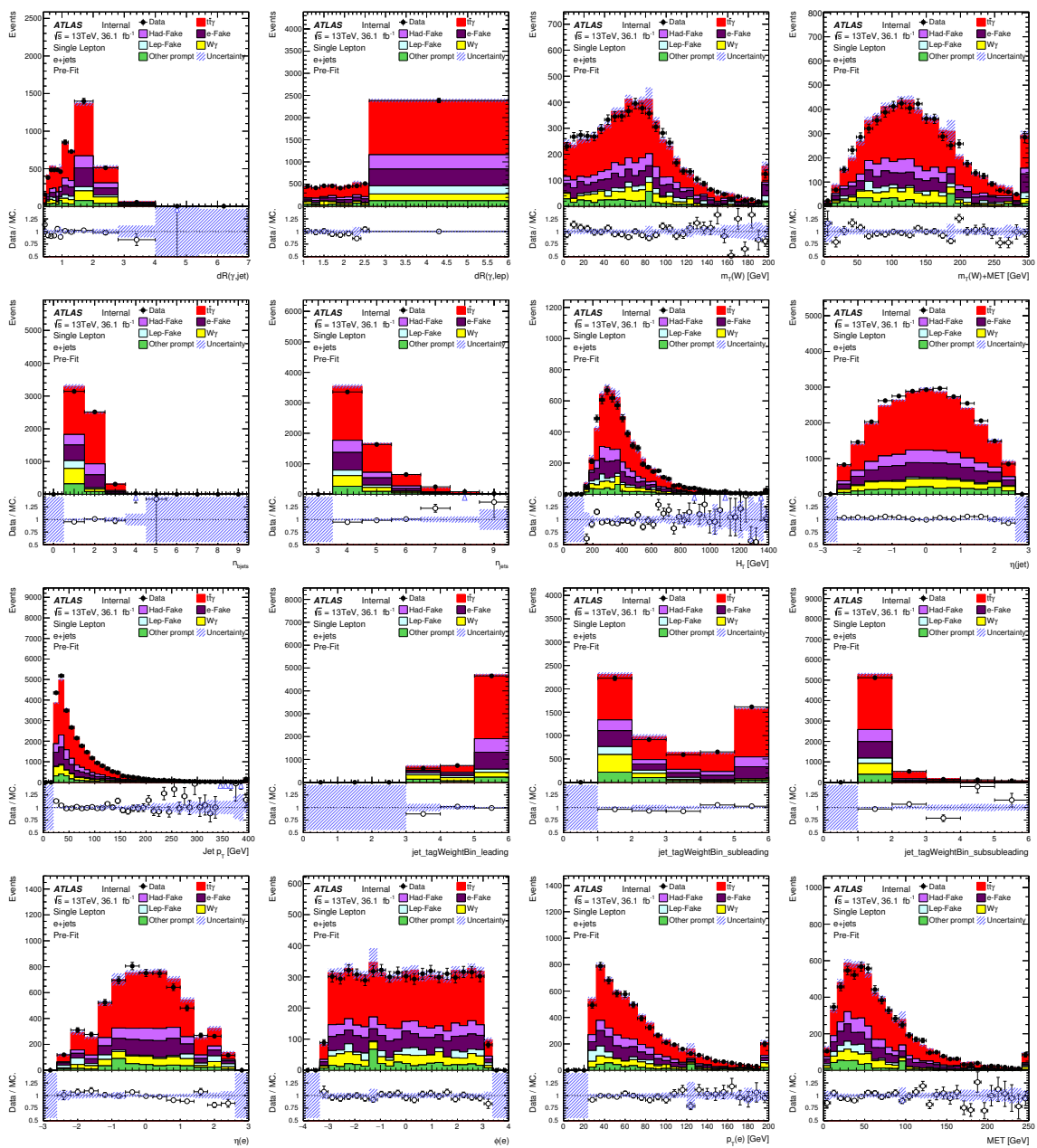


Figure 57: Pre and post-fit distributions for the μ +jets $W\gamma$ validation region, where number of b-tagged jets is 1.

1086 7 Pre-fit distributions with scale factors applied to the single lepton 1087 channels

1088 This section shows the same pre-fit plots as shown in Section 5.1 for single lepton channels. However,
1089 the scale factors derived for the hadronic fake background (Section 6.2) and those for the $e \rightarrow \gamma$ fake
1090 background (6.1) have been applied. Furthermore, the PPT prompt and $e \rightarrow \gamma$ fake scale factors derived
1091 in Section 4.2.2 have been applied to their respective processes. Since the correlation between PPT and
1092 the other variables (except the ELD) is around 0 as seen in Figure 26, we can safely apply these corrections
1093 to all variables. Improvements to data/MC agreement can be seen in Figure 58 and 59. Since there are no
1094 dedicated scale factors for the dilepton channels these are not shown here.

Not reviewed, for internal circulation only



Not reviewed, for internal circulation only

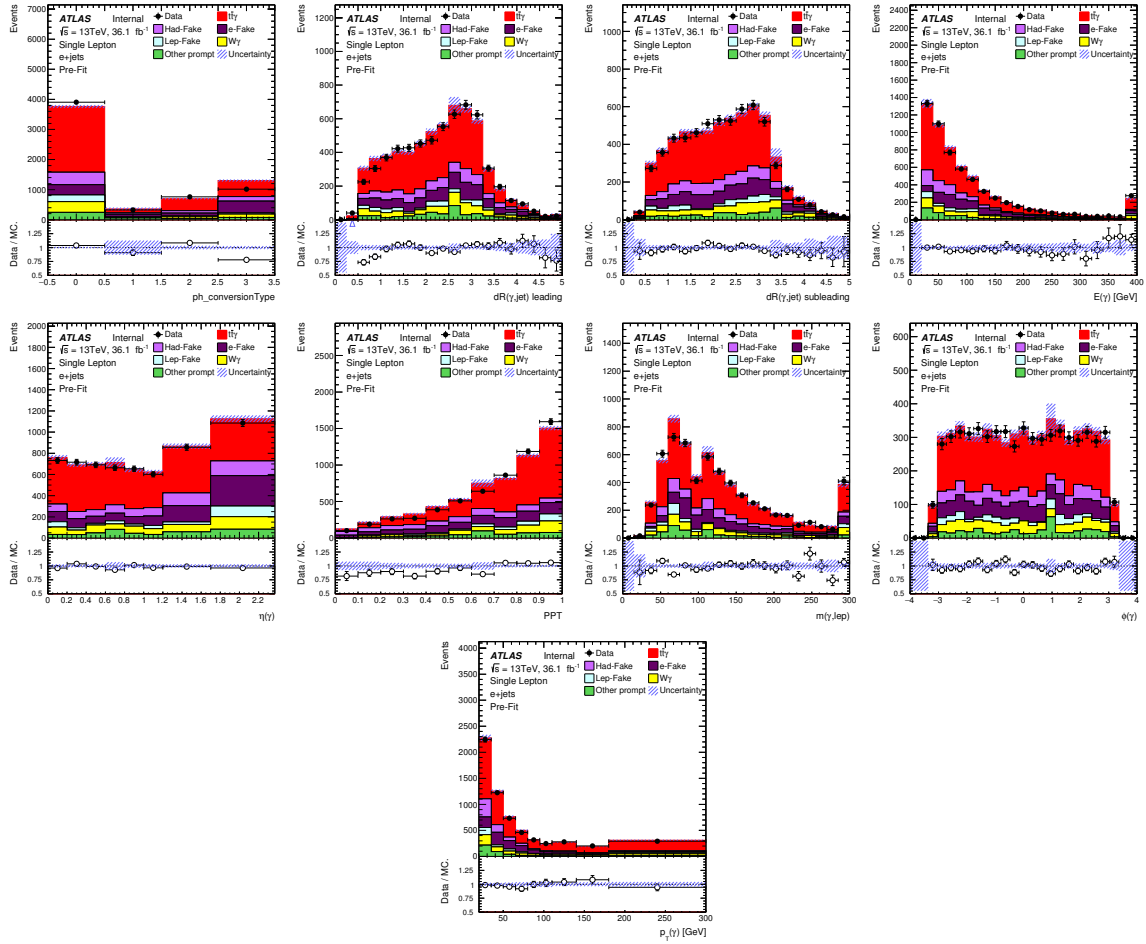
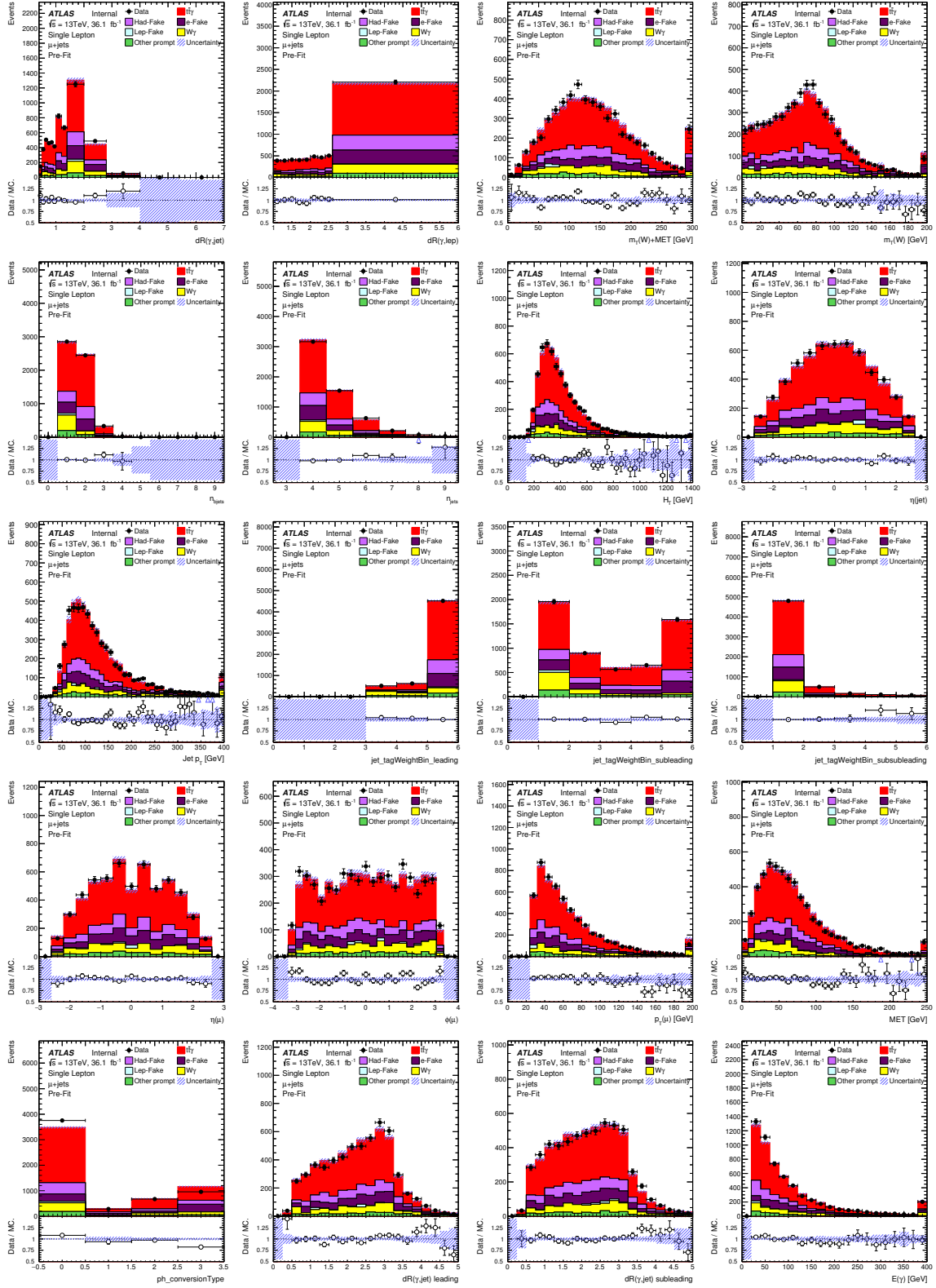


Figure 58: A selection of pre-fit distributions for the $e+jets$ channel with all scale factors applied. Only statistical uncertainties are included.

Not reviewed, for internal circulation only



Not reviewed, for internal circulation only

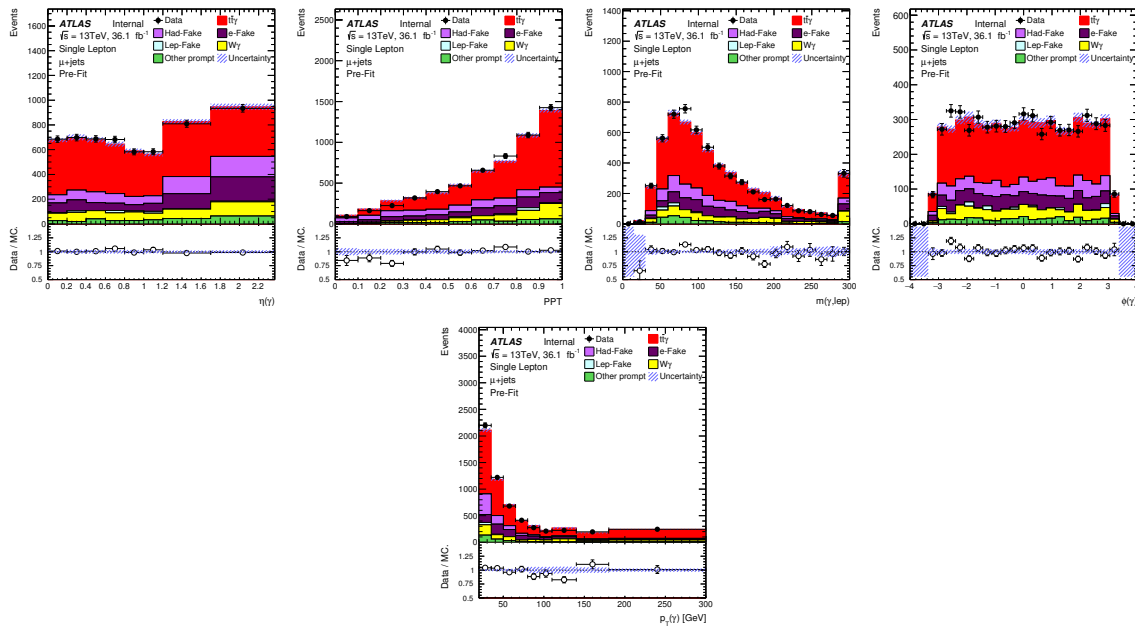


Figure 59: A selection of pre-fit distributions for the dilepton channel with all scale factors applied. Only statistical uncertainties are included.

1095 8 Systematic uncertainties

1096 Various sources of systematic uncertainties are considered for the $t\bar{t}\gamma$ cross section measurement. A
 1097 discussion on how systematics can be smoothed, symmetrised and pruned is presented in Section 8.1.
 1098 The modelling uncertainties of the signal and backgrounds are studied in Section 8.2. The experimental
 1099 uncertainties, which are common to both signal and backgrounds, are explained in Section 8.3. Table 21
 1100 details all the systematics considered for this analysis in the pre-pruning stage.

1101 8.1 Smoothing, symmetrisation and pruning

1102 *Smoothing* and *symmetrisation* are methods in which statistical fluctuations in various systematic sources
 1103 are avoided. Furthermore, the systematic is then centred around a mean value. The first step is symmet-
 1104 risation. *Two-sided* symmetrisation is performed when an up and a down variation is provided for any
 1105 given systematic. The difference between the two variations is calculated then divided by the mean of
 1106 the variations. This value is then taken as positive (for up) and negative (for down). This is described by
 1107 Equation 19.

$$\text{Variation up/down} = \left| \frac{\text{up} - \text{down}}{(\text{up} + \text{down})/2} \right| \quad (19)$$

1108 Thus, the $\pm 1\sigma$ variation is centred around the nominal value. *One-sided* symmetrisation is when only an
 1109 up or down variation is provided. An example is the PPT systematics. In this case the variation is simply
 1110 mirrored to reflect the supplementary variation.

1111 Smoothing algorithms average statistics across bins. This prevents large statistical spikes in many of the
 1112 systematics that are expected to give small contributions. In certain cases such as for signal, $t\bar{t}$ and $Z\gamma$
 1113 modelling, this option is turned off to allow for maximum shape variations.⁸ There are two smoothing
 1114 algorithms used.

- 1115 • The TRexFitter algorithm which is based on two parameters: the *tolerance* and the threshold for
 1116 number of slope variations in the systematic histogram. The first step is for the algorithm to ensure
 1117 that the statistical uncertainty for a group of bins is less than an 8% tolerance. If this isn't the case
 1118 the histogram is re-binned. The number of slope variations of the histogram is then checked. If
 1119 the number of variations in slope is less than or equal to the provided threshold of four bins this
 1120 new histogram is kept. If this isn't the case, then the statistical tolerance is halved, the histogram
 1121 re-binned, and the slope variation checked once again. This procedure is repeated until the slope
 1122 variations is four or less. This process only affects the shape of the systematic histogram with the
 1123 overall normalisation kept fixed to the original histogram.
- 1124 • The second algorithm is more conservative and makes use of ROOT's TH1::Smooth method. Based
 1125 on the integral of the histogram and neighbouring bin information it averages bin contents. This
 1126 method is used when the TRexFitter algorithm over smooths systematic uncertainties in which there
 1127 are many derivative sign changes as well as higher statistical uncertainties for certain processes. To
 1128 be consistent this smoothing is applied to all processes for the given systematic uncertainty. The

⁸ For the dilepton channels, the $t\bar{t}$ modelling is smoothed due to very small background contributions and large statistical fluctuations.

cases where this has been applied are for *Jet eta intercalibration, jet energy resolution, jet flavour response, jet pileup, pileup and MET objects* for all channels.

Pruning is the final step in which systematics that are too small to contribute to the final fit result are removed. This increases the speed of the fit and also grooms various plots and tables in order to make them more human-readable. Four pruning scenarios were tested for each of the five channels. Asimov fits were performed with pruning values set at 0.1%, 0.5%, 0.7% and 1.0%. In each case the error in μ is presented for the up and down variation. These results are summarised in Table 20. An overall trend of a lower uncertainty towards higher pruning values can be seen. However, the largest difference between any two values does not exceed 3%. Thus, a conservative value of 0.7% is chosen.

A non-negligible contribution from the JES Pileup (RhoTopology) nuisance parameter is shown as an example of smoothing (making use of the TH1:Smooth algorithm) and symmetrisation in Figure 60 and 61 for the various signal and background processes that get assigned this systematic in the single lepton and dilepton channels. For backgrounds except for the hadronic fake and $W\gamma$ processes the systematic has a shape as well as a acceptance uncertainty. For the hadronic fake background acceptance uncertainties have been calculated and applied separately. Thus, only a shape aspect is shown in these plots. The $W\gamma$ process is a floating parameter in the fit and so acceptances affects are also removed.

Table 20: Different pruning values for Asimov fits and the results for the error of μ for each channel. These tables do not include the hadronic fake normalisation and shape uncertainties (which are expected to be large) or the MC generator weights (which are expected to be very small).

Pruning value [%]	$e+jets$	$\mu+jets$	ee	$e\mu$	$\mu\mu$
0.1	+0.1139 -0.1037	+0.1141 -0.1051	+0.1215 -0.1126	+0.0730 -0.0690	+0.1119 -0.1030
0.5	+0.1125 -0.1022	+0.1129 -0.1039	+0.1200 -0.1114	+0.0716 -0.0678	+0.1102 -0.1016
0.7	+0.1113 -0.1009	+0.1118 -0.1027	+0.1200 -0.1115	+0.0712 -0.0674	+0.1100 -0.1015
1.0	+0.1108 -0.1005	+0.1123 -0.1030	+0.1201 -0.1115	+0.0711 -0.0674	+0.1100 -0.1015

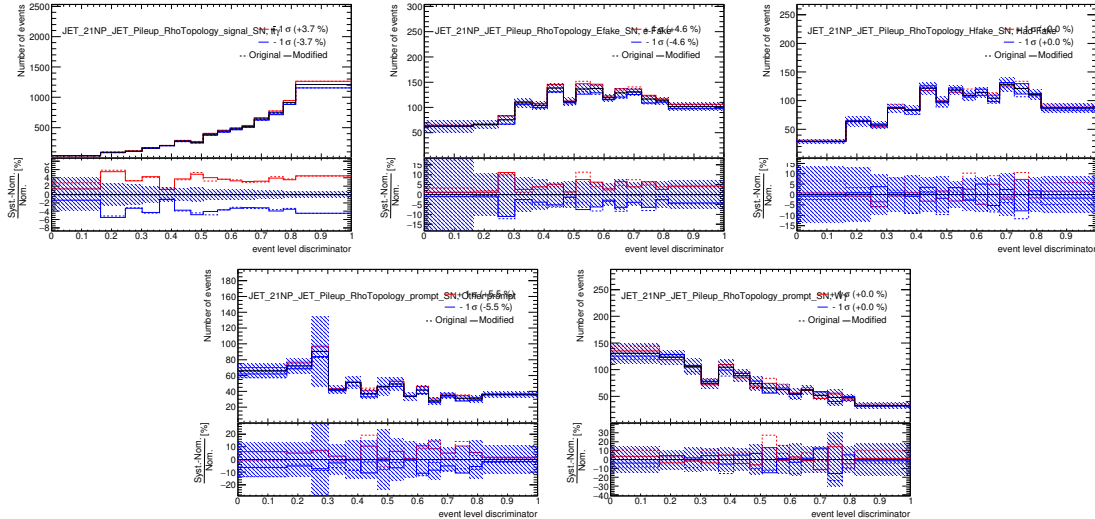


Figure 60: Systematic plots shown for the JES Pileup (RhoTopology) contribution for the single lepton channel. The dotted line represents the systematic before smoothing and symmetrisation has been applied. The solid line represents the after affect and the nuisance parameter that will enter the fit.

Not reviewed, for internal circulation only

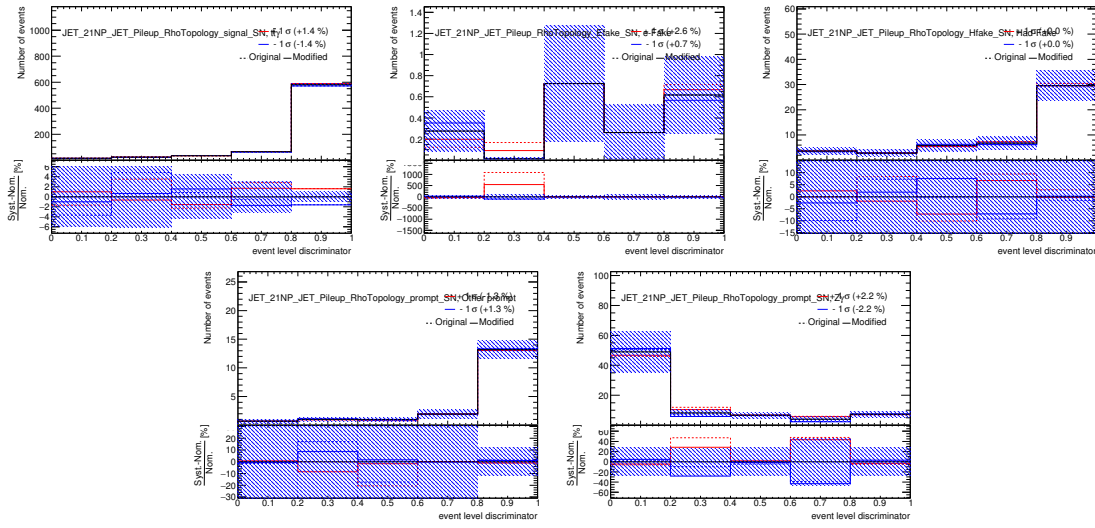


Figure 61: Systematic plots shown for the JES Pileup (RhoTopology) contribution for the dilepton channel. The dotted line represents the systematic before smoothing and symmetrisation has been applied. The solid line represents the after affect and the nuisance parameter that will enter the fit.

1145 8.2 Theoretical Uncertainties

1146 8.2.1 Signal Modeling

- 1147 Renormalisation and Factorisation scales: The effect of the choice of the renormalisation (μ_r)
1148 and factorisation (μ_f) scales (the QCD scale) is estimated by varying μ_r and μ_f simultaneously
1149 or independently up and down by a factor of 2 with respect to the nominal sample value, thus
1150 resulting in 3 sets of up-and-down variations. The variation is done in terms of event weights to
1151 reduce the effect of statistical fluctuations. Furthermore, this systematic is split into a shape and an
1152 acceptance contribution. The final uncertainty on the acceptance is the quadratic sum of the 3 sets
1153 of variations shown in Figure 62, while the shape is varied separately according to each of the three
1154 renormalisation scales. This is shown in Figure 63.
- 1155 Uncertainty due to the parton shower and hadronisation: The uncertainty is estimated by comparing
1156 the $t\bar{t}\gamma$ nominal samples produced using MADGRAPH + PYTHIA8, with HERWIG7 showering the
1157 same MADGRAPH events. The outcome of the shape affecting the nominal signal sample is shown
1158 in Figure 64.
- 1159 Initial and final state radiation uncertainty: The uncertainty is estimated by comparing the $t\bar{t}\gamma$
1160 samples produced using the same MADGRAPH events as for the nominal signal MADGRAPH +
1161 PYTHIA8 sample, but using PYTHIA8 tunes with high or low QCD radiation activity (A14 var3c
1162 eigentune). The affects of only shape are shown in Figure 65.
- 1163 PDF uncertainty: The PDF uncertainty is evaluated by the envelope error of the 100 PDF error sets
1164 in the NNPDF23LO, which are stored as weights in the nominal sample. The total pdf uncertainty
1165 is estimated by computing the standard deviation for each of the 100 pdf variation with respect to

1166

the central value according to the following Equation:

$$\Delta X = \sqrt{\frac{1}{N} \sum_i (X_i - X_0)^2}, \quad (20)$$

1167

where $N=100$, X_0 is the mean value, and X_i is the i -th PDF variation for $i = [1, \dots, 100]$.

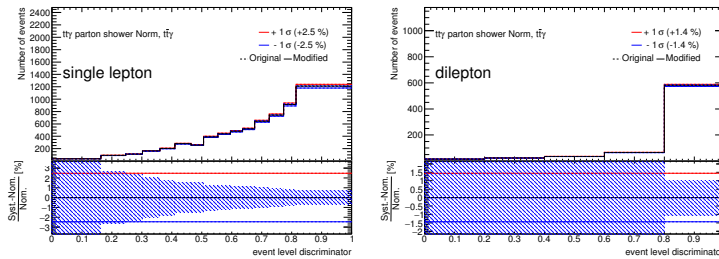


Figure 62: The quadratic sum of the three variations of the renormalisation and factorisation scales applied to the single lepton and dilepton ELD. Only acceptance is shown.

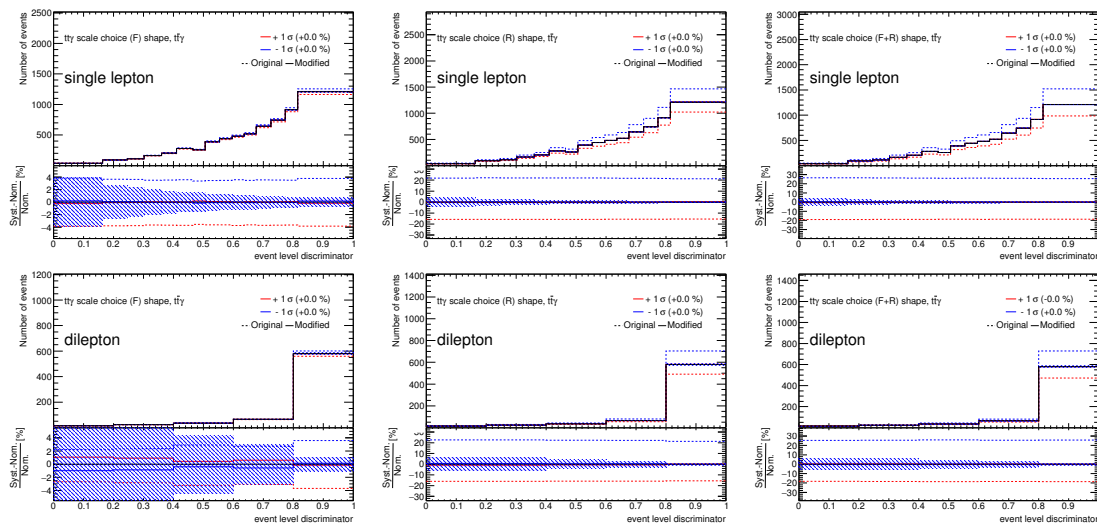


Figure 63: The three separate variations for the renormalisation and factorisation scales applied to the single lepton and dilepton ELD. Only the shape is shown, which in most cases is negligible. The dotted line represents the systematic before symmetrisation and removal of overall acceptance has been applied. The solid line represents the after effect and the nuisance parameter that will enter the fit.

1168

8.2.2 Background Modelling

1169

In addition to those uncertainties detailed in Section 6.1 and Section 6.2 for the $e \rightarrow \gamma$ fake and hadronic fake backgrounds, the $t\bar{t}$ MC modelling systematics which affect the shape for these two backgrounds are included and applied to the respective background events. These are:

1172

- The uncertainty on hard scattering generator and parton shower and hadronisation: This is estimated by comparing the $t\bar{t}$ nominal sample produced by PowHEGBox+PYTHIA8 with the $t\bar{t}$ sample produced

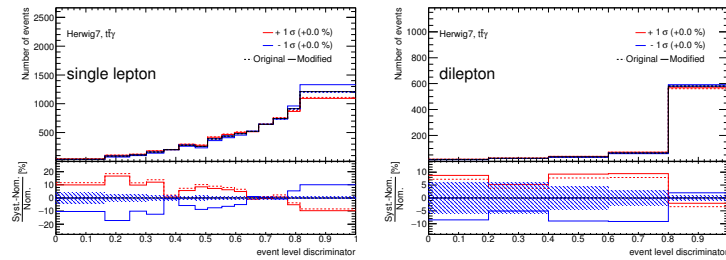


Figure 64: The shape impact on the nominal signal sample compared to HERWIG7 for the single lepton and dilepton samples. The dotted line represents the systematic before symmetrisation and removal of overall acceptance has been applied. The solid line represents the after effect and the nuisance parameter that will enter the fit.

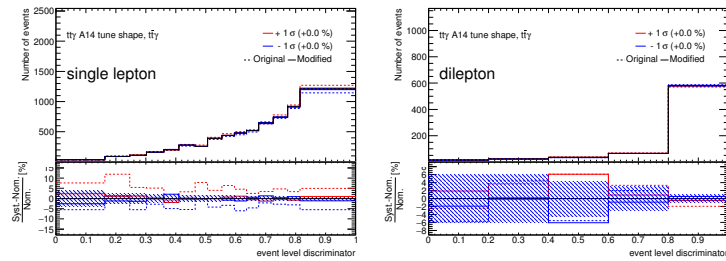


Figure 65: The shape impact for the difference in QCD radiation tunes on the nominal signal sample for the single lepton and dilepton samples. The dotted line represents the systematic before symmetrisation and removal of overall acceptance has been applied. The solid line represents the after effect and the nuisance parameter that will enter the fit.

1174 by SHERPA. The outcome of the shape effect on $e \rightarrow \gamma$ fake and hadronic fake backgrounds for the
 1175 single lepton channel are shown in Figure 66(a). The dilepton contribution is negligible.

- 1176 • The uncertainty on initial and final state radiation: This is estimated by comparing the nominal
 1177 $t\bar{t}$ sample, with two samples produced with different PYTHIA8 tunes with higher or lower QCD
 1178 radiation activity (A14 var3c eigentune), modified factorisation and renormalisation scales (at $\times 0.5$
 1179 and $\times 2$) and modified NLO radiation with $hdamp = 1.5$ and 3 times the mass of the top quark. The
 1180 outcome of the shape effect on $e \rightarrow \gamma$ fake and hadronic fake backgrounds for single lepton are
 1181 shown in Figure 66(b). The dilepton contribution is negligible.

1182 The $W\gamma$ background is floated in the single lepton fit while the $Z\gamma$ background is modelled with
 1183 MG5_AMC@NLO and showered with PYTHIA8.

1184 Other backgrounds with a prompt γ are very small, thus assigned a conservative systematic of 50%.

1185 The estimation on the Lep fake background systematics can be seen in Section 6.3.

1186 8.3 Experimental Uncertainties

1187 Experimental uncertainties common to signal and background processes are discussed in this section.
 1188 These are mainly the uncertainties of the reconstructed physical objects used in the analysis, such as the
 1189 lepton, photon, jet, and E_T^{miss} in terms of their reconstruction and identification efficiencies, momentum
 1190 and energy scales as well as momentum and energy resolutions. In addition, the uncertainties of the jet

Not reviewed, for internal circulation only

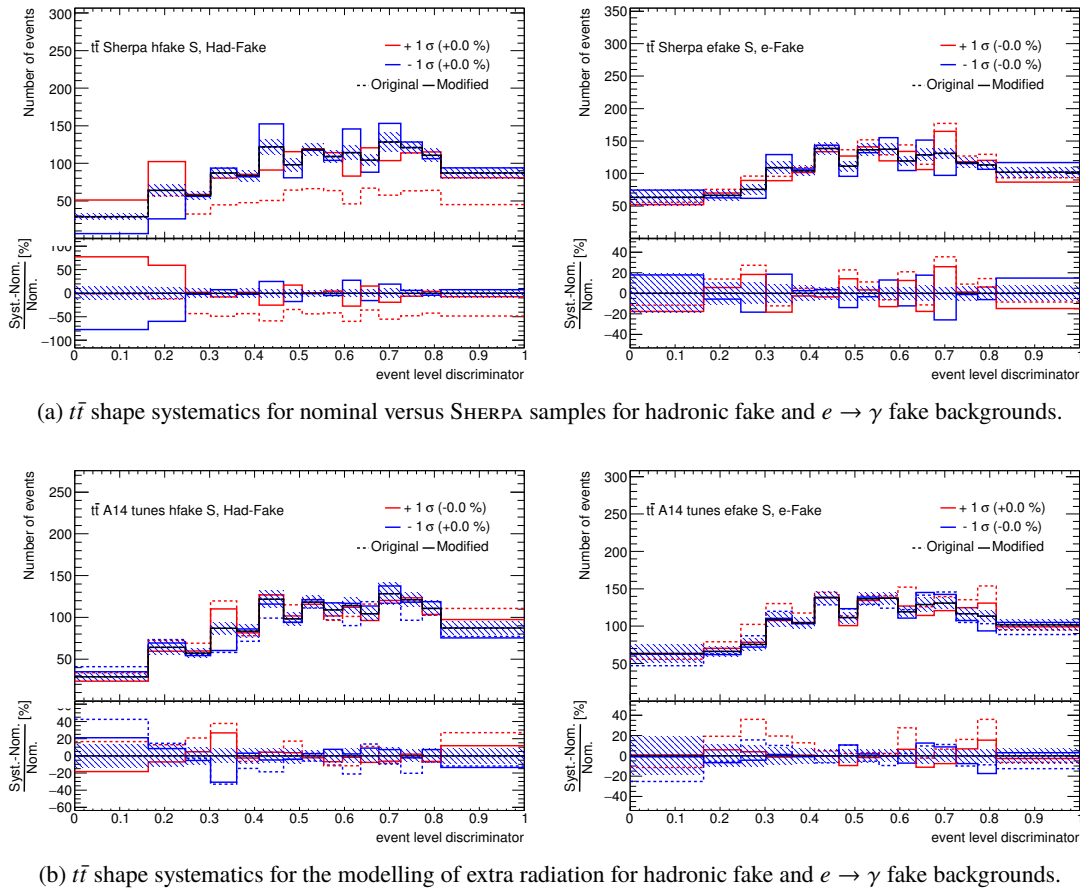


Figure 66: $t\bar{t}$ MC modelling systematics for the single lepton channel. Since the $t\bar{t}$ samples are embedded in the hadronic fake and $e \rightarrow \gamma$ fake background groups, a systematic needs to be defined for each, which are then correlated in the fit.

flavour tagging, the jet vertex fraction cut and the integrated luminosity as well as the pile-up simulation are also described in this section. In the following, the sources of experimental uncertainties are introduced.

8.3.1 Sources of experimental uncertainties

Leptons

- Lepton Efficiency** - The lepton efficiency refers to the reconstruction and identification efficiencies, isolation efficiency as well as the trigger efficiency. For Monte Carlo (MC) samples, these efficiencies are corrected by applying scale factors, which are calculated as the ratio between the efficiencies measured in data and those in simulation using tag-and-probe method on $Z \rightarrow ee$ and $J/\Psi \rightarrow ee$ ($Z \rightarrow \mu\mu$) decays for electrons (muons). These scale factors, which are E_T and η dependent, are varied up and down by one standard deviation to study the impact of lepton efficiency uncertainties on the analysis result [28][31].
- Lepton energy (momentum) scale and resolution** - The measured lepton energy (momentum) is calibrated using MC-based techniques. Correction factors, which are derived from the study

of dileptonic decays of the Z-boson are applied to correct possible detector mis-modelings in the calibration. These correction factors, are varied up and down by one standard deviation to study the lepton energy (momentum) scale uncertainty. For electrons, the energy scale and resolution are calculated together with photons as EGamma scale and resolution.

Photons

- Photon efficiency** - The photon identification efficiency is measured with samples of photons from the radiative decays of the Z-boson and electrons and positrons from Z decays exploiting the similarity between electron and photon electromagnetic (EM) showers. Scale factors are defined as the ratio between efficiencies measured in data and those in MC samples and are applied to MC samples to correct possible detector mismodelings. The scale factors for photon isolation have been measured [32]. These scale factors are varied up and down by one standard deviation to study their impacts on the analysis.
- Photon energy scale and resolution** - The photon energy calibration and the study of its scale and resolution uncertainties are calculated together with the electrons as EGamma scale and resolution.
- Prompt Photon Tagger (PPT)** - The strategy of deriving systematic uncertainties of the PPT is described in Section 4.2.2. The four types of systematics as applied to the ELD are shown in Figure 67.

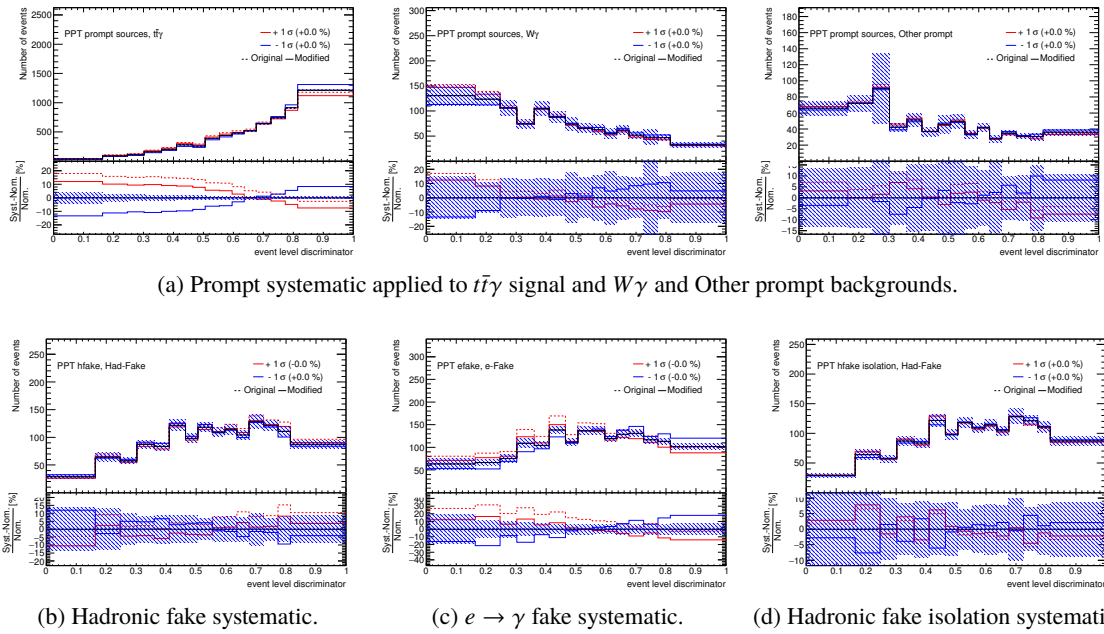


Figure 67: PPT shape systematics for the single lepton channel.

Jets

- Jet Energy Scale** - The jet energy calibration, or jet energy scale (JES) used in this analysis follows the globally reduced parameter configurations of 21NPs [48, 49]. The calibration is done in several steps, combining Monte Carlo simulation and *in situ* measurements, to correct for topo-cluster energy, pile-up effect, etc. Its uncertainty is split into several independent categories: modelling

1226 and statistical uncertainties on the extrapolation of the jet calibration from the central region, high-
 1227 p_T jet behaviour, b -jet energy scale uncertainties, uncertainties due to pile-up, uncertainties on *in*
 1228 *situ* jet energy corrections, etc. In one category, there are usually more than one physical source of
 1229 the uncertainty. To study the JES uncertainty, each source is varied up and down independently by
 1230 its corresponding uncertainty.

- 1231 • **Jet Energy Resolution** - The jet energy resolution (JER) is measured using the balance between
 1232 jets and well measured objects like photons or Z bosons, and it is found to be in agreement between
 1233 data and MC. There is a single source of uncertainty for the JER, which is varied by one sigma to
 1234 study its impacts on the analysis.
- 1235 • **Jet Vertex Tagging** - The systematic uncertainty associated to the jet vertex tagging(JVT) is obtained
 1236 by varying up and down the JVT cut using the *JetVertexTaggerTool*[36]

1237 ***b*-tagging**

1238 Jets coming from a b -quark is called a b -jet. It has its own topological feature, e.g. long lived b -hadrons,
 1239 and can be distinguished from the other lighter flavour jets, with a procedure called b -tagging. The
 1240 b -tagging in this analysis is performed with the MV2c10 algorithm for few different working points. Each
 1241 jet can be assigned to a different working point (a procedure called "pseudo-continuous b -tagging"), and
 1242 the b -tagging uncertainties on this jet are derived for this specific working point. Those uncertainties are
 1243 accounted for by varying the calibration scale factors provided by Flavour Tagging group for b -, c -, and
 1244 light-flavour jets up and down by their corresponding systematic uncertainties independently. For each
 1245 jet category, the uncertainties are decomposed into several uncorrelated components using eigenvector
 1246 method, for example, there are 30, 15 and 80 eigenvectors for b -, c -, and light-flavour jets uncertainties,
 1247 respectively [50].

1248 **Missing Transverse Energy**

1249 The E_T^{miss} is reconstructed[38] from the vector sum of several terms corresponding to different types of
 1250 reconstructed objects. The estimated uncertainties for electrons, muons, photons and jets are propagated
 1251 into the uncertainty of E_T^{miss} . Thus, the only new contribution is the systematic uncertainty of the soft
 1252 terms $E_{x,y}^{\text{RefSoftJet}}$ and $E_{x,y}^{\text{CellOut}}$.

- 1253 • **Soft term scale and resolution** - The systematic uncertainty of the soft-term scale is estimated
 1254 by comparing the ratio of MC simulation to data. The average deviation of the ratio from unity
 1255 is taken as a flat uncertainty on the absolute scale. The systematic uncertainty of the soft-term
 1256 resolution is estimated by evaluating the level of agreement between data and MC in the E_x^{miss} and
 1257 E_y^{miss} resolution. Both the scale and resolution of the soft term are varied up and down by one
 1258 standard deviation to study their impact on the analysis.

1259 **Pile Up**

1260 The systematics due to pile-up has been studied by variation of the μ rescaling from the nominal value of
 1261 1.09 to 1.0(up) or 1.18(down) [51].

1262 **Luminosity**

1263 The total integrated luminosity has an uncertainty of 2.1%. It is derived, following a methodology
 1264 similar to that detailed in [43], from a calibration of the luminosity scale using x-y beam-separation scans
 1265 performed in August 2015 and May 2016.

Table 21: Complete list of systematics considered before pruning is applied. A “N” indicates that only normalisation (or acceptance) has been considered as a systematic. A “S” indicates that only the shape is considered as a systematic. “SN” indicates that both shape and normalisation have been considered as a systematic.

Systematic name	Type	# of components
Miscellaneous		
Luminosity	N	1
Pileup reweighting	SN	1
Background modelling		
$W\gamma$ (single lepton)	free floating	1
$W\gamma$ (dilepton)	N	1
$Z\gamma$ (single lepton)	N	1
$Z\gamma$ (dilepton)	SN	1
VV	N	1
ST	N	1
Lep fake	SN	1
$e \rightarrow \gamma$ fake	SN	11
hadronic fake d.d.	SN	5
$t\bar{t}$ Sherpa	S	1
$t\bar{t}$ A14 Tunes	S	1
Prompt Photon Tagger		
Prompt photons	S	1
$e \rightarrow \gamma$ fake	S	1
hadronic fake	S	1
hadronic fake isolation	S	1
Object reconstruction		
Electrons (trigger, reco, ID, isolation)	SN	5
Egamma (resolution, scale)	SN	2
Muons (trigger, reco, ID, isolation)	SN	15
MET (resolution, scale)	SN	3
Photons (efficiency, isolation)	SN	3
Jet energy scale	SN	21
Jet energy resolution	SN	1
Jet vertex tagger	SN	1
b-tagging efficiency	SN	30
c-tagging efficiency	SN	15
Light-jet tagging efficiency	SN	80
b-tagging extrapolation	SN	1
Signal modelling		
$t\bar{t}\gamma$ A14 Tunes	S	1
HERWIG7	S	1
Renormalisation and factorisation scales	S	3
Specific to fiducial measurement		
Renormalisation and factorisation scales	N	1
PDF's	N	1
ISR/FSR	N	1
Parton shower	N	1

1266 8.4 Propagation of the systematic uncertainties to the unfolding framework

1267 The same systematic uncertainties described above are propagated to the unfolding results. The systematic
 1268 shifts are applied either directly to the physics objects themselves, or as weights in events. The input to be

1269 unfolded is shifted with the corresponding systematic variation, and the unfolding is performed for each
1270 shifted input using the nominal migration matrix.

1271 The uncertainty is estimated as the relative difference between the nominal unfolded result and the
1272 shifted ones. The final uncertainty is the quadrature sum of all variations. The size of each shifted $t\bar{t}\gamma$
1273 reconstructed distribution compared to the nominal one is shown in Appendix H. It can be seen that the
1274 number of events in the shifted samples is largely the same as the nominal sample, and therefore the
1275 majority of differences are expected to be significant.

Not reviewed, for internal circulation only

1276 9 Cross section definitions

1277 This section defines the fiducial region, in which the inclusive and differential cross sections will be
 1278 measured. The various factors (for correcting signal efficiency, migration, and etc.) needed for the
 1279 extraction of the cross sections from observation are also explained.

1280 **9.1 Fiducial region**

1281 The fiducial region is defined to mimic the signal region at reconstruction level, described in Section 5, in
 1282 terms of both object selection and event selection. Thus, there are five fiducial regions corresponding to
 1283 the five channels.

1284 **9.1.1 Particle definition for fiducial region**

1285 • **Leptons:**

1286 Electrons and muons are selected dressed with close by photons (photons which are not originating
 1287 from hadrons, in a $\Delta R < 0.1$ cone around the lepton). Leptons are required to have $p_T > 25$ GeV
 1288 and $|\eta| < 2.5$, and not being originated from hadron decays.

1289 • **Jets:**

1290 Jets are clustered with the anti- k_t algorithm with a radius of $R = 0.4$. Non-interacting particles and
 1291 muons are not considered in the clustering. Jets are required to have $p_T > 25$ GeV and $|\eta| < 2.5$.

1292 • **b-jets:**

1293 The flavour of the jet is determined by ghost matching [52].

1294 • **Photons:**

1295 Photons are required to not originate from a hadron decay. Photons are required to have $E_T > 25$ GeV
 1296 and $|\eta| < 2.37$.

1297 • **Overlap Removal:**

1298 The overlap removal is done between the following object, in the following order:

1299 (i) Muon-jet: The jets with $\Delta R(\mu, j) \leq 0.4$ are removed.

1300 (ii) Electron-jet: The jets with $\Delta R(e, j) \leq 0.4$ are removed.

1301 (iii) Photon-jet: The jets with $\Delta R(j, \gamma) \leq 0.4$ to an isolated photon are removed. Isolation computed
 1302 from charged stable particles in a $R = 0.3$ cone. Photon is considered as isolated if $p_T^{\text{cone}30}/p_T < 0.1$.

1303 **9.1.2 Event selection for fiducial region**

1304 • **Leptons:**

1305 Exactly one good electron (muon) is required in the $e+\text{jets}$ ($\mu+\text{jets}$) channel. Exactly two good
 1306 electrons (muons) are required in the ee ($\mu\mu$) channel. Exactly one good electron and one good
 1307 muon are required in the $e\mu$ channel.

1308 • **Jets:**

1309 At least four (two) good jets in the single lepton (dilepton) channel are required, among which at
 1310 least one should be a b -jet.

1311 • **Photon:**

1312 Exactly one good photon is required. The event is dropped if the photon has a $\Delta R(j, \gamma) < 0.4$ with
 1313 any good jet, or a $\Delta R(l, \gamma) < 1.0$ with any good lepton.

1314 **9.1.3 Acceptance and correction factor**

1315 The signal acceptance is defined as the fraction of events falling into the fiducial region, out of the total
 1316 generated events:

$$A_i = \frac{N_{\text{gen}}^{\text{fid},i}}{N_{\text{gen}}^{\text{all}}}, \quad (21)$$

1317 where $N_{\text{gen}}^{\text{all}}$ is the total number of generated events and $N_{\text{gen},i}^{\text{fid}}$ is the number of events generated inside the
 1318 fiducial region i , with i running over the five channels.

1319 The correction factor is used to unfold the number of signal events selected at reconstruction level $N_{\text{reco},i}$
 1320 in channel i to the number of signal events generated in the fiducial region $N_{\text{gen}}^{\text{fid},i}$ corresponding to channel
 1321 i :

$$N_{\text{gen}}^{\text{fid},i} = \frac{N_{\text{reco},i}}{C_i}. \quad (22)$$

1322 To do the unfolding, first the non-fiducial signal events in $N_{\text{reco},i}$ should be removed:

$$N_{\text{reco},i}^{\text{fid},i} = N_{\text{reco},i} \times (1 - f_{\text{mig},i}), \quad (23)$$

1323 where $N_{\text{reco},i}^{\text{fid},i}$ is the number of events generated in fiducial region i and selected at reconstruction level
 1324 in channel i , and $f_{\text{mig},i}$ is the fraction of events selected at reconstruction level in channel i that are not
 1325 generated from the fiducial region i :

$$f_{\text{mig},i} = \frac{N_{\text{reco},i}^{\text{non-fid},i}}{N_{\text{reco},i}}. \quad (24)$$

1326 e.g. events generated with true photon $p_T < 20$ GeV can be reconstructed as a photon with $p_T > 20$ GeV
 1327 due to resolution effects of the detector, or events generated from other fiducial regions can be reconstructed
 1328 into this fiducial region.

1329 Not all of the generated events in the fiducial region will be reconstructed and selected, because of the
 1330 event reconstruction and selection efficiencies. Thus, to get the true generated events in the fiducial region,
 1331 an additional efficiency correction should be applied:

$$N_{\text{gen}}^{\text{fid},i} = \frac{N_{\text{reco},i}^{\text{fid},i}}{\epsilon_i}, \quad (25)$$

1332 where ϵ_i is the efficiency of events generated in fiducial region i being selected at reconstruction level in
 1333 channel i :

$$\epsilon_i = \frac{N_{\text{reco},i}^{\text{fid},i}}{N_{\text{gen}}^{\text{fid},i}}. \quad (26)$$

1334 Combining the Equation 23 and Equation 25, the correction factor can be expressed as:

$$C_i = \frac{N_{\text{reco},i}}{N_{\text{gen}}^{\text{fid},i}} = \frac{\epsilon_i}{1 - f_{\text{mig},i}}. \quad (27)$$

1335 The first equation shows the exact way of calculation of C_i while the second one shows the physical
 1336 meaning of this factor.

1337 The values of the acceptances and correction factors are summarized in Table 22. The numbers are shown
 1338 not only for the five channels but also for the merged single lepton and dilepton channels. Also, the signal
 1339 modelling systematics as described in Section 8.2 are shown.

Table 22: Acceptances and correction factors for the five channels as well as the two merged channels. The nominal values are shown in %. The systematics are shown as relative uncertainties in %. The uncertainties after “ \pm ” signs are statistical uncertainties.

Channel	$e+\text{jets}$	$\mu+\text{jets}$	ee	$e\mu$	$\mu\mu$	single lepton	dilepton
Acceptance (%)	4.09 ± 0.00	4.10 ± 0.00	0.24 ± 0.00	0.47 ± 0.00	0.24 ± 0.00	8.20 ± 0.00	0.96 ± 0.00
Scale sys (%)	0.72	0.72	0.71	0.70	0.73	0.72	0.71
PDF sys (%)	0.48	0.48	0.55	0.60	0.58	0.48	0.58
ISR/FSR Up (%)	4.51 ± 0.03	4.90 ± 0.03	-0.79 ± 0.42	2.41 ± 0.22	2.12 ± 1.00	4.71 ± 0.02	1.53 ± 0.29
ISR/FSR Dn (%)	-4.42 ± 0.02	-4.35 ± 0.02	-0.79 ± 0.42	0.82 ± 0.21	-1.84 ± 0.97	-4.38 ± 0.02	-0.25 ± 0.29
PS sys (%)	-1.10 ± 0.03	-0.99 ± 0.03	-0.60 ± 0.45	0.38 ± 0.23	-0.84 ± 1.03	-1.04 ± 0.02	-0.17 ± 0.31
Correction (%)	35.97 ± 0.15	35.96 ± 0.15	23.71 ± 0.50	35.49 ± 0.46	28.69 ± 0.53	35.96 ± 0.11	30.81 ± 0.29
Scale sys (%)	0.23	0.08	0.48	0.23	0.28	0.15	0.27
PDF sys (%)	0.09	0.06	0.23	0.10	0.15	0.07	0.12
ISR/FSR Up (%)	-0.25 ± 0.60	0.30 ± 0.59	-6.04 ± 2.85	-2.78 ± 1.73	0.88 ± 2.68	0.02 ± 0.42	-2.35 ± 1.30
ISR/FSR Dn (%)	0.27 ± 0.61	0.79 ± 0.61	-4.54 ± 2.87	-1.30 ± 1.77	4.24 ± 2.81	0.53 ± 0.43	-0.51 ± 1.33
PS sys (%)	2.48 ± 0.62	2.46 ± 0.61	-3.76 ± 2.94	-0.59 ± 1.79	-1.95 ± 2.69	2.47 ± 0.44	-1.44 ± 1.33

1340 9.2 Fiducial cross section

1341 After subtracting background events $N_{\text{bkgs},i}$ from data $N_{\text{data},i}$ and applying the correction factor C_i , the
 1342 true number of generated signal events in the fiducial region i can be derived. Dividing this number by the
 1343 integrated luminosity, the fiducial cross section can be measured. These are summarized in the following
 1344 expression:

$$\sigma_i^{\text{fid}} = \frac{N_{\text{data},i} - N_{\text{bkgs},i}}{L \times C_i}. \quad (28)$$

1345 On the other hand, if the total cross section is known from theory prediction, the predicted fiducial cross
 1346 section can be calculated from:

$$\sigma_i^{\text{fid}} = \sigma^{\text{tot}} \times A_i. \quad (29)$$

1347 This will be described in detail in Section 12.

1348 9.3 Total cross section

1349 The measured number of signal events can be directly unfolded to the total phase space in order to measure
 1350 the total cross section:

$$\sigma_{\text{tot}} = \frac{N_{\text{data},i} - N_{\text{bkgs},i}}{L \times C_i \times A_i}. \quad (30)$$

1351 Acceptance factor A_i is sensitive to physics modelling since it extrapolates the measurement from the
 1352 fiducial phase space to a much larger phase space, where no measurement is performed.

1353 Besides, this should be noted that since there are always some minimum cuts applied at generation level,
1354 either to remove divergence or to increase generation efficiency, the total cross section is not the integral
1355 over all the phase space, but just over a much larger phase space than the fiducial one.

1356 The predicted total cross section will be described in Section 12.

1357 9.4 Differential cross section

1358 In the fiducial region, the cross section can be measured as a function of an observable, e.g. photon p_T or
1359 η , which means a differential cross section measurement.

1360 For this goal, first the signal spectrum of this observable $N_{\text{reco},j}$ is measured from data spectrum subtracting
1361 background spectrum:

$$N_{\text{reco},j} = N_{\text{data},j} - N_{\text{bkgs},j}, \quad (31)$$

1362 where j is the binning index of the observable at reconstruction level and the channel index i is left out
1363 for simplicity.

1364 Then, the differential cross section σ_k^{diff} can be related to the signal spectrum by:

$$N_{\text{reco},j} = \frac{1}{1 - f_{\text{mig},j}} \times \sum_k (L \times \sigma_k^{\text{diff}} \times \epsilon_k \times M_{kj}), \quad (32)$$

1365 where k is the binning index of the observable at truth level (i.e. particle level), which is not necessarily
1366 binned in the same way as at reconstruction level, and

- 1367 • $f_{\text{mig},j}$ is the fraction of signal events migrated from outside the fiducial region into the bin j of the
1368 reconstructed distribution,
- 1369 • ϵ_k is the efficiency of signal events generated in bin k of the truth distribution to be reconstructed
1370 and selected,
- 1371 • M_{kj} is the bin-by-bin migration matrix, representing the probability of signal events generated in
1372 bin k of the truth distribution and observed in bin j of the reconstructed distribution.

1373 To be noted, the migration matrix M_{kj} is calculated by using the signal events generated in the fiducial
1374 region and passing the reconstruction level event selection, and there are two types of migration here.

1375 Solving the above equation, the differential cross section can be expressed as:

$$\sigma_k^{\text{diff}} = \frac{1}{L} \times \frac{1}{\epsilon_k} \times \sum_j M_{jk}^{-1} \times (N_{\text{data},j} - N_{\text{bkgs},j}) \times (1 - f_{\text{mig},j}), \quad (33)$$

1376 where M_{jk}^{-1} is the inversion of the bin-by-bin migration matrix.

1377 On the other hand, the differential acceptance is defined as:

$$A_k = \frac{N_{\text{gen}}^{\text{diff},k}}{N_{\text{gen}}^{\text{all}}}, \quad (34)$$

1378 from which, with the knowledge of the total cross section, the theory prediction for the differential cross
 1379 section can be derived:

$$\sigma_k^{\text{diff}} = \sigma^{\text{tot}} \times A_k . \quad (35)$$

1380 The exact prediction is documented in Section 12.

1381 Only two channels are defined for the differential cross section measurement, which are the single lepton
 1382 and dilepton channel. This is due to the similarity of each single lepton (dilepton) channels and for the
 1383 aim of increasing data statistics in the low populated region of the distributions.

1384 The binning of the distributions to be unfolded are optimized taking into account of the detector's resolution
 1385 effect as well as the expected data fluctuation. More specifically: 1) the bin width is chosen to be wider
 1386 than twice of the variable's resolution, so that more than 68% of the events will be in the same bin of the
 1387 truth and reconstructed distributions, 2) the bin width can not get narrower than a size that has more than
 1388 10% (15%) statistical uncertainty of the bin for the single lepton (dilepton) channel. A re-binning can be
 1389 performed for the final unfolded results, in the case of the statistical uncertainties getting larger. Another
 1390 choice of binning is shown in Appendix I.

1391 Figure 68 shows the efficiency and outside migration fraction in the dilepton channel, for the observables
 1392 photon p_T , photon η , ΔR_{\min} (lepton, γ), $\Delta\eta$ (lepton, lepton) and $\Delta\phi$ (lepton, lepton), while Figure 69 shows
 1393 them for the single lepton channel, for the observables photon p_T , photon η and ΔR (lepton, γ). Figures 70
 1394 and 71 show the corresponding bin-by-bin migration matrices, normalized to the number of events in each
 1395 row, in the dilepton and single lepton channels, respectively.

Not reviewed, for internal circulation only

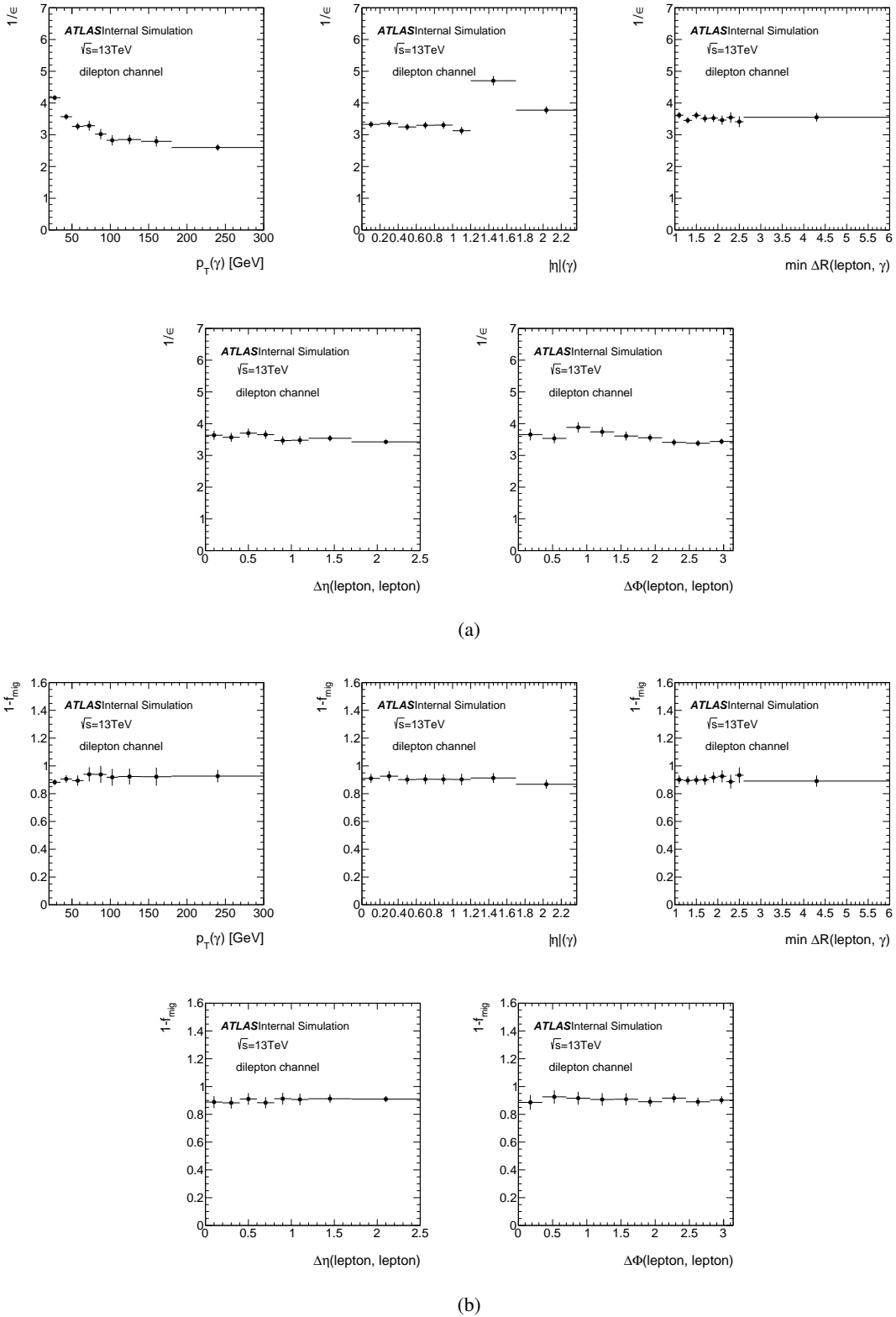


Figure 68: The inverse of signal efficiency $1/\epsilon$ (a) and fraction of non-outside migration ($1 - f_{\text{mig}}$) (b) for five different observables in the dilepton channel.

Not reviewed, for internal circulation only

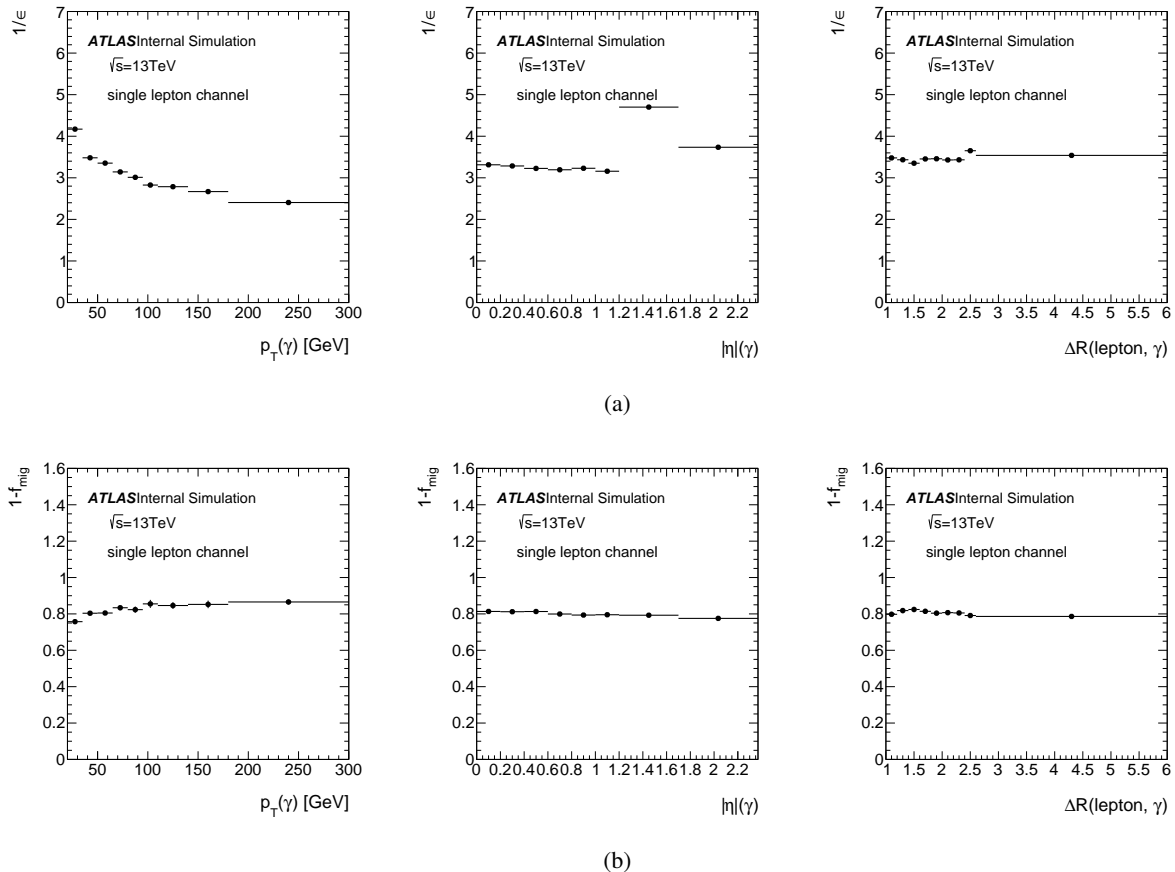


Figure 69: The inverse of signal efficiency $1/\epsilon$ (a) and fraction of non-outside migration ($1 - f_{\text{mig}}$) (b) for three different observables in the single lepton channel.

Not reviewed, for internal circulation only

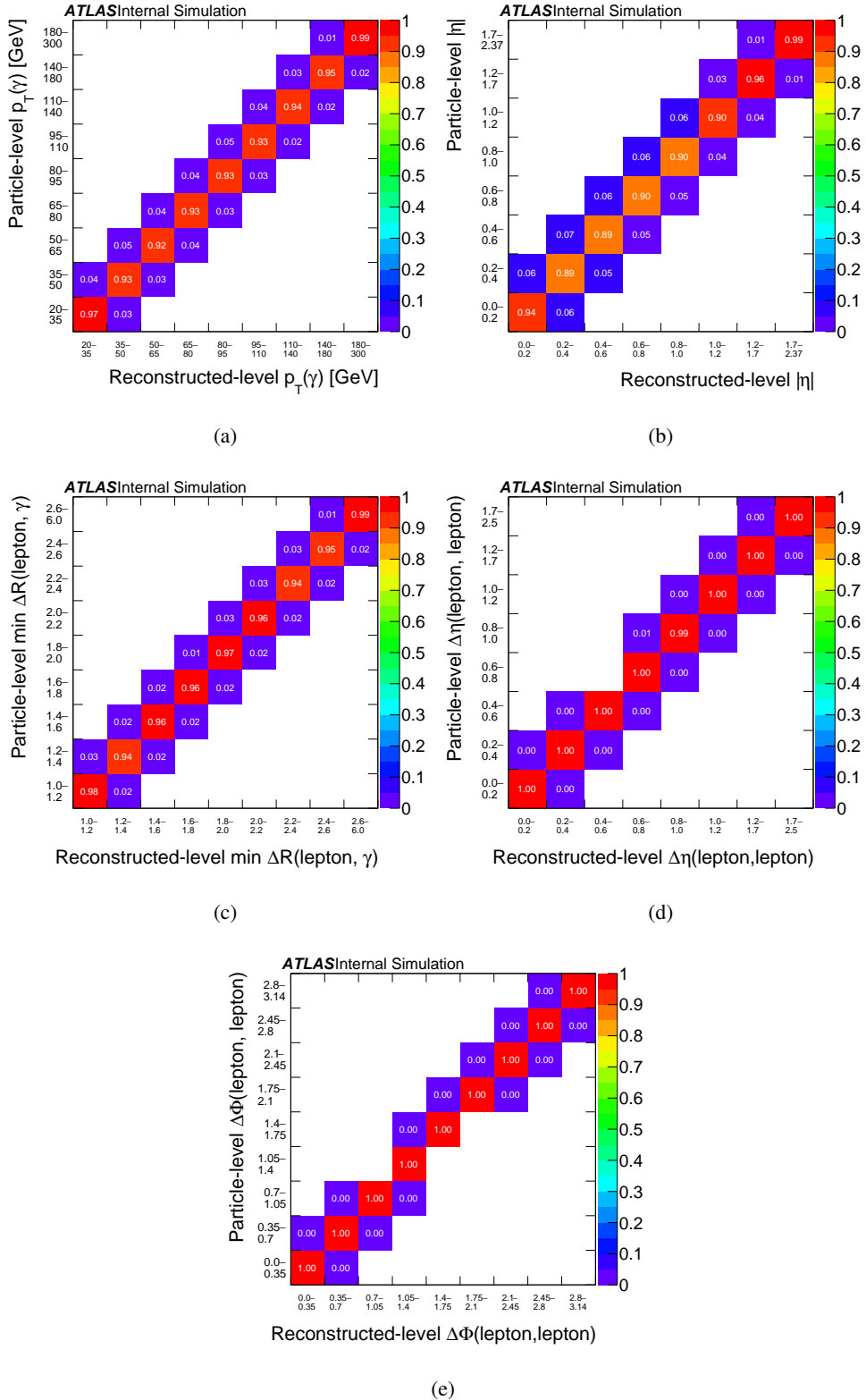


Figure 70: The bin-by-bin migration matrix of the photon p_T (a), the photon $|\eta|$ (b), $\Delta R_{\min}(\text{lepton}, \gamma)$ (c), $\Delta\eta(\text{lepton}, \text{lepton})$ (d) and $\Delta\phi(\text{lepton}, \text{lepton})$ (e), in the dilepton channel.

Not reviewed, for internal circulation only

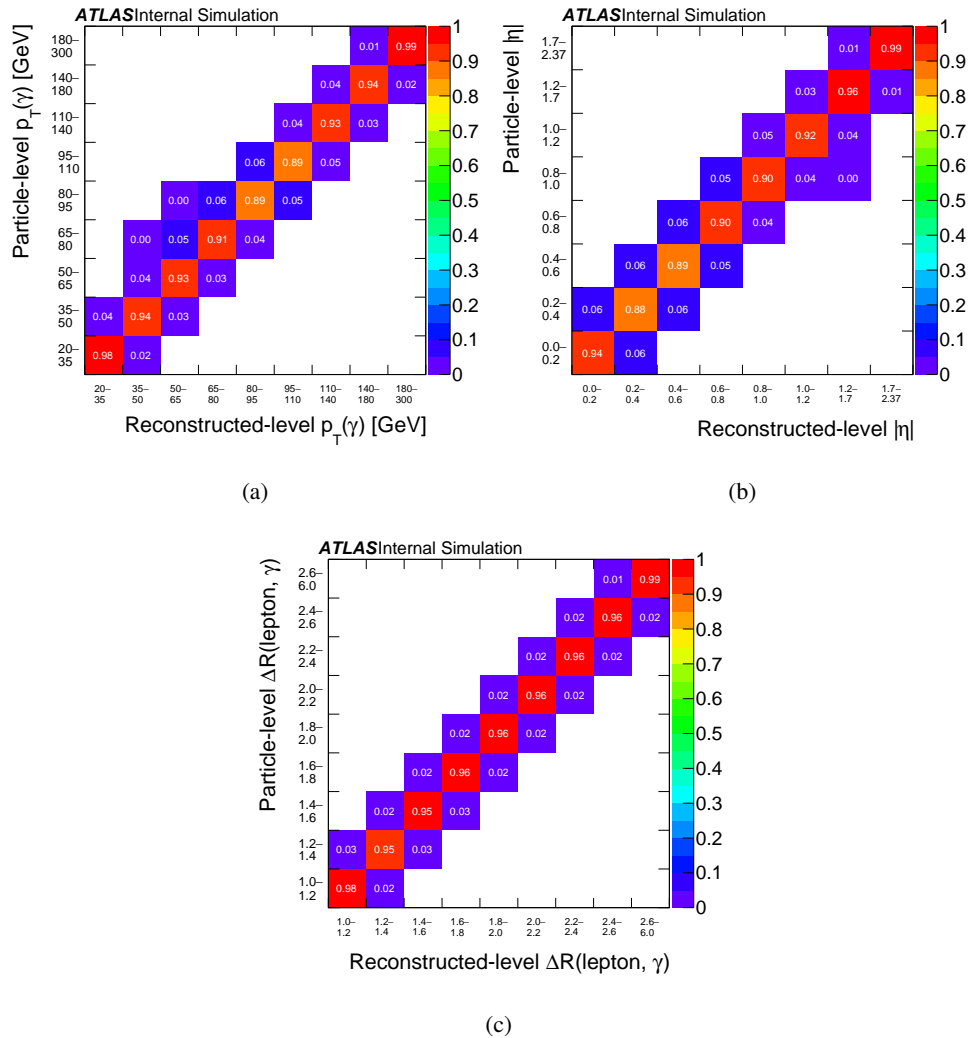


Figure 71: The bin-by-bin migration matrix of the photon p_T (a), the photon $|\eta|$ (b), and $\Delta R(\text{lepton}, \gamma)$ (c), in the single lepton channel.

1396 10 Fit strategy

1397 The events selected in the signal region, as described in Section 5, subtracting the estimated background
 1398 events as detailed in Section 6, are the observed signal events, which can be used to:

- 1399 • be compared with the MC predicted signal events and use their ratio, denoted as μ and called signal
 1400 strength, to quantify the agreement between observation and SM at the reconstruction level.
- 1401 • extract the fiducial cross section, after correcting for the signal efficiency loss and migration from
 1402 outside fiducial region using MC. Furthermore, with the MC predicted signal acceptance, the fiducial
 1403 phase space can be extrapolated to the total phase space, thus a total cross section measurement is
 1404 possible.
- 1405 • with the background subtraction done differentially, perform differential cross section measurement.

1406 In the following, the strategies for the above measurements are described in details.

1407 10.1 Likelihood function

1408 Before introducing the detailed strategies, the general likelihood function, which is the base for all sort of
 1409 physical interpretation, should be introduced. The most general form of the likelihood is as follows:

$$\mathcal{L} = \mathcal{L}(p.o.i, \theta | \text{ELD}), \quad (36)$$

1410 where ELD is the observed event level discriminator to be fitted as introduced in Section 5.2, $p.o.i$ is the
 1411 parameter(s) of interest which could be the signal strength, fiducial cross section, total cross section, or
 1412 differential cross section, and θ is the modeling of the systematic uncertainties described in section 8.

1413 In practise, a binned maximum likelihood fit is performed and in each bin, the observed number of data
 1414 follows a Poisson distribution. Thus, the likelihood can also be expressed as:

$$\mathcal{L} = \prod_j \prod_i P(N_{i,j} | N_{i,j}^s + \sum_b N_{i,j}^b) \times \prod_t G(\vartheta | \theta_t, 1), \quad (37)$$

1415 where

- 1416 • $P(N_{i,j} | N_{i,j}^s + \sum_b N_{i,j}^b)$ is the Poisson function,
- 1417 • $N_{i,j}$, $N_{i,j}^s$ and $N_{i,j}^b$ are the observed number of data, signal events and background events in bin i of
 1418 the ELD of channel j , respectively,
- 1419 • j could run over $e+jets$, $\mu+jets$, ee , $e\mu$, and $\mu\mu$ channels,
- 1420 • $G(\vartheta | \theta_t, 1)$ is a Gaussian function modeling the systematic uncertainty $\theta_t \in \theta$, with a mean of 0 and
 1421 a standard deviation of 1. θ_t will enter the expressions for $N_{i,j}^s$ and $N_{i,j}^b$ in a way that when it varies
 1422 within $[-1, +1]$, the corresponding predictions vary within their estimated standard deviation.

1423 Depending on the definition of the $p.o.i$, it will enter the expressions for $N_{i,j}^s$ differently, thus corresponding
 1424 to different interpretation of the data, which will be discussed below.

1425 10.2 Signal strength

1426 The signal strength is defined as the ratio between the observed number of signal events over the expected
 1427 one:

$$\mu = \frac{N_s^{obs}}{N_s^{SM}}. \quad (38)$$

1428 If more than one channel is involved in the fit, μ will be the average of ratios in each channel. Alternatively,
 1429 one can also define multiple μ 's, one for each channel j :

$$\mu_j = \frac{N_{s,j}^{obs}}{N_{s,j}^{SM}}. \quad (39)$$

1430 Signal strength enters the likelihood according to:

$$N_{i,j}^s = \mu \times N_{s,j}^{SM} \times f_{i,j}^{ELD} \quad (40)$$

1431 or

$$N_{i,j}^s = \mu_j \times N_{s,j}^{SM} \times f_{i,j}^{ELD}, \quad (41)$$

1432 where $N_{s,j}^{SM}$ is the predicted number of signal events in the channel j and $f_{i,j}^{ELD}$ is the fraction of events
 1433 falling into a particular ELD bin i of channel j , which is in fact the shape information of the ELD.

1434 This way of parametrisation is used most often since it compares between observation and SM prediction
 1435 without any need of unfolding.

1436 10.3 Fiducial cross section

1437 When the *p.o.i* is the fiducial cross section σ_j^{fid} , as defined in Section 9, the expression for $N_{i,j}^s$ becomes:
 1438

$$N_{i,j}^s = L \times \sigma_j^{fid} \times C_j \times f_{i,j}^{ELD}, \quad (42)$$

1439 where L is the integrated luminosity and C_j is the correction factor (corrects for signal efficiency and
 1440 migration), as described in Section 9.1.

1441 In this way, the measurement does not depend on the prediction of the normalisation of signal event.

1442 Usually there will be one fiducial cross section for one channel. But sometimes, the fiducial regions of
 1443 each channel can be combined into one region so that a combined fiducial cross section is measured.

1444 10.4 Total cross section

1445 When the *p.o.i* is the total cross section, as defined in Section 9, the expression for $N_{i,j}^s$ is similar as for
 1446 the case of fiducial cross section:

$$N_{i,j}^s = L \times \sigma^{tot} \times A_j \times C_j \times f_{i,j}^{ELD} \quad (43)$$

1447 with an additional parameter A_j , which is the acceptance, as described in Section 9.1.

1448 Fitting the total cross section requires knowledge about the acceptance, which usually introduce significant
 1449 additional uncertainty, so it's usually more preferable to do fiducial rather than total cross section
 1450 measurement.

1451 10.5 Differential cross section

1452 In this case, there will be n *p.o.i*'s, with n being the number of bins of the observable, and the expression
 1453 for likelihood function extends to:

$$\mathcal{L} = \prod_k \prod_j \prod_i P(N_{i,j,k} | N_{i,j,k}^s + \sum_b N_{i,j,k}^b) \times \prod_t G(\vartheta | \theta_t, 1), \quad (44)$$

1454 where the new index k is the binning index of the observable. For different channels there can be different
 1455 binning for the same observable (due to different statistics available), in which case k should be written
 1456 as k_j , being channel dependent.

1457 The *p.o.i*'s, which are the differential cross sections σ_p^{diff} enter the likelihood through the numbers of
 1458 observed signal events $N_{i,j,k}^s$. The index p is the binning index of the truth level observable. It can be
 1459 written as (for simplicity, the channel and ELD binning indexes i and j are temporarily omitted):

$$N_k^s = \frac{1}{1 - f_{\text{mig},k}} \times \sum_p (L \times \sigma_p^{\text{diff}} \times \epsilon_p \times M_{pk}). \quad (45)$$

1460 All quantities are already defined in Section 9.4.

1461 This way of parametrisation is called unfolding with maximum-likelihood method. It has the advantage
 1462 of being able to correlate all the systematics correctly. But the fit will be very sensitive to data fluctuation
 1463 if the bin-by-bin migration (off-diagonal of the migration matrix) gets too large.

1464 There is another way of performing differential measurement, where the reconstructed signal spectrum is
 1465 firstly measured by subtracting post-fit background spectrum from data and then unfolded to truth level
 1466 spectrum. The key of this approach is the inversion of the migration matrix, introduced in Equation 33,
 1467 which could be done by e.g Iterative Bayesian method. This is the benchmark method used in this analysis.
 1468 More details are given in Section 11.

1469 11 Unfolding

1470 The procedure of retrieving the truth spectrum of an observable from the measured spectrum is called
 1471 unfolding [53]. The measured spectrum is unfolded to the particle level, i.e., after the hadronisation and
 1472 showering processes. The unfolding is performed in order to correct for the detector effects due to limited
 1473 resolution and acceptance, this enables the measured distributions to be compared to the prediction of an
 1474 existing theory. Unfolding also enables the comparison with other experiments which could have different
 1475 migration matrices.

1476 The main problem of unfolding is the inversion of the migration matrix. To derive the inverse of
 1477 the migration matrix, various methods have been developed. In this section, different methods for
 1478 unfolding (to particle level) are introduced and compared [53, 54]: the benchmark method which is the
 1479 iterative Bayesian method (IBS) [55] is introduced in 11.1, and two other methods, the singular value
 1480 decomposition (SVD) [56] and the bin-by-bin approach [54], which are used as cross-check methods,
 1481 are introduced in 11.2. Another method which could be used for cross-check is the maximum likelihood
 1482 method (ML), which was already described in Section 10.5 and [54]. All of the methods except for the
 1483 ML are implemented in the RooUnfold package [57].

1484 For each of the unfolding methods, the same inputs are used: efficiency, outside fiducial region migration,
 1485 and bin-by-bin migration matrix, which are all already introduced in Section 9.4. Some illustrations for
 1486 these inputs can be found in Figures 68 and 69 for efficiencies and outside migrations, and in Figures 70
 1487 and 71 for bin-by-bin migration matrices, in the dilepton and the single lepton channels respectively.

1488 Besides, for simplicity, a simple cut-and-count analysis, instead of ELD template fit, is performed in each
 1489 bin of the observable.

1490 11.1 Iterative Bayesian method

1491 Before introducing the method, it will be convenient to rewrite the Equation 33 for differential cross
 1492 section as following:

$$N_{\text{gen},k}^{\text{corr}} = \sum_j M_{jk}^{-1} \times N_{\text{reco},j}^{\text{corr}}, \quad (46)$$

1493 where $N_{\text{gen},k}^{\text{corr}}$ is the efficiency corrected truth spectrum:

$$N_{\text{gen},k}^{\text{corr}} = L \times \sigma_k^{\text{diff}} \times \epsilon_k, \quad (47)$$

1494 and $N_{\text{reco},j}^{\text{corr}}$ is the observed spectrum with background and outside fiducial migration corrected:

$$N_{\text{reco},j}^{\text{corr}} = (N_{\text{data},j} - N_{\text{bkgs},j}) \times (1 - f_{\text{mig},j}). \quad (48)$$

1495 Then the differential cross section measurement is reduced to the problem of converting the corrected
 1496 observed spectrum $N_{\text{reco},j}^{\text{corr}}$ to the corrected truth spectrum $N_{\text{gen},k}^{\text{corr}}$ by using the inverted migration matrix
 1497 M_{jk}^{-1} .

1498 To revert the migration matrix, the iterative Bayesian method is proposed by D'Agostini, and explained
 1499 in more details in his paper [55]. Concepts of cause and effect are introduced where E means effect,
 1500 corresponding to the measured values and C means cause, corresponding to the truth ones. The migration
 1501 matrix can be expressed as:

$$M_{kj} = P(E_j|C_k), \quad (49)$$

1502 which means the probability for observing an effect in bin j , given a cause in bin k . Then its inversion
 1503 M_{jk}^{-1} can be expressed as:

$$M_{jk}^{-1} = P(C_k|E_j), \quad (50)$$

1504 which means the probability for a cause in bin k , given the observation of an effect in bin j . According to
 1505 Bayesian theorem, $P(C_k|E_j)$ can be written in the following equation:

$$P(C_k|E_j) = \frac{P(E_j|C_k) \cdot P_0(C_k)}{\sum_l P(E_j|C_l) \cdot P_0(C_l)}, \quad (51)$$

1506 given some prior truth distribution $P_0(C_l)$, from e.g. the MC sample.

1507 Then this inversion matrix can be used to derive an unfolded distribution, which again can be fed into the
 1508 calculation of the reversion matrix as a prior. Finally, when the unfolded distribution and the prior, which
 1509 is the unfolded distribution from the last iteration, converge, the iteration stops. The differential cross
 1510 section can be then easily derived by solving Equation 47.

1511 11.1.1 The pseudo-data

1512 As the unfolding is an iterative procedure, the convergence point is needed to be determined and the point
 1513 will be known as the number of iterations. The determined number will be used later to perform various
 1514 checks in order to confirm that the unfolding study is not biased against the bin choice and the specific
 1515 choice of the MC sample to obtain the truth spectrum and the measured spectrum. To perform these
 1516 checks, the measured spectrum is replaced by the pseudo-data.

1517 The pseudo-data is generated using the $t\bar{t}\gamma$ MC events which are randomly sampled into two parts, *testing*
 1518 and *training*, in a way that the testing part has the equivalent statistical power as the observed signal. The
 1519 training sample is used to build the migration matrix from, and the testing sample is being unfolded. 100
 1520 pseudo-data sets are generated in this way.

1521 The following Sections 11.1.2, 11.1.3 and 11.1.4 are using the same pseudo-data.

1522 11.1.2 Optimising the number of iterations

1523 In order to choose the number of iterations to be used for the unfolding, two methods are employed. The
 1524 final chosen number of iterations is a compromise between having a low difference in the unfolded results
 1525 between different iterations, having a stable statistical uncertainty in all bins, and having no bias against
 1526 any number of iterations.

1527 In the first method, the convergence of the unfolded results are checked. 1000 pseudo-data sets are
 1528 generated by using a Poisson distribution, from the reconstructed-level distribution which is obtained
 1529 from the testing part. The new pseudo-data is then unfolded using the migration matrix from the training
 1530 part. The unfolding is done for different number of iterations. The number of pseudo-unfolded events

1531 after $i + 1$ iterations, is compared to the previous number of unfolded events obtained after i iterations.
 1532 The relative difference between the two numbers is calculated and plotted versus the observable. The
 1533 result of the test is shown in Figure 72 in the dilepton channel and Figure 73 in the single lepton channel.
 1534 The first number of iterations that results in the relative difference as low as less than 1% in all the bins,
 1535 is taken into account:

$$\frac{N^{\text{unf}, i+1} - N^{\text{unf}, i}}{N^{\text{unf}, i+1}} < 1\%. \quad (52)$$

1536 From Figures 72 and 73, the number of iterations 3 seems to be preferred. However, the decision should
 1537 not be taken before checking the RMS.
 1538 In the second method, to check the statistical uncertainty on the unfolded pseudo-data, the 100 pseudo-data
 1539 sets described previously are used. The training pseudo-data is used to get the migration matrix, while
 1540 the pseudo-data of the testing reconstructed-level is unfolded. The quantity RMS is calculated to compare
 1541 the unfolded reconstructed distribution to the pseudo-particle level distribution:

$$\text{RMS} = \frac{(\text{truth} - \text{unfolded})}{\text{unfolded}}. \quad (53)$$

1542 A small bias against some number of iterations is observed in the dilepton channel in the photon p_T , η and
 1543 minimum $\Delta R(\text{lepton}, \gamma)$, as shown in Figure 74, Figure 75 and Figure 76, while the other two observables
 1544 ($\Delta\eta(\text{lepton}, \text{lepton})$ and $\Delta\phi(\text{lepton}, \text{lepton})$) are stable, as shown in Figure 77 and Figure 78. Furthermore,
 1545 the uncertainty is mostly stable, only increasing slightly with more number of iterations. For the single
 1546 lepton channel, most of the bins are stable and no clear bias is observed, as can be seen in Figure 79,
 1547 Figure 80 and Figure 81 for the photon p_T , η , and $\Delta R(\text{lepton}, \gamma)$, respectively.
 1548 Since in the first method, the two variables and channels agree for 3 iterations, and in the second method
 1549 most of bins are also stable after 3 iterations, the 3 iterations are chosen, to be harmonised among all the
 1550 observables and the both channels.

1551 11.1.3 The closure test

1552 The closure test is performed to check if the unfolding procedure can recover the truth spectrum. To
 1553 do that, the 100 pseudo-data distributions of the testing part at the reconstruction-level are unfolded, using
 1554 the migration matrix from the training part. A perfect closure is obtained, as can be seen in Figure 82 for
 1555 the dilepton channel and in Figure 83 for single lepton channel.

1556 11.1.4 Pull study

1557 The binning of the observables are initially chosen according to the criteria described earlier in Section 9.4.
 1558 The stability of the binning choice is checked by performing the pull tests.
 1559 The same pseudo-data described in Section 11.1.1 is used and another 1000 pseudo-experiments are built
 1560 from the reconstructed-level in the testing part using the Poisson distribution, and then unfolded. The

Not reviewed, for internal circulation only

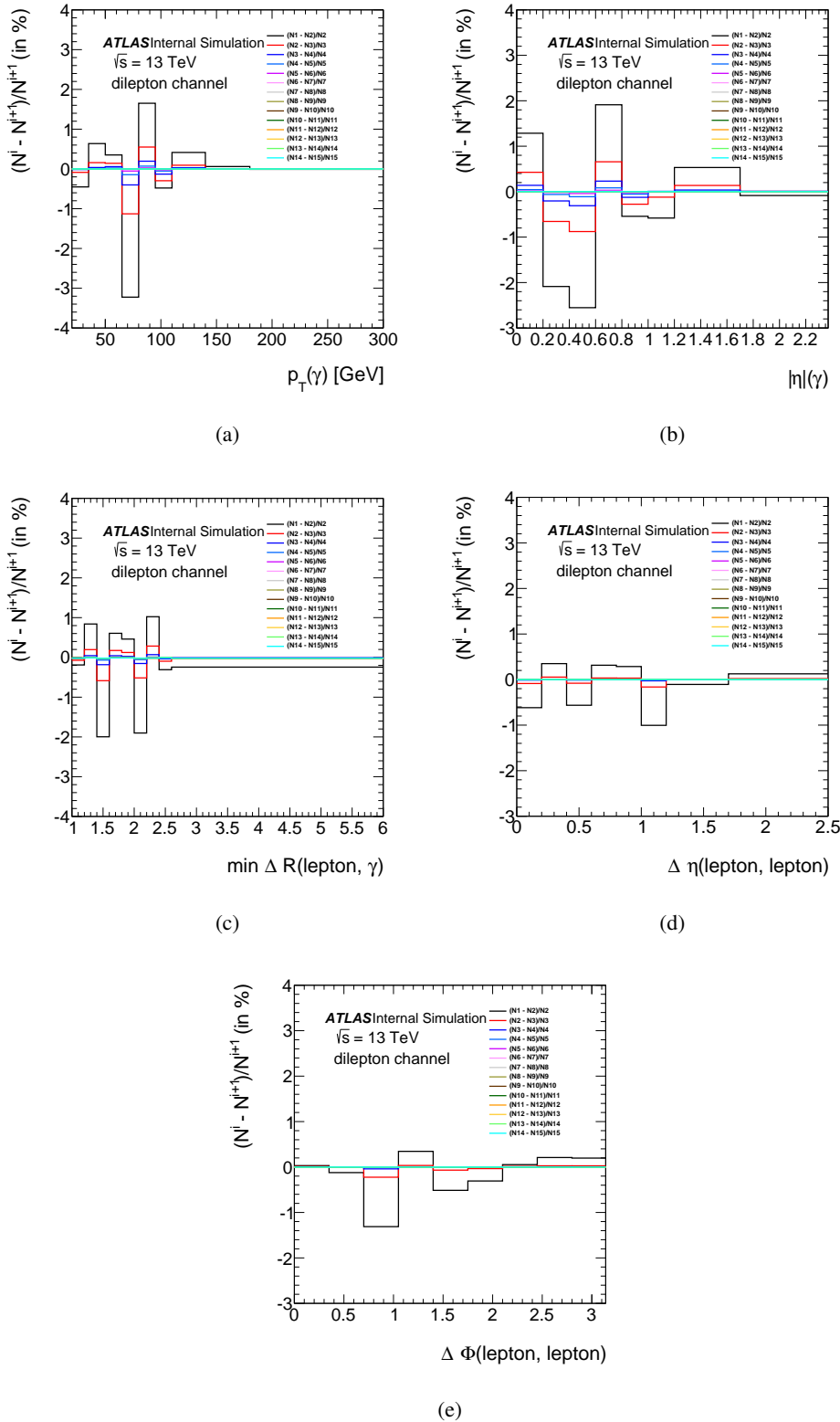


Figure 72: The relative difference on the unfolded result after two successive iterations, as a function of five different observables in dilepton channel.

Not reviewed, for internal circulation only

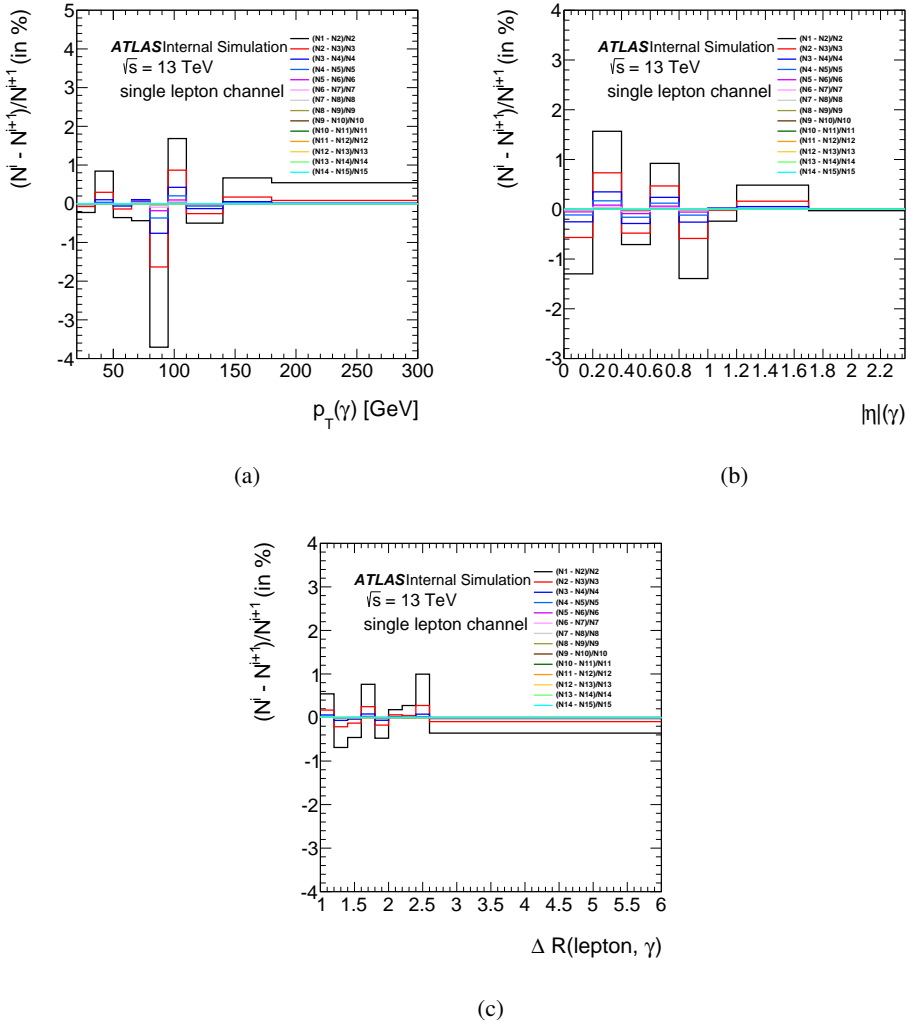


Figure 73: The relative difference on the unfolded result after two successive iterations as a function of the photon p_T (a), the photon $|\eta|$ (b), and $\Delta R(\text{lepton}, \gamma)$ (c) in the single lepton channel.

Not reviewed, for internal circulation only

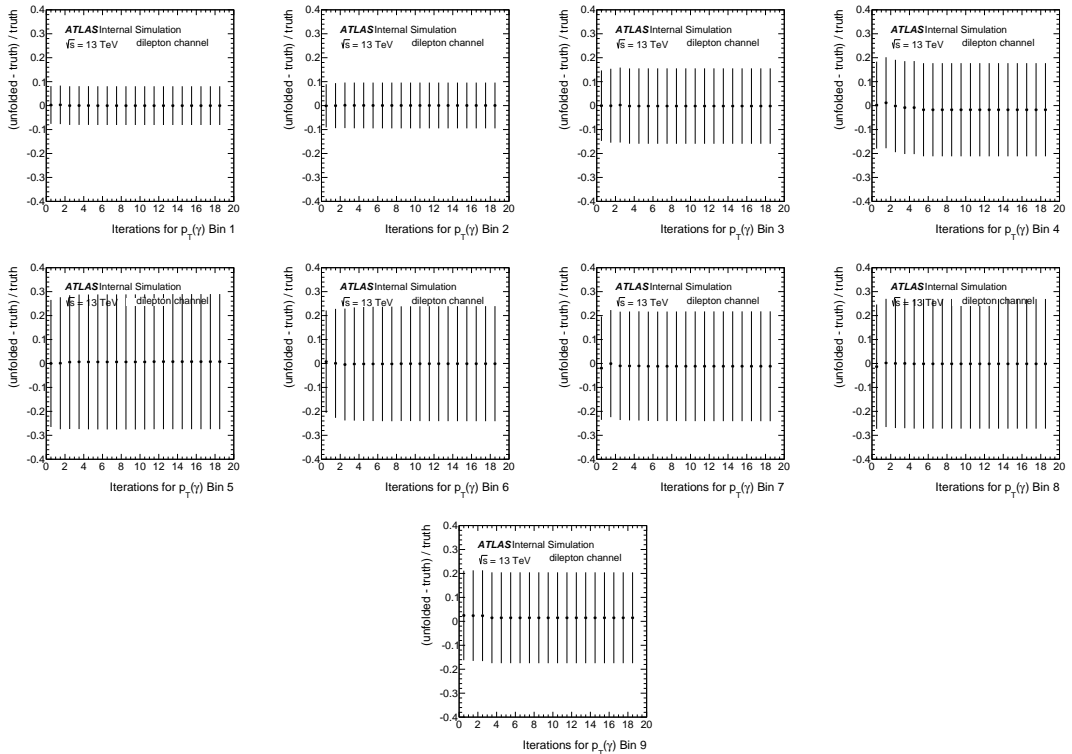


Figure 74: The RMS against the number of iterations for the 9 bins in p_T in the dilepton channel.

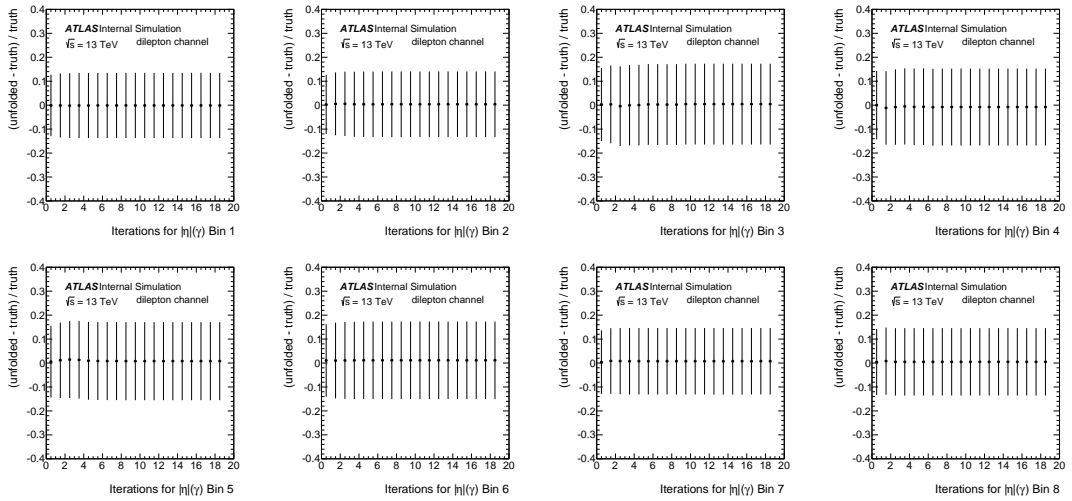


Figure 75: The RMS against the number of iterations for the 8 bins in η in the dilepton channel.

Not reviewed, for internal circulation only

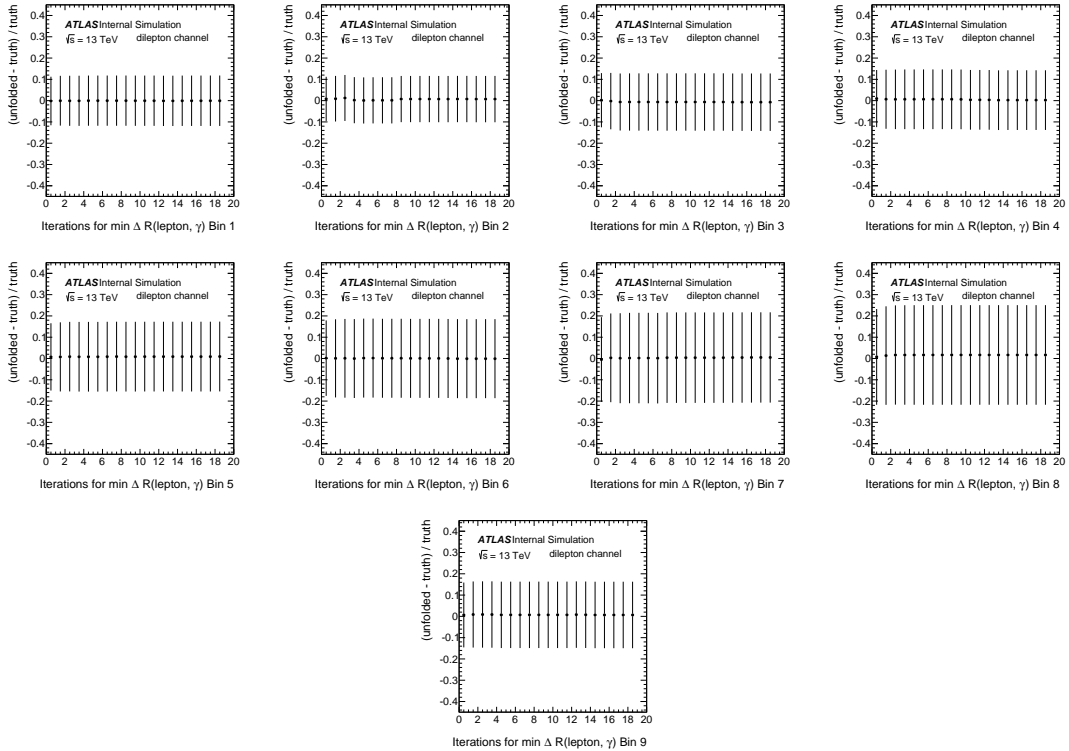


Figure 76: The RMS against the number of iterations for the 9 bins in the minimum $\Delta R(\text{lepton}, \gamma)$ in the dilepton channel.

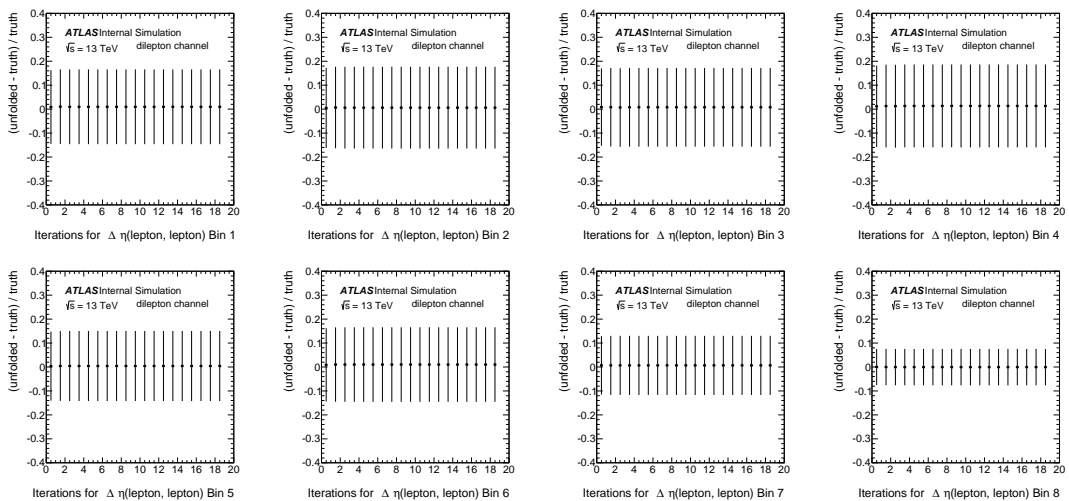


Figure 77: The RMS against the number of iterations for the 8 bins in $\Delta\eta(\text{lepton}, \text{lepton})$ in the dilepton channel.

Not reviewed, for internal circulation only

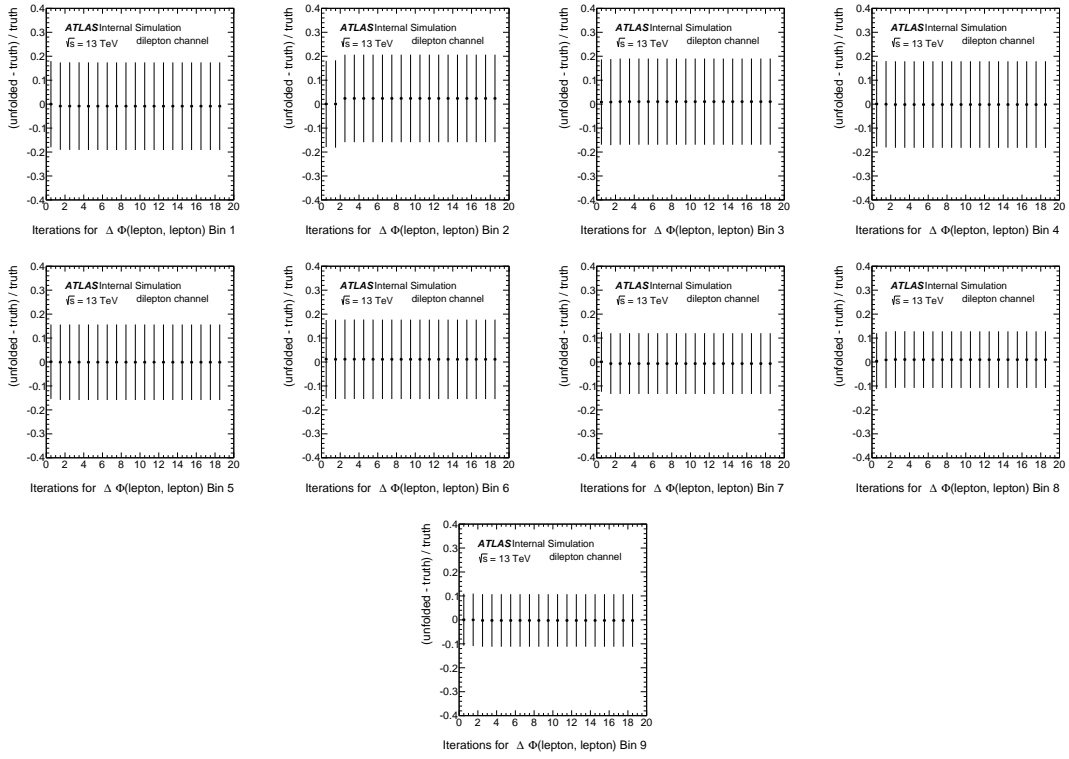


Figure 78: The RMS against the number of iterations for the 9 bins in $\Delta\phi(\text{lepton}, \text{lepton})$ in the dilepton channel.

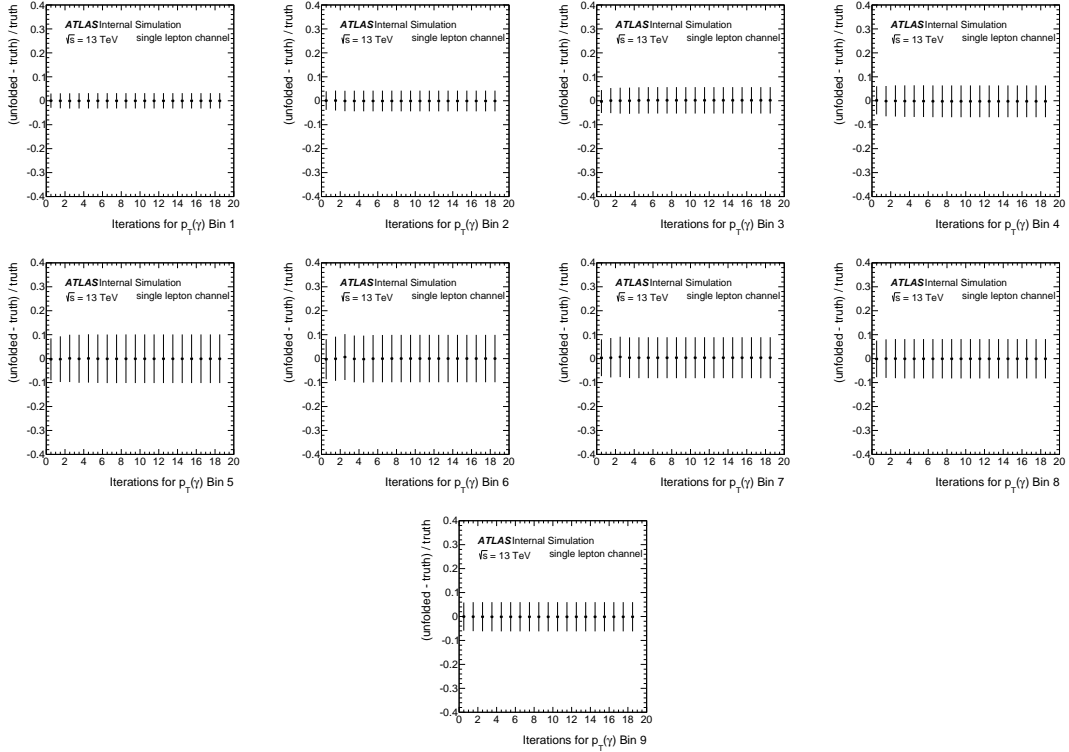


Figure 79: The RMS against the number of iterations for the 9 bins in p_T in the single-lepton channel.

Not reviewed, for internal circulation only

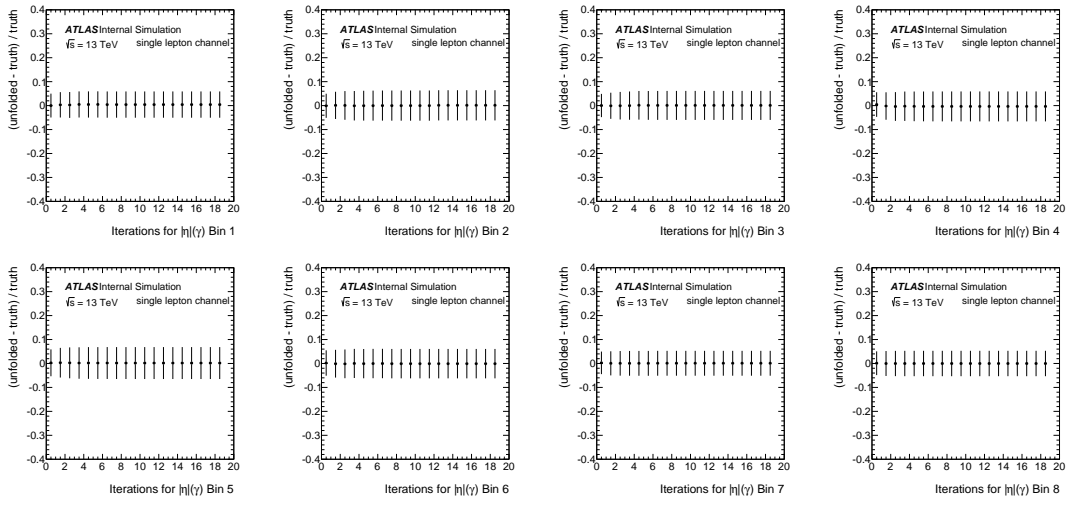


Figure 80: The RMS against the number of iterations for the 8 bins in η in the single-lepton channel.

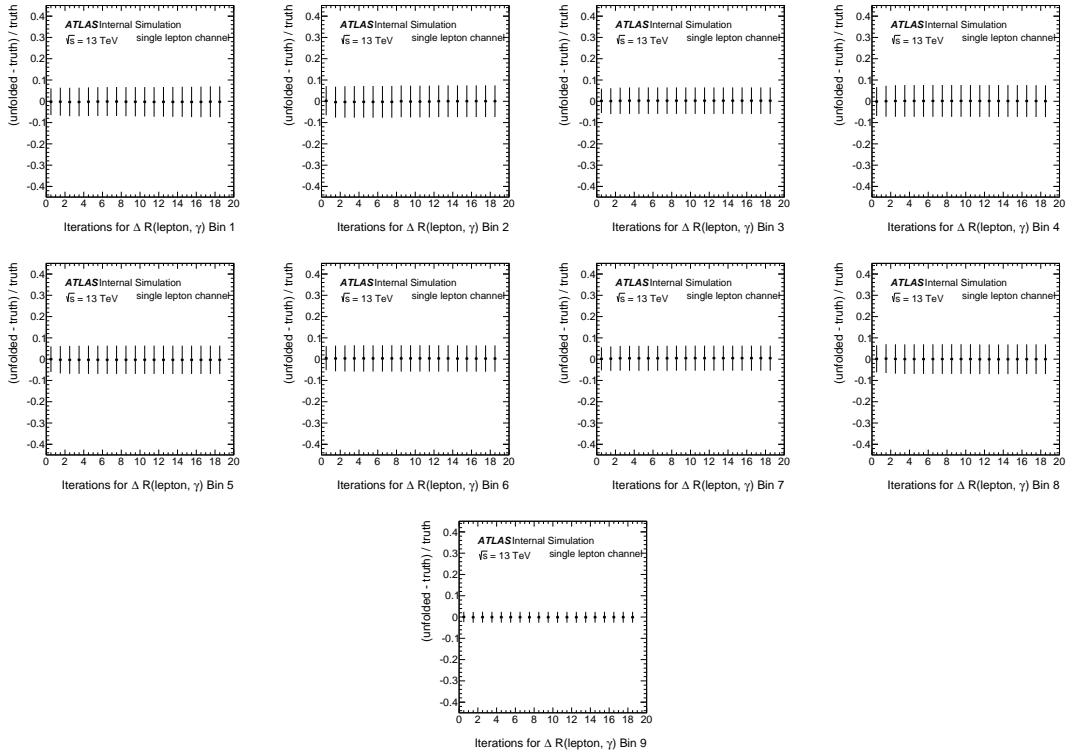


Figure 81: The RMS against the number of iterations for the 9 bins in $\Delta R(\text{lepton}, \gamma)$ in the single-lepton channel.

Not reviewed, for internal circulation only

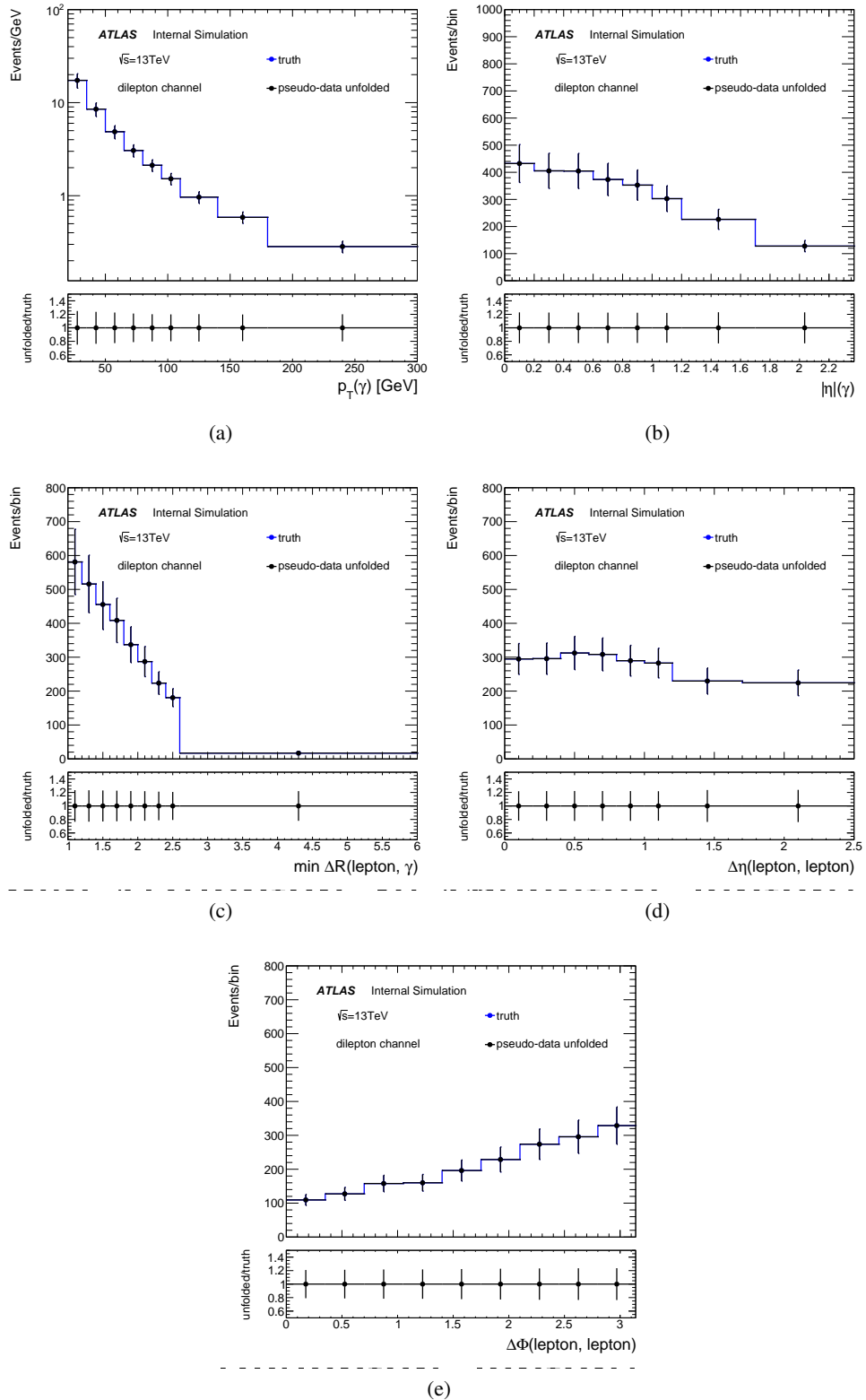


Figure 82: The ratio of the number of unfolded events for one pseudo-data after 3 iterations to the number of truth events in the dilepton channel.

Not reviewed, for internal circulation only

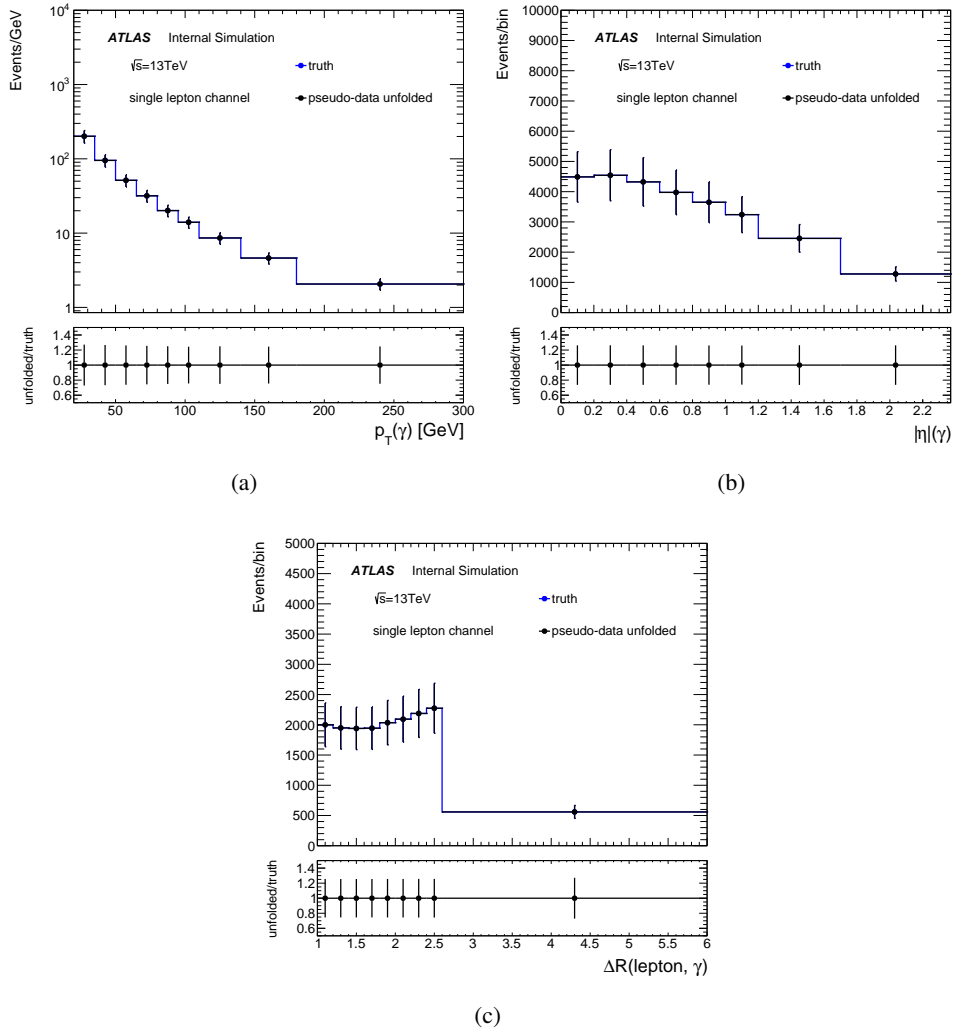


Figure 83: The ratio of the number of unfolded events for one pseudo-data after 3 iterations to the number of truth events, as a function of the photon p_T (a), the photon η (b), and $\Delta R(\text{lepton}, \gamma)$ (c) in the single lepton channel.

1561 unfolded pseudo-results are then compared to the pseudo-particle level. The pulls are calculated per bin
 1562 as:

$$\text{Pull} = \frac{(\text{truth} - \text{unfolded})}{\sigma_{\text{unfold}}}, \quad (54)$$

1563 and then fit by a Gaussian function (see Appendix J). The pull is expected to have a mean value of zero,
 1564 which indicates no bias, and a width of one, which could mean that the statistical uncertainty is estimated
 1565 correctly. Figure 84 shows the result of the test for dilepton channel and Figure 85 for single lepton
 1566 channel. No bias in the bin choice is seen and the width is consistent with one.

1567 **11.1.5 Stress tests**

1568 The stress test is performed in order to verify that the unfolding procedure is not biased to any specific
 1569 shape of the particle level distribution. The particle-level and reconstruction-level distributions obtained
 1570 from the nominal MC sample are reweighted, and then the reweighted reconstructed distribution is unfolded
 1571 using the nominal inputs from the MC sample, and the unfolded results are compared to the corresponding
 1572 particle level distribution.

1573 Different weights have been checked, the first one is by taking the observed difference between data and
 1574 MC as the following:

$$\text{weight} = 1 + Y \cdot \frac{\text{data}_i - \text{MC}_i}{\text{data}_i} = 1 + Y \cdot \text{Obs}, \quad (55)$$

1575 where i is the bin index and $Y = 1, -1$. The result of the stress test is shown in Figure 86 and Figure 87
 1576 for the dilepton and single lepton channels, respectively. The unfolding is able to retrieve the reweighted
 1577 particle distribution for all observables in both channels.

1578 A different weight, corresponding to a linear skewness of the shape, is also used. It is defined as the
 1579 following, in case of the photon p_T :

$$\text{weight} = 1 + y \cdot \frac{100 - i}{300} = 1 + y \cdot X, \quad (56)$$

1580 while given by the following for the photon η :

$$\text{weight} = 1 + y \cdot \frac{1.2 - i}{2.37} = 1 + y \cdot X, \quad (57)$$

1581 and for the minimum $\Delta R(\text{lepton}, \gamma)$ by:

$$\text{weight} = 1 + y \cdot \frac{1.8 - i}{6} = 1 + y \cdot X, \quad (58)$$

Not reviewed, for internal circulation only

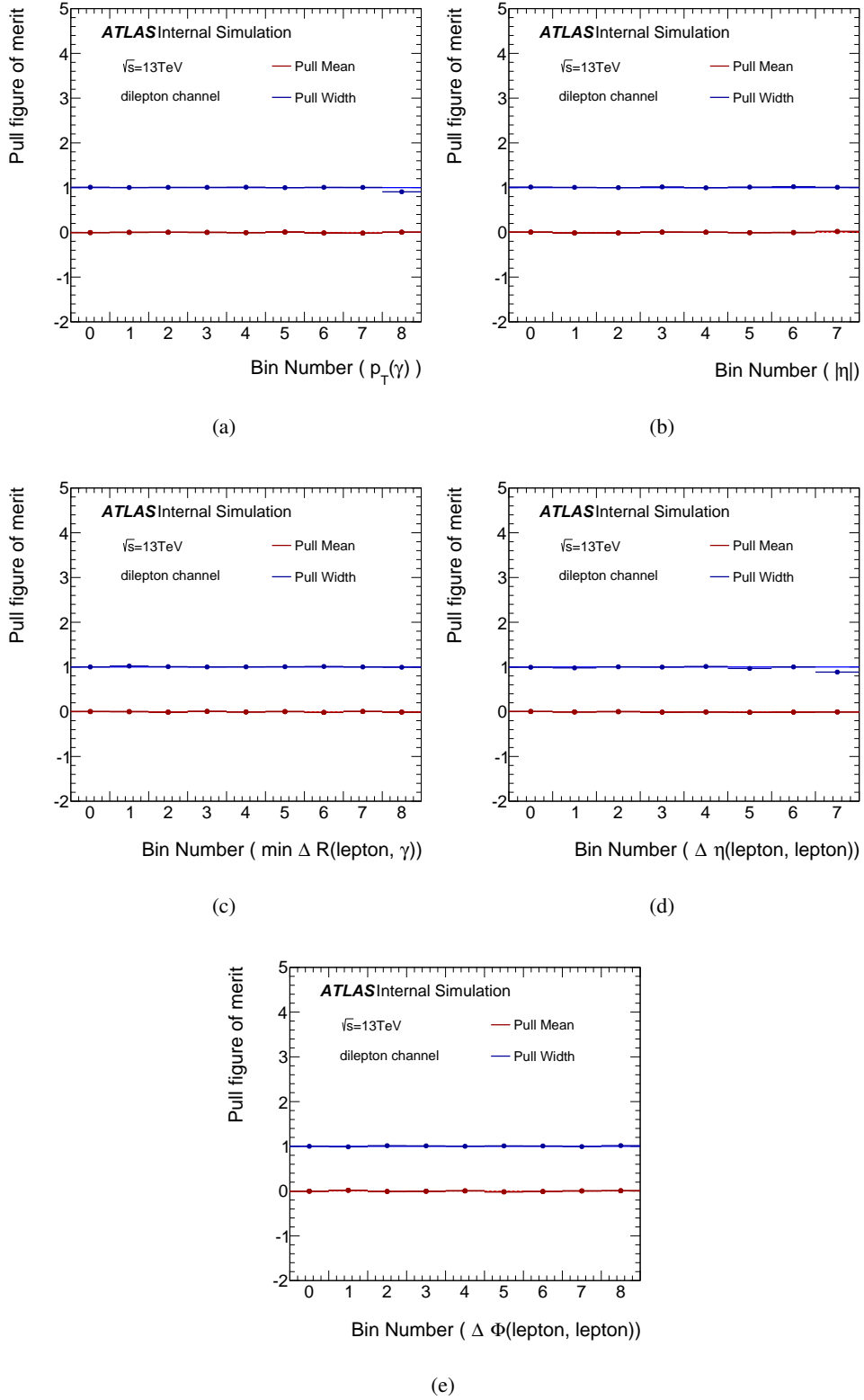


Figure 84: The pull test in each bin of the five observables, obtained after 3 iterations, in the dilepton channel.

Not reviewed, for internal circulation only

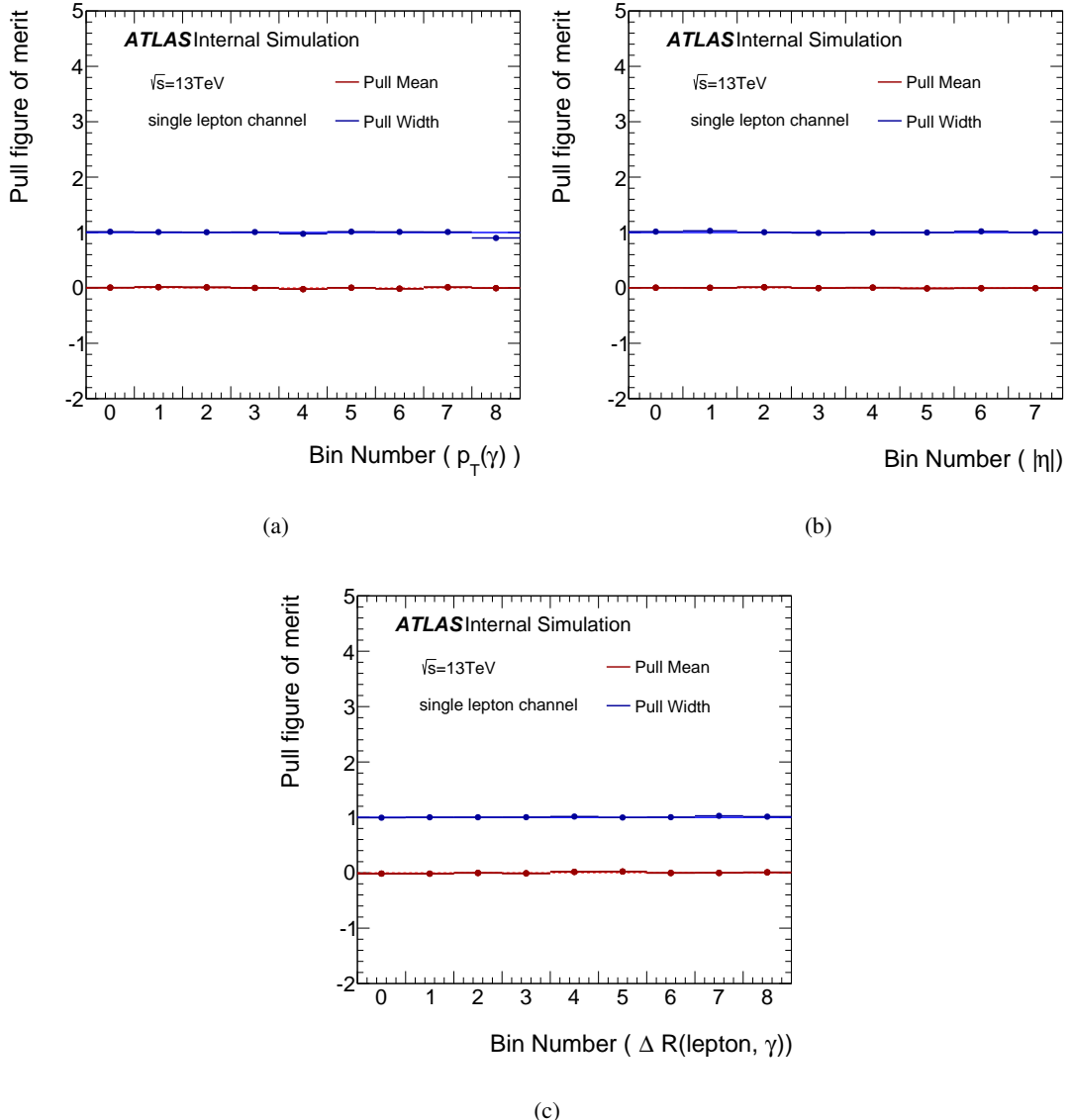


Figure 85: The pull test in each bin of the photon p_T (a), the photon η (b) and the $\Delta R(\text{lepton}, \gamma)$ (c), obtained after 3 iterations, in the single lepton channel.

1582 and for the $\Delta\eta(\text{lepton}, \text{lepton})$ by:

$$\text{weight} = 1 + y \cdot \frac{1.2 - i}{2.5} = 1 + y \cdot X, \quad (59)$$

1583 and for the $\Delta\phi(\text{lepton}, \text{lepton})$ by:

$$\text{weight} = 1 + y \cdot \frac{1.75 - i}{3.14} = 1 + y \cdot X, \quad (60)$$

1584 where $y = -1, 1$, and i is the bin centre. The results of the second stress test are shown in the same Figures 86
1585 and 87. The reweighted particle level distributions are in different shapes from the nominal ones, and the
1586 unfolding procedure is able to retrieve the reweighted particle level distributions in all observables in both
1587 channels.

1588 11.2 Cross-check methods

1589 11.2.1 Bin-by-bin correction method

1590 The method is based on extracting a bin-by-bin correction factor from MC. This method is only favoured
1591 with a very low bin-to-bin migration. The correction factor is defined by the ratio of the reconstructed
1592 MC distribution to the particle-level distribution. The unfolded particle-level spectrum is given by the
1593 following equation:

$$\left(\frac{N_k^{\text{reco}}}{N_k^{\text{part}}} \right) \cdot N_k^{\text{unf,part}} = N_k^{\text{data}} - N_k^{\text{bkgs}} \quad (61)$$

1594 11.2.2 The singular value decomposition method

1595 The singular value decomposition method described in [56], simplifies the inversion process of the
1596 migration matrix by decomposing the migration matrix of other matrices:

$$M = US^{-1}V^T, \quad (62)$$

1597 where U and V are $n \times n$ orthogonal matrices and S is $n \times n$ diagonal matrix. Then:

$$M^{-1} = VS^{-1}U^T. \quad (63)$$

1598 The method also introduces a normalization term to regularize the solution. The term acts as cut-off for
1599 the large sensitivity to the small fluctuations. Since the method is used here only for a cross-check, the
1600 regularization parameters is set here to the default value, which is the number of bins divided by 2; No
1601 optimisation work is done.

Not reviewed, for internal circulation only

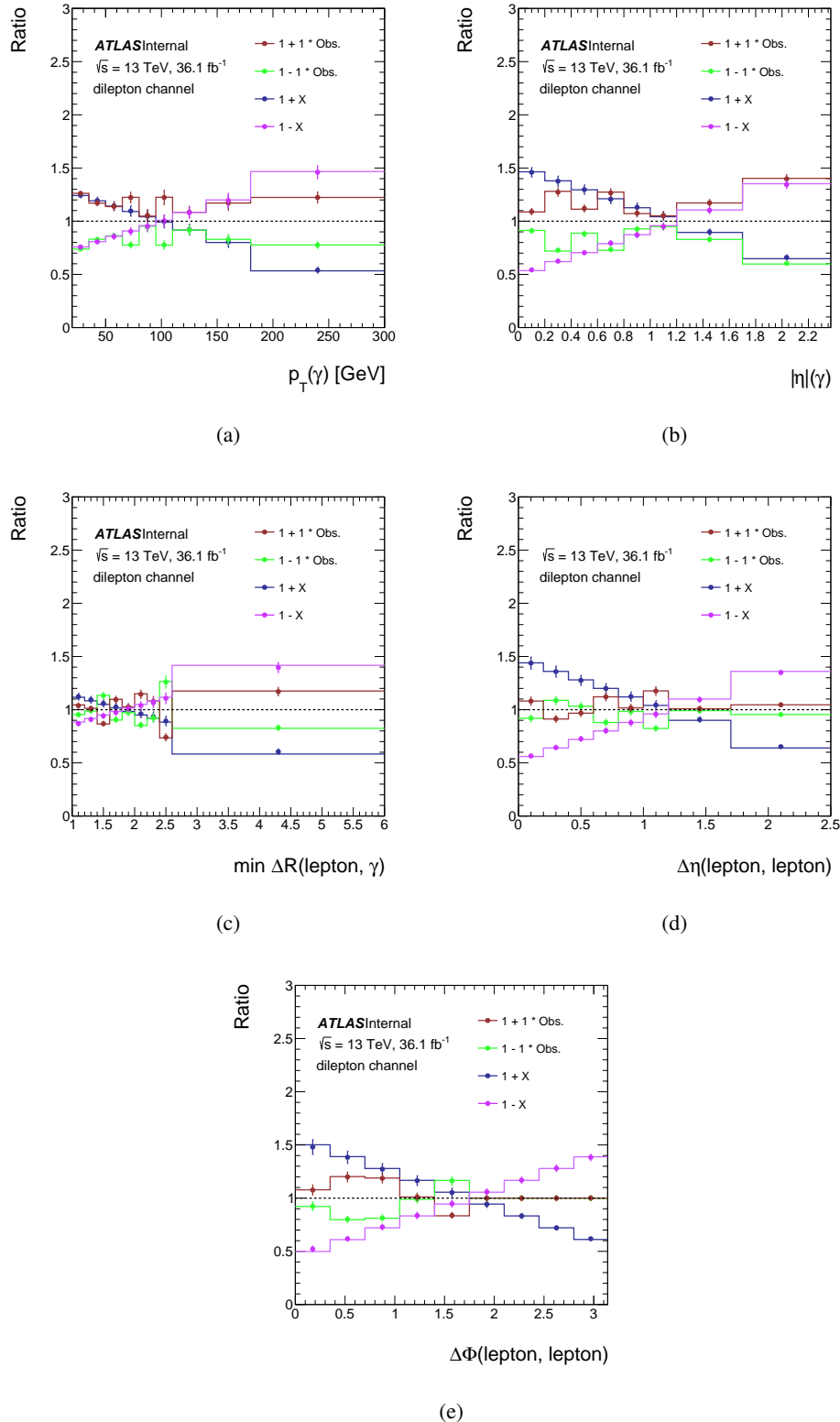


Figure 86: The stress test for the five observables in the dilepton channel. Both the dots and lines are ratios made with respect to the nominal particle level. The dots are the ratio of the unfolded reweighted distributions to the nominal particle level distribution, while the solid lines are the ratio of the reweighted particle level distributions to the nominal one. Obs. is defined in Equation 55, and X in Equations 56 – 60.

Not reviewed, for internal circulation only

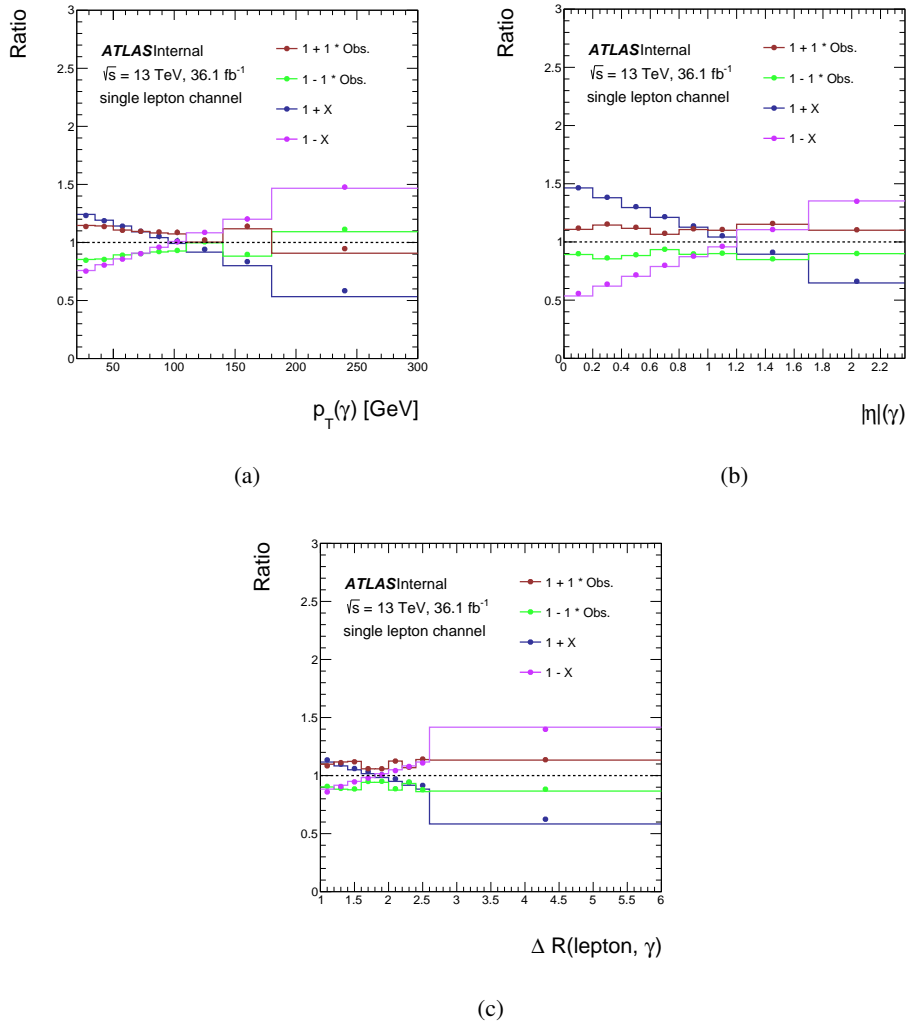


Figure 87: The stress test for the photon p_T (top), the photon η (middle), $\Delta R(\text{lepton}, \gamma)$ (bottom), in the single-lepton channel. Both the dots and lines are ratios made with respect to the nominal particle level. The dots are the ratio of the unfolded reweighted distributions to the nominal particle level distribution, while the solid lines are the ratio of the reweighted particle level distributions to the nominal one. Obs. is defined in Equation 55, and X in Equations 56 – 58.

1602 11.2.3 Comparison test

1603 The test is done here to compare different methods by unfolding the reconstruction-level distribution,
1604 which is estimated from MC. Figure 88 and Figure 89 show the different unfolded results with different
1605 methods, compared to the truth distribution in the dilepton and single lepton channels, respectively. The
1606 SVD method, show always slightly different central values from the other methods, but agrees within
1607 the statistical uncertainties. Here, the SVD method should be taken as first approximation since its
1608 regularisation parameter is not optimised.

Not reviewed, for internal circulation only

Not reviewed, for internal circulation only

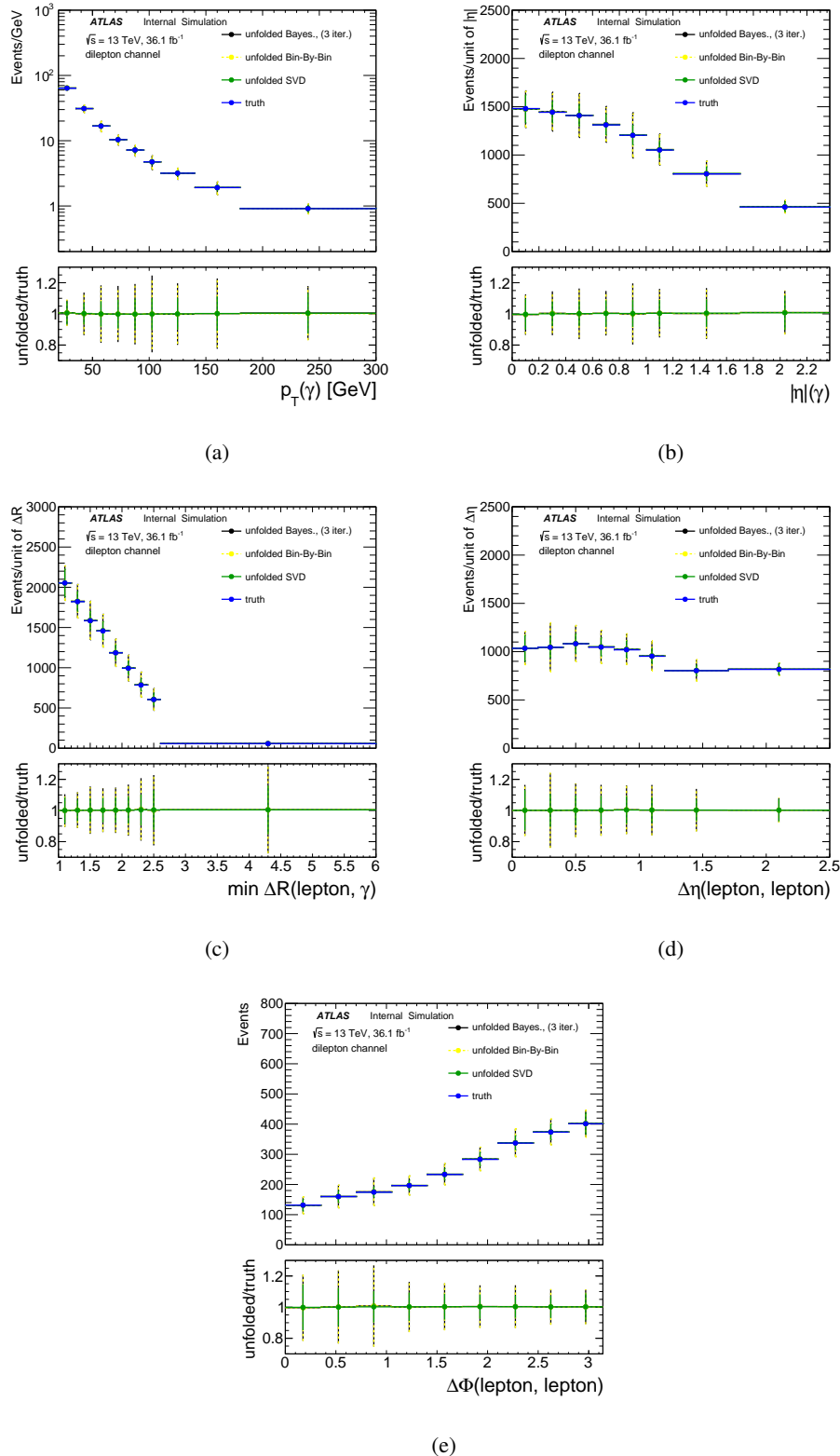


Figure 88: The number of unfolding events in the dilepton channel, obtained by the iterative Bayesian method after 3 iterations in black, the SVD in red and the bin-by-bin in yellow. All are compared to the truth distribution in blue (the ratio plot), and normalized to a luminosity of 36.1 fb^{-1} .

Not reviewed, for internal circulation only

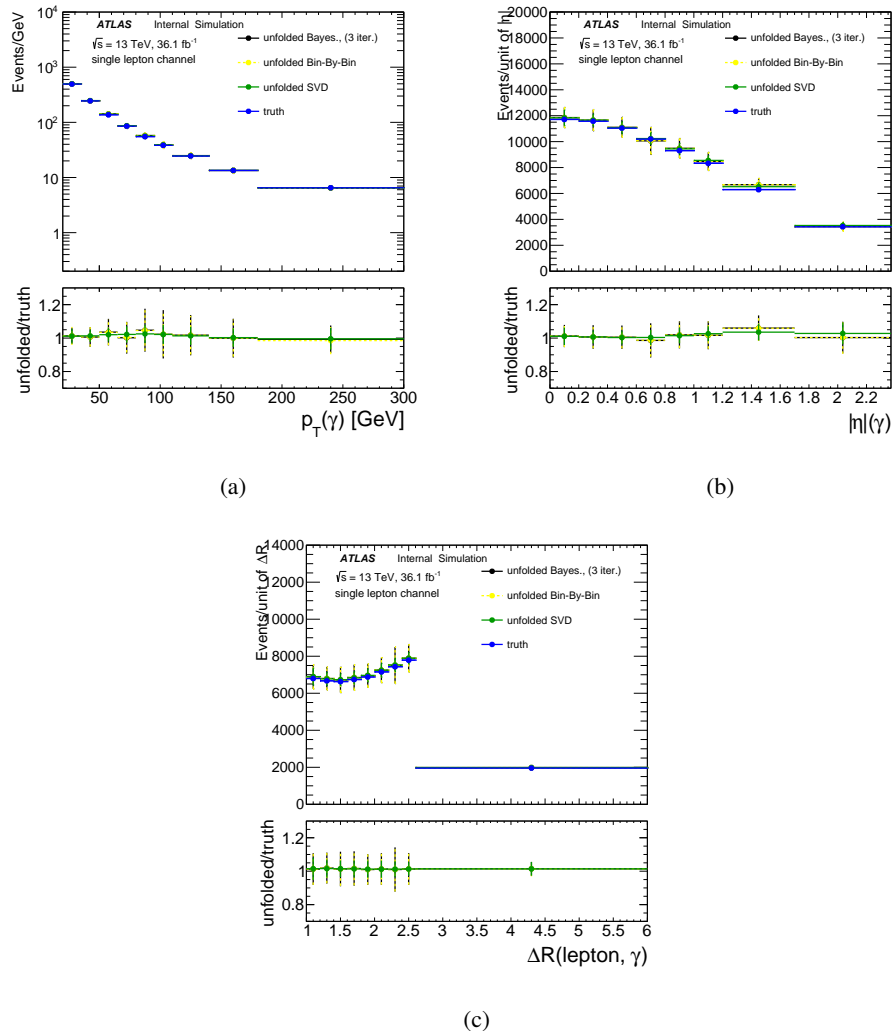


Figure 89: The number of unfolding events as a function of the photon p_T (a), the photon η (b), and the $\Delta R(\text{lepton}, \gamma)$ (c) in the single lepton channel, obtained by the iterative Bayesian method after 3 iterations in black, the SVD in red and the bin-by-bin in yellow. All are compared to the truth distribution in blue (the ratio plot), and normalized to a luminosity of 36.1 fb^{-1} .

1609 12 Theory prediction

1610 Next-to-leading order (NLO) QCD corrections to the production of a $t\bar{t}$ pair in association with a hard
 1611 photon are available by K. Melnikov et al. [14], extending the results of Duan et. al. [58] performed
 1612 in the approximation of stable top quarks. The calculation of [14] allows for decays of top quarks and it
 1613 includes photon radiation in both the production and decay stages of the $t\bar{t}$ pair. The method of generalised
 1614 D-dimensional unitarity extended to massive particles and the dipole formalism are used respectively to
 1615 calculate one-loop virtual amplitudes and real emission corrections. Top quarks are treated in the narrow
 1616 width approximation with all spin correlations retained. The hadronic decays of W-bosons are considered
 1617 into two families of light quarks, always treated as massless. The W-bosons are considered in their
 1618 mass-shells and no QCD radiative corrections to the hadronic decays are considered. The strong coupling
 1619 constant is evaluated using one- and two-loop running with five massless flavours.

1620 While the results presented in [14] are calculated at the centre-of-mass energy of $\sqrt{s} = 14$ TeV, a dedicated
 1621 calculation at $\sqrt{s} = 13$ TeV has been performed in the single lepton and dilepton channels, in a phase
 1622 space very close to the fiducial region of the measurement, as described in Section 9.1. The NNPDF set
 1623 was used, and a fine structure constant of $\alpha_{QED} = 1/137$ is used. The renormalisation and factorisation
 1624 scales $\mu_R = \mu_f = \mu = m_t$ are used.

1625 The NLO calculation as well as its phase space are described in 12.1. The corresponding LO prediction
 1626 by MADGRAPH in the same phase space is described in 12.2. And the resulting NLO kfactor as well as
 1627 the final predicted fiducial cross-sections are presented in 12.3.

1628 12.1 NLO cross-section

1629 To get a NLO correction as precise as possible, the phase space of the theory calculation is defined to be very
 1630 close to the fiducial region of the measurement. At least one lepton is required to have $p_T > 25$ GeV and
 1631 $|\eta| < 2.5$. The photon is required to have $p_T > 20$ GeV, $|\eta| < 2.37$. Jets are reconstructed from stable
 1632 particles using the anti- k_T algorithm ($R = 0.4$), and are considered if they have $p_T > 25$ GeV and $|\eta| < 2.5$.
 1633 For single lepton (dilepton) channel, it is required to have at least four (two) jets. There are several overlap
 1634 removal requirements: jets are required to be separated from photon with $\Delta R(\gamma, \text{jet}) > 0.4$; leptons are
 1635 required to be separated from photon with $\Delta R(\gamma, \text{lepton}) > 1.0$; if it's dilepton channel, leptons are
 1636 required to be separated from jets with $\Delta R(\text{jet}, \text{lepton}) > 0.4$.

1637 The calculated NLO cross sections are 112 fb and 28.3 fb for the single lepton and dilepton channels,
 1638 respectively. These numbers are then scaled up by 7% to take into account the difference of top and W
 1639 widths between those used for theory calculation and those from ATLAS recommendation.

1640 12.2 LO cross-section

1641 The NLO calculation is performed at parton level. In principle, the LO cross-section should also be done
 1642 at parton level. But since there is jet multiplicity cut involved in the definition of the phase space, using a
 1643 parton level LO cross-section will over-estimate the kfactor, which will be applied to a particle level LO
 1644 MC sample. This is due to that part of the NLO effect on the acceptance has already been accounted for
 1645 by the parton shower of the MC sample.

1646 To use particle level sample to calculate the LO cross-section, one has to carefully define the objects to
 1647 mimic those used in the NLO calculation for defining the phase space. The leptons and photon can be
 1648 easily taken as their matrix element correspondents, but now with slightly changed kinematics due to the
 1649 recoil caused effect caused by the additional QCD radiation from the parton shower. Besides, the leptons
 1650 have all their PS-added QED radiations reabsorbed since the NLO calculation considers only 1 QED
 1651 radiation. Jets are defined using the same anti- k_T algorithm of cone size 0.4 and use as input all the final
 1652 state particles, except for the above photon, leptons and their corresponding lepton neutrinos.

1653 After defining the objects as above, the same phase space cuts as in the previous section are applied.
 1654 The resulting LO cross-sections are 66.8 fb and 15.4 fb for the single lepton and dilepton channels,
 1655 respectively.

1656 12.3 Kfactor and fiducial cross-section

1657 The NLO kfactor is defined as:

$$k = \frac{\sigma_{NLO}^{parton}}{\sigma_{LO}^{particle}}. \quad (64)$$

1658 σ_{NLO}^{parton} is the parton level NLO cross-section from theory calculation and $\sigma_{LO}^{particle}$ is the particle level
 1659 LO cross-section from **MADGRAPH**. The resulting kfactors are 1.80 and 1.97 for the single lepton and
 1660 dilepton channels, respectively.

1661 From the equation, it can be seen that theoretical uncertainties could enter via both of its numerator and
 1662 denominator.

1663 To estimate the uncertainty of σ_{NLO}^{parton} , the renormalization and factorization scales are varied up-and-
 1664 down by a factor of 2 simultaneously, resulting in an uncertainty of 13%. The PDF is also varied from
 1665 NNPDF to MMHT2014 or CT14, resulting in an uncertainty of 5% (2%) for the single lepton (dilepton)
 1666 channel.

1667 To estimate the uncertainty of $\sigma_{LO}^{particle}$, it's mainly the non-perturbative effect and the arbitrary jet cone
 1668 size that should be considered. The non-perturbative effect brought by the parton shower includes the
 1669 multiple parton interaction (MPI) and the hadronization of the partons. The MPI systematics is derived
 1670 by tuning the parton shower to have rather low MPI effect. The hadronization systematics is evaluated by
 1671 turning off the hadronization of the parton shower. The jet cone size is varied from 0.4 to 0.3 and 0.5 as
 1672 up and down variation. The results of these systematics are summarized in Table 23, together with the
 1673 systematics of the σ_{NLO}^{parton} . The final systematics for the kfactors are also given.

Channel	Kfactor	$\delta\sigma_{LO}^{particle}$				$\delta\sigma_{NLO}^{parton}$ Scale/Pdf	$\delta K\text{factor}$
		Jet cone	MPI	Hadron.	Sum		
single lepton	1.80	-11%/+4%	-7%	+4%	14%	14%	20%
dilepton	1.97	-6%/+3%	-2%	+3%	7%	13%	15%

Table 23: The systematics of the NLO kfactor, decomposed into systematics of σ_{NLO}^{parton} and that of $\sigma_{LO}^{particle}$.

1674 Using these kfactor and their uncertainties, the fiducial cross-sections can be calculated by $\sigma_{LO} \times A_i \times k_i$,
 1675 where σ_{LO} is the total cross-section of 3.356 pb by **MADGRAPH** and A_i and k_i are the acceptance,

¹⁶⁷⁶ calculated in Section 9.1.3, and the kfactor, calculated as above, of channel i . The results are summarized
¹⁶⁷⁷ in Table 24.

Table 24: The theoretical fiducial NLO cross sections as well as their uncertainties in single lepton and dilepton channels taking into account the branching ratio for each channel.

	$e + \text{jets}$	$\mu + \text{jets}$	ee	$e\mu$	$\mu\mu$	single lepton	dilepton
Xsec. (fb)	247.14 ± 49.43	247.95 ± 49.59	15.88 ± 2.38	31.37 ± 4.71	15.93 ± 2.39	495.10 ± 99.02	63.18 ± 9.48

1678 13 Results

1679 13.1 Fit model and results

1680 The unblinded fit results for the analysis are presented in this section for the single lepton, dilepton and
 1681 inclusive combined channels. The best μ is presented along with post-fit plots and yields as well as
 1682 nuisance parameter rankings relative to μ . In the case of the single lepton channel the $W\gamma$ background is
 1683 an extra floating parameter in the fit.

1684 13.1.1 μ , best-fit

1685 Figure 90 shows the observed $t\bar{t}\gamma$ signal strength with the total uncertainty. The total uncertainty is further
 1686 split into a statistical and systematic contribution. μ is shown for each channel, for single lepton and
 1687 dilepton and for a 5 channel inclusive fit. The vertical dotted line represents the standard model prediction
 1688 of 1. The shaded region represents the theoretical uncertainty.

1689 The observed best fit value for the single lepton channel is $\mu_{t\bar{t}\gamma}^{\text{SL}} = 1.067^{+0.091}_{-0.087}(\text{sys.})^{+0.019}_{-0.019}(\text{stat.})$ while the
 1690 observed best fit value for the dilepton channel is $\mu_{t\bar{t}\gamma}^{\text{DL}} = 1.097^{+0.067}_{-0.059}(\text{sys.})^{+0.042}_{-0.041}(\text{stat.})$. The observed 5
 1691 channel inclusive fit has a best fit value of $\mu_{t\bar{t}\gamma}^{\text{Incl.}} = 1.070^{+0.062}_{-0.059}(\text{sys.})^{+0.017}_{-0.017}(\text{stat.})$. All measurements agree
 1692 with theory within uncertainties.

1693 In the case of the single lepton channel, $W\gamma$ SF = 0.805 ± 0.336 (tot.), while for the inclusive combined
 1694 fit $W\gamma$ SF = 0.824 ± 0.268 (tot.).

1695 13.1.2 Post-fit plots and yields

1696 Figure 91 show the post-fit distributions for the single lepton channels while Figure 92 shows post-fit
 1697 distributions for the dilepton channels. Individual channel distributions can be seen in Appendix K.1.

1698 The ELD is used as the discriminating variable in the maximum likelihood fit. Larger uncertainty bands
 1699 can especially be seen in the first bin of the dilepton ELD distribution. This is due to larger SHERPA weights
 1700 and is explained in more detail in Appendix O.

1701 Final yields are shown in Table 25.

1702 13.1.3 Nuisance parameters

1703 The relative uncertainties in relation to the best μ for combined single lepton and dilepton are shown
 1704 in Table 26. The greatest contribution comes from jet objects, which can be further broken down into
 1705 individual subcategories. This is shown in Table 27. The PPT shape systematic uncertainties can be
 1706 broken down into their separate contributions, as is shown in Table 28.

1707 The total contributions relative to μ are also summarised in Figure 93. The JES contribution includes *Jet*
 1708 *flavour composition*, *Jet flavour response*, *Jet eta intercalibration*, *Jet pileup* (with the largest contribution
 1709 coming from *RhoTopology*), *Jet effective NP*, *Jet single particle HightPt*, *Jet Punchthrough MC15* and *Jet*
 1710 *BJES response*.

Not reviewed, for internal circulation only

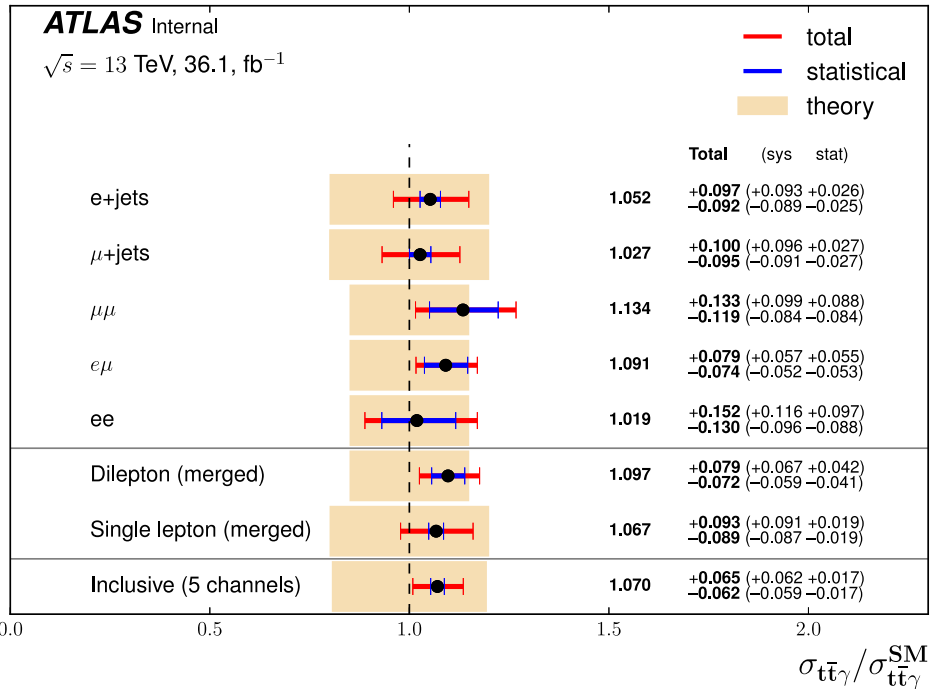


Figure 90: The observed signal strength for individual as well as combined channels. The standard model prediction of 1 is represented by the vertical line. The theoretical uncertainty for each fit is represented by the shaded region.

	single lepton	dilepton
$t\bar{t}\gamma$	7028 ± 410	790 ± 40
hadronic fake	1395 ± 280	49 ± 16
$e \rightarrow \gamma$ fake	1624 ± 200	2 ± 1
Lep fake	196 ± 69	-
$W\gamma$	906 ± 380	-
$Z\gamma$	-	47 ± 26
Other prompt	553 ± 180	18 ± 7
Total	11701 ± 180	905 ± 38
Data	11662	902

Table 25: Post-fit yields for each background for the single lepton and dilepton channels. All uncertainties are included.

1711 Individual channel nuisance parameters can be seen in Appendix K.1.

1712 Ranking plots with finer granularity showing the largest 20 contributions for single lepton and dilepton
 1713 channels are shown in Figures 94 with the corresponding full nuisance parameter pull plots shown
 1714 in Figure 95. The dilepton channel pull plot shows a heavily constrained $Z\gamma$ modelling systematic
 1715 uncertainty. This is due to larger generator weights as explored in Appendix O.

1716 Finally, Figure 96 and 97 show the correlations between the nuisance parameters and the signal strength,
 1717 μ , for given thresholds above 15%.

Not reviewed, for internal circulation only

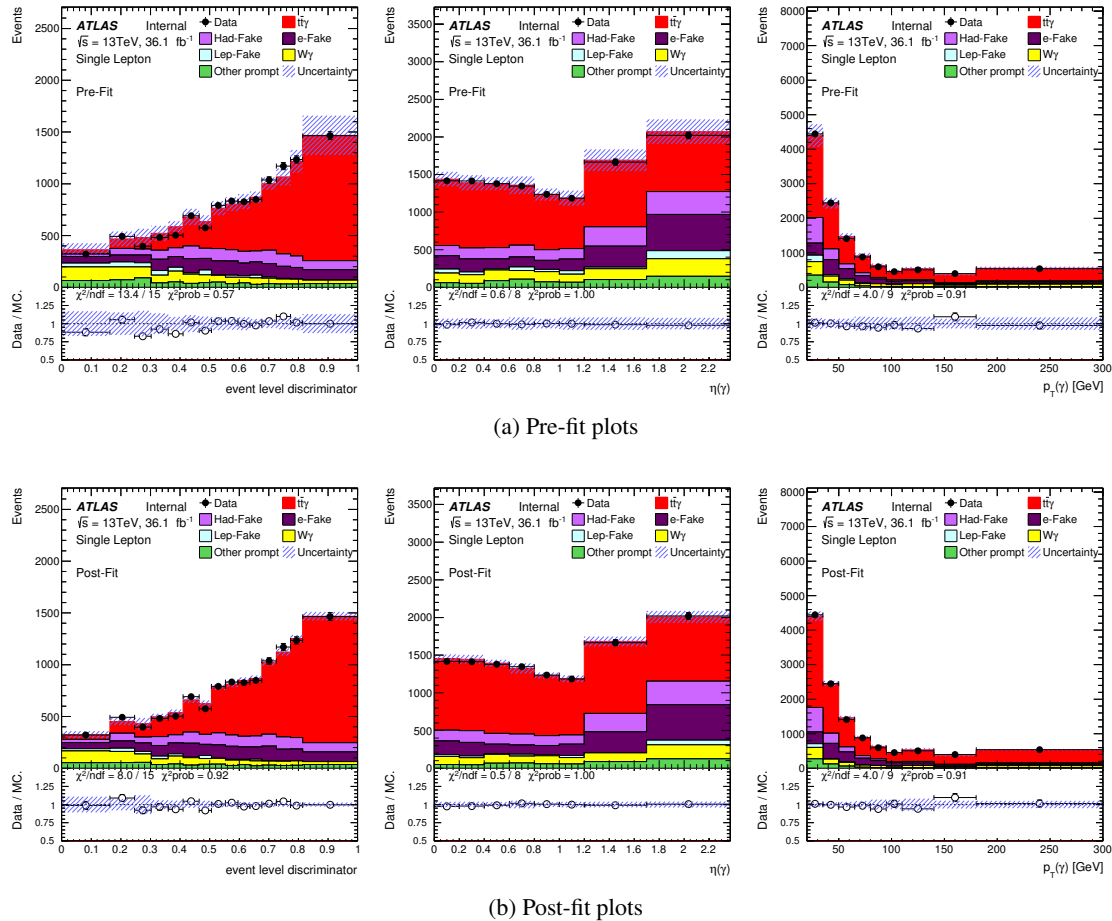


Figure 91: Pre- and post-fit plots for the single lepton channel where the ELD is used as the discriminating variable in the fit.

1718 13.2 Fiducial cross section

1719 From the theoretical calculations from Chapter 12 and the results in Section 13.1, we obtain $\sigma_{\text{fid}}^{\text{SL}} =$
 1720 $528.30^{+44.90}_{-43.11}(\text{sys.})^{+9.23}_{-9.20}(\text{stat.}) \text{ fb}$ and $\sigma_{\text{fid}}^{\text{DL}} = 69.30^{+4.24}_{-3.71}(\text{sys.})^{+2.65}_{-2.59}(\text{stat.}) \text{ fb}$ for the single lepton and
 1721 dilepton channels, respectively, and $\sigma_{\text{fid}}^{\text{Incl.}} = 597.53^{+34.88}_{-33.09}(\text{sys.})^{+9.67}_{-9.45}(\text{stat.}) \text{ fb}$ for the combined inclusive
 1722 fit to all channels. The cross sections are summarised in Table 29. All measurements agree with theoretical
 1723 predictions within uncertainty.

Not reviewed, for internal circulation only

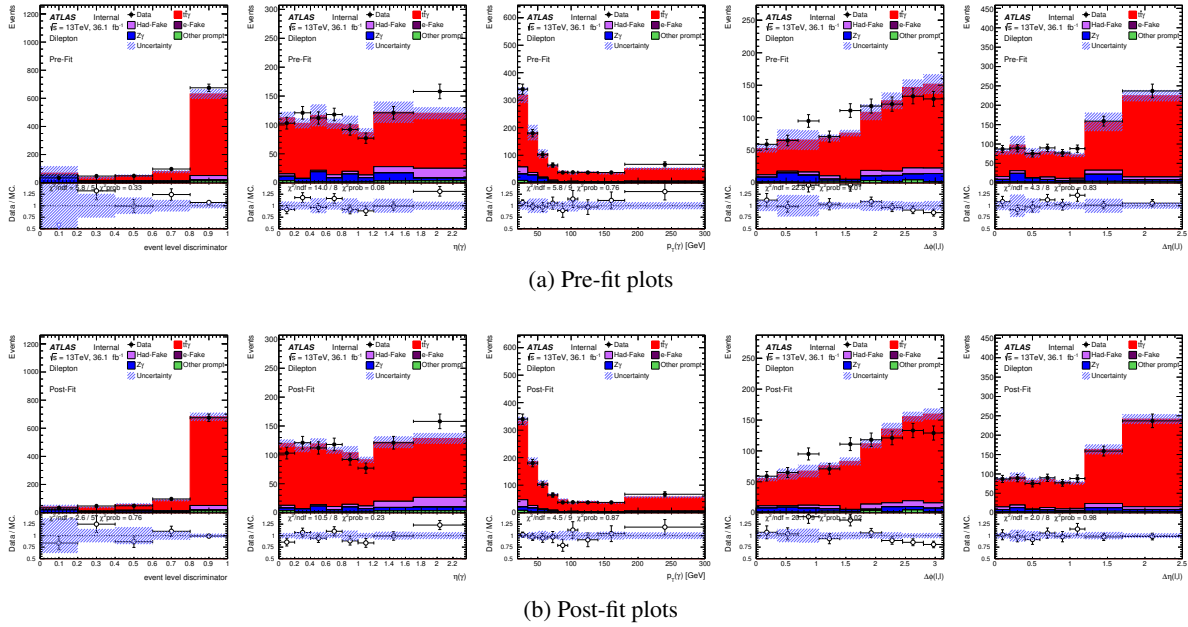


Figure 92: Pre- and post-fit plots for the dilepton channel where the ELD is used as the discriminating variable in the fit.

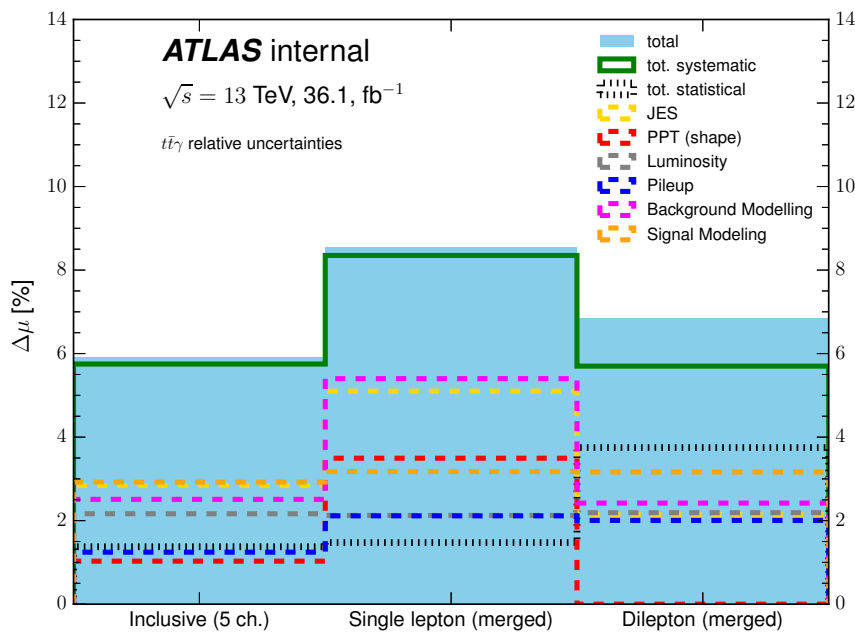


Figure 93: Select grouped uncertainties for the single lepton and dilepton channels relative to the signal strength.

	Inclusive		Single lepton		Dilepton	
	+ [%]	- [%]	+ [%]	- [%]	+ [%]	- [%]
Signal Modelling	3.03	2.82	3.29	3.06	3.28	3.05
Jets	3.02	2.66	5.40	4.80	2.64	2.58
Background modelling	2.54	2.48	5.40	5.40	2.38	2.46
Luminosity	2.28	2.05	2.26	1.99	2.31	2.07
Template Statistics	1.55	1.41	2.17	1.98	1.71	1.60
Pileup	1.32	1.17	2.18	2.05	2.19	1.82
Photon Efficiencies	1.07	0.96	1.04	0.94	1.08	0.97
Leptons	1.01	0.94	0.16	0.19	1.35	1.30
Prompt photon tagger (shape)	1.00	1.06	3.39	3.60	-	-
b-Tagging	0.15	0.15	0.85	0.97	0.23	0.27
E γ	0.08	0.10	0.02	0.04	0.20	0.23
Total systematic	5.9	5.6	8.5	8.2	5.9	5.5
Total statistical	1.4	1.4	1.5	1.5	3.8	3.7
Total	6.1	5.7	8.7	8.4	7.0	6.7

Table 26: Relative difference to μ due to the up and down variation of the systematic sources for single lepton and dilepton channels.

	Inclusive		Single lepton		Dilepton	
	+ [%]	- [%]	+ [%]	- [%]	+ [%]	- [%]
Jet Pileup (RhoTopology)	2.24	2.02	3.8	3.47	1.79	1.70
Jet Effective NP	1.67	1.42	2.89	2.46	1.15	1.05
Jet Flavour Composition	0.36	0.32	0.93	0.94	0.16	0.20
Jet Flavour Response	0.31	0.26	1.81	1.59	0.40	0.45
Jet EtaInterCalibration	0.29	0.23	1.08	0.96	0.43	0.54

Table 27: Breakdown of the larger jet systematic components for single lepton and dilepton channels showing the total contribution to the relative difference in μ .

	Single lepton	
	+ [%]	- [%]
Prompt sources	2.36	2.47
Efake sources	1.57	1.66
Hfake sources	0.56	0.62
Hfake isolation	0.19	0.27

Table 28: Breakdown of the PPT shape systematics for single lepton channel showing the total contribution to the relative difference in μ .

	σ_{fid} [fb]	Systematic uncertainty		Statistical uncertainty	
		+ [fb]	- [fb]	+ [fb]	- [fb]
e+jets	260.06	23.02	21.91	6.34	6.29
μ +jets	254.62	23.79	22.68	6.68	6.62
$\mu\mu$	18.07	1.58	1.34	1.40	1.34
$e\mu$	34.23	1.79	1.63	1.73	1.67
ee	16.18	1.84	1.53	1.55	1.39
single lepton	528.30	44.90	43.11	9.23	9.20
dilepton	69.30	4.24	3.71	2.65	2.59
Inclusive (5 channels)	597.53	34.88	33.09	9.67	9.45

Table 29: Fiducial cross section summary for all channels.

Not reviewed, for internal circulation only

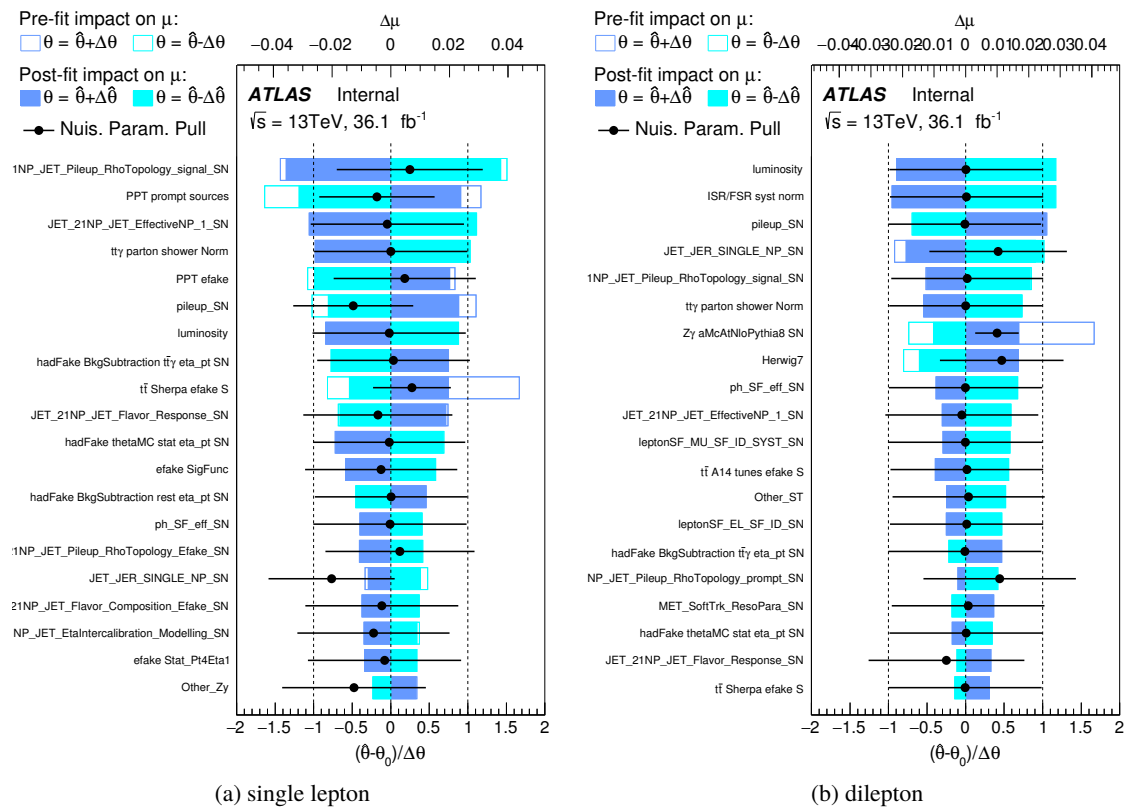


Figure 94: Systematic uncertainty ranking plots for the largest 20 contributions in the single lepton and dilepton channels.

Not reviewed, for internal circulation only

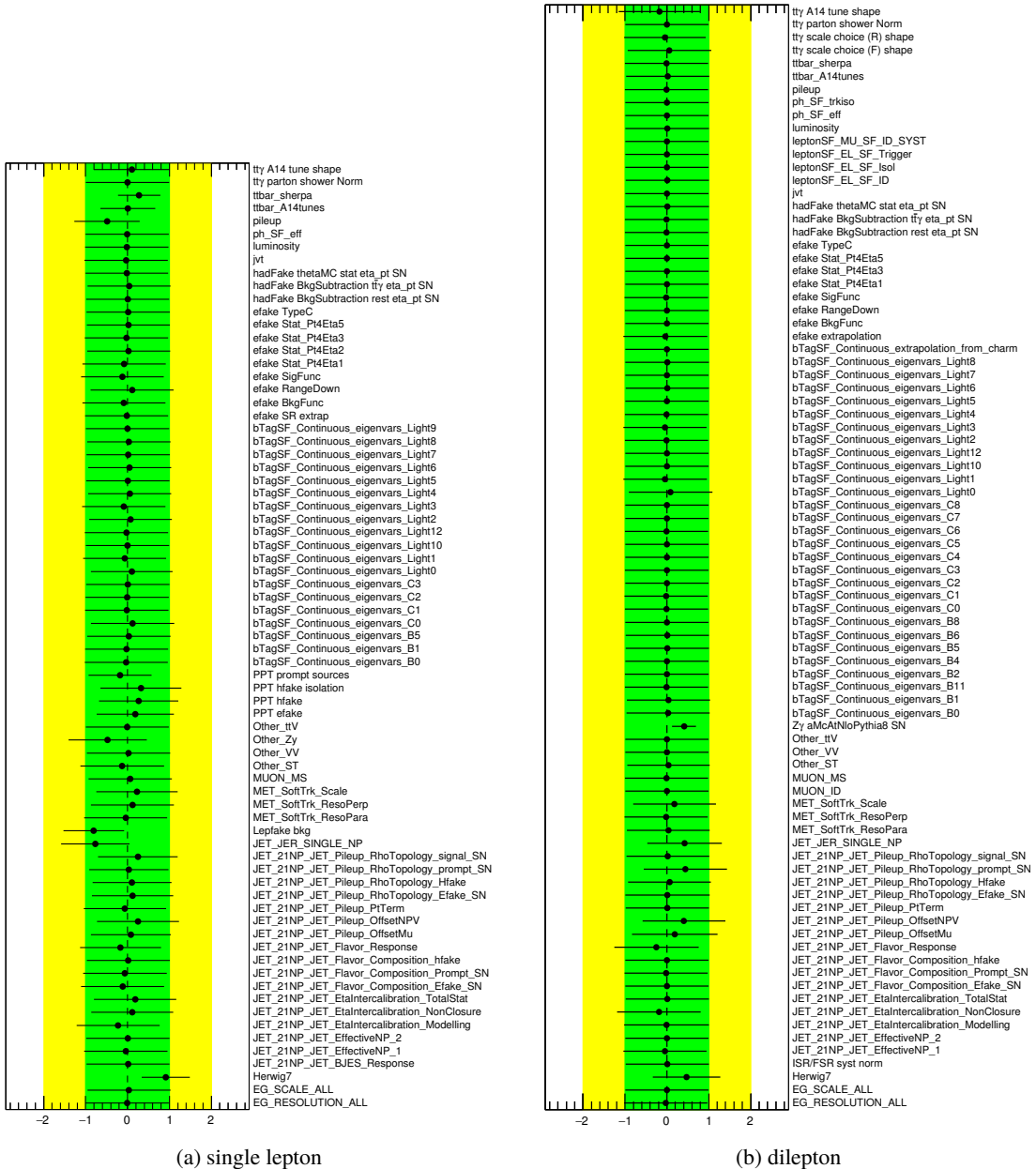


Figure 95: Pull plots for all nuisance parameters in the single lepton and dilepton channels after a 0.7% pruning has been applied.

Not reviewed, for internal circulation only

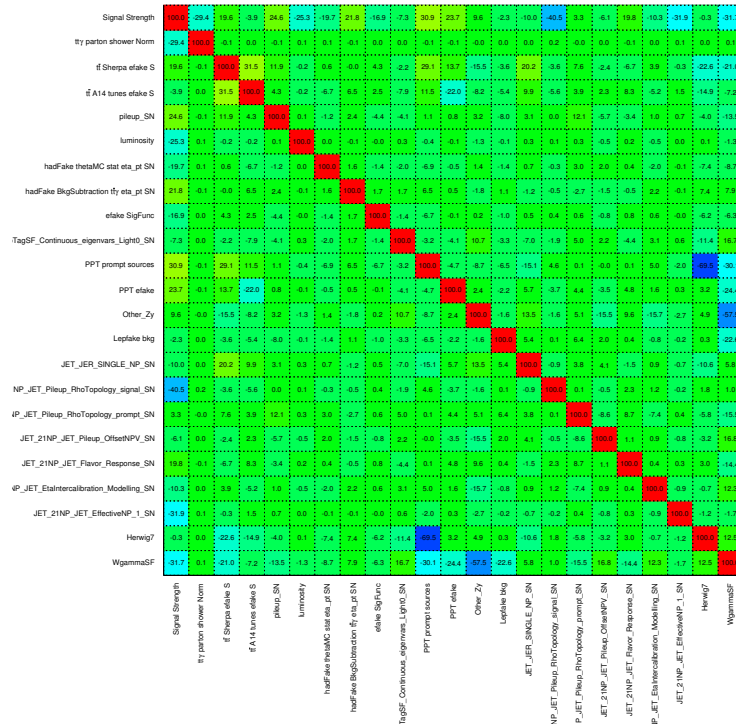


Figure 96: Correlation matrix plot for the single lepton channel showing the correlation between each nuisance parameter and the signal strength for values greater than 15%.

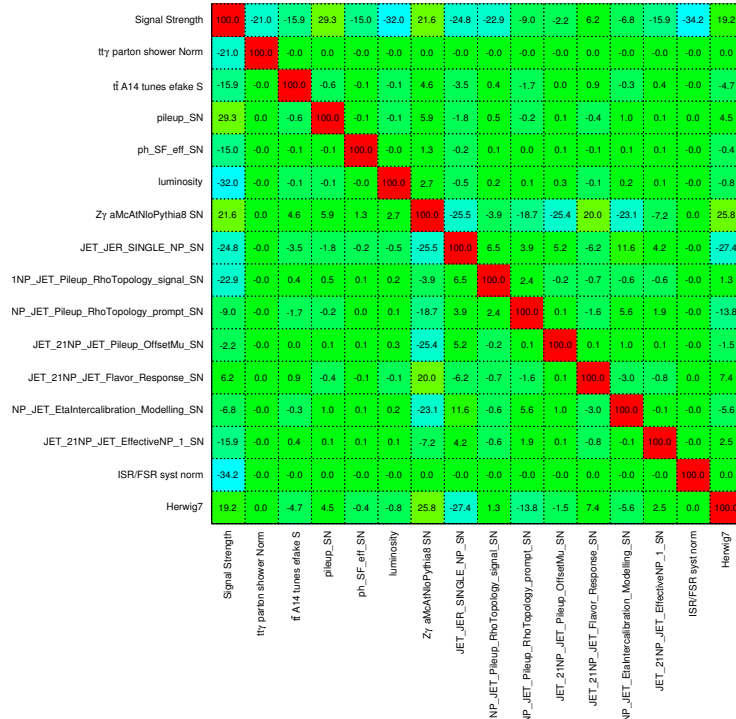


Figure 97: Correlation matrix plot for the dilepton channel showing the correlation between each nuisance parameter and the signal strength for values greater than 15%.

1724 13.3 Differential cross section

1725 The measured differential cross sections are shown in Figure 98 and Figure 99 in the single-lepton and
 1726 dilepton channels, respectively. The results are obtained by unfolding the measured signal distribution
 1727 employing the iterative Bayesian method, where three iterations are used. The unfolded results are then
 1728 compared to the particle-level distribution obtained from the nominal MC signal sample. Data to MC
 1729 agreement is observed, similarly as in the fiducial measurement. The impact of the statistical uncertainty
 1730 on the measured cross section is dominant. However, the systematic uncertainty has also a sizeable
 1731 impact. The leading ones in the single-lepton channel are due to the background modelling and the
 1732 jet identification and reconstruction. The dominant uncertainties In the dilepton channel are due to the
 1733 background modelling, pile-up scale factor and the signal modelling which gets large in some bins due to
 1734 the particular choice of the generator for parton showering.

1735 The effect of all systematics on the differential cross section are shown in Tables 30, 31, 32 in the
 1736 single-lepton channel and Tables 33, 34, 35, 36 and 37 in the dilepton channel.

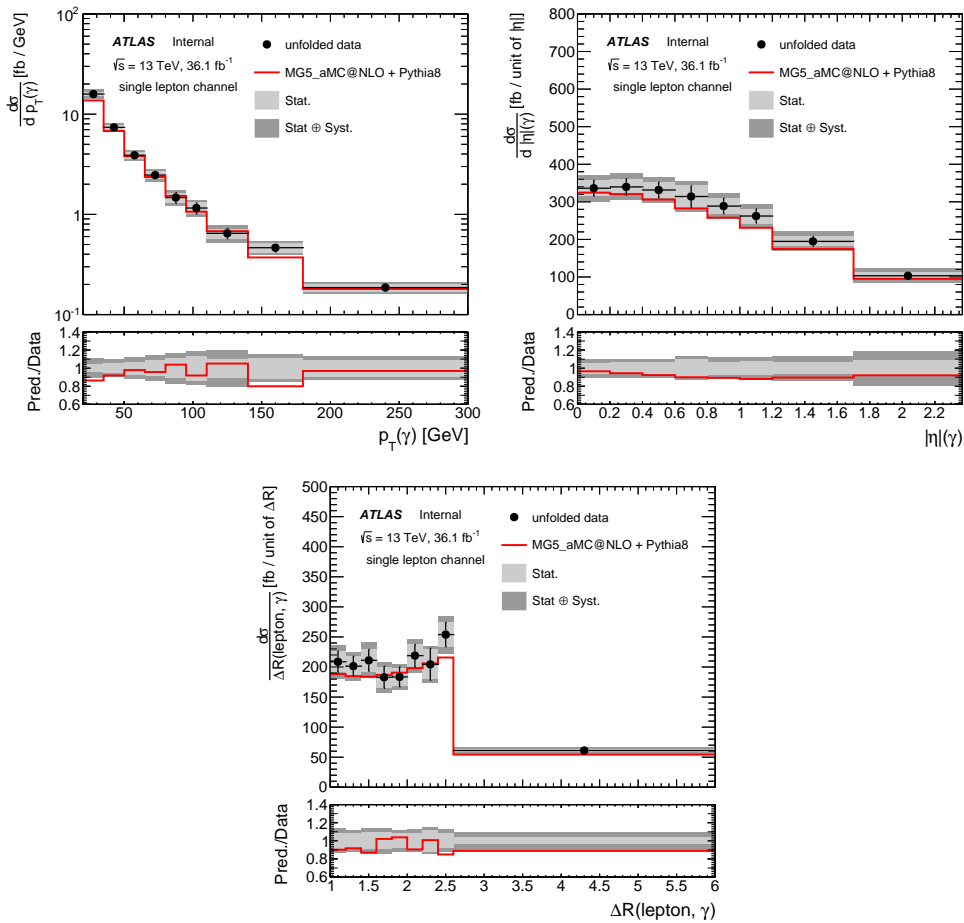


Figure 98: The differential cross section in p_T bins (top-left), $|\eta|$ bins (top-right) and min $\Delta R(\text{lepton}, \gamma)$ (bottom), in the single-lepton channel. The unfolded distribution (dots) is compared to the particle level distribution (red line).

Not reviewed, for internal circulation only

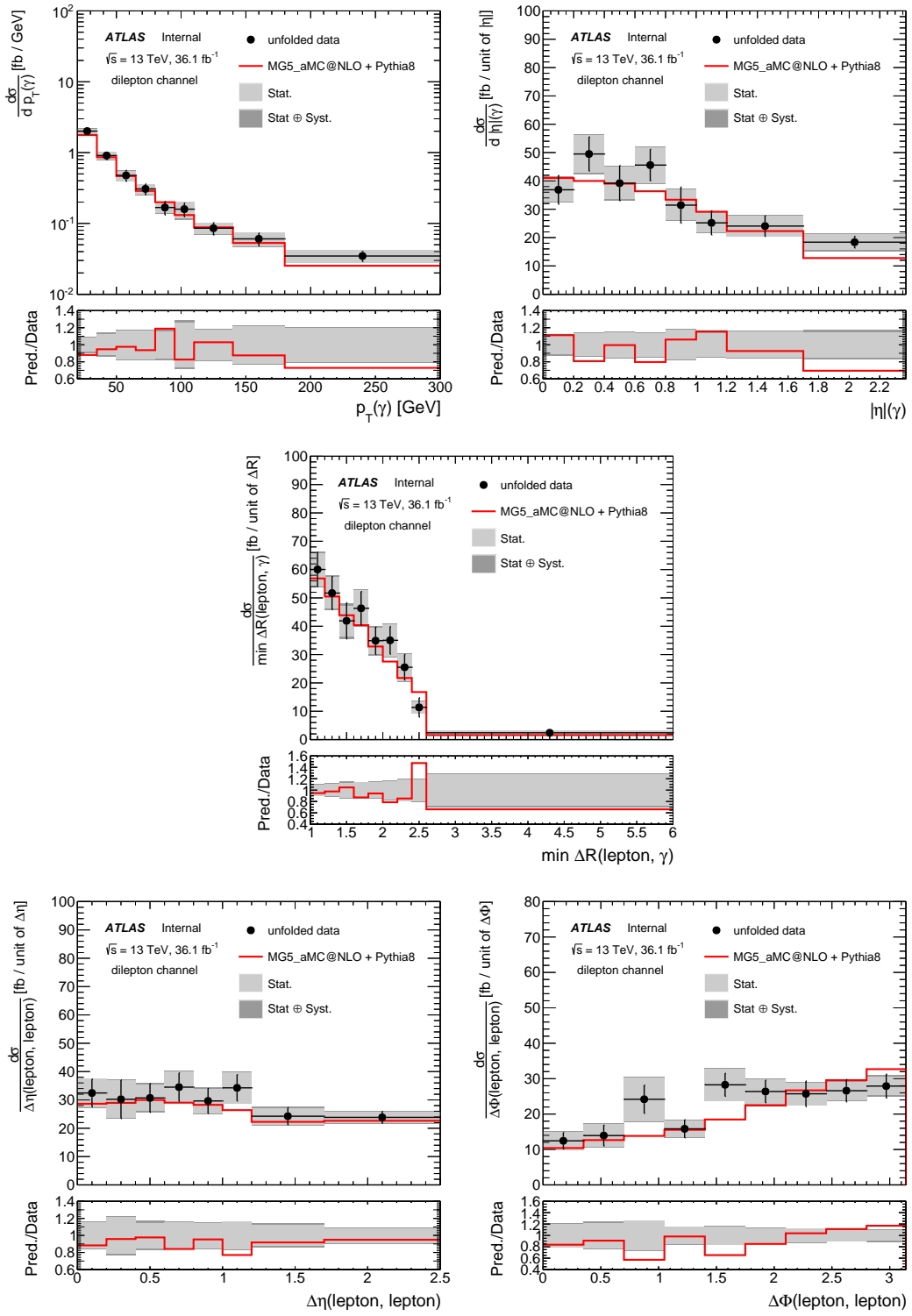


Figure 99: The differential cross section in p_T bins (top-left), $|\eta|$ bins (top-right), minimum $\Delta R(\text{lepton}, \gamma)$ (centre), $\Delta\eta(\text{lepton}, \text{lepton})$, and $\Delta\phi(\text{lepton}, \text{lepton})$ in the dilepton channel. The unfolded distribution (dots) is compared to the particle level distribution (red line).

Table 30: Summary of the sources of uncertainty on the absolute differential cross section for $p_T(\gamma)$ at particle level, presented as a percentage of the measured cross section in each bin in the single lepton channel. Entries of 0.0 are uncertainties that are less than 0.005 in magnitude. Any asymmetric systematic uncertainties have been symmetrised.

$p_T(\gamma)$ [Gev]	20.0 - 35.0	35.0 - 50.0	50.0 - 65.0	65.0 - 80.0	80.0 - 95.0	95.0 - 110.0	110.0 - 140.0	140.0 - 180.0	180.0 - 300.0
Source	systematic uncertainty (%)								
Signal Scale Variation	±0.0	±0.0	±0.0	±0.0	±0.0	±0.0	±0.0	±0.0	±0.0
Signal ISR/FSR Setting	±0.25	±0.88	±0.26	±0.76	±1.04	±1.25	±1.35	±2.33	±0.25
Signal Parton Showering	±1.72	±0.11	±0.73	±0.8	±0.89	±3.4	±1.33	±1.23	±4.08
Background Modelling	±7.81	±6.03	±7.01	±9.88	±11.63	±11.51	±16.39	±8.6	±7.28
Luminosity	±2.09	±2.09	±2.09	±2.09	±2.09	±2.09	±2.09	±2.09	±2.09
Pileup Effects	±1.39	±1.05	±0.94	±1.36	±0.53	±0.99	±1.08	±0.99	±0.67
Photon Scale Factors	±1.27	±0.9	±0.71	±0.48	±0.46	±0.51	±0.59	±1.25	±1.47
Lepton Identification and Reconstruction	±0.0	±0.0	±0.01	±0.01	±0.0	±0.0	±0.0	±0.0	±0.0
E/Gamma Resolution and Scale	±0.15	±0.2	±0.22	±0.27	±0.47	±0.77	±0.97	±1.01	±1.0
Jet Identification and Reconstruction	±5.36	±4.96	±5.08	±4.67	±4.6	±4.45	±4.2	±3.63	±3.15
b -tagging	±0.51	±0.54	±0.55	±0.55	±0.51	±0.42	±0.43	±0.47	±0.44
Missing Transverse Momentum Reconstruction	±0.0	±0.0	±0.0	±0.0	±0.0	±0.0	±0.0	±0.0	±0.0
PPT	±0.96	±0.28	±2.59	±0.39	±3.76	±1.1	±0.84	±1.32	±1.88
Total systematics	±10	±8	±9	±11	±13	±13	±17	±10	±10
Data statistics	±4	±5	±7	±9	±11	±13	±10	±11	±9
Total uncertainty	±11	±10	±12	±14	±17	±19	±20	±15	±13

Table 31: Summary of the sources of uncertainty on the absolute differential cross section for $|\eta|(\gamma)$ at particle level, presented as a percentage of the measured cross section in each bin in the single lepton channel. Entries of 0.0 are uncertainties that are less than 0.005 in magnitude. Any asymmetric systematic uncertainties have been symmetrised.

$ \eta (\gamma)$	0.0 - 0.2	0.2 - 0.4	0.4 - 0.6	0.6 - 0.8	0.8 - 1.0	1.0 - 1.2	1.2 - 1.7	1.7 - 2.37
Source	systematic uncertainty (%)							
Signal Scale Variation	±0.0	±0.0	±0.0	±0.0	±0.0	±0.0	±0.0	±0.0
Signal ISR/FSR Setting	±0.25	±0.48	±0.57	±0.73	±0.87	±0.75	±0.13	±0.17
Signal Parton Showering	±0.51	±0.18	±0.44	±0.17	±0.11	±1.94	±0.35	±1.67
Background Modelling	±6.64	±6.41	±6.02	±6.2	±7.07	±7.35	±8.89	±15.73
Luminosity	±2.09	±2.09	±2.09	±2.09	±2.09	±2.09	±2.09	±2.09
Pileup Effects	±0.93	±1.76	±1.32	±0.34	±1.14	±0.56	±1.92	±0.83
Photon Scale Factors	±0.63	±0.65	±0.65	±1.12	±1.07	±1.08	±1.23	±1.45
Lepton Identification and Reconstruction	±0.01	±0.0	±0.0	±0.0	±0.01	±0.02	±0.02	±0.01
E/Gamma Resolution and Scale	±0.06	±0.14	±0.24	±0.36	±0.45	±0.5	±0.5	±0.5
Jet Identification and Reconstruction	±4.6	±4.55	±4.87	±4.72	±5.06	±4.85	±5.03	±5.33
b -tagging	±0.52	±0.55	±0.44	±0.51	±0.53	±0.57	±0.46	±0.51
Missing Transverse Momentum Reconstruction	±0.0	±0.0	±0.0	±0.0	±0.0	±0.0	±0.0	±0.0
PPT	±0.23	±0.51	±0.55	±2.65	±0.4	±0.5	±4.42	±1.36
Total systematics	±8	±8	±8	±9	±9	±9	±12	±17
Data statistics	±6	±6	±6	±9	±7	±7	±6	±9
Total uncertainty	±10	±10	±10	±13	±12	±12	±13	±19

Table 32: Summary of the sources of uncertainty on the absolute differential cross section for $\min \Delta R(\text{lepton}, \gamma)$ at particle level, presented as a percentage of the measured cross section in each bin in the single lepton channel. Entries of 0.0 are uncertainties that are less than 0.005 in magnitude. Any asymmetric systematic uncertainties have been symmetrised.

$\min \Delta R(\text{lepton}, \gamma)$	1.0 - 1.2	1.2 - 1.4	1.4 - 1.6	1.6 - 1.8	1.8 - 2.0	2.0 - 2.2	2.2 - 2.4	2.4 - 2.6	2.6 - 6.0
Source	systematic uncertainty (%)								
Signal Scale Variation	±0.0	±0.0	±0.0	±0.0	±0.0	±0.0	±0.0	±0.0	±0.0
Signal ISR/FSR Setting	±0.6	±0.73	±1.53	±0.47	±0.1	±0.17	±0.7	±0.77	±0.13
Signal Parton Showering	±1.15	±0.79	±0.05	±1.59	±0.22	±0.17	±0.4	±2.56	±0.24
Background Modelling	±9.01	±6.21	±9.13	±8.98	±6.64	±7.81	±6.75	±6.53	±6.82
Luminosity	±2.09	±2.09	±2.09	±2.09	±2.09	±2.09	±2.09	±2.09	±2.09
Pileup Effects	±1.15	±0.95	±1.39	±1.44	±2.04	±1.54	±0.67	±1.4	±0.81
Photon Scale Factors	±0.96	±0.98	±0.97	±0.97	±0.96	±0.95	±0.97	±0.96	±0.99
Lepton Identification and Reconstruction	±0.04	±0.03	±0.02	±0.02	±0.01	±0.0	±0.0	±0.0	±0.01
E/Gamma Resolution and Scale	±0.31	±0.31	±0.31	±0.31	±0.31	±0.35	±0.35	±0.35	±0.35
Jet Identification and Reconstruction	±4.61	±4.35	±4.52	±4.33	±4.52	±4.54	±4.75	±5.26	±5.3
b -tagging	±0.67	±0.48	±0.56	±0.55	±0.49	±0.48	±0.5	±0.54	±0.49
Missing Transverse Momentum Reconstruction	±0.0	±0.0	±0.0	±0.0	±0.0	±0.0	±0.0	±0.0	±0.0
PPT	±0.3	±0.33	±0.11	±0.25	±0.37	±0.03	±0.22	±0.17	±0.0
Total systematics	±11	±8	±11	±10	±9	±9	±9	±9	±9
Data statistics	±8	±8	±9	±9	±8	±8	±12	±8	±4
Total uncertainty	±13	±12	±14	±14	±12	±13	±15	±12	±10

Table 33: Summary of the sources of uncertainty on the absolute differential cross section for $p_T(\gamma)$ at particle level, presented as a percentage of the measured cross section in each bin in the dilepton channel. Entries of 0.0 are uncertainties that are less than 0.005 in magnitude. Any asymmetric systematic uncertainties have been symmetrised.

$p_T(\gamma)$ [Gev]	20.0 - 35.0	35.0 - 50.0	50.0 - 65.0	65.0 - 80.0	80.0 - 95.0	95.0 - 110.0	110.0 - 140.0	140.0 - 180.0	180.0 - 300.0
Source	systematic uncertainty (%)								
Signal Scale Variation	±0.75	±0.33	±0.11	±0.16	±0.29	±0.81	±1.14	±1.56	±2.72
Signal ISR/FSR Setting	±0.71	±3.66	±3.7	±2.06	±5.08	±2.5	±3.52	±4.21	±0.0
Signal Parton Showering	±0.72	±1.6	±0.39	±1.02	±5.64	±10.99	±0.37	±3.18	±2.79
Background Modelling	±2.81	±4.15	±3.24	±2.63	±3.52	±2.39	±1.33	±1.55	±2.09
Luminosity	±2.09	±2.09	±2.09	±2.09	±2.09	±2.09	±2.09	±2.09	±2.09
Pileup Effects	±2.47	±1.08	±0.6	±2.8	±1.42	±3.78	±2.67	±2.51	±0.95
Photon Scale Factors	±1.27	±1.03	±0.84	±0.68	±0.67	±0.64	±0.72	±1.26	±1.45
Lepton Identification and Reconstruction	±1.09	±1.09	±1.1	±1.09	±1.15	±1.16	±1.17	±1.12	±1.27
E/Gamma Resolution and Scale	±0.31	±0.44	±0.5	±0.5	±0.49	±0.47	±0.47	±0.47	±0.47
Jet Identification and Reconstruction	±2.01	±2.04	±2.33	±1.94	±1.17	±1.4	±1.39	±1.17	±0.84
<i>b</i> -tagging	±0.77	±0.9	±0.76	±0.94	±0.97	±1.25	±0.96	±0.74	±0.65
Missing Transverse Momentum Reconstruction	±0.04	±0.24	±0.2	±0.25	±0.25	±0.36	±0.37	±0.39	±0.38
Total systematics	±5	±7	±6	±6	±9	±13	±6	±7	±5
Data statistics	±8	±12	±17	±17	±16	±26	±18	±22	±20
Total uncertainty	±9	±14	±18	±18	±18	±29	±19	±23	±21

Table 34: Summary of the sources of uncertainty on the absolute differential cross section for $|\eta|(\gamma)$ at particle level, presented as a percentage of the measured cross section in each bin in the dilepton channel. Entries of 0.0 are uncertainties that are less than 0.005 in magnitude. Any asymmetric systematic uncertainties have been symmetrised.

$ \eta (\gamma)$	0.0 - 0.2	0.2 - 0.4	0.4 - 0.6	0.6 - 0.8	0.8 - 1.0	1.0 - 1.2	1.2 - 1.7	1.7 - 2.37
Source	systematic uncertainty (%)							
Signal Scale Variation	±0.01	±0.09	±0.12	±0.04	±0.17	±0.05	±0.09	±0.33
Signal ISR/FSR Setting	±0.76	±0.74	±0.71	±0.17	±2.11	±2.74	±1.14	±0.16
Signal Parton Showering	±1.02	±4.03	±0.22	±0.53	±3.15	±1.96	±1.62	±4.86
Background Modelling	±2.44	±0.86	±3.92	±2.08	±2.26	±2.0	±3.55	±5.77
Luminosity	±2.09	±2.09	±2.09	±2.09	±2.09	±2.09	±2.09	±2.09
Pileup Effects	±3.22	±0.84	±1.28	±2.19	±0.43	±1.0	±0.9	±2.16
Photon Scale Factors	±0.72	±0.73	±0.73	±1.14	±1.14	±1.1	±1.31	±1.56
Lepton Identification and Reconstruction	±1.12	±1.11	±1.08	±1.1	±1.13	±1.11	±1.12	±1.16
E/Gamma Resolution and Scale	±0.13	±0.15	±0.2	±0.33	±0.5	±0.63	±0.68	±0.7
Jet Identification and Reconstruction	±1.84	±1.6	±2.08	±1.56	±1.61	±2.48	±1.89	±1.66
<i>b</i> -tagging	±0.79	±0.87	±0.77	±0.93	±0.81	±0.81	±0.83	±0.76
Missing Transverse Momentum Reconstruction	±0.08	±0.13	±0.12	±0.25	±0.13	±0.29	±0.32	±0.34
Total systematics	±5	±5	±5	±4	±5	±6	±5	±9
Data statistics	±11	±13	±14	±14	±17	±13	±15	±15
Total uncertainty	±12	±14	±15	±14	±18	±14	±16	±17

Table 35: Summary of the sources of uncertainty on the absolute differential cross section for $\min \Delta R(\text{lepton}, \gamma)$ at particle level, presented as a percentage of the measured cross section in each bin in the dilepton channel. Entries of 0.0 are uncertainties that are less than 0.005 in magnitude. Any asymmetric systematic uncertainties have been symmetrised.

$\min \Delta R(\text{lepton}, \gamma)$	1.0 - 1.2	1.2 - 1.4	1.4 - 1.6	1.6 - 1.8	1.8 - 2.0	2.0 - 2.2	2.2 - 2.4	2.4 - 2.6	2.6 - 6.0
Source	systematic uncertainty (%)								
Signal Scale Variation	±0.09	±0.12	±0.15	±0.06	±0.02	±0.24	±0.1	±0.5	±0.11
Signal ISR/FSR Setting	±0.7	±0.83	±0.24	±0.29	±1.74	±3.34	±1.96	±1.09	±2.6
Signal Parton Showering	±0.7	±3.26	±6.93	±2.06	±1.14	±2.0	±1.29	±4.21	±5.1
Background Modelling	±0.96	±1.22	±2.13	±1.05	±2.31	±2.71	±3.67	±4.55	±9.14
Luminosity	±2.09	±2.09	±2.09	±2.09	±2.09	±2.09	±2.09	±2.09	±2.09
Pileup Effects	±1.32	±0.57	±0.52	±1.4	±5.01	±1.71	±0.81	±0.71	±2.47
Photon Scale Factors	±1.03	±1.02	±1.03	±1.02	±1.04	±1.08	±1.06	±1.09	±1.15
Lepton Identification and Reconstruction	±1.11	±1.14	±1.15	±1.11	±1.1	±1.1	±1.11	±1.08	±1.1
E/Gamma Resolution and Scale	±0.43	±0.41	±0.4	±0.4	±0.4	±0.4	±0.4	±0.4	±0.4
Jet Identification and Reconstruction	±1.78	±1.56	±2.08	±1.43	±1.91	±2.25	±2.36	±2.27	±1.53
<i>b</i> -tagging	±0.81	±0.82	±0.9	±0.92	±0.81	±0.85	±0.78	±0.6	±0.78
Missing Transverse Momentum Reconstruction	±0.22	±0.13	±0.1	±0.14	±0.19	±0.15	±0.23	±0.26	±0.25
Total systematics	±4	±5	±8	±4	±7	±6	±6	±7	±12
Data statistics	±10	±11	±13	±14	±13	±16	±19	±19	±27
Total uncertainty	±10	±12	±15	±14	±15	±17	±20	±20	±30

Table 36: Summary of the sources of uncertainty on the absolute differential cross section for $\Delta\eta(\text{lepton, lepton})$ at particle level, presented as a percentage of the measured cross section in each bin in the dilepton channel. Entries of 0.0 are uncertainties that are less than 0.005 in magnitude. Any asymmetric systematic uncertainties have been symmetrised.

$\Delta\eta(\text{lepton, lepton})$	0.0 - 0.2	0.2 - 0.4	0.4 - 0.6	0.6 - 0.8	0.8 - 1.0	1.0 - 1.2	1.2 - 1.7	1.7 - 2.5
Source	systematic uncertainty (%)							
Signal Scale Variation	± 0.81	± 1.05	± 0.7	± 0.65	± 0.59	± 0.19	± 0.17	± 1.13
Signal ISR/FSR Setting	± 0.68	± 0.41	± 0.32	± 1.5	± 0.97	± 0.71	± 0.1	± 0.49
Signal Parton Showering	± 1.16	± 2.45	± 6.3	± 1.24	± 4.17	± 0.62	± 4.13	± 2.92
Background Modelling	± 2.89	± 5.22	± 2.93	± 2.41	± 2.03	± 2.32	± 3.96	± 0.81
Luminosity	± 2.09	± 2.09	± 2.09	± 2.09	± 2.09	± 2.09	± 2.09	± 2.09
Pileup Effects	± 0.45	± 1.71	± 2.62	± 1.96	± 1.77	± 1.18	± 2.36	± 0.9
Photon Scale Factors	± 1.06	± 1.06	± 1.06	± 1.04	± 1.09	± 1.08	± 1.04	± 1.01
Lepton Identification and Reconstruction	± 1.09	± 1.09	± 1.1	± 1.12	± 1.1	± 1.12	± 1.1	± 1.15
E/Gamma Resolution and Scale	± 0.38	± 0.39	± 0.4	± 0.42	± 0.43	± 0.42	± 0.41	± 0.41
Jet Identification and Reconstruction	± 2.17	± 3.04	± 2.33	± 1.43	± 1.35	± 1.19	± 1.75	± 1.84
b -tagging	± 0.76	± 0.96	± 0.83	± 0.61	± 0.82	± 0.65	± 0.85	± 0.85
Missing Transverse Momentum Reconstruction	± 0.21	± 0.19	± 0.18	± 0.2	± 0.14	± 0.11	± 0.14	± 0.22
Total systematics	± 5	± 7	± 8	± 5	± 6	± 4	± 7	± 5
Data statistics	± 15	± 22	± 15	± 16	± 14	± 16	± 12	± 8
Total uncertainty	± 16	± 23	± 17	± 16	± 16	± 17	± 14	± 10

Table 37: Summary of the sources of uncertainty on the absolute differential cross section for $\Delta\phi(\text{lepton, lepton})$ at particle level, presented as a percentage of the measured cross section in each bin in the dilepton channel. Entries of 0.0 are uncertainties that are less than 0.005 in magnitude. Any asymmetric systematic uncertainties have been symmetrised.

$\Delta\phi(\text{lepton, lepton})$	0.0 - 0.35	0.35 - 0.7	0.7 - 1.05	1.05 - 1.4	1.4 - 1.75	1.75 - 2.1	2.1 - 2.45	2.45 - 2.8	2.8 - 3.14
Source	systematic uncertainty (%)								
Signal Scale Variation	± 0.89	± 0.65	± 0.45	± 0.46	± 0.2	± 0.07	± 0.25	± 0.37	± 0.42
Signal ISR/FSR Setting	± 0.34	± 2.17	± 0.49	± 2.51	± 0.75	± 2.35	± 0.26	± 1.26	± 2.09
Signal Parton Showering	± 1.3	± 7.36	± 4.5	± 2.31	± 1.52	± 0.72	± 0.69	± 0.34	± 1.48
Background Modelling	± 2.33	± 6.04	± 4.49	± 3.85	± 1.02	± 2.62	± 1.41	± 2.59	± 2.49
Luminosity	± 2.09	± 2.09	± 2.09	± 2.09	± 2.09	± 2.09	± 2.09	± 2.09	± 2.09
Pileup Effects	± 2.58	± 1.39	± 1.67	± 2.69	± 0.54	± 1.52	± 1.81	± 0.52	± 2.61
Photon Scale Factors	± 1.08	± 1.05	± 1.06	± 1.04	± 1.03	± 1.05	± 1.03	± 1.04	± 1.05
Lepton Identification and Reconstruction	± 1.07	± 1.01	± 1.02	± 1.04	± 1.08	± 1.08	± 1.13	± 1.18	± 1.24
E/Gamma Resolution and Scale	± 0.44	± 0.44	± 0.43	± 0.41	± 0.38	± 0.36	± 0.37	± 0.4	± 0.43
Jet Identification and Reconstruction	± 1.2	± 2.02	± 1.16	± 2.01	± 2.0	± 1.91	± 1.87	± 2.18	± 1.93
b -tagging	± 0.9	± 0.77	± 0.87	± 0.76	± 0.54	± 0.96	± 0.95	± 0.83	± 0.84
Missing Transverse Momentum Reconstruction	± 0.48	± 0.27	± 0.16	± 0.13	± 0.1	± 0.19	± 0.17	± 0.23	± 0.25
Total systematics	± 5	± 10	± 7	± 7	± 4	± 5	± 4	± 5	± 6
Data statistics	± 21	± 22	± 25	± 15	± 16	± 13	± 12	± 10	± 9
Total uncertainty	± 21	± 25	± 26	± 16	± 16	± 14	± 13	± 11	± 11

1737 **14 Conclusion**

[Not reviewed, for internal circulation only]

1738 References

- [1] U. Husemann, *Top-Quark Physics: Status and Prospects*, *Prog. Part. Nucl. Phys.* **95** (2017) 48, arXiv: [1704.01356 \[hep-ex\]](https://arxiv.org/abs/1704.01356).
- [2] U. Baur, A. Juste, L. H. Orr and D. Rainwater, *Probing electroweak top quark couplings at hadron colliders*, *Phys. Rev.* **D71** (2005) 054013, arXiv: [hep-ph/0412021 \[hep-ph\]](https://arxiv.org/abs/hep-ph/0412021).
- [3] A. O. Bouzas and F. Larios, *Electromagnetic dipole moments of the Top quark*, *Phys. Rev.* **D87** (2013) 074015, arXiv: [1212.6575 \[hep-ph\]](https://arxiv.org/abs/1212.6575).
- [4] R. Röntsch and M. Schulze, *Probing top-Z dipole moments at the LHC and ILC*, *JHEP* **08** (2015) 044, arXiv: [1501.05939 \[hep-ph\]](https://arxiv.org/abs/1501.05939).
- [5] M. Schulze and Y. Soreq, *Pinning down electroweak dipole operators of the top quark*, *Eur. Phys. J.* **C76** (2016) 466, arXiv: [1603.08911 \[hep-ph\]](https://arxiv.org/abs/1603.08911).
- [6] O. Bessidskaia Bylund, F. Maltoni, I. Tsirikos, E. Vryonidou and C. Zhang, *Probing top quark neutral couplings in the Standard Model Effective Field Theory at NLO in QCD*, *JHEP* **05** (2016) 052, arXiv: [1601.08193 \[hep-ph\]](https://arxiv.org/abs/1601.08193).
- [7] P.-F. Duan, Y. Zhang, Y. Wang, M. Song and G. Li, *Electroweak corrections to top quark pair production in association with a hard photon at hadron colliders*, *Phys. Lett.* **B766** (2017) 102, arXiv: [1612.00248 \[hep-ph\]](https://arxiv.org/abs/1612.00248).
- [8] T. Aaltonen et al., *Evidence for $t\bar{t}\gamma$ Production and Measurement of $\sigma_t\bar{t}\gamma/\sigma_t\bar{t}$* , *Phys. Rev.* **D84** (2011) 031104, arXiv: [1106.3970 \[hep-ex\]](https://arxiv.org/abs/1106.3970).
- [9] ATLAS Collaboration, *Measurement of the inclusive $t\bar{t}\gamma$ cross section at $\sqrt{s} = 7$ TeV with the ATLAS detector*, ATLAS-CONF-2011-153, 2011, URL: <https://cds.cern.ch/record/1398197>.
- [10] ATLAS Collaboration, *Observation of top-quark pair production in association with a photon and measurement of the $t\bar{t}\gamma$ production cross section in pp collisions at $\sqrt{s} = 7$ TeV using the ATLAS detector*, *Phys. Rev.* **D91** (2015) 072007, arXiv: [1502.00586 \[hep-ex\]](https://arxiv.org/abs/1502.00586).
- [11] *Measurement of the inclusive top-quark pair + photon production cross section in the muon + jets channel in pp collisions at 8 TeV*, tech. rep. CMS-PAS-TOP-13-011, CERN, 2014, URL: <https://cds.cern.ch/record/1644573>.
- [12] *Measurement of the $t\bar{t}+\gamma$ production cross-section in pp collisions at $\sqrt{s} = 8$ TeV*, tech. rep. CMS-PAS-TOP-14-008, CERN, 1900, URL: <https://cds.cern.ch/record/2216566>.
- [13] M. Aaboud et al., *Measurement of the $t\bar{t}\gamma$ production cross section in proton-proton collisions at $\sqrt{s} = 8$ TeV with the ATLAS detector*, (2017), arXiv: [1706.03046 \[hep-ex\]](https://arxiv.org/abs/1706.03046).
- [14] K. Melnikov, M. Schulze and A. Scharf, *QCD corrections to top quark production in association with a photon at hadron colliders*, *Phys. Rev.* **D 83** (2011) (), eprint: [arXiv:1102.1967 \[hep-ph\]](https://arxiv.org/abs/1102.1967), URL: <http://arxiv.org/abs/1102.1967>.
- [15] ATLAS Collaboration, *The ATLAS Experiment at the CERN Large Hadron Collider*, *JINST* **3** (2008) S08003.

- 1779 [16] M. Capeans et al., *ATLAS Insertable B-Layer Technical Design Report*,
 1780 tech. rep. CERN-LHCC-2010-013. ATLAS-TDR-19, 2010,
 1781 URL: <https://cds.cern.ch/record/1291633>.
- 1782 [17] *ATLAS Insertable B-Layer Technical Design Report Addendum*,
 1783 tech. rep. CERN-LHCC-2012-009. ATLAS-TDR-19-ADD-1,
 1784 Addendum to CERN-LHCC-2010-013, ATLAS-TDR-019, 2012,
 1785 URL: <https://cds.cern.ch/record/1451888>.
- 1786 [18] J. Alwall et al., *The automated computation of tree-level and next-to-leading order differential*
 1787 *cross sections, and their matching to parton shower simulations*, **JHEP 07 (2014) 079**,
 1788 arXiv: [1405.0301 \[hep-ph\]](https://arxiv.org/abs/1405.0301).
- 1789 [19] J. Pumplin et al.,
 1790 *New generation of parton distributions with uncertainties from global QCD analysis*,
 1791 **JHEP 07 (2002) 012**, arXiv: [hep-ph/0201195 \[hep-ph\]](https://arxiv.org/abs/hep-ph/0201195).
- 1792 [20] T. Sjöstrand et al., *An Introduction to PYTHIA 8.2*, **Comput. Phys. Commun. 191 (2015) 159**,
 1793 arXiv: [1410.3012 \[hep-ph\]](https://arxiv.org/abs/1410.3012).
- 1794 [21] *ATLAS Run 1 Pythia8 tunes*, tech. rep. ATL-PHYS-PUB-2014-021, CERN, 2014,
 1795 URL: <https://cds.cern.ch/record/1966419>.
- 1796 [22] S. Frixione, P. Nason and C. Oleari,
 1797 *Matching NLO QCD computations with Parton Shower simulations: the POWHEG method*,
 1798 **JHEP 11 (2007) 070**, arXiv: [0709.2092 \[hep-ph\]](https://arxiv.org/abs/0709.2092).
- 1799 [23] T. Gleisberg et al., *Event generation with SHERPA 1.1*, **JHEP 0902 (2009) 007**.
- 1800 [24] H.-L. Lai, M. Guzzi, J. Huston, Z. Li, P. M. Nadolsky et al.,
 1801 *New parton distributions for collider physics*, **Phys.Rev. D82 (2010) 074024**,
 1802 arXiv: [1007.2241 \[hep-ph\]](https://arxiv.org/abs/1007.2241).
- 1803 [25] P. Z. Skands, *Tuning Monte Carlo Generators: The Perugia Tunes*, **Phys. Rev. D82 (2010) 074018**,
 1804 arXiv: [1005.3457 \[hep-ph\]](https://arxiv.org/abs/1005.3457).
- 1805 [26] E. Barberio, B. van Eijk, and Z. Was,
 1806 *Photos- a universal Monte Carlo for QED radiative corrections in decays*,
 1807 **Comput. Phys. Commun. 66 (1991) 155**, 1991.
- 1808 [27] ATLAS Collaboration, *AnalysisTop framework (restricted)*,
 1809 URL: <https://twiki.cern.ch/twiki/bin/view/AtlasProtected/AnalysisTop>.
- 1810 [28] ATLAS Collaboration, *Electron efficiency measurements with the ATLAS detector using the 2015*
 1811 *LHC proton–proton collision data*, ATLAS-CONF-2016-024, 2016,
 1812 URL: <https://cds.cern.ch/record/2157687>.
- 1813 [29] ATLAS Collaboration, *ATLAS electron, photon and muon isolation in Run 2: The isolation*
 1814 *variables reconstruction and performance for Run 2 are documented.*,
 1815 tech. rep. ATL-COM-PHYS-2017-290, This note contains the Moriond 2017 recommendations. It
 1816 will be updated when new recommendations become available.: CERN, 2017,
 1817 URL: <https://cds.cern.ch/record/2256658>.
- 1818 [30] ATLAS Collaboration, *Electron and photon energy calibration with the ATLAS detector using*
 1819 *data collected in 2015 at $\sqrt{s} = 13$ TeV*, ATL-PHYS-PUB-2016-015, 2016,
 1820 URL: <https://cds.cern.ch/record/2203514>.

- 1821 [31] ATLAS Collaboration, *Muon reconstruction performance of the ATLAS detector in proton–proton*
 1822 *collision data at $\sqrt{s} = 13$ TeV*, Eur. Phys. J. C **76** (2016) 292, arXiv: [1603.05598 \[hep-ex\]](https://arxiv.org/abs/1603.05598).
- 1823 [32] ATLAS Collaboration, *Photon identification in 2015 ATLAS data*, ATL-PHYS-PUB-2016-014,
 1824 2016, URL: <https://cds.cern.ch/record/2203125>.
- 1825 [33] M. Cacciari, G. P. Salam and G. Soyez, *The Anti- $k(t)$ jet clustering algorithm*,
 1826 JHEP **04** (2008) 063, arXiv: [0802.1189 \[hep-ph\]](https://arxiv.org/abs/0802.1189).
- 1827 [34] ATLAS Collaboration, *Properties of jets and inputs to jet reconstruction and calibration with the*
 1828 *ATLAS detector using proton–proton collisions at $\sqrt{s} = 13$ TeV*, ATL-PHYS-PUB-2015-036,
 1829 2015, URL: <https://cds.cern.ch/record/2044564>.
- 1830 [35] M. Aaboud et al., *Jet energy scale measurements and their systematic uncertainties in*
 1831 *proton–proton collisions at $\sqrt{s} = 13$ TeV with the ATLAS detector*, (2017),
 1832 arXiv: [1703.09665 \[hep-ex\]](https://arxiv.org/abs/1703.09665).
- 1833 [36] ATLAS Collaboration, *Tagging and suppression of pileup jets with the ATLAS detector*,
 1834 ATLAS-CONF-2014-018, 2014, URL: <https://cds.cern.ch/record/1700870>.
- 1835 [37] ATLAS Collaboration, *Expected performance of the ATLAS b-tagging algorithms in Run-2*,
 1836 ATL-PHYS-PUB-2015-022, 2015, URL: <https://cds.cern.ch/record/2037697>.
- 1837 [38] ATLAS Collaboration, *Performance of missing transverse momentum reconstruction with the*
 1838 *ATLAS detector using proton–proton collisions at $\sqrt{s} = 13$ TeV*,
 1839 tech. rep. ATL-COM-PHYS-2016-407, CERN, 2016,
 1840 URL: <https://cds.cern.ch/record/2149445>.
- 1841 [39] F. Chollet et al., *Keras*, <https://github.com/fchollet/keras>, 2015.
- 1842 [40] D. H. Guest, M. Paganini, M. Kagan, J. W. Smith and M. Lanfermann,
 1843 *lwtnn/lwtnn: Release for Athena v21*, 2017,
 1844 URL: <https://doi.org/10.5281/zenodo.290682>.
- 1845 [41] C. Anastopoulos et al., *Photon identification pre-recommendations for run 2*,
 1846 tech. rep. ATL-COM-PHYS-2015-496, CERN, 2015,
 1847 URL: <https://cds.cern.ch/record/2022342>.
- 1848 [42] S. Ioffe and C. Szegedy,
 1849 *Batch Normalization: Accelerating Deep Network Training by Reducing Internal Covariate Shift*,
 1850 CoRR **abs/1502.03167** (2015), URL: <http://arxiv.org/abs/1502.03167>.
- 1851 [43] M. Aaboud et al.,
 1852 *Luminosity determination in pp collisions at $\sqrt{s} = 8$ TeV using the ATLAS detector at the LHC*,
 1853 Eur. Phys. J. C**76** (2016) 653, arXiv: [1608.03953 \[hep-ex\]](https://arxiv.org/abs/1608.03953).
- 1854 [44] M. Aaboud et al., *Performance of the ATLAS Trigger System in 2015*,
 1855 Eur. Phys. J. C**77** (2017) 317, arXiv: [1611.09661 \[hep-ex\]](https://arxiv.org/abs/1611.09661).
- 1856 [45] ATLAS Collaboration,
 1857 *Selection of jets produced in 13 TeV proton–proton collisions with the ATLAS detector*,
 1858 ATL-COM-PHYS-2015-029, 2015, URL: <https://cds.cern.ch/record/2037702>.
- 1859 [46] ATLAS Collaboration, *Measurement of the photon identification efficiencies with the ATLAS*
 1860 *detector using LHC Run-1 data*, (2016), arXiv: [1606.01813 \[hep-ex\]](https://arxiv.org/abs/1606.01813).

- 1861 [47] ATLAS Collaboration, *Estimation of fake lepton background for top analyses using the Matrix*
 1862 *Method with the 2015 dataset at $\sqrt{s} = 13$ TeV with AnalysisTop-2.3.41*,
 1863 tech. rep. ATL-COM-PHYS-2016-198, CERN, 2016,
 1864 URL: <https://cds.cern.ch/record/2135116>.
- 1865 [48] ATLAS Collaboration, *Jet energy scale measurements and their systematic uncertainties in*
 1866 *proton-proton collisions at $\sqrt{s}=13$ TeV with the ATLAS detector*, *Phys. Rev. D* **96** (2017) 072002,
 1867 arXiv: [1703.09665v2 \[hep-ex\]](https://arxiv.org/abs/1703.09665v2).
- 1868 [49] ATLAS Collaboration, *Jet energy measurement and its systematic uncertainty in proton-proton*
 1869 *collisions at $\sqrt{s}=7$ TeV with the ATLAS detector*, *Eur. Phys. J. C* **75** (2015) 17,
 1870 arXiv: [1406.0076v3 \[hep-ex\]](https://arxiv.org/abs/1406.0076v3).
- 1871 [50] ATLAS Collaboration, *Optimisation of the ATLAS b-tagging performance for the 2016 LHC Run*,
 1872 tech. rep. ATL-PHYS-PUB-2016-012, CERN, 2016,
 1873 URL: <http://cdsweb.cern.ch/record/2160731>.
- 1874 [51] ATLAS Collaboration, *Pile up reweighting tool (restricted)*, URL: <https://twiki.cern.ch/twiki/bin/viewauth/AtlasProtected/ExtendedPileupReweighting>.
- 1876 [52] M. Cacciari, G. P. Salam and G. Soyez, *The Catchment Area of Jets*, *JHEP* **04** (2008) 005,
 1877 arXiv: [0802.1188 \[hep-ph\]](https://arxiv.org/abs/0802.1188).
- 1878 [53] V. Blobel, ‘An Unfolding method for high-energy physics experiments’, *Advanced Statistical*
 1879 *Techniques in Particle Physics. Proceedings, Conference, Durham, UK, March 18-22, 2002*, 2002
 1880 258, arXiv: [hep-ex/0208022 \[hep-ex\]](https://arxiv.org/abs/hep-ex/0208022), URL:
<http://www.ippp.dur.ac.uk/Workshops/02/statistics/proceedings/blobel2.pdf>.
- 1882 [54] F. Spano, ‘Unfolding in particle physics: a window on solving inverse problems’,
 1883 *Proceedings, 6th International Workshop on Top Quark Physics (TOP2013): Durbach, Germany,*
 1884 *September 14-19, 2013*, 2014 256,
 1885 URL: <http://inspirehep.net/record/1344095/files/P52.pdf>.
- 1886 [55] G. D’Agostini, *Improved iterative Bayesian unfolding*, (),
 1887 eprint: [arXiv:1010.0632v1\[physics.data-an\]](https://arxiv.org/abs/1010.0632v1),
 1888 URL: <https://arxiv.org/abs/1010.0632>.
- 1889 [56] A. Hocker and V. Kartvelishvili, *SVD approach to data unfolding*,
 1890 *Nucl. Instrum. Meth.* **A372** (1996) 469, arXiv: [hep-ph/9509307 \[hep-ph\]](https://arxiv.org/abs/hep-ph/9509307).
- 1891 [57] *RooUnfold package*,
 1892 URL: <http://hepunx.rl.ac.uk/~adye/software/unfold/RooUnfold.html>.
- 1893 [58] D. Peng-Fei et al., *QCD corrections to associated production of $t\bar{t}\gamma$ at hadron colliders*, (2009),
 1894 arXiv: [0907.1324 \[hep-ph\]](https://arxiv.org/abs/0907.1324).
- 1895 [59] ATLAS Collaboration, *Measurement of the $t\bar{t}$ production cross-section using $e\mu$ events with*
 1896 *b-tagged jets in pp collisions at $\sqrt{s}=13$ TeV with the ATLAS detector*, *Phys. Lett. B* **761** (2016) 136,
 1897 arXiv: [1606.02699 \[hep-ex\]](https://arxiv.org/abs/1606.02699).

1898 **Appendices**

[Not reviewed, for internal circulation only]

A Additional information for PPT
A.1 Comparison of different architectures of PPT

Tab. 38 summarises the AUC values and the information whether the training and test ROC curves are in agreement of all PPT configurations tested. Tab. 39 contains information on the three different architectures considered.

archi-tecture	features	AUC (training)	AUC (test)	ROC agreement
1	$R_\eta, R_\phi, f_{\text{side}}, w_{\eta 1}$	0.8249	0.8266	✓
	$R_\eta, R_\phi, f_{\text{side}}, w_{\eta 1}, R_{\text{had}}$	0.8414	0.8401	✓
	$R_\eta, R_\phi, f_{\text{side}}, w_{\eta 1}, R_{\text{had}}, w_{\eta 2}$	0.8486	0.8477	✓
2	$R_\eta, R_\phi, f_{\text{side}}, w_{\eta 1}$	0.8411	0.8419	✓
	$R_\eta, R_\phi, f_{\text{side}}, w_{\eta 1}, R_{\text{had}}$	0.8668	0.8657	✓
	$R_\eta, R_\phi, f_{\text{side}}, w_{\eta 1}, R_{\text{had}}, w_{\eta 2}$	0.8654	0.8649	✓
3	$R_\eta, R_\phi, f_{\text{side}}, w_{\eta 1}$	0.8460	0.8452	✓
	$R_\eta, R_\phi, f_{\text{side}}, w_{\eta 1}, R_{\text{had}}$	0.8631	0.8621	✓
	$R_\eta, R_\phi, f_{\text{side}}, w_{\eta 1}, R_{\text{had}}, w_{\eta 2}$	0.8693	0.8690	✓

Table 38: Three different architectures tested for the PPT. Starting with one layer, further layers are added successively. The output layer is included in all cases.

architectures	
1 (input layer)	relu, 64 neurons
2	+ batchnormalisation + softmax, 40 neurons
3	+ batchnormalisation + softmax, 52 neurons
output layer	sigmoid, 1 neuron

Table 39: Visualisation of the NN architecture used for the PPT.

A.2 Further data/MC plots for PPT systematics

Figure 100 shows control plots for various observables in the PPT hadronic fake control region, where the signal contribution is increased to 150%. Figure 101 shows the corresponding PPT output distribution.

A.3 Derivations used for training

Table 40 summarises the derivations used for training and testing the PPT.

Not reviewed, for internal circulation only

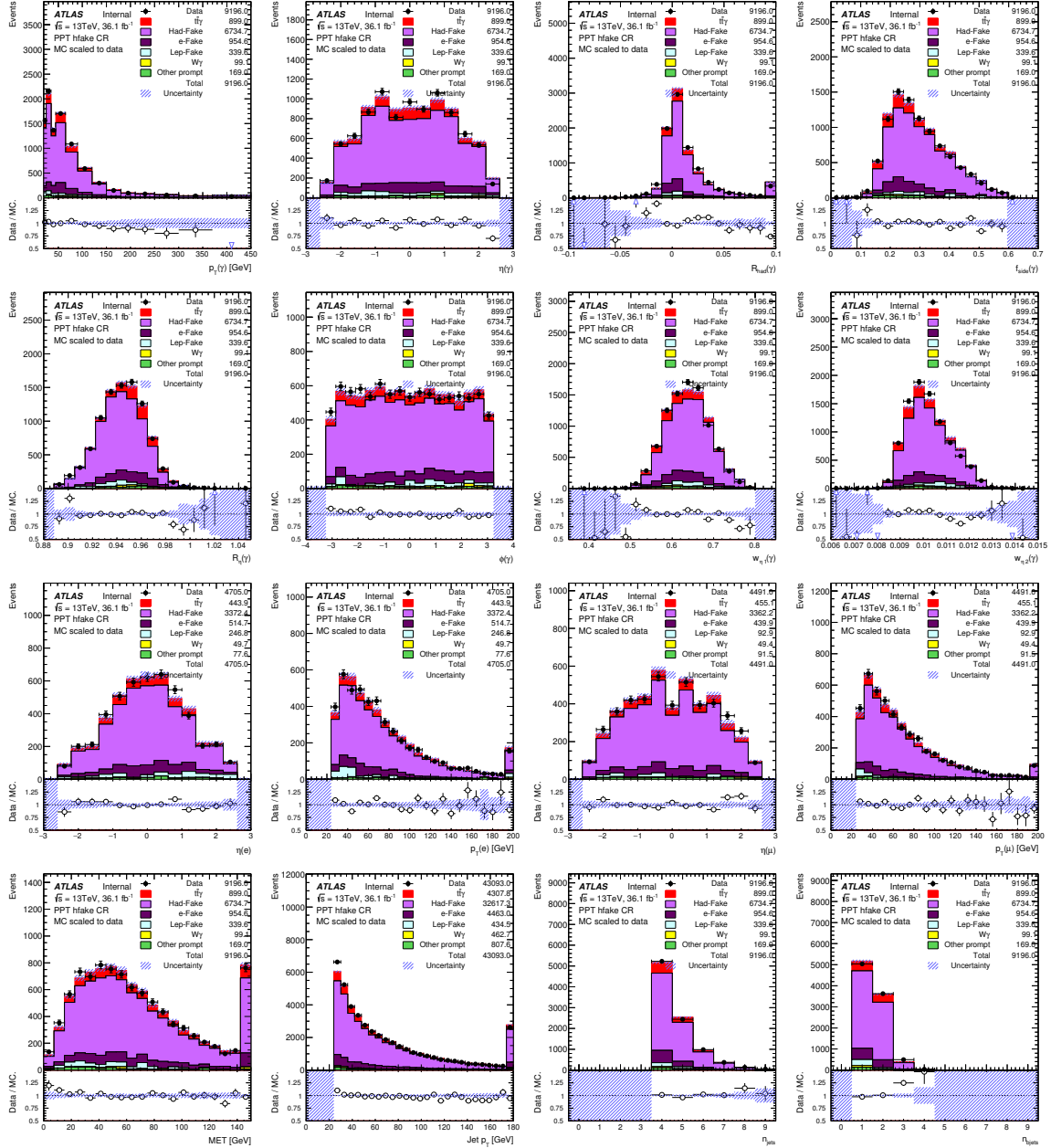


Figure 100: Control plots in the PPT hadronic fake control region including distributions of the photon shower shape variables R_{had} , f_{side} , R_η , R_ϕ , $w_{\eta 1}$ and $w_{\eta 2}$ used as input to the NN. The signal contribution is increased to 150% and MC is scaled to data for shape comparisons. Only statistical uncertainties are included.

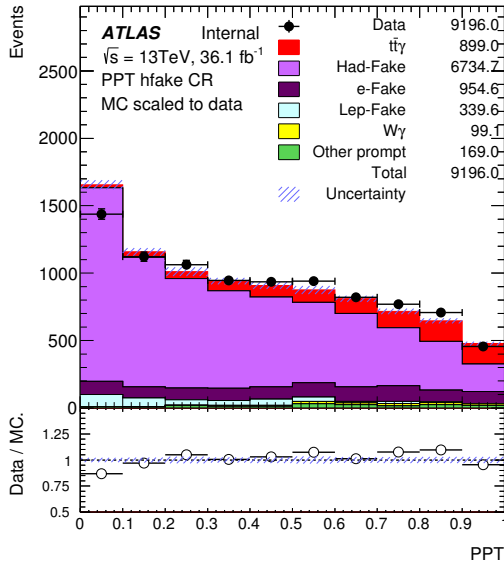


Figure 101: PPT distributions in hadronic fake control regions where the signal contribution is scaled to 150%. MC is scaled to data for shape comparison and only statistical uncertainties are included.

single photons, QCD compton (training)

```

mc15_13TeV.423099.Pythia8EvtGen_A14NNPDF23LO_gammajet_DP8_17.merge.DAOD_STDM2.e4453_s2726_r7725_r7676_p2669/
mc15_13TeV.423100.Pythia8EvtGen_A14NNPDF23LO_gammajet_DP17_35.merge.DAOD_STDM2.e3791_s2608_s2183_r7725_r7676_p2669/
mc15_13TeV.423101.Pythia8EvtGen_A14NNPDF23LO_gammajet_DP35_50.merge.DAOD_STDM2.e3904_s2608_s2183_r7725_r7676_p2669/
mc15_13TeV.423102.Pythia8EvtGen_A14NNPDF23LO_gammajet_DP50_70.merge.DAOD_STDM2.e3791_s2608_s2183_r7725_r7676_p2669/
mc15_13TeV.423103.Pythia8EvtGen_A14NNPDF23LO_gammajet_DP70_140.merge.DAOD_STDM2.e3791_s2608_s2183_r7725_r7676_p2669/
mc15_13TeV.423104.Pythia8EvtGen_A14NNPDF23LO_gammajet_DP140_280.merge.DAOD_STDM2.e3791_s2608_s2183_r7725_r7676_p2669/
mc15_13TeV.423105.Pythia8EvtGen_A14NNPDF23LO_gammajet_DP280_500.merge.DAOD_STDM2.e3791_s2608_s2183_r7725_r7676_p2669/
mc15_13TeV.423106.Pythia8EvtGen_A14NNPDF23LO_gammajet_DP500_800.merge.DAOD_STDM2.e3791_s2608_s2183_r7725_r7676_p2669/
mc15_13TeV.423107.Pythia8EvtGen_A14NNPDF23LO_gammajet_DP800_1000.merge.DAOD_STDM2.e4453_s2726_r7725_r7676_p2669/
mc15_13TeV.423108.Pythia8EvtGen_A14NNPDF23LO_gammajet_DP1000_1500.merge.DAOD_STDM2.e4453_s2726_r7725_r7676_p2669/
mc15_13TeV.423109.Pythia8EvtGen_A14NNPDF23LO_gammajet_DP1500_2000.merge.DAOD_STDM2.e4453_s2726_r7725_r7676_p2669/
mc15_13TeV.423110.Pythia8EvtGen_A14NNPDF23LO_gammajet_DP2000_2500.merge.DAOD_STDM2.e4453_s2726_r7725_r7676_p2669/
mc15_13TeV.423111.Pythia8EvtGen_A14NNPDF23LO_gammajet_DP2500_3000.merge.DAOD_STDM2.e4453_s2726_r7725_r7676_p2669/
mc15_13TeV.423112.Pythia8EvtGen_A14NNPDF23LO_gammajet_DP3000_inf.merge.DAOD_STDM2.e4453_s2726_r7725_r7676_p2669/

```

QCD di-jet (training)

```

mc15_13TeV.423300.Pythia8EvtGen_A14NNPDF23LO_perf_JF17.merge.DAOD_STDM2.e3848_s2608_s2183_r7725_r7676_p2666/
mc15_13TeV.423301.Pythia8EvtGen_A14NNPDF23LO_perf_JF23.merge.DAOD_STDM2.e3848_s2608_s2183_r7725_r7676_p2666/
mc15_13TeV.423302.Pythia8EvtGen_A14NNPDF23LO_perf_JF35.merge.DAOD_STDM2.e3848_s2608_s2183_r7725_r7676_p2666/
mc15_13TeV.423303.Pythia8EvtGen_A14NNPDF23LO_perf_JF50.merge.DAOD_STDM2.e3848_s2608_s2183_r7725_r7676_p2666/

```

Radiative Z, Z → e⁺e⁻γ (evaluation, MC)

```

mc15_13TeV.301535.Sherpa_CT10_eegammaPt10_35.merge.DAOD_EGAM3.e3952_s2608_s2183_r7725_r7676_p2613
mc15_13TeV.301899.Sherpa_CT10_eegammaPt35_70.merge.DAOD_EGAM3.e3952_s2608_s2183_r7725_r7676_p2613
mc15_13TeV.301900.Sherpa_CT10_eegammaPt70_140.merge.DAOD_EGAM3.e3952_s2608_s2183_r7725_r7676_p2613

```

Table 40: Summary of derivations used for training and evaluation of the PPT.

1909 **A.4 Shower shape comparisons in different p_T and η regions**

1910 The topology of the detector is not homogeneous. For instance, the granularity in the calorimeters is
 1911 a function of η and different sub-components cover slightly different kinematic regions. Furthermore,
 1912 material upstream is present in the detector. Since shower shapes evolve due to the photon interacting with
 1913 the detector material, they consequently depend on the kinematic region they are measured in. Especially
 1914 the granularity of the strip layer in the end-caps of the electromagnetic calorimeter gets coarser with
 1915 increasing $|\eta|$ [15]. Figs. 102 and 103 shows the shower shape distributions of R_{had} , R_η , R_ϕ , $w_{\eta 1}$, $w_{\eta 2}$
 1916 and f_{side} in 3 different bins of p_T and η , respectively.

1917 The classification performance of the PPT can hence expected to be different between the training on
 1918 QCD-Compton and di-jet events and the application to $t\bar{t}\gamma$ signal and background events. For instance,
 1919 Fig. 104 shows the comparison of the PPT distribution of prompt photons in QCD-Compton events and
 1920 $t\bar{t}\gamma$ signal events.

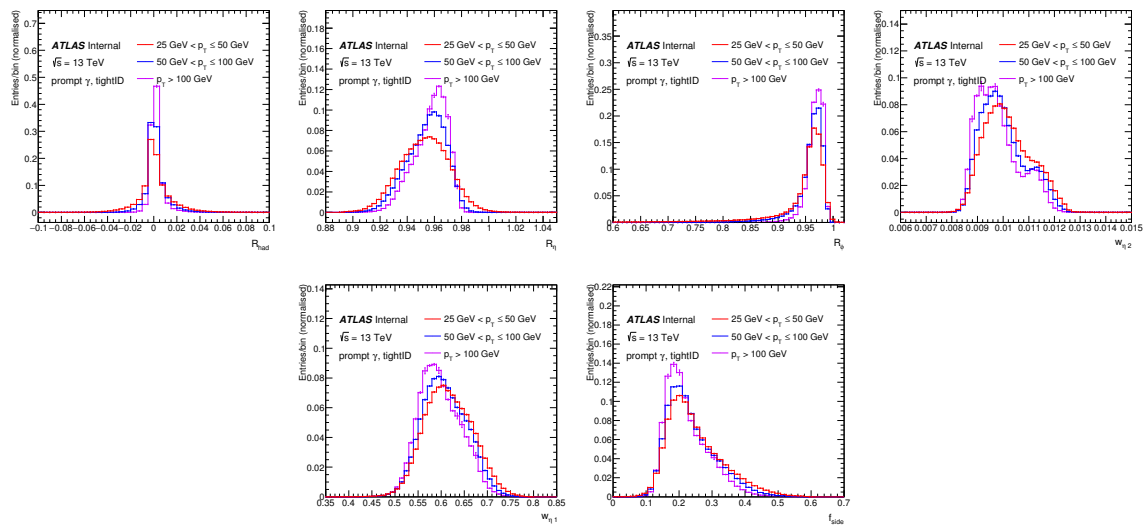


Figure 102: Photon shower shapes R_{had} , R_η , R_ϕ , $w_{\eta 1}$, $w_{\eta 2}$ and f_{side} in three different bins of p_T .

1921 **A.5 Shower shape comparisons for training and test split**

1922 Figure 105 shows shower shape distributions for the six observables used as input to the NN, randomly
 1923 split into 80% training and 20% testing sets.

Not reviewed, for internal circulation only

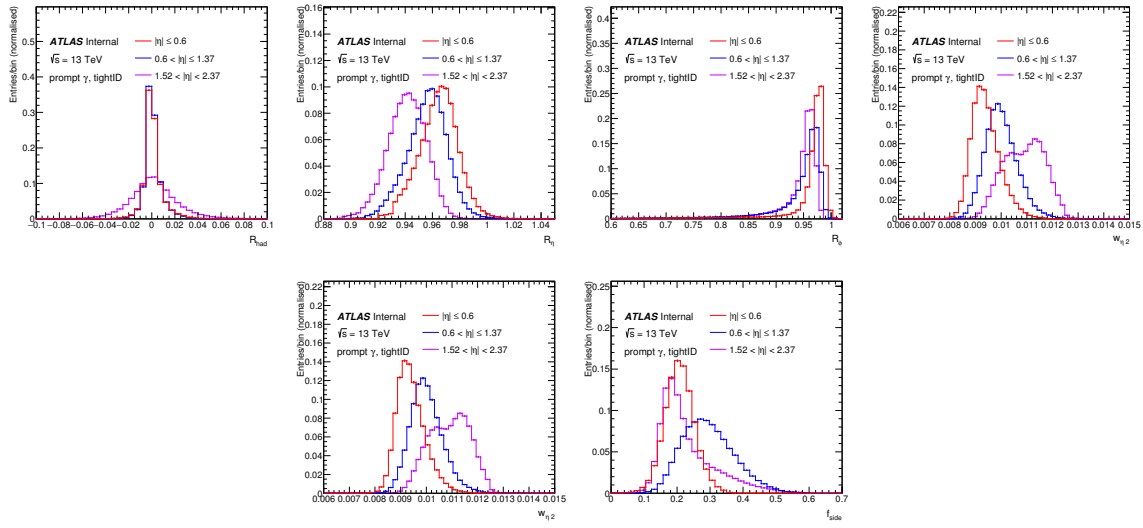


Figure 103: Photon shower shapes R_{had} , R_η , R_ϕ , $w_{\eta 1}$, $w_{\eta 2}$ and f_{side} in three different bins of η .

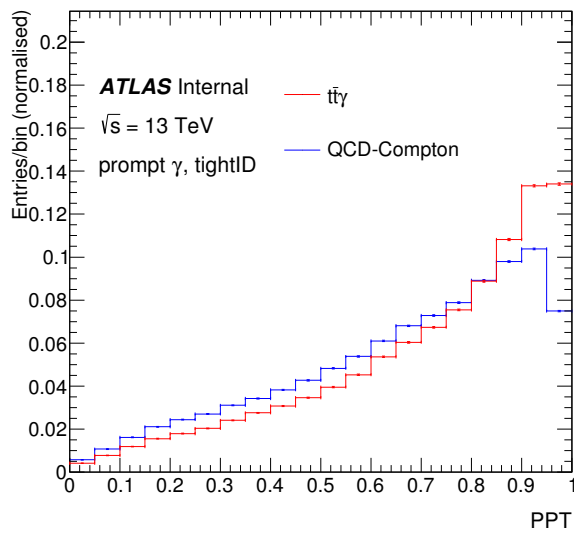


Figure 104: PPT distribution of prompt photons in QCD-Compton events and $t\bar{t}\gamma$ signal events.

Not reviewed, for internal circulation only

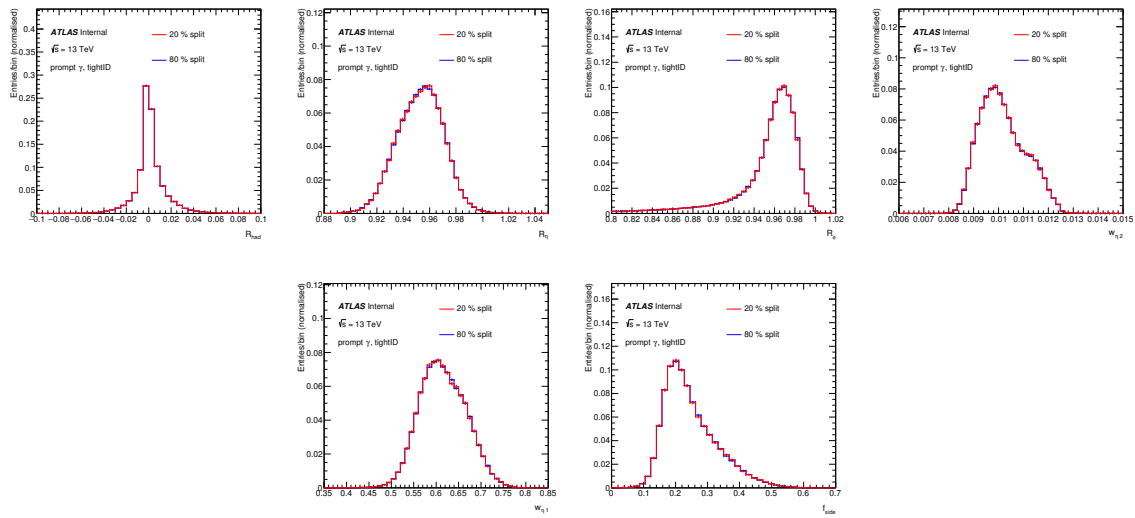


Figure 105: Shower shape distributions R_{had} , R_η , R_ϕ , $w_{\eta 1}$, $w_{\eta 2}$ and f_{side} of prompt photons where all samples are randomly split into orthogonal 80 % training and 20 % test sets.

1924 B Cuts optimization

1925 The cut optimization is done based on reducing the total relative uncertainty on the expected cross section.
 1926 The expected cross section is given by the following:

$$\hat{\sigma} = \frac{N_{\text{expected}} - N_{\text{background}}}{\epsilon \cdot \mathcal{L}} = \frac{(N_{\text{signal}} + N_{\text{background}}) - N_{\text{background}}}{\epsilon \cdot \mathcal{L}} = \frac{N_{\text{signal}}}{\epsilon \cdot \mathcal{L}} \quad (65)$$

1927 The cross section in Equation 65 includes the Luminosity \mathcal{L} , the efficiency ϵ and the expected number of
 1928 events in data N_{expected} . The efficiency ϵ is given by:

$$\epsilon = \frac{N_{\text{signal}}}{N_{\text{signal}}^{\text{initial}}} \quad (66)$$

1929 Where N_{signal} is the number of events in the signal sample after the full selection and $N_{\text{signal}}^{\text{initial}}$ is the number
 1930 of events generated initially in the MC signal sample.

1931 The uncertainty on the cross section can be given by:

$$\Delta\hat{\sigma} = \sqrt{(\Delta\hat{\sigma}_{\text{stat}})^2 + (\Delta\hat{\sigma}_{\text{syst}})^2}. \quad (67)$$

$$\Delta\hat{\sigma}_{\text{stat}} = \sqrt{\left(\frac{\Delta(N_{\text{signal}} + N_{\text{background}})}{\epsilon \cdot \mathcal{L}}\right)^2 + \left(\frac{\Delta N_{\text{background}}}{\epsilon \cdot \mathcal{L}}\right)^2} = \frac{\sqrt{N_{\text{signal}} + N_{\text{background}}}}{\epsilon \cdot \mathcal{L}} \quad (68)$$

$$\Delta\hat{\sigma}_{\text{syst}} = \sqrt{\left(\frac{\Delta N_{\text{background}}^{\text{syst}}}{\epsilon \cdot \mathcal{L}}\right)^2 + \left(\hat{\sigma} \cdot \frac{\Delta\epsilon}{\epsilon}\right)^2 + \left(\hat{\sigma} \cdot \frac{\Delta\mathcal{L}}{\mathcal{L}}\right)^2} \quad (69)$$

1932 B.1 Cuts optimization in the single lepton channel

1933 The simulated MC samples described in Section 3 are used here, normalized to their cross section and an
 1934 integrated luminosity of 36.47 fb^{-1} (Note: The cut optimisation was done with an older calculation of the
 1935 total luminosity, different from the current number which is 36.1 fb^{-1} .).

1936 The following systematic uncertainties are considered (Note: The cut optimisation was done with an older
 1937 conservative set of systematics, different from the current systematics numbers.):

- 1938 • Luminosity uncertainty: 5.5%
- 1939 • hadronic fakes background modelling: 5%
- 1940 • $e \rightarrow \gamma$ fakes background modelling: 10%
- 1941 • other backgrounds modelling: 50%

1942 The optimization is done for a cut on each variable independently from the other, so it is a one dimensional
 1943 optimization. The selection cuts are optimized for the following set of variables:

- 1944 • E_T^{miss} in a range of [0,100] GeV
 1945 • $m_T(W)$ in a range of [0,100] GeV

1946 For the optimization of a variable, the other variable is set to the minimum.

1947 **B.1.1 Results in the single lepton channel**

1948 The missing transverse momentum distributions in both single lepton channels and the expected relative
 1949 uncertainties on the cross section for a shorter range of the variable are shown in Figure 106. The same is
 1950 shown for $m_T(W)$ in Figure 107. For both variables systematic uncertainty is dominating.

1951 For both variables, the relative total uncertainty on the expected cross section shows a rather flat behaviour
 1952 in the smaller values and increases for the larger values. Therefore, it is decided to apply no cuts on E_T^{miss} ,
 1953 $m_T(W)$ for the signal region selection.

1954 **B.2 Cuts optimization in the dilepton channel**

1955 The simulated MC samples described in Section 3 are used here, normalized to their cross section and an
 1956 integrated luminosity of 36.47 fb^{-1} (Note: The cut optimisation was done with an older calculation of
 1957 the total luminosity, different from the current number which is 36.1 fb^{-1} .).

1958 The following systematic uncertainties are considered (Note: The cut optimisation was done with an older
 1959 conservative set of systematics, different from the current systematics numbers.):

- 1960 • Luminosity uncertainty: 2.9%
 1961 • Background modelling: 10%
 1962 • b -tagging, jet, leptons scales uncertainties are taken from the published $t\bar{t}$ differential cross section
 1963 measurement in the $e\mu$ channel [59]
 1964 • Photon identification uncertainty

1965 The optimization is done for a cut on each variable independently from the other, so it is a one dimensional
 1966 optimization. The selection cuts are optimized for the following set of variables:

- 1967 • The distance between the photon and the jet in a range of [0.4, 1.0]
 1968 • The distance between the photon and any lepton is a range of [0.4, 1.0]
 1969 • The missing transverse momentum in the same flavour channels in a range of [0, 70] GeV
 1970 • The number of b -tagged jets in a range of [0, 2] b -tagged jets

1971 For the optimization of any of the first three variables, their values are set to the minimum, while other
 1972 selections described in Section 5 are used. Similarly, for optimizing the number of b -tagged jets, no b -tag
 1973 requirement was asked, a cut on missing transverse momentum of 30 GeV(see Figure 108) was applied to
 1974 reduce background from fake leptons and hence reducing its uncertainty on the cross section, while the
 1975 two distances variables are set to minimum.

Not reviewed, for internal circulation only

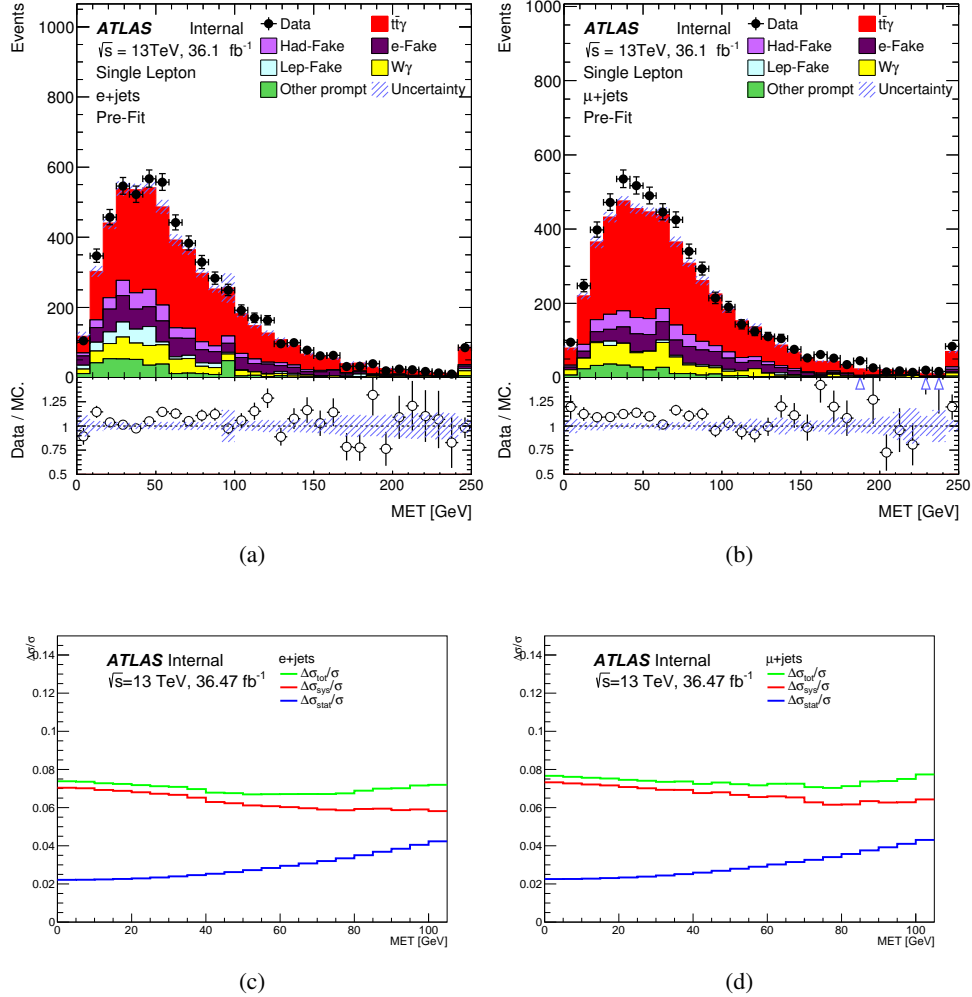


Figure 106: The missing transverse momentum distributions in $e+jets$ (a) and $\mu+jets$ (b), and the relative uncertainty on the expected cross section as a function of the variable in $e+jets$ (c) and $\mu+jets$ (d), with the systematic uncertainty in red, the statistical uncertainty in blue and the total uncertainty in green.

Not reviewed, for internal circulation only

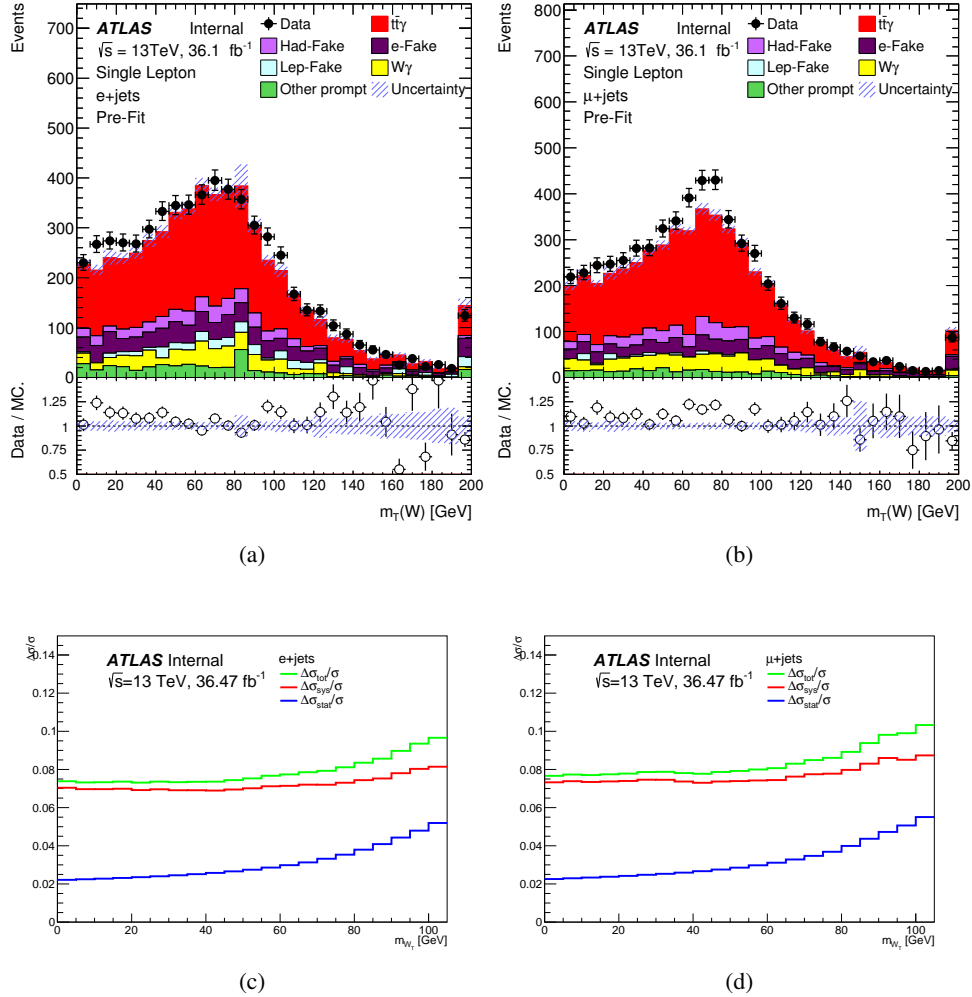


Figure 107: The $m_T(W)$ distributions in $e+jets$ (a) and $\mu+jets$ (b), and the relative uncertainty on the expected cross section as a function of the variable in $e+jets$ (c) and $\mu+jets$ (d), with the systematic uncertainty in red, the statistical uncertainty in blue and the total uncertainty in green.

1976 B.2.1 Results in the dilepton channel

1977 The result of optimizing the missing transverse momentum is shown in Figure 108, including the distri-
1978 butions in the three channels and the expected uncertainty on the cross section for a shorter range of the
1979 variable. The systematic uncertainty is dominant for this variable. A minimum of the total uncertainty at
1980 30 GeVis observed for ee and $\mu\mu$ channels and hence a cut at this value is preferred, while applying no
1981 cut in the $e\mu$ channel is preferred.

1982 The result of optimizing the distance between the lepton and the photon is shown in Figure 109. The
1983 statistical uncertainty is dominant for this variable. A minimum of the total uncertainty at 0.5 is observed
1984 for ee and $\mu\mu$ channels, while no preferred value for $e\mu$ channel. However a cut of 1.0 is applied in all
1985 the three channels in order to enhance the radiative photons production, as a result of the study which is
1986 documented in Appendix C).

1987 The result of optimizing the distance between the jet and the photon is shown in Figure 110. The statistical
1988 uncertainty is dominant for this variable. No preferred value for minimizing the total uncertainty is
1989 observed in any of three channels. Hence no cut at event selection will be applied (the cut at the value 0.4
1990 which can be seen in the distributions comes from the object level selection, from the jet-photon overlap
1991 removal described in Section 4.1).

1992 The result of optimizing the number of b -tagged jets is shown in Figure 111. The statistical uncertainty
1993 is dominant for this variable. A minimum of the total uncertainty at a cut of at least one b -tagged jet is
1994 observed in the three channels, hence this cut value is included in the signal selection.

Not reviewed, for internal circulation only

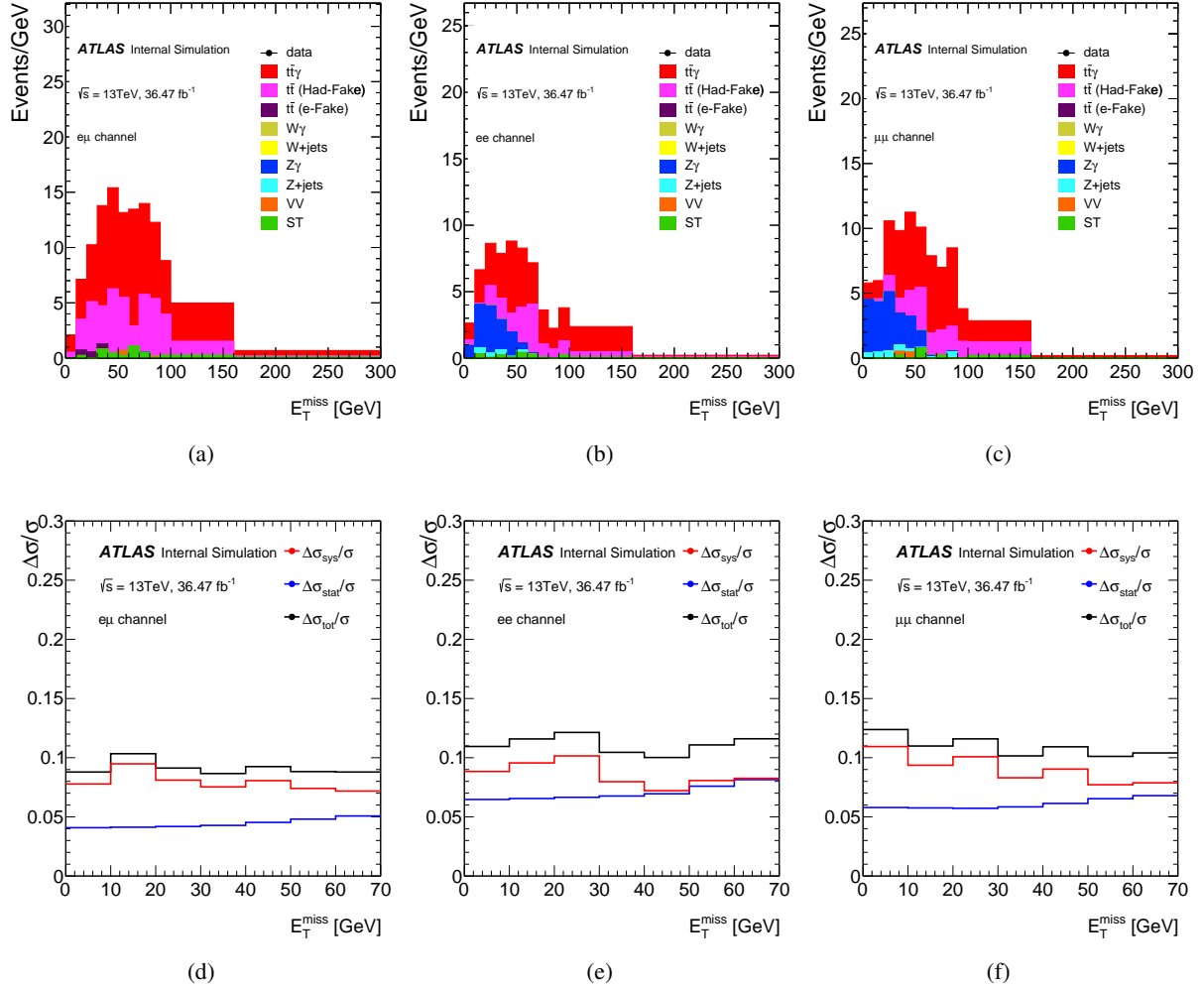


Figure 108: The transverse momentum distributions in $e\mu$ (a), ee (b) and $\mu\mu$ (c). The uncertainty on the expected cross section as a function of the variable in $e\mu$ (d), ee (e) and $\mu\mu$ (f). The systematic uncertainty in red, the statistical uncertainty on blue and the total uncertainty in black.

Not reviewed, for internal circulation only

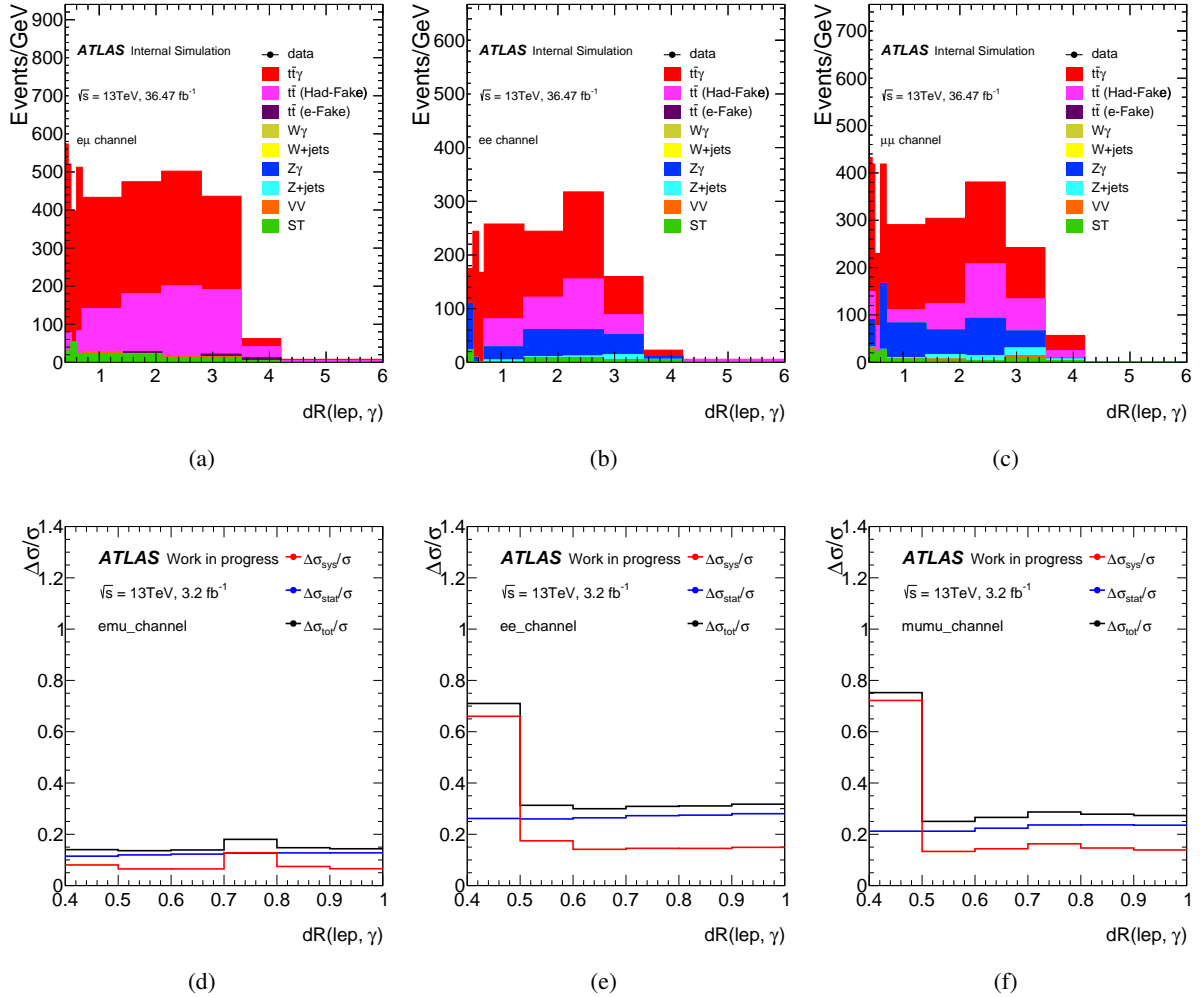


Figure 109: The distance between the photon and the lepton distributions in $e\mu$ (a), ee (b) and $\mu\mu$ (c). The uncertainty on the expected cross section as a function of the variable in $e\mu$ (d), ee (e) and $\mu\mu$ (f). The systematic uncertainty in red, the statistical uncertainty on blue and the total uncertainty in black.

Not reviewed, for internal circulation only

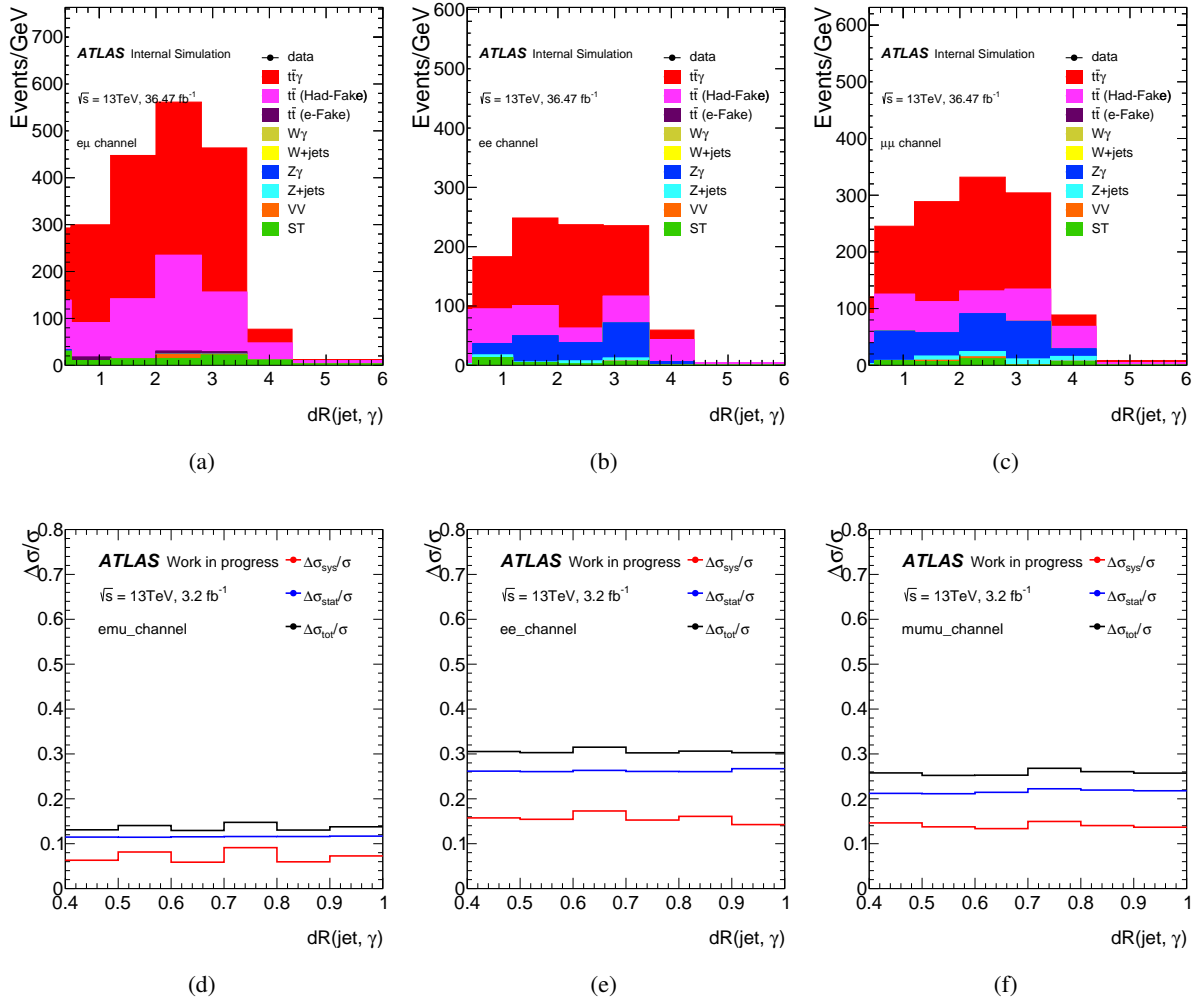


Figure 110: The distance between the photon and the jet distributions in $e\mu$ (a), ee (b) and $\mu\mu$ (c). The uncertainty on the expected cross section as a function of the variable in $e\mu$ (d), ee (e) and $\mu\mu$ (f). The systematic uncertainty in red, the statistical uncertainty on blue and the total uncertainty in black.

Not reviewed, for internal circulation only

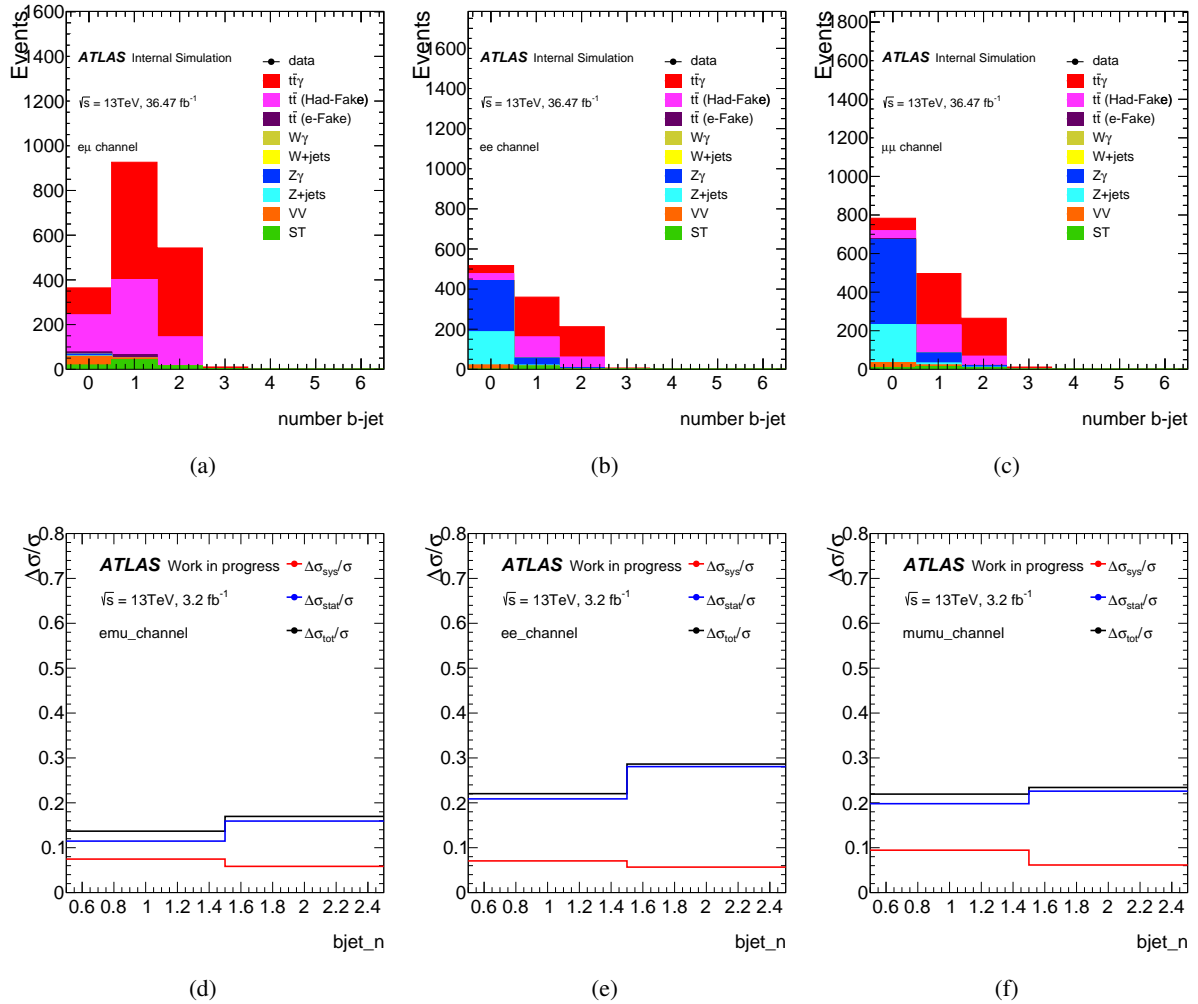


Figure 111: The number of b -tagged jets distributions in $e\mu$ (a), ee (b) and $\mu\mu$ (c). The uncertainty on the expected cross section as a function of the variable in $e\mu$ (d), ee (e) and $\mu\mu$ (f). The systematic uncertainty in red, the statistical uncertainty on blue and the total uncertainty in black.

1995 C Radiative photon decay versus radiative production

1996 A brief study is done here, to check what is the fraction of photon that are radiated from initial state or
 1997 off-shell top quark (called radiative photon production) out of all photons survived some selections in the
 1998 $t\bar{t}\gamma$ signal sample.

1999 The results in percentages are summarized in Table 41. The first column is using the basic $t\bar{t}$ selections
 2000 with a photon, the second column is using the selections described in Section 5 (the isolation cut wasn't
 2001 used here) but keeping the distance between the leptons and the photon at 0.7, the third column is using
 2002 the same selections but changing the distance variable to 1.0, where the fraction of the radiative photon
 2003 production is enhanced in the dilepton channel. The fourth column is using the selections described in
 2004 Section 5, but changing the photon transverse momentum to 40 GeV

Table 41: The fraction of radiative photon production after different sets of selections

Process	$t\bar{t}$ sel + photons	$t\bar{t}\gamma$ sel. with $\Delta R(\text{lepton}, \gamma) > 0.7$	change $\Delta R(\text{lepton}, \gamma) > 0.7$ to 1.0	change $p_T(\gamma)$ from 20 to 40 GeV.
$e + \text{jets}$	35	44	45	55
$\mu + \text{jets}$	35	44	45	55
$e\mu$	34	48	55	67
$\mu\mu$	33	40	54	63
ee	34	39	59	68

2005 D Photon isolation cut

2006 A comparison before and after applying the photon isolation cut. This cut has a large effect in reducing
 2007 the main background from hadronic fakes as shown in the tables. The optimised cuts which are described
 2008 in Section 5 were used.

Table 42: The number of selected data events and the expected yields from MC after applying the photon isolation cut. Normalized to an integrated luminosity of 3.2fb^{-1}

Process	$e\mu$	$\mu\mu$	ee
Data	85	35	35
$t\bar{t}\gamma$	38.53 ± 3.19	21.62 ± 2.41	14.96 ± 1.94
Hadron fake	24.09 ± 2.25	9.36 ± 1.37	8.95 ± 1.34
egamma fake	2.06 ± 0.67	1.32 ± 0.54	0.01 ± 0.004
$Z\gamma + \text{jets}$	0.003 ± 0.002	2.16 ± 0.67	2.93 ± 0.93
Single top + γ	1.70 ± 0.62	1.05 ± 0.47	0.71 ± 0.33
Diboson + γ	0.12 ± 0.12	0.06 ± 0.03	0.007 ± 0.004

Table 43: The number of selected data events and the expected yields from MC after applying the photon isolation cut, normalised to an integrated luminosity of 3.2fb^{-1} . Note: In these numbers table the ph_iso weight is not included.

Process	$e\mu$	$\mu\mu$	ee
Data	50	19	18
$t\bar{t}\gamma$	32.94 ± 2.95	17.12 ± 2.15	12.58 ± 1.84
Hadron fake	1.48 ± 2.25	0.78 ± 0.41	0.94 ± 0.43
egamma fake	0.36 ± 0.27	0.33 ± 0.33	0.001 ± 0.0007
$Z\gamma + \text{jets}$	0.003 ± 0.002	1.99 ± 0.67	2.02 ± 0.70
Single top + γ	1.22 ± 0.67	0.64 ± 0.37	0.49 ± 0.28
Diboson + γ	0.12 ± 0.12	0.02 ± 0.02	0.004 ± 0.004

Not reviewed, for internal circulation only

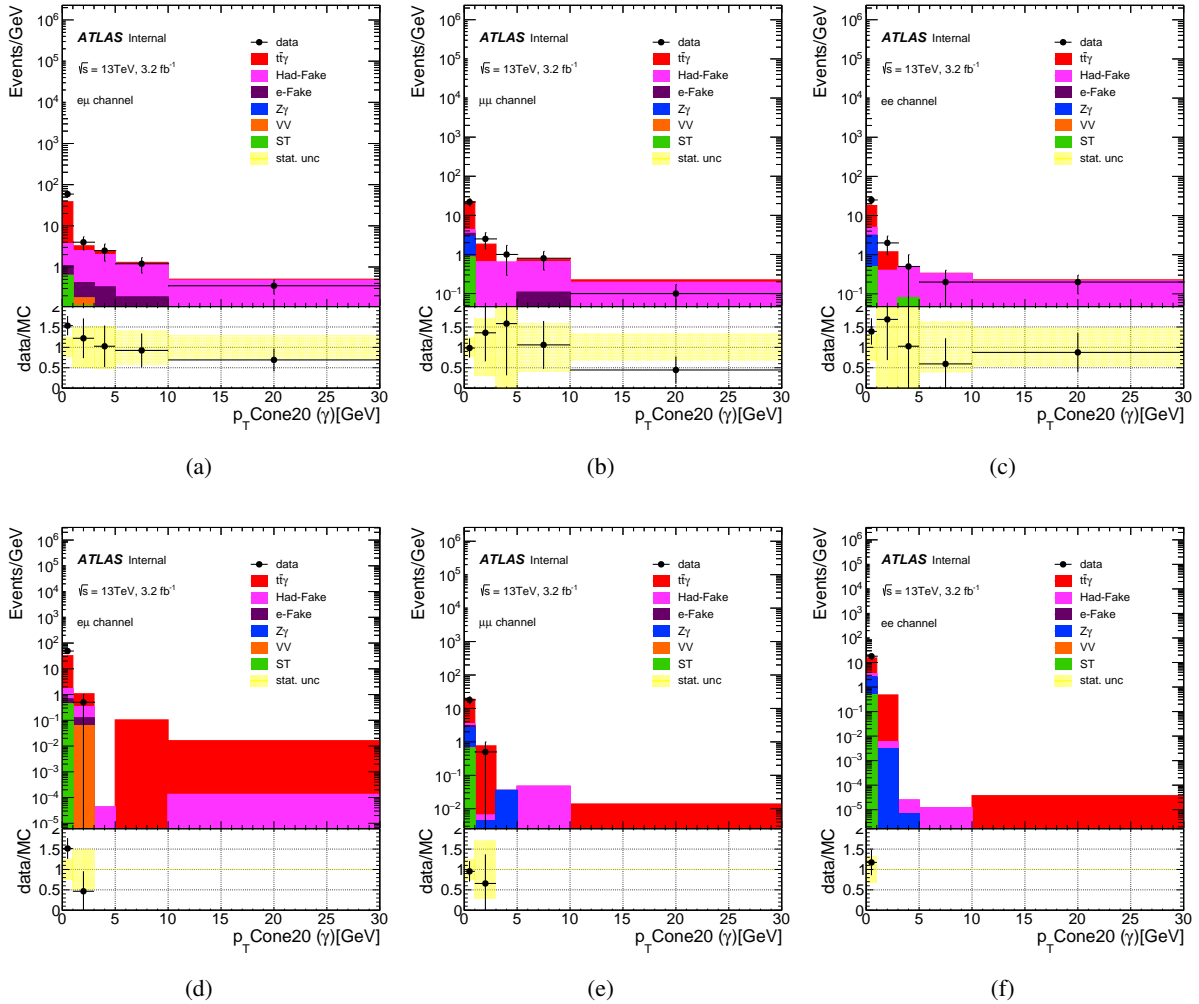


Figure 112: The p_T cone20 variable after applying all the optimised selecten which are described in Section 5 and before appyling the photon isolation cut in $e\mu$ (a), ee (b) and $\mu\mu$ (c). The p_T cone20 variable after appying the same selections described in Section 5 after appyling the photon isolation cut in $e\mu$ (a), ee (b) and $\mu\mu$ (c).

2009 E Hadronic-fake background appendix

2010 E.1 Data-driven double ratio

2011 The double ratio from Equation 10 is additionally calculated by a data-driven method.
 2012 One can not use the same A, B, C and D regions in Equation 10 to calculate the data-driven double
 2013 ratio, as the number of hadronic fakes in region D (signal region) in data is the unknown. However, an
 2014 equivalent double ratio, $\theta'_{\text{d.d.}}$, can be calculated from four new control regions, A', B', C' and D', which
 2015 are derived by dividing regions B and C after the isolation gap $p_T^{\text{cone}20} > 3 \text{ GeV}$ is removed. A schematic
 2016 representation from these control regions are illustrated in Figure 113.

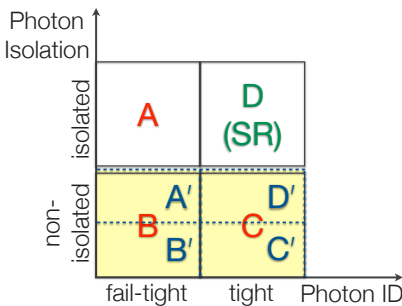


Figure 113: An illustration of the regions A', B', C' and D' which are used to calculate the $\theta'_{\text{d.d.}}$ and are derived from dividing regions B and C after the isolation gap is removed.

2017 Then, the data-driven double ratio is calculated as:

$$\theta'_{\text{d.d.}} = \frac{N_{D',\text{data}}^{\text{h-fake}} / N_{C',\text{data}}^{\text{h-fake}}}{N_{A',\text{data}}^{\text{h-fake}} / N_{B',\text{data}}^{\text{h-fake}}}, \quad (70)$$

2018 where same as in Equation 9, the non-hadronic-fakes and QCD background are subtracted from data.

2019 To obtain the A', B', C' and D' regions, the $p_T^{\text{cone}20}$ distribution of regions B and C after the removal of
 2020 the isolation gap is used. These distributions can be seen in Figure 114 for inclusive photon p_T , η and
 2021 conversion type.

2022 The boundaries of A', B', C' and D' are varied, by setting different cuts on the $p_T^{\text{cone}20}$. The lower boundary
 2023 of A' and D' are varied by three different cuts on $p_T^{\text{cone}20}$ at 1, 2 and 3 GeV. The upper boundary of A' and
 2024 D', which is the same as the lower boundary of B' and C', are varied by nine different cuts on $p_T^{\text{cone}20}$ at
 2025 7, 8, 9, 10, 11, 12, 13, 14 and 15 GeV. Regions B' and C' don't have an upper boundary.

2026 The resulting $\theta'_{\text{d.d.}}$ are shown in Figure 115(a) for inclusive photon p_T , η and conversion type, in Figure 115(b) for converted and in Figure 115(c) for unconverted photons. Also, it is shown in Figures 116 and 117 for different photon p_T and η ranges. In all the above figures the $\theta'_{\text{d.d.}}$ is compared to the equivalent
 2027 MC derived θ'_{MC} which is calculated from same A', B', C' and D' regions, only by replacing the data by
 2028 MC in Equation 70. The systematic uncertainty of $\theta'_{\text{d.d.}}$ is due to the subtraction of non-hadronic-fakes
 2029 and QCD background from data and the systematic uncertainty of θ'_{MC} comes from the $t\bar{t}$ MC sample
 2030 modelling.

Not reviewed, for internal circulation only

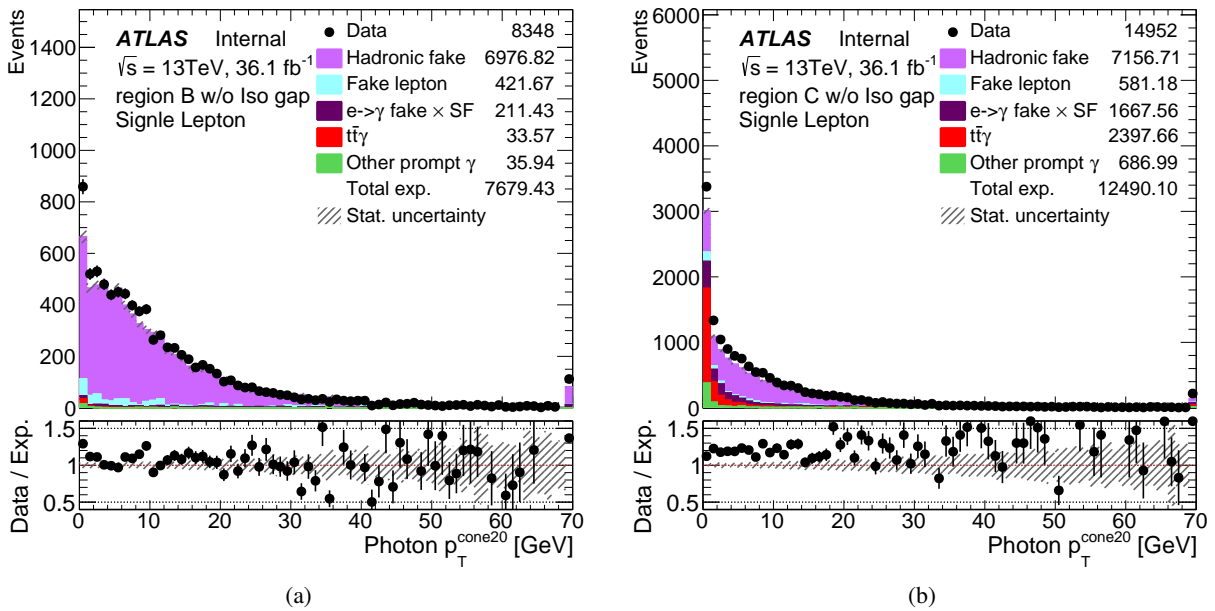


Figure 114: The $p_T^{\text{cone}20}$ distribution of (a) region B without the isolation gap and (b) region C without the isolation gap.

2033 The measured $\theta'_{\text{d.d.}}$ is not distributed flat against the different choices boundaries of A', B', C' and
 2034 D' regions. Therefore, the nominal $\theta'_{\text{d.d.}}$ is calculated from $1 < p_T^{\text{cone}20} < 12$ GeV as A' and D' and
 2035 $p_T^{\text{cone}20} > 12$ GeV as B' and C', and then the difference of minimum and maximum of $\theta'_{\text{d.d.}}$ in the 27
 2036 different choices of region definitions is taken as an extra systematic uncertainty.

2037 Using $\theta'_{\text{d.d.}}$, the estimated number of hadronic fake in signal region is calculated as

$$N_{\text{est.}}^{\text{h-fake}} = \frac{N_{A,\text{data}}^{\text{h-fake}} \cdot N_{C,\text{data}}^{\text{h-fake}}}{N_{B,\text{data}}^{\text{h-fake}}} \times \theta'_{\text{d.d.}} \quad (71)$$

2038 and then the SF^{h-fake} is calculated from Equation 12. The resulting SF^{h-fake} using $\theta'_{\text{d.d.}}$ is compared with
 2039 the calculated SF^{h-fake} using θ_{MC} , which is the baseline method, in Figure 118.

2040 Within the uncertainties, the two methods agree in most bins. However, the θ_{MC} is chosen as the baseline
 2041 method, for several reasons: 1) Extending the A' and D' are to the low isolation values ($p_T^{\text{cone}20} > 1$ GeV)
 2042 is needed to make a fair extrapolation of isolated vs non-isolated regions (A' and D' vs B' and C') but
 2043 in the other hand it introduces prompt photon contamination. 2) In the final fit the systematics due to
 2044 background subtraction in $\theta'_{\text{d.d.}}$ and in $N_{\text{est.}}^{\text{h-fake}}$ must be correlated and this is technically difficult.

Not reviewed, for internal circulation only

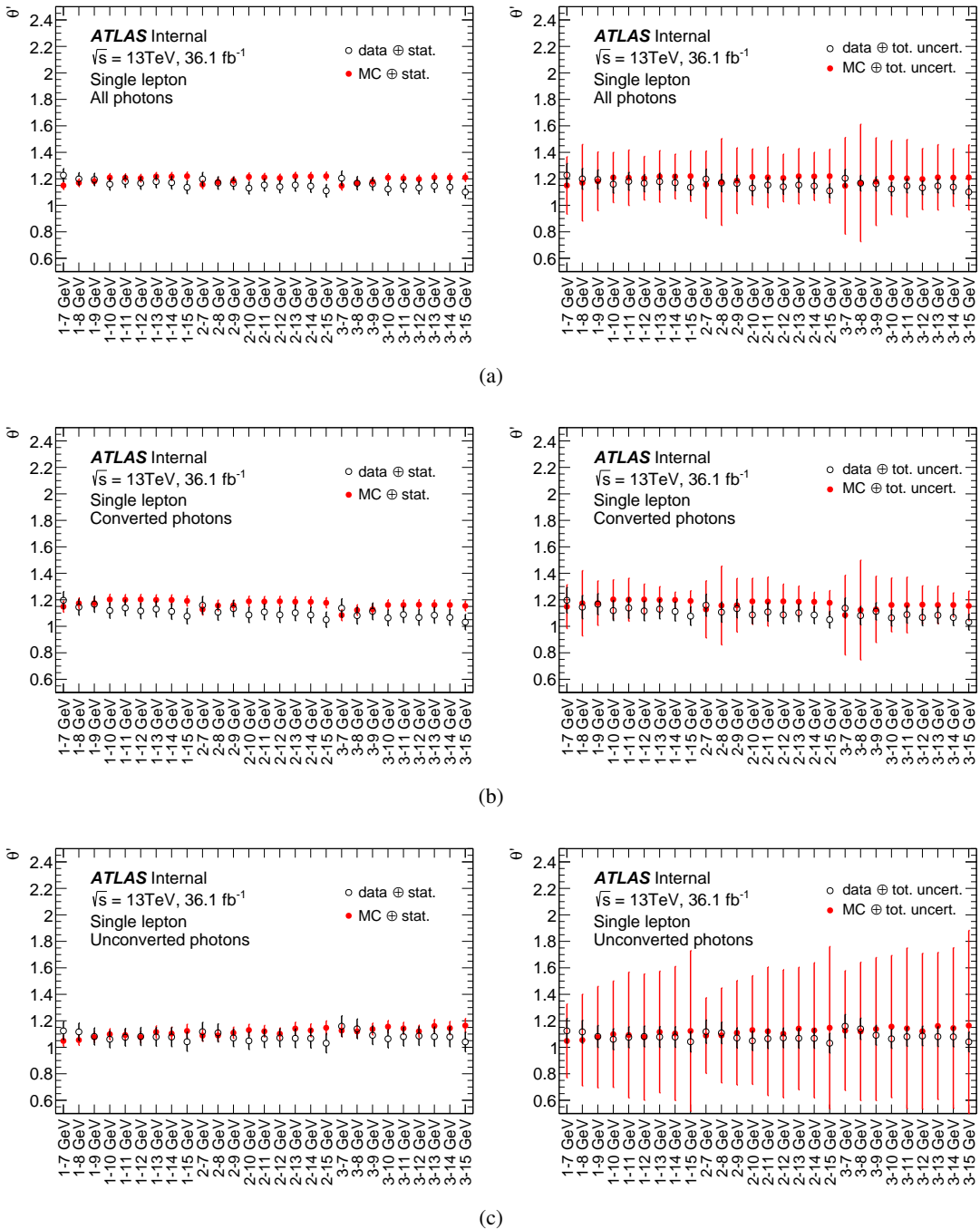


Figure 115: $\theta'_{d,d}$ for different choices of A' , B' , C' and D' regions for (a) inclusive (b) converted and (c) unconverted photons, compared to MC. The x axis shows the boundaries of A' and D' region which are defined by cuts on $p_T^{\text{cone}20}$ in GeV. The lower boundaries of B' and C' are identical as upper boundaries of A' and D' and they go up to infinity in $p_T^{\text{cone}20}$.

Not reviewed, for internal circulation only

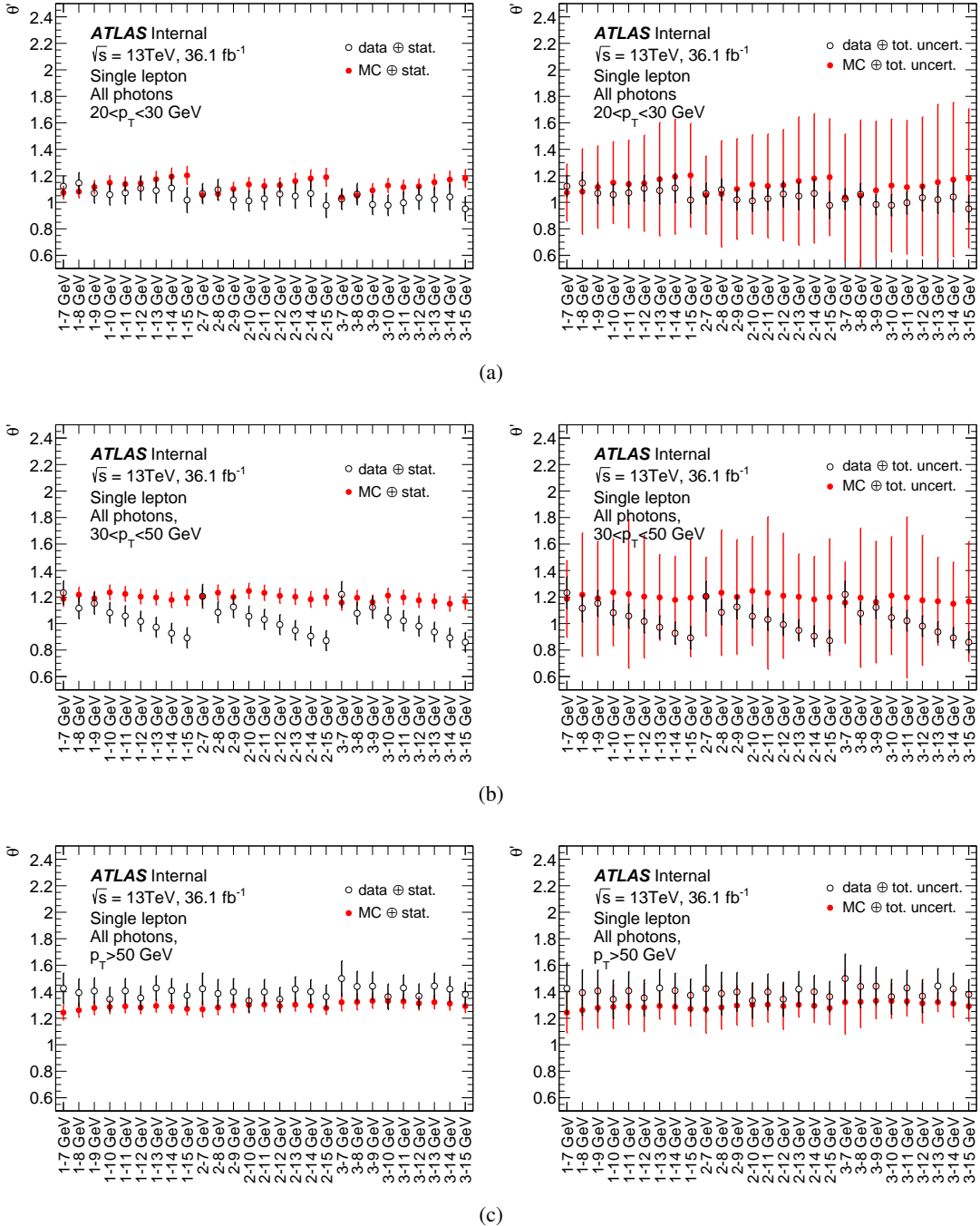


Figure 116: $\theta'_{d,d}$ for different choices of A' , B' , C' and D' regions for different photon p_T ranges, compared to MC. The x axis shows the boundaries of A' and D' region which are defined by cuts on p_T^{cone20} in GeV. The lower boundaries of B' and C' are identical as upper boundaries of A' and D' and they go up to infinity in p_T^{cone20} .

Not reviewed, for internal circulation only

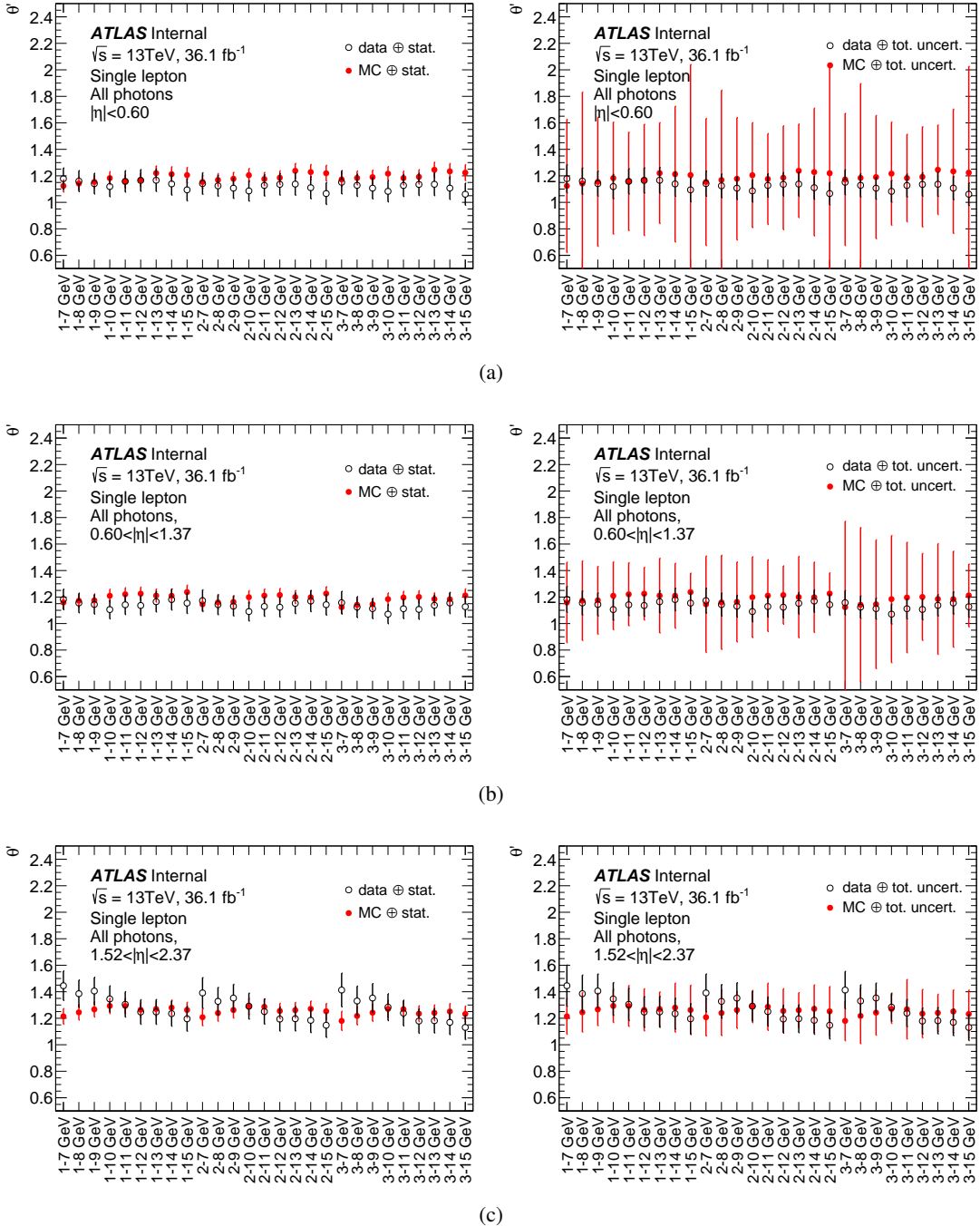


Figure 117: $\theta'_{\text{d.d.}}$ for different choices of A', B', C' and D' regions for different photon η ranges, compared to MC. The x axis shows the boundaries of A' and D' region which are defined by cuts on $p_T^{\text{cone}20}$ in GeV. The lower boundaries of B' and C' are identical as upper boundaries of A' and D' and they go up to infinity in $p_T^{\text{cone}20}$.

Not reviewed, for internal circulation only

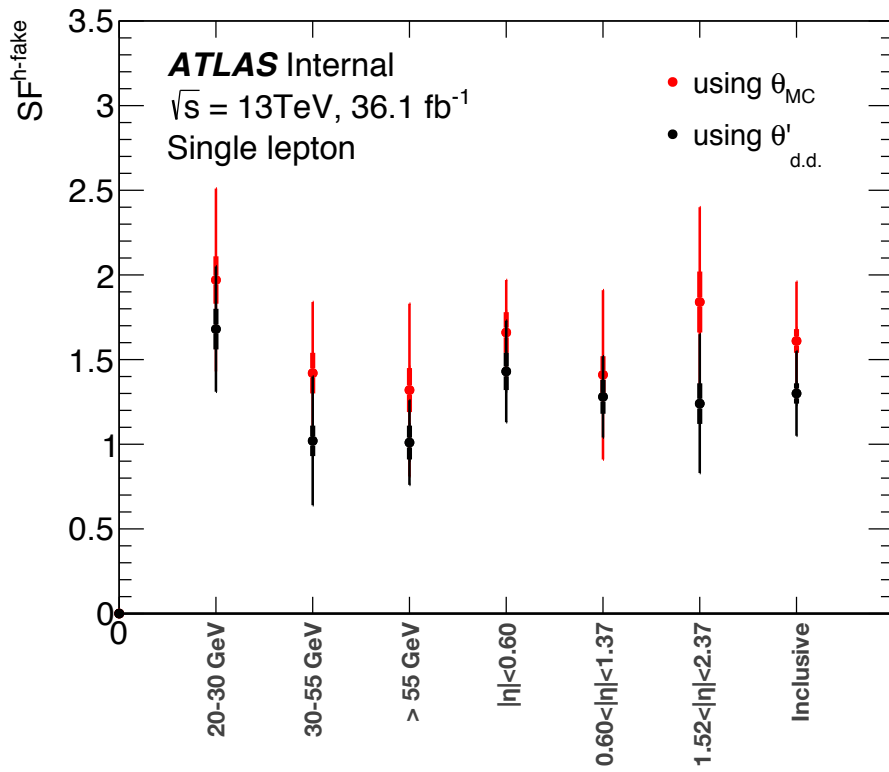


Figure 118: $SF^{h\text{-fake}}$ calculated by using $\theta'_{d.d.}$ (cross-check method) compared to $SF^{h\text{-fake}}$ calculated by using θ_{MC} (baseline method). The error bars show the total uncertainty where the thick lines are only statistical uncertainty.

2045 F $Z\gamma$ light jet validation region

2046 The $Z\gamma$ validation region for light jets (i.e. number of bjets = 0). You can see good data/MC agreement
2047 with $SF_{ee} = 1.119 + 0.022$ and $SF_{\mu\mu} = 1.149 \pm 0.017$ for the ee and $\mu\mu$ fits, respectively.

[Not reviewed, for internal circulation only]

Not reviewed, for internal circulation only

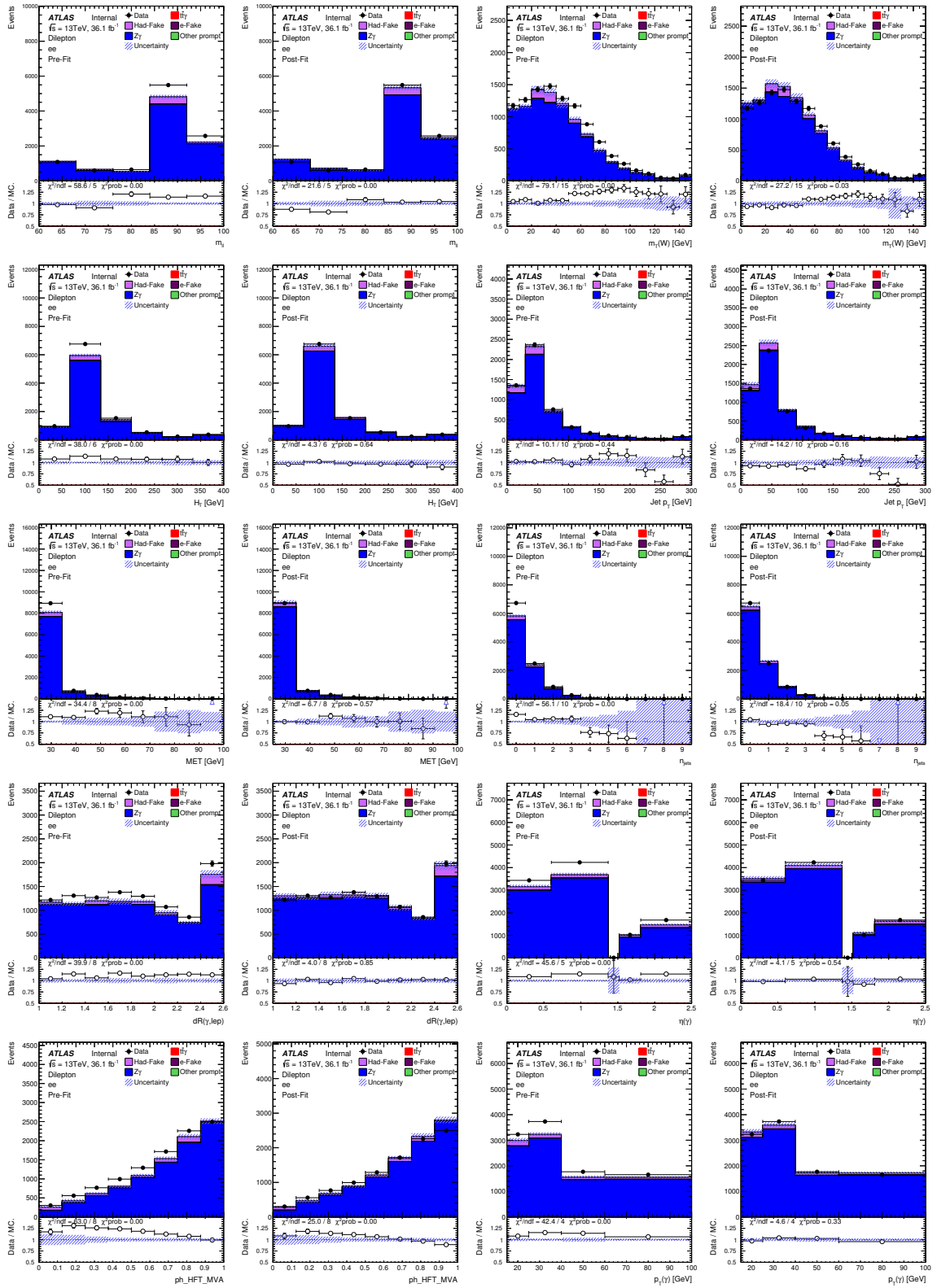


Figure 119: Pre and post-fit distributions for the ee $Z\gamma$ validation region, where number of b-tagged jets is 0.

Not reviewed, for internal circulation only

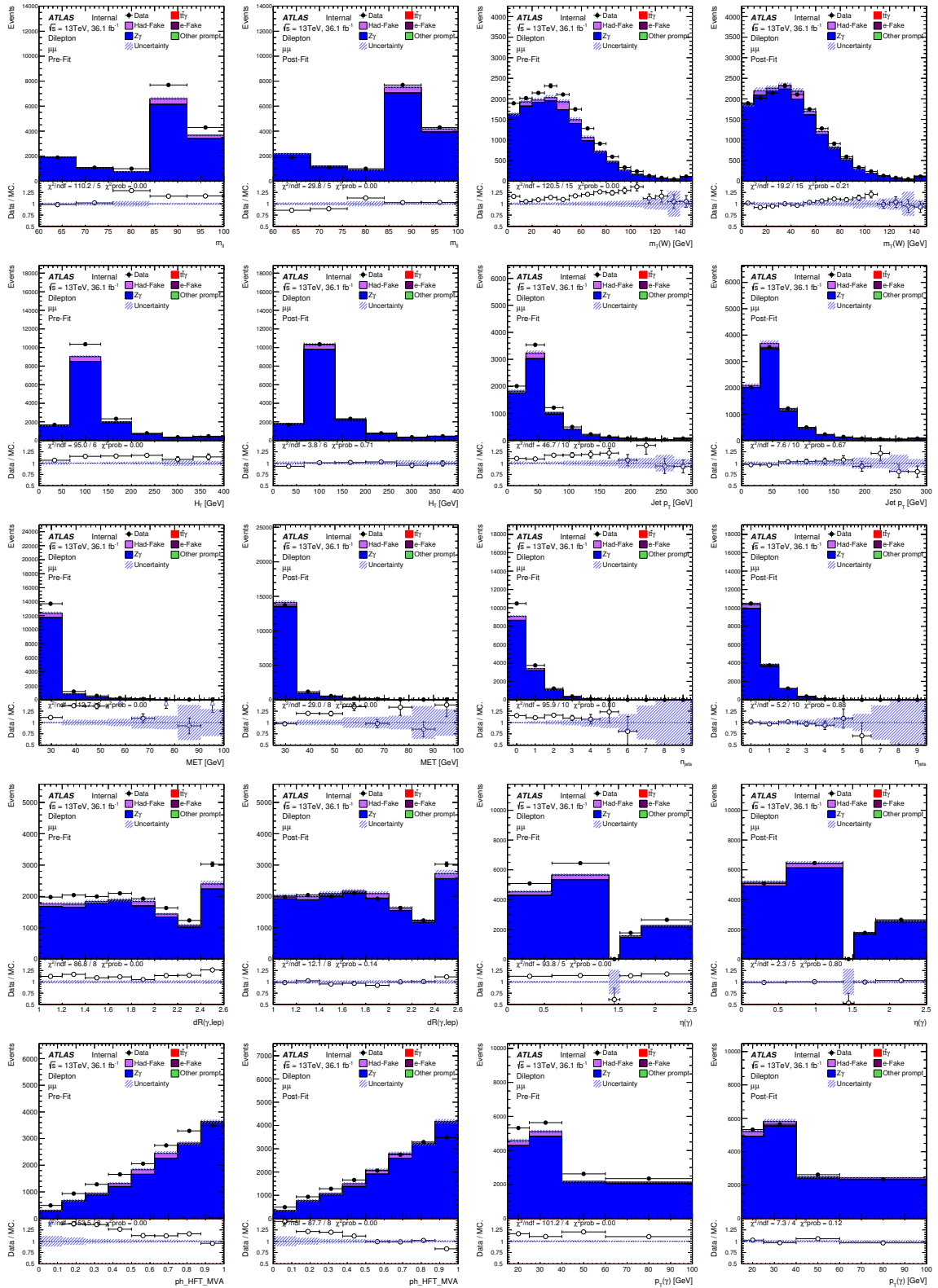


Figure 120: Pre and post-fit distributions for the $\mu\mu Z\gamma$ validation region, where number of b-tagged jets is 0.

G $W\gamma$ light jet validation region

2048 The $W\gamma$ validation region for light jets (i.e. number of bjets = 0). You can see good data/MC agreement
2050 with SF=1.017 ± 0.031 and SF=1.120 + 0.024 for e +jets and μ +jets, respectively.

[Not reviewed, for internal circulation only]

Not reviewed, for internal circulation only

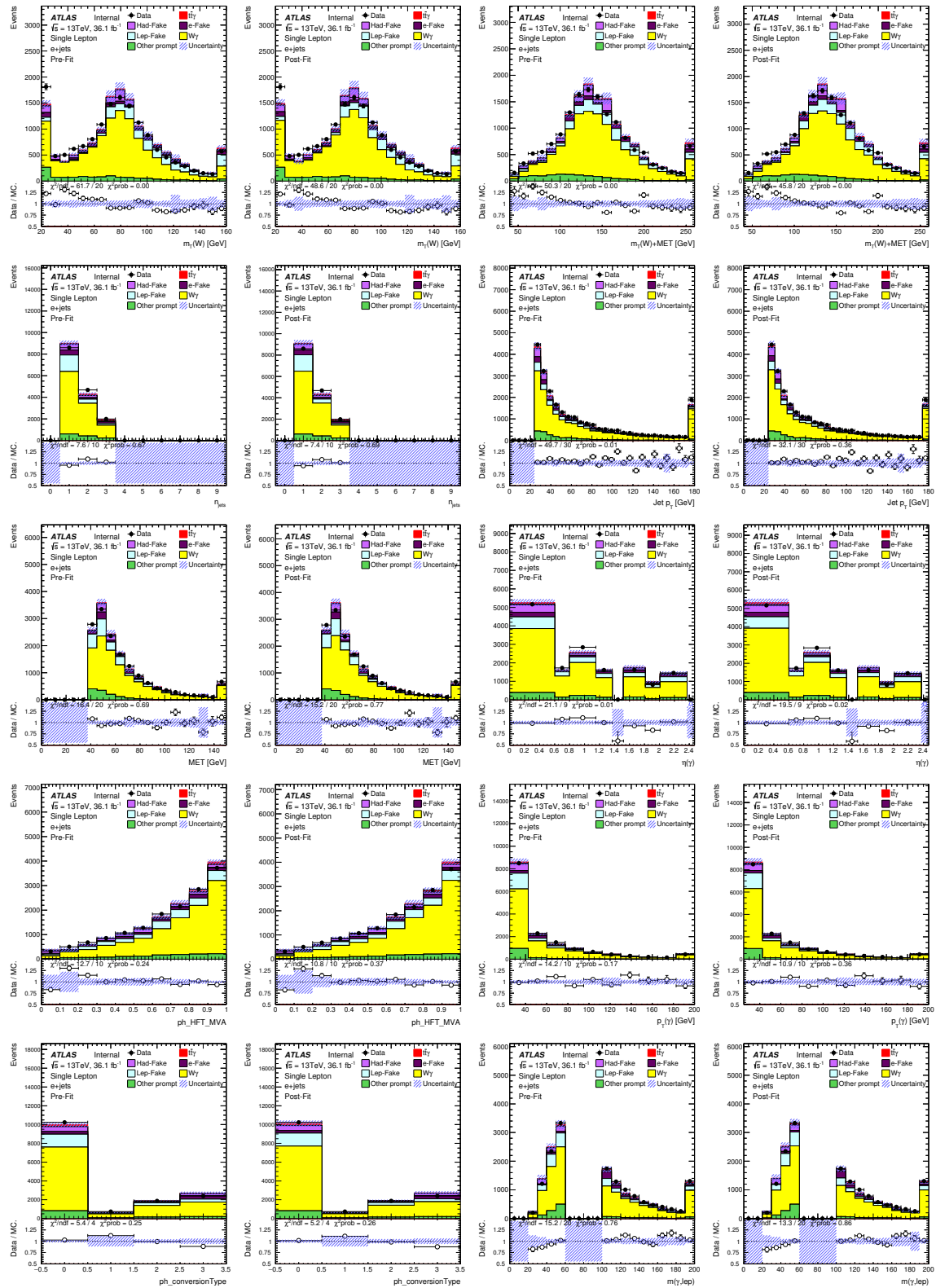


Figure 121: Pre and post-fit distributions for the $e+\text{jets } W\gamma$ validation region, where number of b-tagged jets is 0.

Not reviewed, for internal circulation only

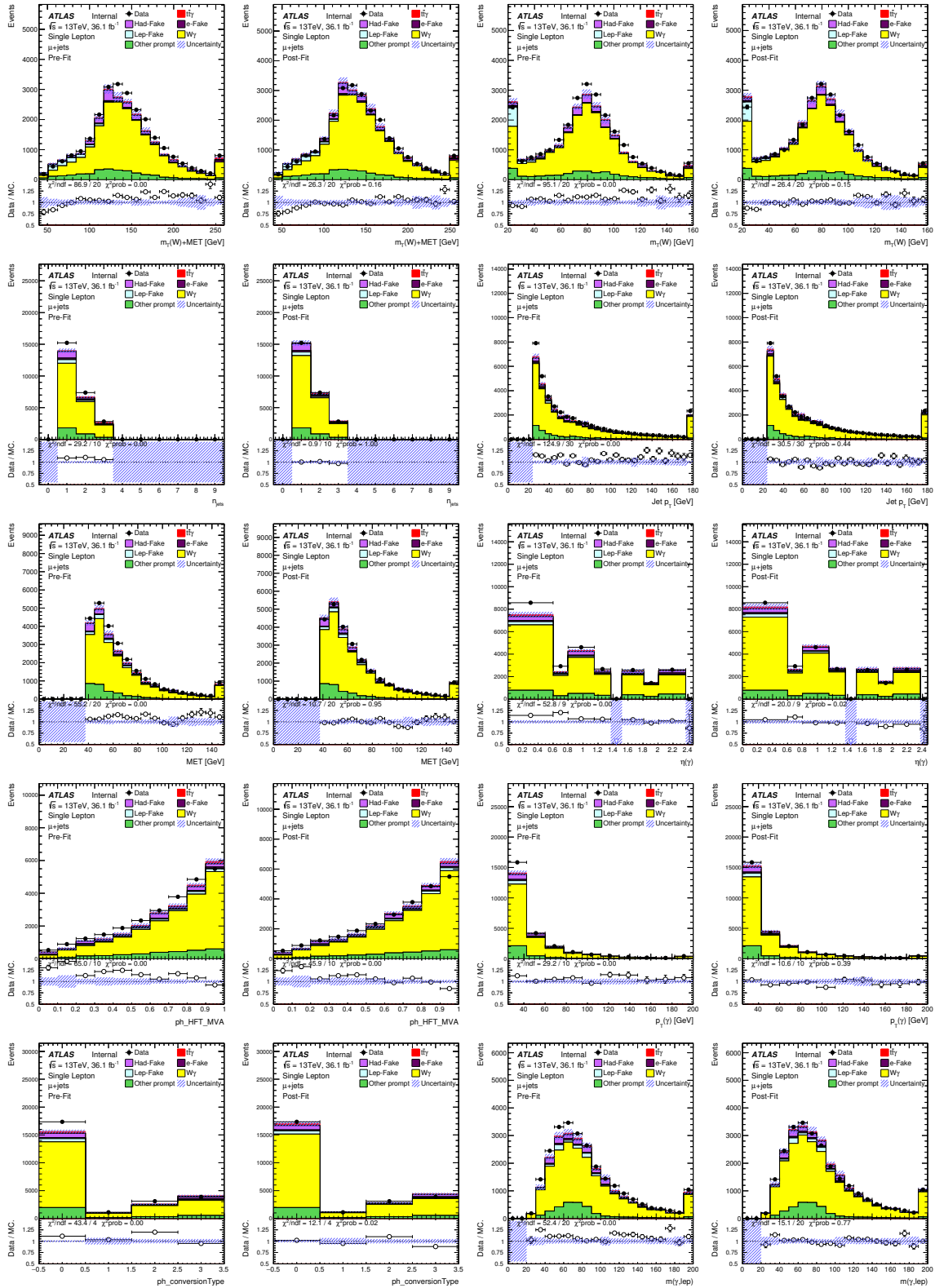


Figure 122: Pre and post-fit distributions for the μ +jets $W\gamma$ validation region, where number of b-tagged jets is 0.

2051 H Systematic uncertainty breakdown

2052 The size of the shifted $t\bar{t}\gamma$ reconstructed distribution due to the luminosity estimation, the choice of the
 2053 parton shower generator of the signal sample and the pile-up scale factor, is compared to the nominal
 2054 distribution and shown in Figure 123 and Figure 124 in bins of the reconstructed object. It can be seen
 2055 that the number of events in the shifted samples is mostly the same as the nominal sample, and therefore
 2056 the majority of differences due to systematic shifts are expected to be significant.

Not reviewed, for internal circulation only

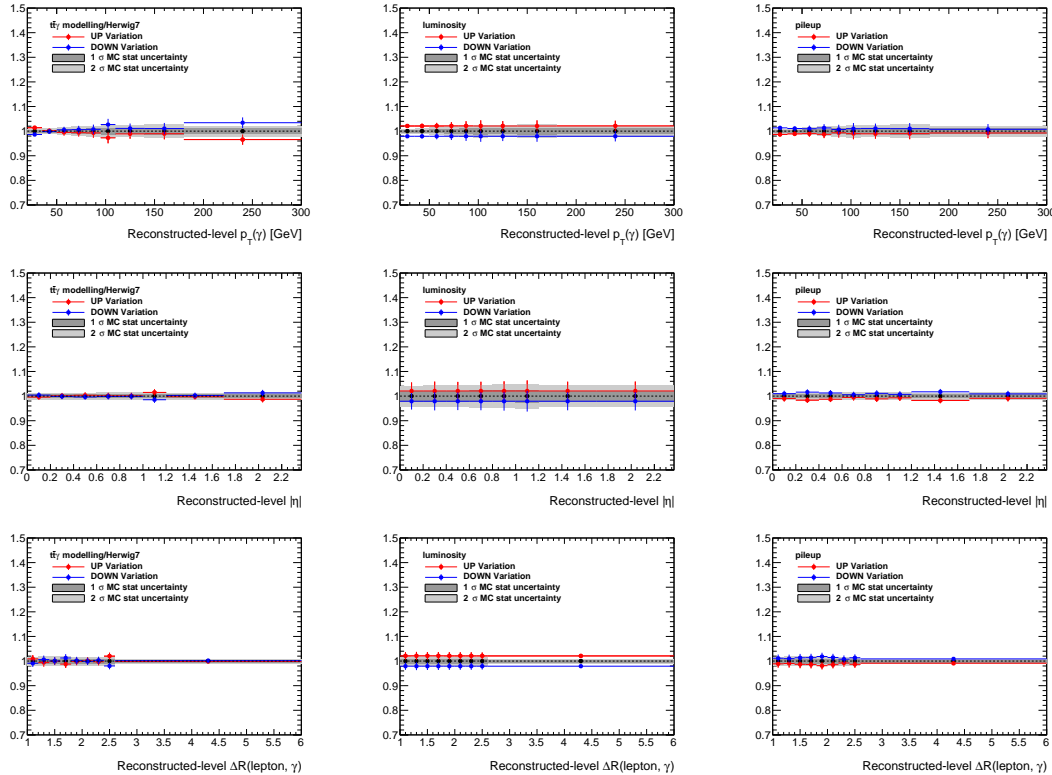


Figure 123: Reconstructed-level distributions of the size of the relative systematic shifts due to signal modelling (left), luminosity (centre) and pile-up (right), in bins of p_T (first row), $|\eta|$ (second row), minimum $\Delta R(\ell, \gamma)$ (third row) in the single-lepton channel.

Not reviewed, for internal circulation only

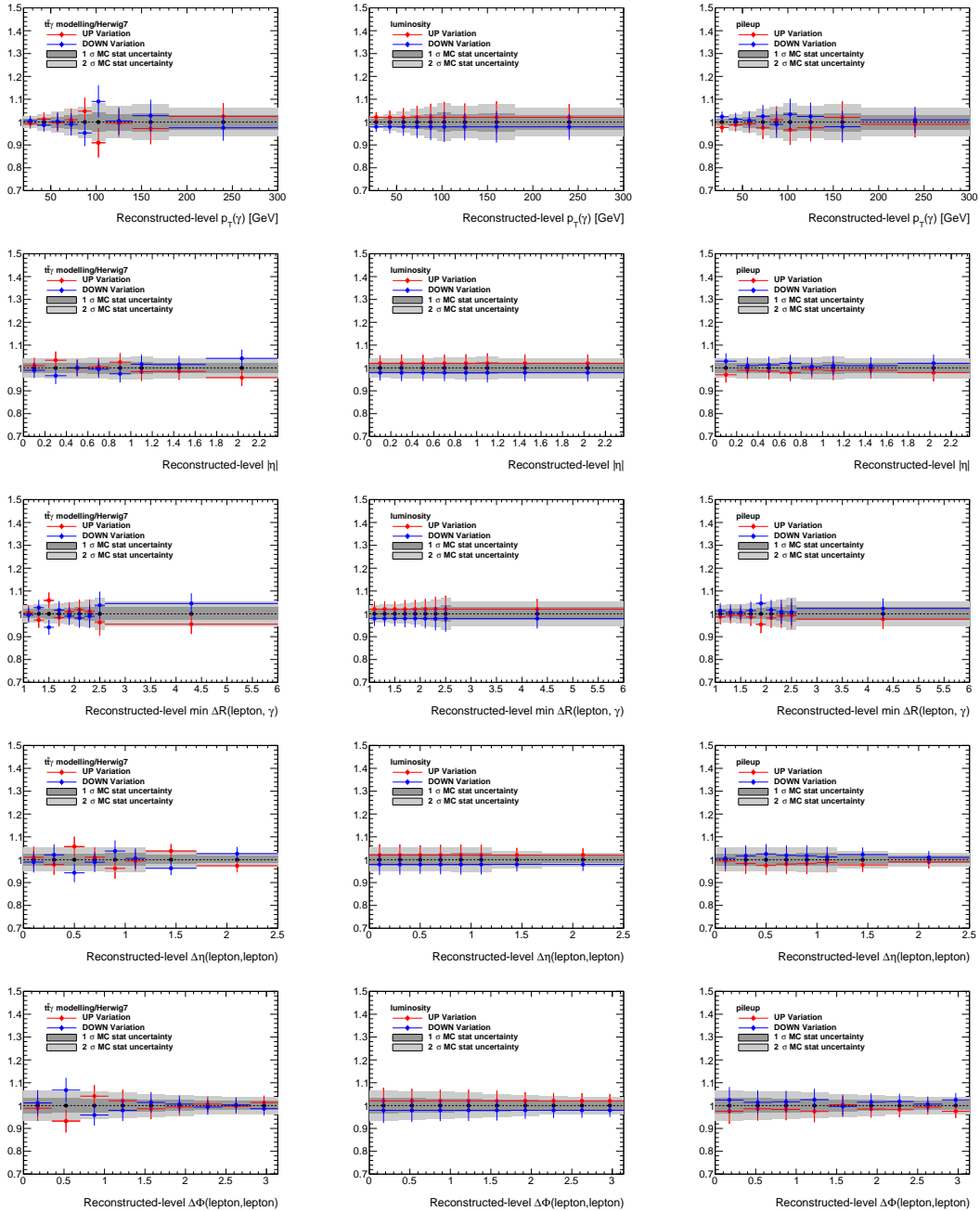


Figure 124: Reconstructed-level distributions of the size of the relative systematic shifts due to signal modelling (left), luminosity (centre) and pile-up (right), in bins of p_T (first row), $|\eta|$ (second row), minimum $\Delta R(\ell, \ell')$ (third row), $\Delta\eta(\ell, \ell')$ (fourth row) and $\Delta\phi(\ell, \ell')$ in the dilepton channel.

2057 I Unfolding using fine binning

2058 The binning used in this Appendix is optimised based only on the resolution and expected data statistics
 2059 checks. However, the final binning used in the analysis and shown in the main body of the note is further
 2060 optimised based on the final statistical uncertainty on the unfolded results. It turned out that after unfolding
 2061 the statistical uncertainty was magnified, thus a re-binning is performed and number of bins is reduced.
 2062 All checks are repeated for finer and wider binning.

2063 **I.1 Inputs**

2064 Figure 125 shows $1/\epsilon$ and $(1 - f_{\text{mig}})$ in the dilepton channel, while Figure 126 in the single lepton channel.
 2065 The migrations are shown in Figure 127 and Figure 128 in the dilepton and single lepton channels.

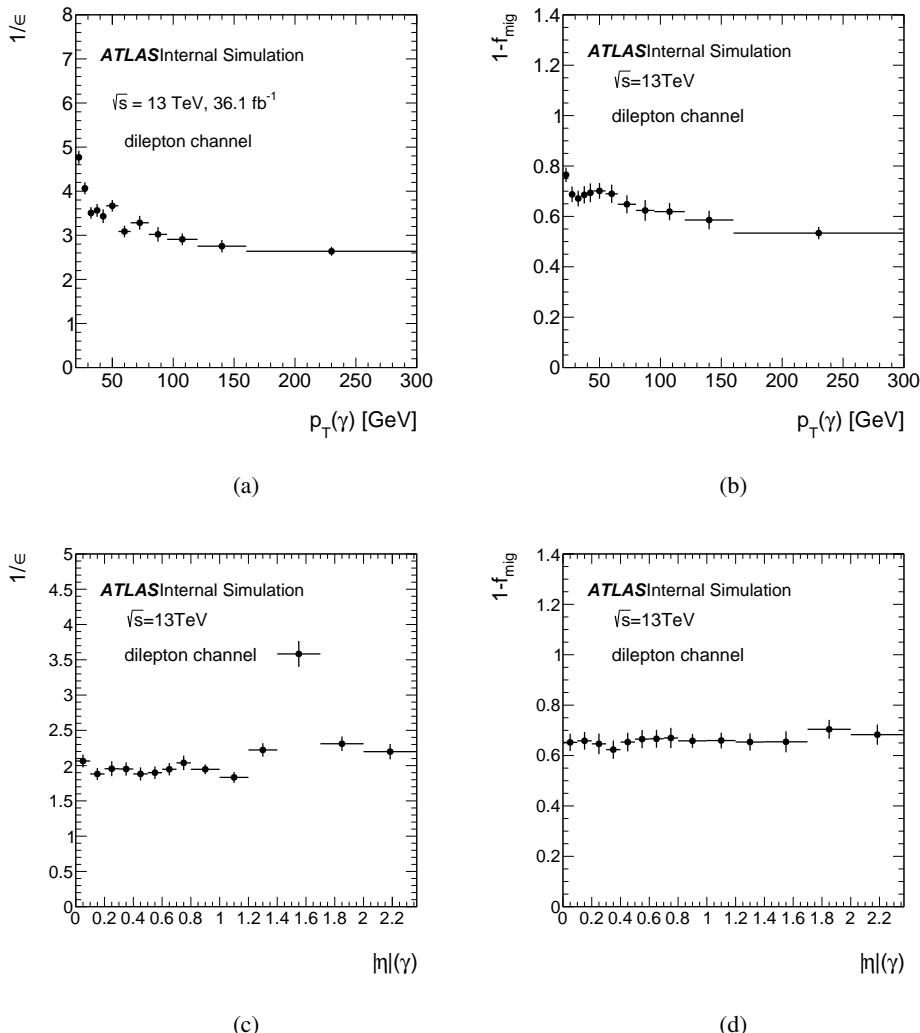


Figure 125: The inverse of signal efficiency $1/\epsilon$ (left) and fraction of non-outside migration $(1 - f_{\text{mig}})$ (right) as a function of (a), (b) the photon p_T , (c), (d) the photon $|\eta|$ in the dilepton channel.

Not reviewed, for internal circulation only

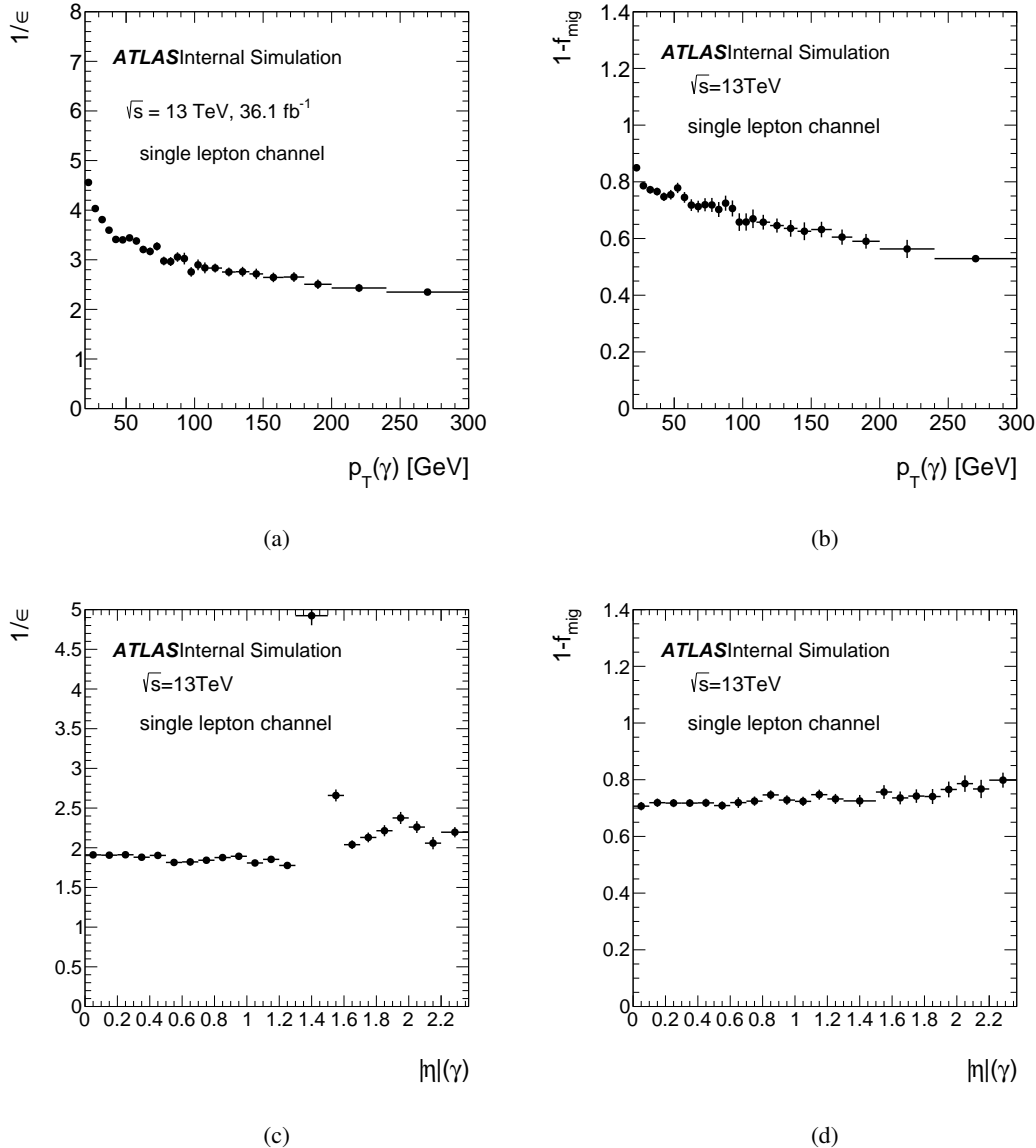


Figure 126: The inverse of signal efficiency $1/\epsilon$ (left) and fraction of non-outside migration ($1 - f_{\text{mig}}$) (right) as a function of (a), (b) the photon p_T , (c), (d) the photon $|\eta|$ in the single lepton channel.

Not reviewed, for internal circulation only

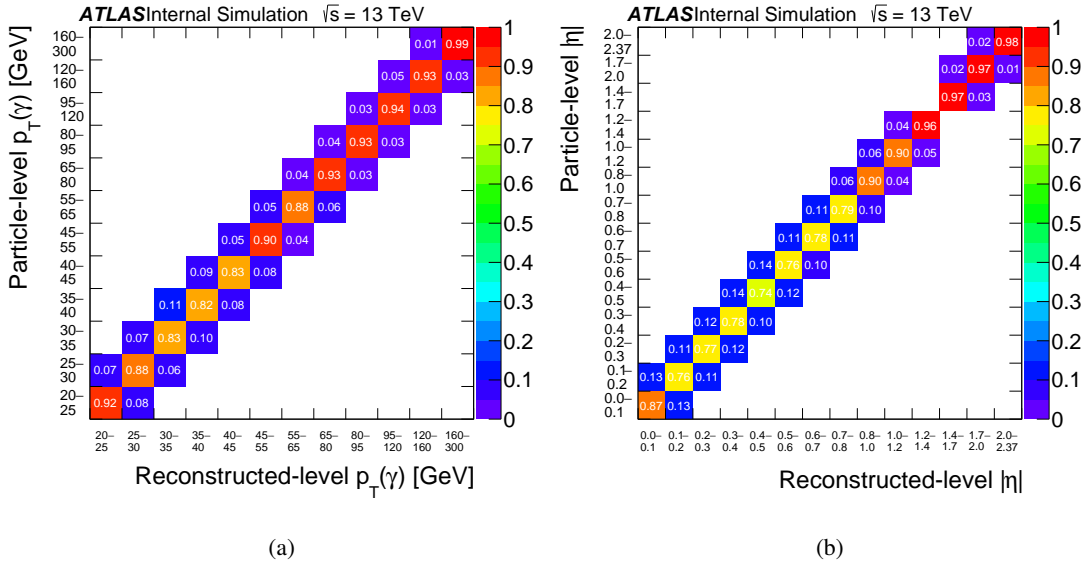


Figure 127: The bin-by-bin migration matrix of (a) the photon p_T and (b) the photon $|\eta|$ in the dilepton channel.

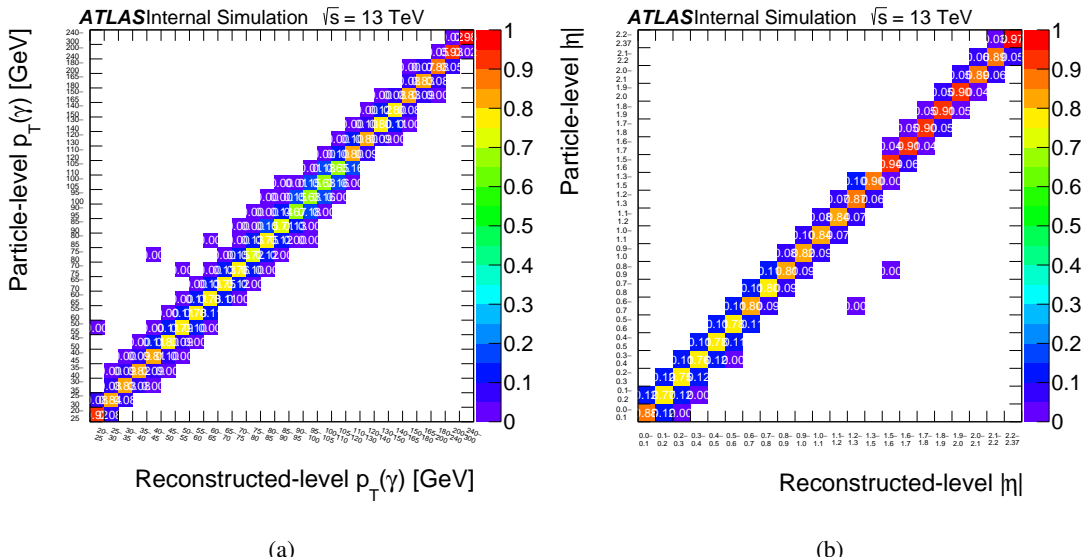


Figure 128: The bin-by-bin migration matrix of (a) the photon p_T and (b) the photon $|\eta|$ in the single lepton channel.

2066 **I.1.1 Optimising the number of iterations**

2067 In order to choose the number of iterations that to be used for unfolding, two methods are employed. The
 2068 final chosen number of iterations is a compromise between having a low difference in the unfolded results
 2069 between different iterations, having a stable statistical uncertainty in all bins, and having no bias against
 2070 any number of iterations.

2071 For the first method, the convergence of the unfolded results, is shown in Figure 129.

$$\frac{N^{\text{unf}, i+1} - N^{\text{unf}, i}}{N^{\text{unf}, i+1}} < 1\% \quad (72)$$

2072 The results of the RMS test are shown in Figure 130 for p_T and Figure 131 for η in the dilepton channel.
 2073 While for single lepton channel, are shown in Figure 132 for the photon's p_T , and Figure 133 for the
 2074 photon η .
 2075 From the first methods, the two variables and channels agree for 6 iterations, and most of bins are stable
 2076 after 6 iterations from the second method.

$$\text{RMS} = \frac{(\text{truth} - \text{unfolded})}{\text{unfolded}} \quad (73)$$

2077 **I.1.2 The closure test**

2078 The closure test is performed to check if the the unfolding procedure can recover the reconstructed
 2079 spectrum. To do that, the 100 pseudo data distributions of the testing par at the reconstruction-level are
 2080 unfolded using the migration matrix from the training part. A perfect closure is obtained, and shown in
 2081 Figure 134 for the dilepton and single lepton channels.

2082 **I.1.3 Pull study**

2083 The binning was chosen initially to have more diagonal matrices, with more than 50% of particle-level
 2084 events are reconstructed, as shown earlier in Section 9. The stability of the bin choice is checked
 2085 by performing pull tests. The same pseudo-data described in Section 11.1.1 is used and another 1000
 2086 pseudo-experiments are built from the reconstructed-level in the testing part using the Poisson distribution,
 2087 and then unfolded. The unfolded pseudo-results are then compared to the pseudo-particle level. The pulls
 2088 are calculated per bin (Equation 74) and fit by a Gaussian function (see Appendix J). The pull is expected
 2089 to have a mean value of zero, which indicates no bias, while a width of one which could mean that the
 2090 statistical uncertainty is estimated correctly. Figure 135 shows no bias in the bin choice, and the width is
 2091 consistent with one.

$$\text{Pull} = \frac{(\text{truth} - \text{unfolded})}{\sigma_{\text{unfold}}} \quad (74)$$

Not reviewed, for internal circulation only

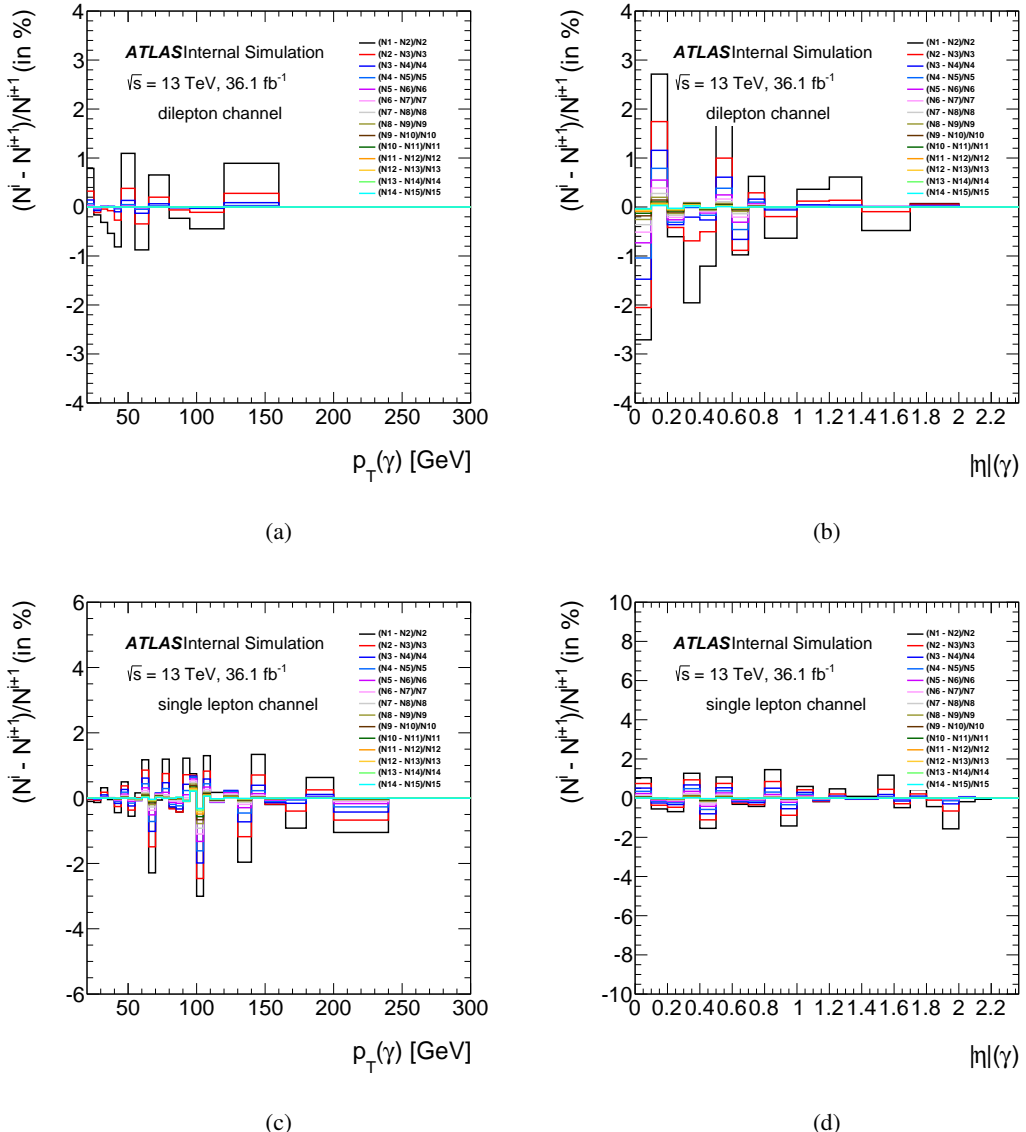


Figure 129: The relative difference on the unfolded result after two successive iterations as a function of the photon p_T (left) and the photon $|\eta|$ (right), (a) and (b) in dilepton channel, (c) and (d) in the single lepton channel.

Not reviewed, for internal circulation only

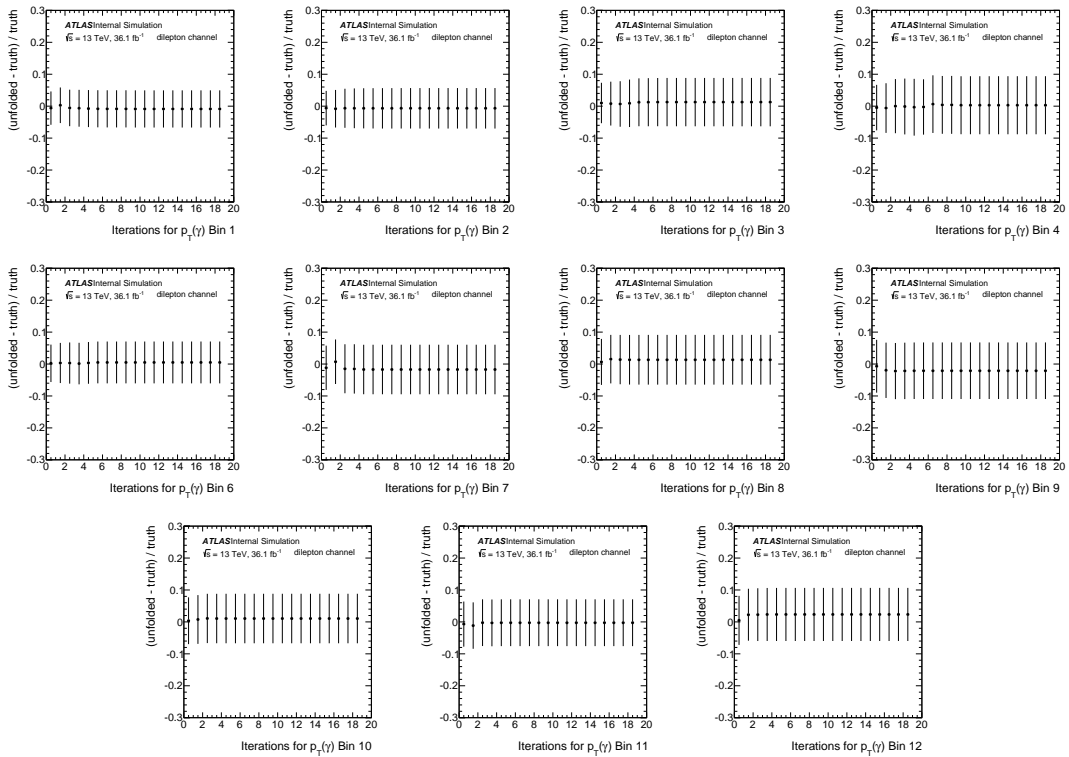


Figure 130: The RMS against the number of iterations for the 12 Bins in p_T in the dilepton channel.

2092 I.1.4 Stress tests

2093 The stress test is performed in order to verify that the unfolding procedure isn't biased to any specific shape
 2094 of the particle level distribution. The particle level and reconstructed level distributions obtained from the
 2095 nominal MC sample are reweighted, the reweighted reconstructed distribution is then unfolded using the
 2096 nominal inputs from the MC sample, and the unfolded results are compared to the corresponding particle
 2097 level distribution. Different weights have been checked, the first is by taking the observed difference
 2098 between data and MC as the following:

$$\text{weight} = 1 + Y \cdot \frac{\text{data}_i - \text{MC}_i}{\text{data}_i} = 1 + Y \cdot \text{Obs}, \quad (75)$$

2099 where i is the bin index and $Y = 1, -1$. The result of the stress test is shown in Figure 136. The unfolding
 2100 is able to retrieve the reweighted particle distribution for both variables η or p_T .

2101 A different weight is tried, and defined as the following in case of the photon's p_T :

$$\text{weight} = 1 + y \cdot \frac{100 - i}{300} = 1 + y \cdot X, \quad (76)$$

2102 while for the photon's η is given by:

$$\text{weight} = 1 + y \cdot \frac{1.2 - i}{2.37} = 1 + y \cdot X, \quad (77)$$

Not reviewed, for internal circulation only

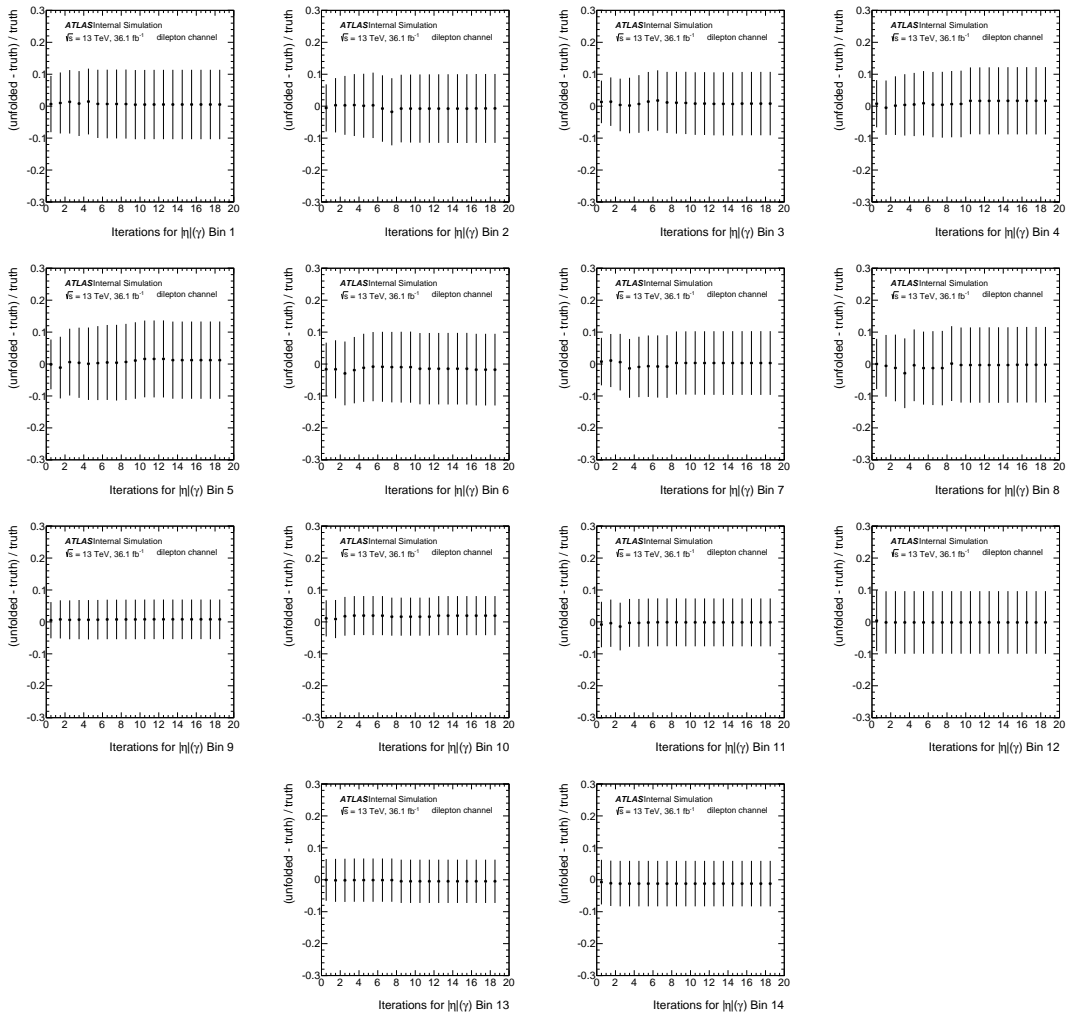


Figure 131: The RMS against the number of iterations for the 14 Bins in η in the dilepton channel.

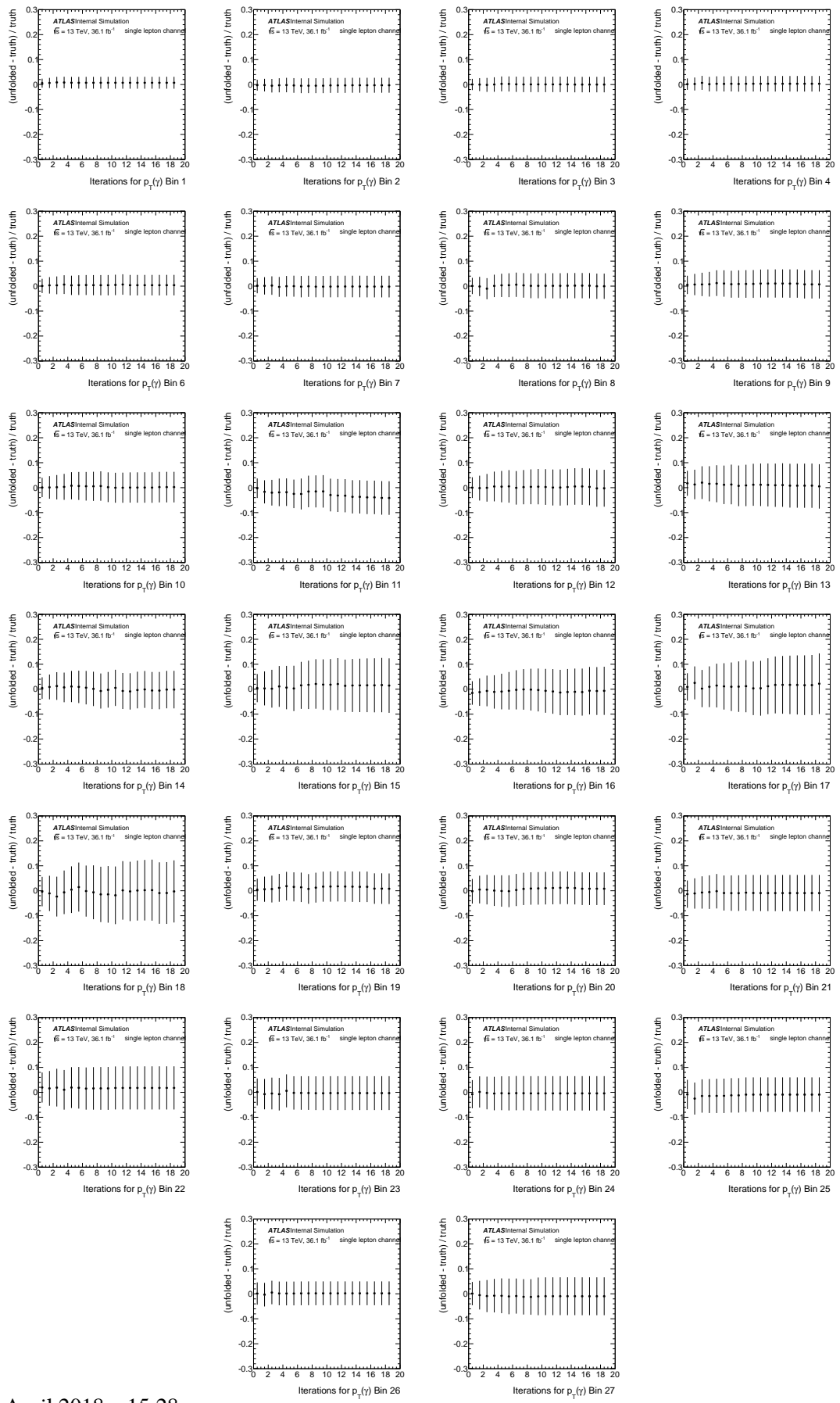
2103 where $y = -1, 1$ and i is the bin centre. The result of the second test is shown in the same Figure 136.
 2104 The reweighted particle level distribution are in different shapes from the nominal ones, and the unfolding
 2105 procedure is able to retrieve the reweighted particle level distributions in both channels.

2106 I.2 Cross-check methods

2107 I.2.1 Closure tests

2108 The test is done here to compare different methods by unfolding the reconstructed-level distribution, which
 2109 is estimated from MC. Figures 137 and 137 show the different unfolded results with different methods,
 2110 compared to the truth distribution in the dilepton and single lepton channels. The SVD method, show
 2111 always slightly different central values from the other methods, but agrees within the statistical uncertainty,
 2112 very good closure is achieved in photon's p_T .

Not reviewed, for internal circulation only

Figure 132: The RMS against the number of iterations for the 27 Bins in p_T in the single lepton channel.

Not reviewed, for internal circulation only

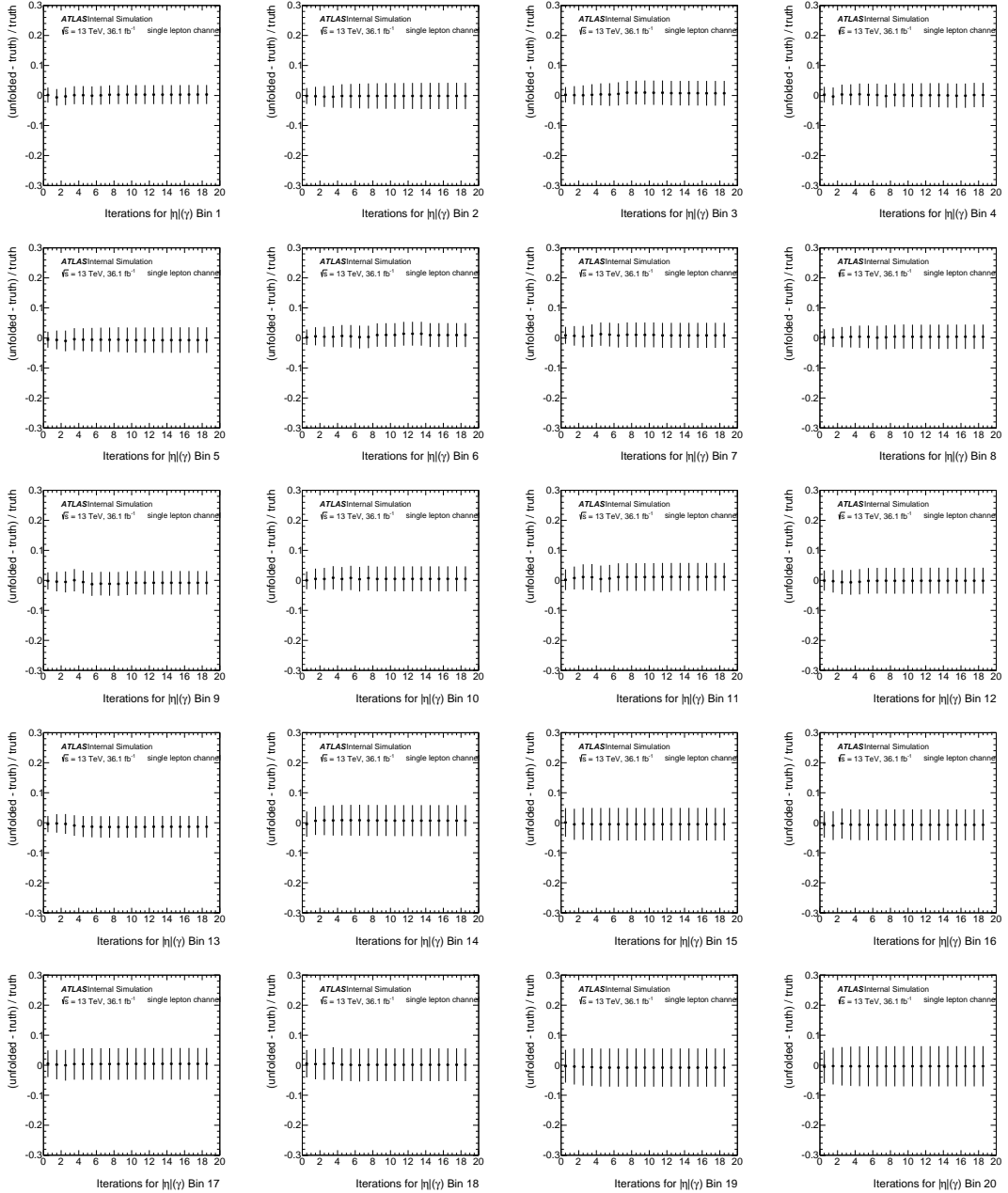


Figure 133: The RMS against the number of iterations for the 20 Bins in η in the single lepton channel.

Not reviewed, for internal circulation only

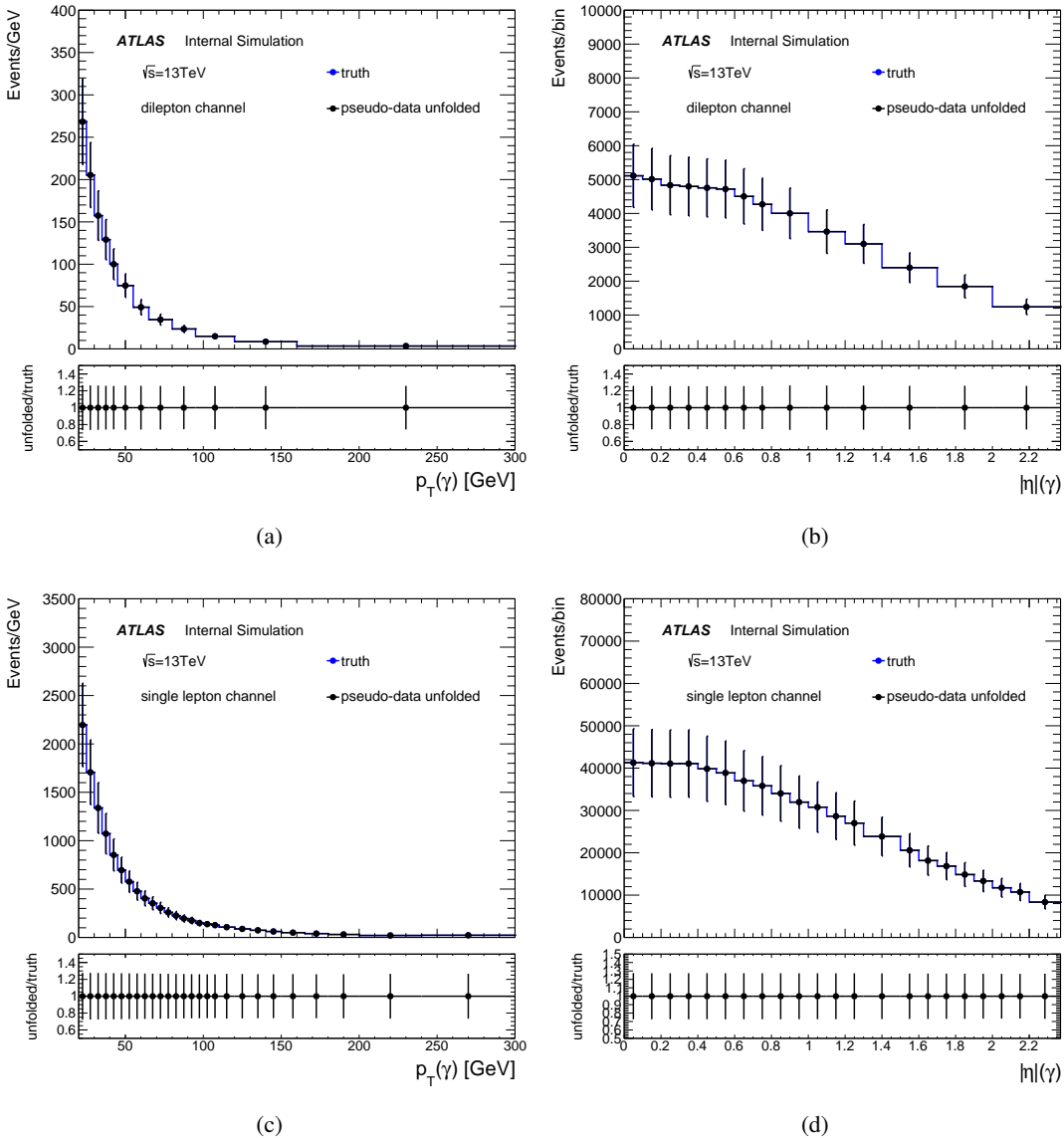


Figure 134: The ratio of the number of unfolded events for one pseudo-data after 6 iterations to the number of truth events, as a function of the photon p_T (left) and the photon η (right) in (a) and (b) the dilepton channel, (c) and (d) the single lepton channel.

Not reviewed, for internal circulation only

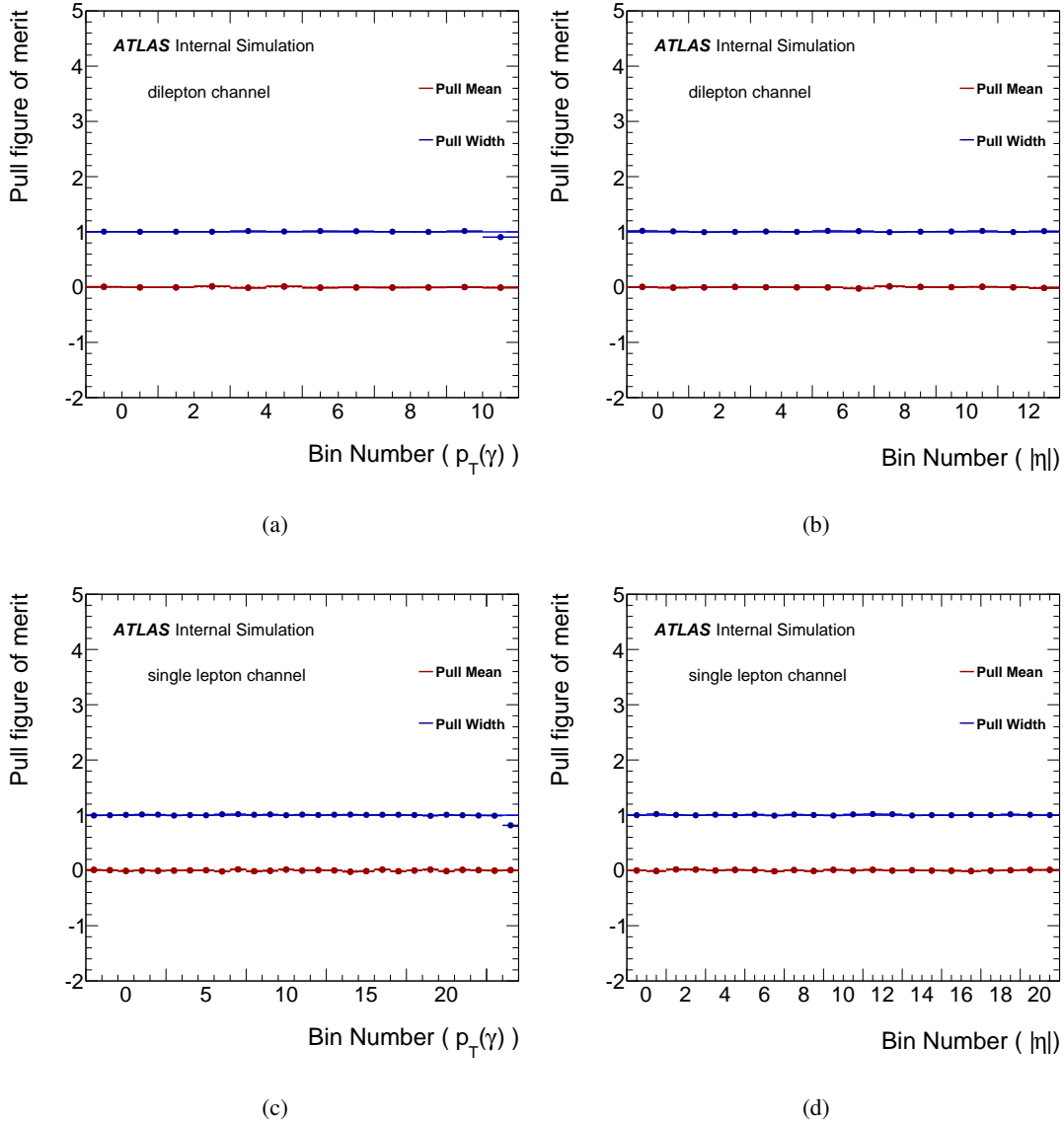


Figure 135: The pull test in each bin of the photon p_T (left), the photon η (right), after 6 iterations in (a) and (b) the dilepton channel, (c) and (d) the single lepton channel.

Not reviewed, for internal circulation only

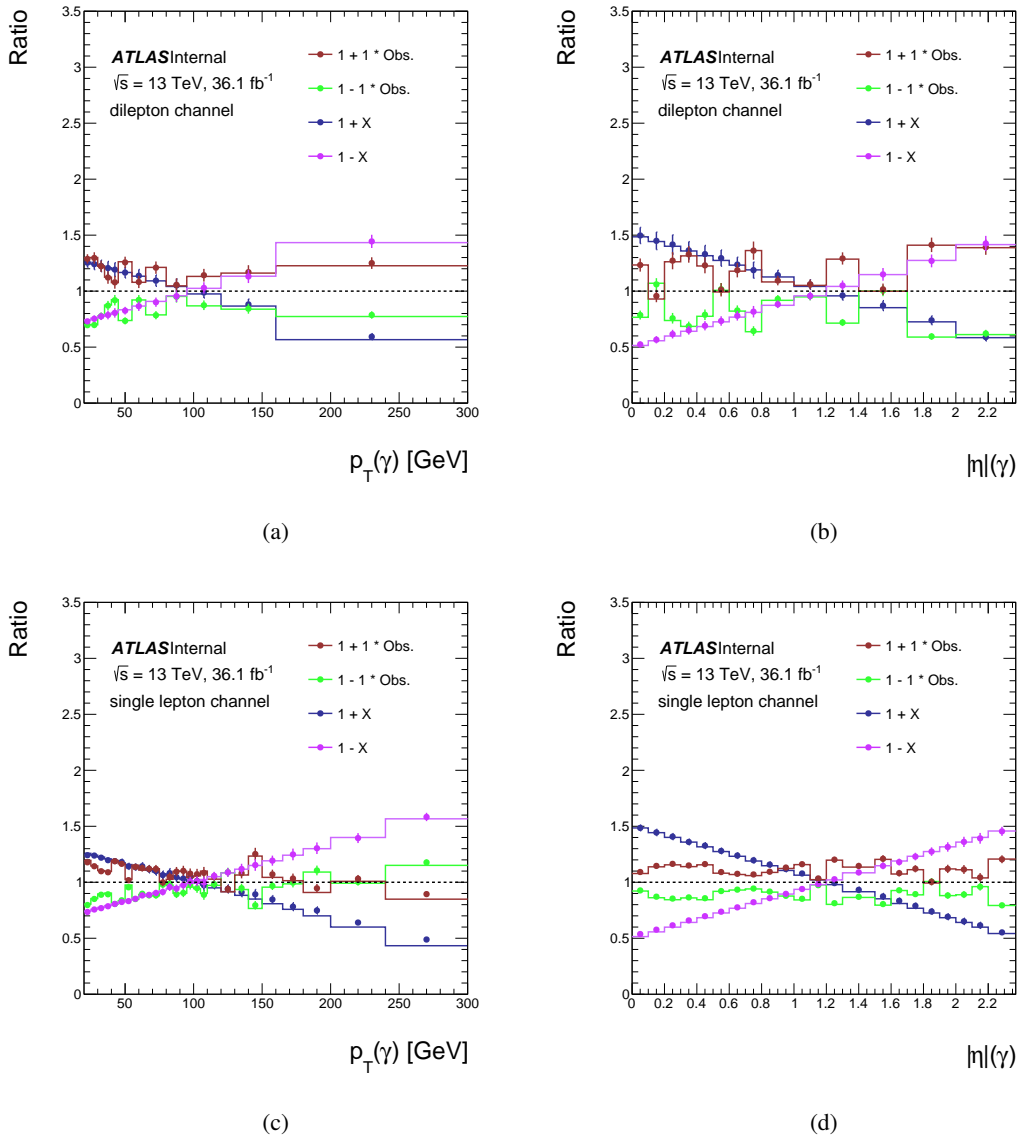


Figure 136: The stress test for the photon p_T (left), the photon η (right), in (a) and (b) the dilepton channel, (c) and (d) the single lepton channel. Both the dots and lines are ratios made with respect to the nominal particle level. The dots are the ratio of the unfolded reweighted distributions to the nominal particle level distribution, while the solid lines are the ratio of the reweighted particle level distributions to the nominal one. Obs. is defined in Equation 75, and X in Equations 76 and 77.

Not reviewed, for internal circulation only

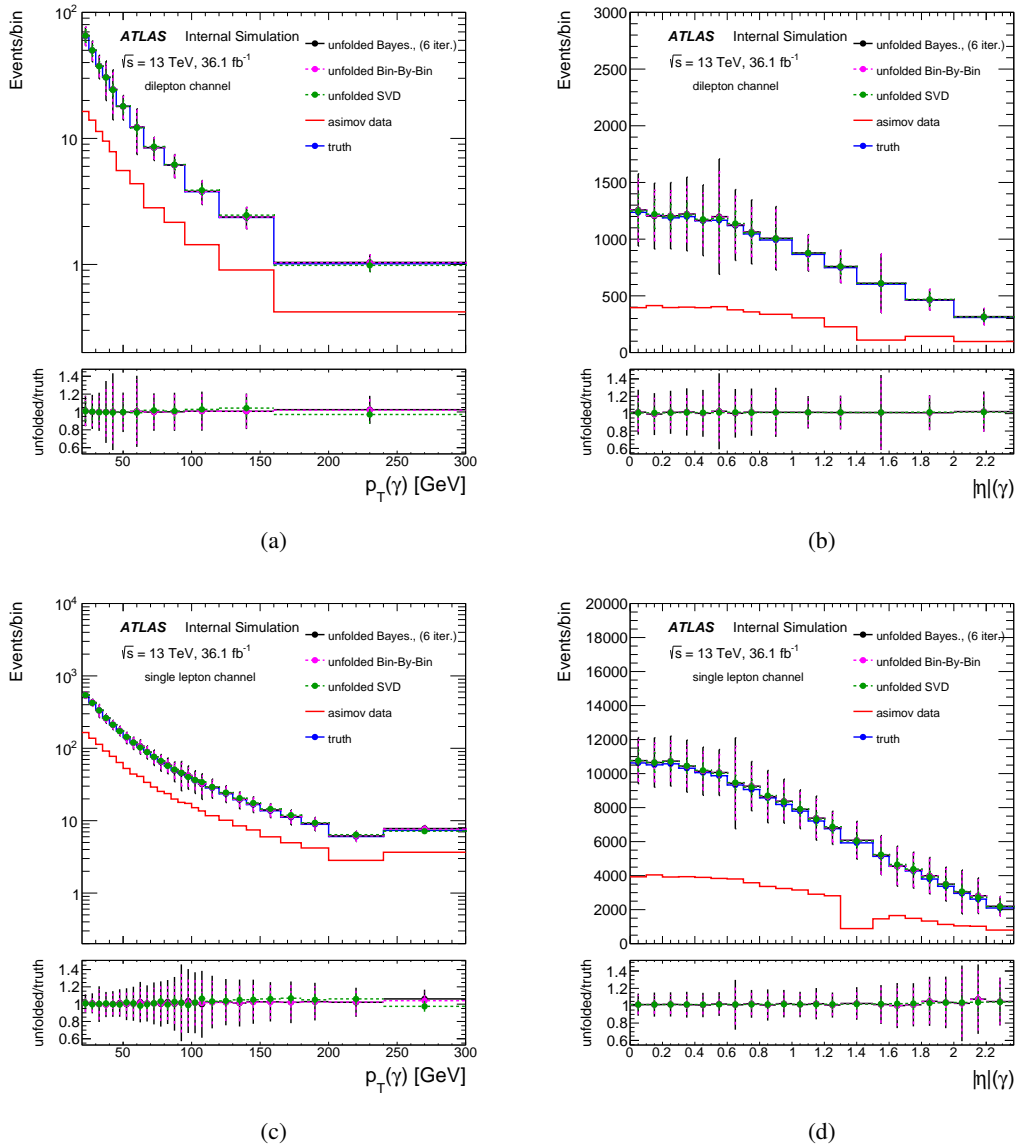


Figure 137: The number of unfolding events as a function of the photon p_T (left) and the photon η (right) in (a) and (b) the dilepton channel, (c) and (d) in the single lepton channel, obtained by the iterative method in black, after 6 iterations, the SVD in red and the bin-by-bin in magenta, in the dilepton channel. All are compared to the truth distribution in blue (the ratio plot). The yellow distribution is the original reconstructed distribution before unfolding. The distribution are normalized to a luminosity of 36.1 fb^{-1} .

2113 J Pull study for unfolding with IBS

2114 Example distributions of the pulls calculated per photon p_T and photon $|\eta|$ bins in the dilepton channel
 2115 (see Section 11.1.4) are shown in Figure 138 and Figure 139, respectively. The Gaussian fit is shown in
 2116 red.

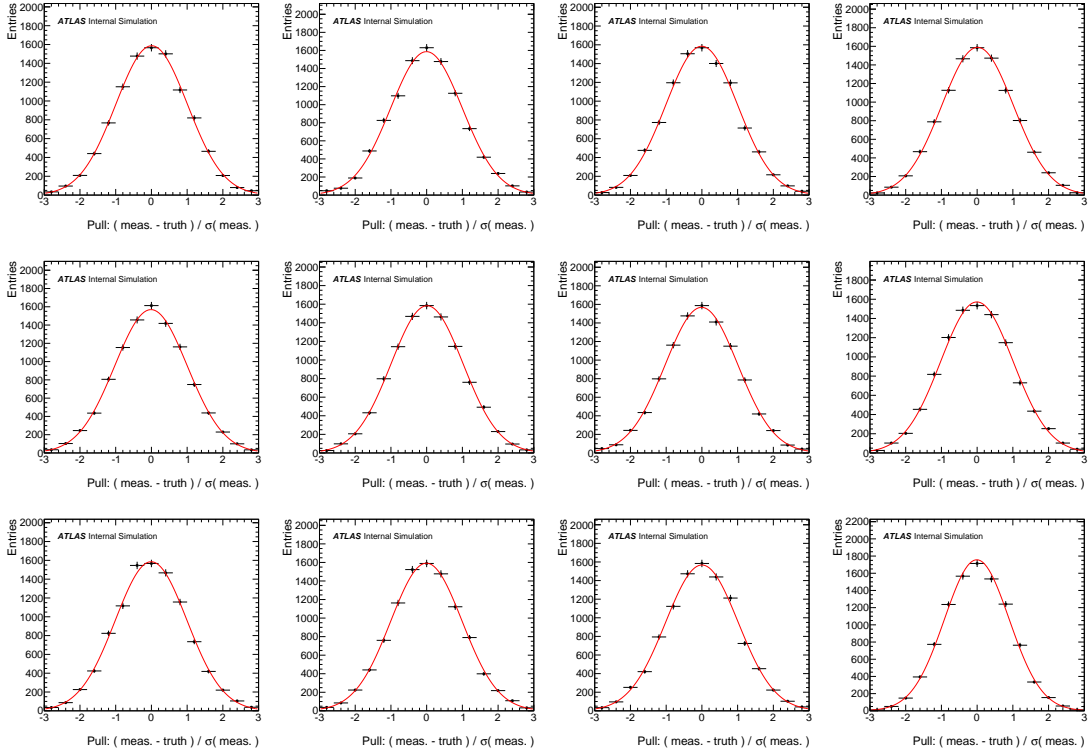


Figure 138: The distributions of the pull in each bin of p_T (black dots) in the dilepton channel. The Gaussian fit is shown in red.

Not reviewed, for internal circulation only

Not reviewed, for internal circulation only

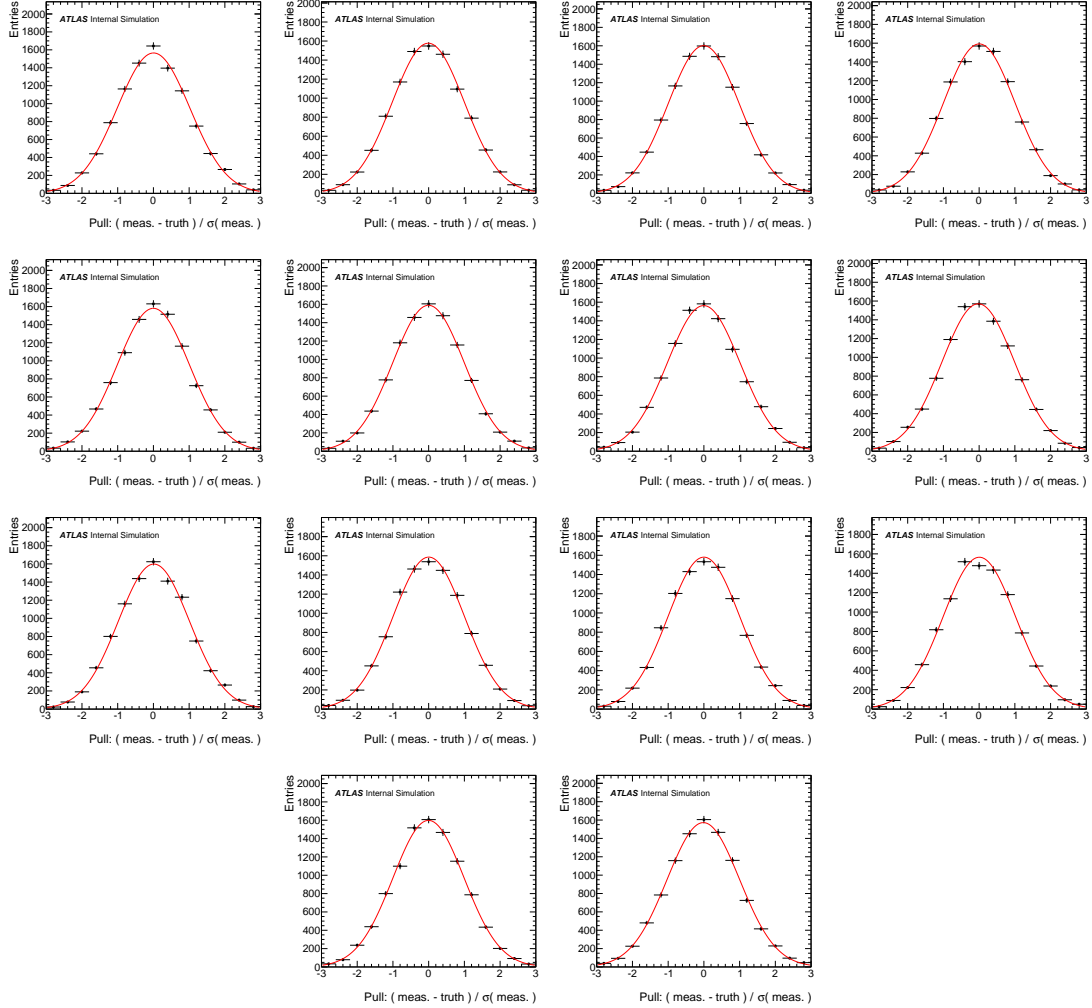


Figure 139: The distributions of the pull in each bin of η (black dots) in the dilepton channel. The Gaussian fit is shown in red.

2117 K Results appendix

2118 K.1 Results for $e+jets$, $\mu+jets$, ee , $\mu\mu$ and $e\mu$

2119 This section contains the results for each of the individual channels that make up the single lepton and
2120 dilepton channels. Pre- and post-fit plots can be seen in Figures 140, 141, 142, 143 and 144.

2121 The total contributions relative to μ are summarised in Figure 145. The JES contribution includes *Jet*
2122 *flavour composition*, *Jet flavour response*, *Jet eta intercalibration*, *Jet pileup* (with the largest contribution
2123 coming from *RhoTopology*), *Jet effective NP*, *Jet single particle HightPt*, *Jet Punchthrough MC15* and *Jet*
2124 *BJES response*.

2125 Nuisance parameter pull plots are shown in Figure 146 and Figure 147.

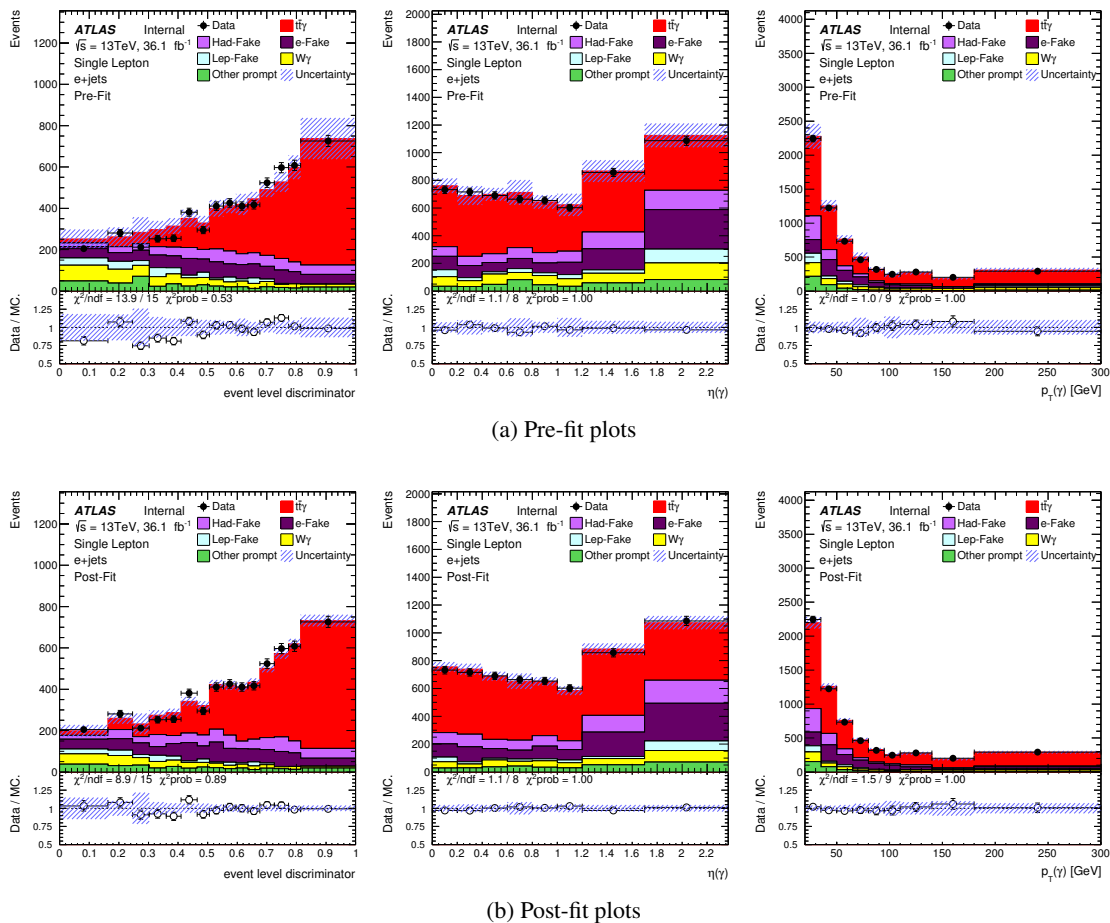


Figure 140: Pre- and post-fit plots for the $e+jets$ channel where the ELD is used as the discriminating variable in the fit.

Not reviewed, for internal circulation only

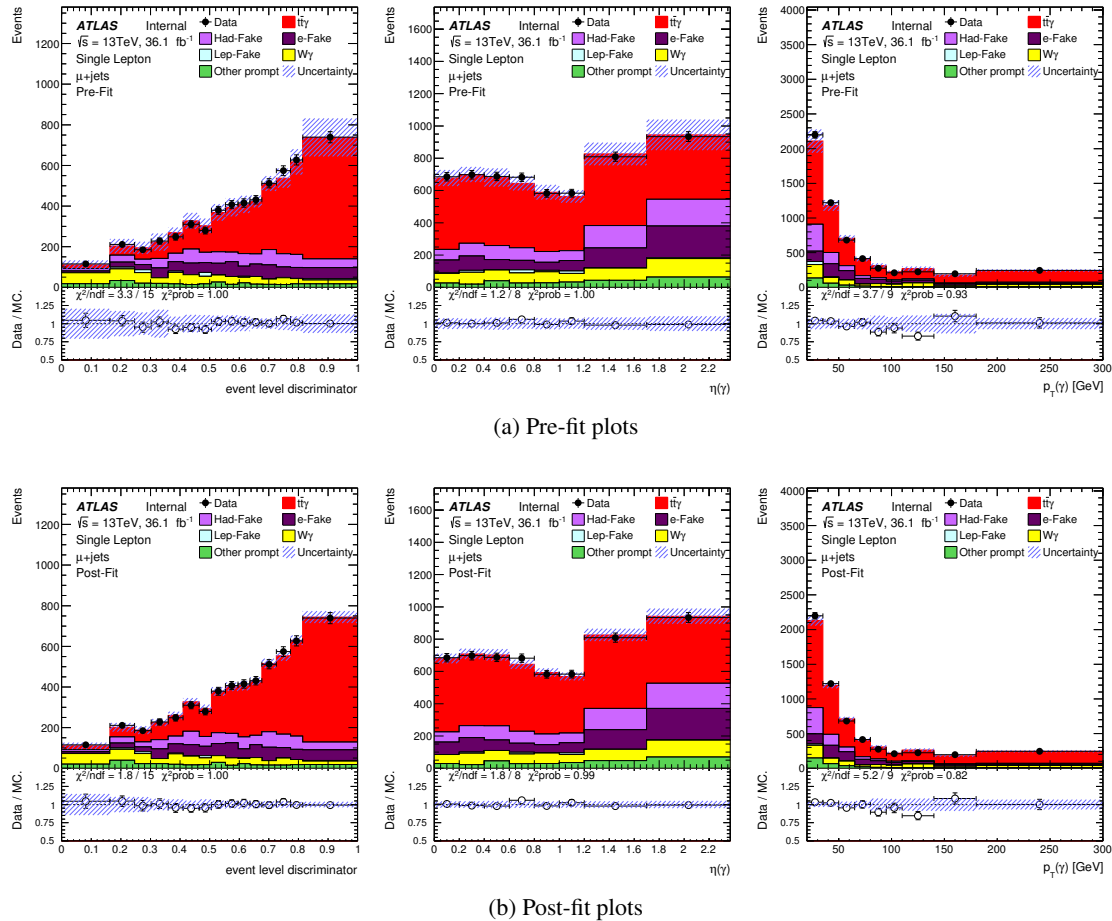


Figure 141: Pre- and post-fit plots for the $\mu+jets$ channel where the ELD is used as the discriminating variable in the fit.

2126 K.2 Asimov fit scenarios: $V\gamma$ floating or constrained

2127 Two Asimov fit scenarios are considered: either fixing $V\gamma$ backgrounds to MC prediction with a 50%
2128 uncertainty or floating them.

2129 The fits results for are summarised in Table 44, from which it can be found that the difference in terms
2130 of signal strength between these two scenarios is very small. In the same table, it is attempted to split
2131 one signal region into two signal regions according to the number of b -jets, of which the results are very
2132 similar to the case without splitting, except that a tighter constraint can be imposed on the floated $V\gamma$
2133 normalisation.

2134 These fits make use of an older k-factor and also contain the k-factor theoretical uncertainty. However,
2135 since they are self-contained tests on Asimov data the behaviour of the fit is still relevant.

2136 K.2.1 single lepton and dilepton combined pull plots

2137 The pull plots for the single lepton and dilepton combined fits are shown in Figure 148 and 149.

Not reviewed, for internal circulation only

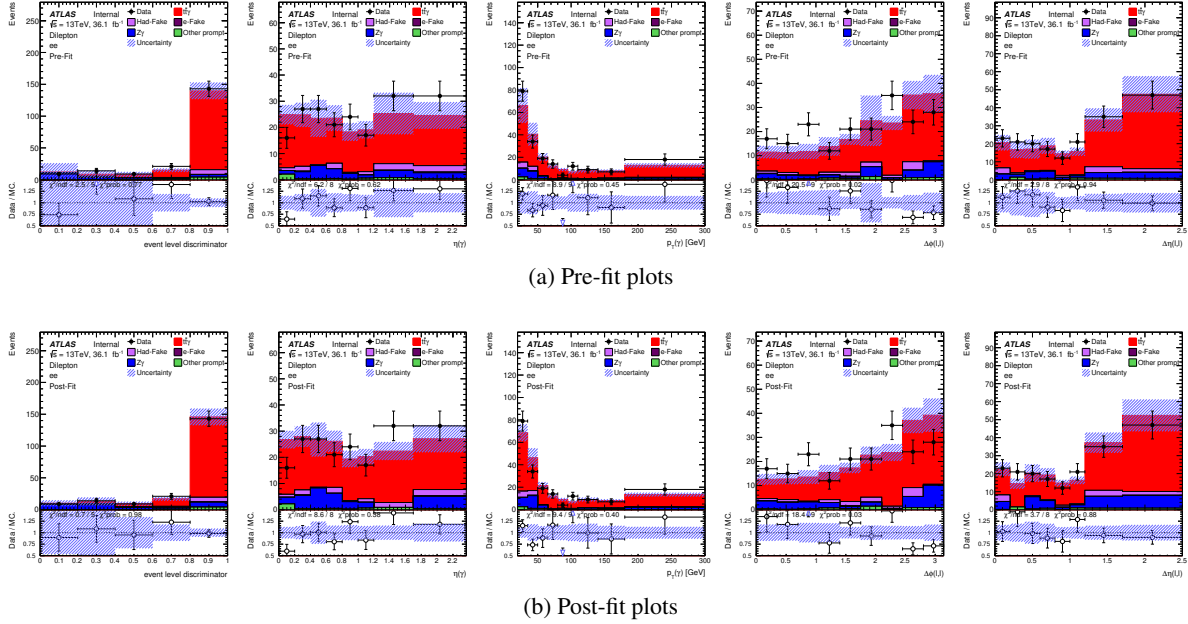


Figure 142: Pre- and post-fit plots for the ee channel where the ELD is used as the discriminating variable in the fit.

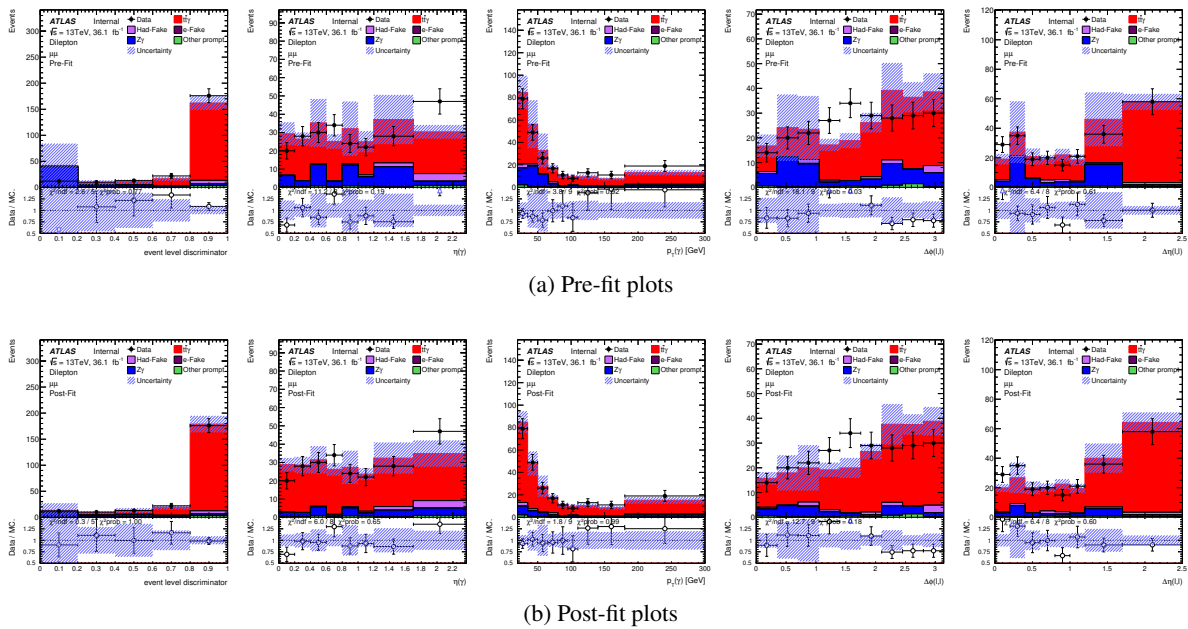


Figure 143: Pre- and post-fit plots for the $\mu\mu$ channel where the ELD is used as the discriminating variable in the fit.

Not reviewed, for internal circulation only

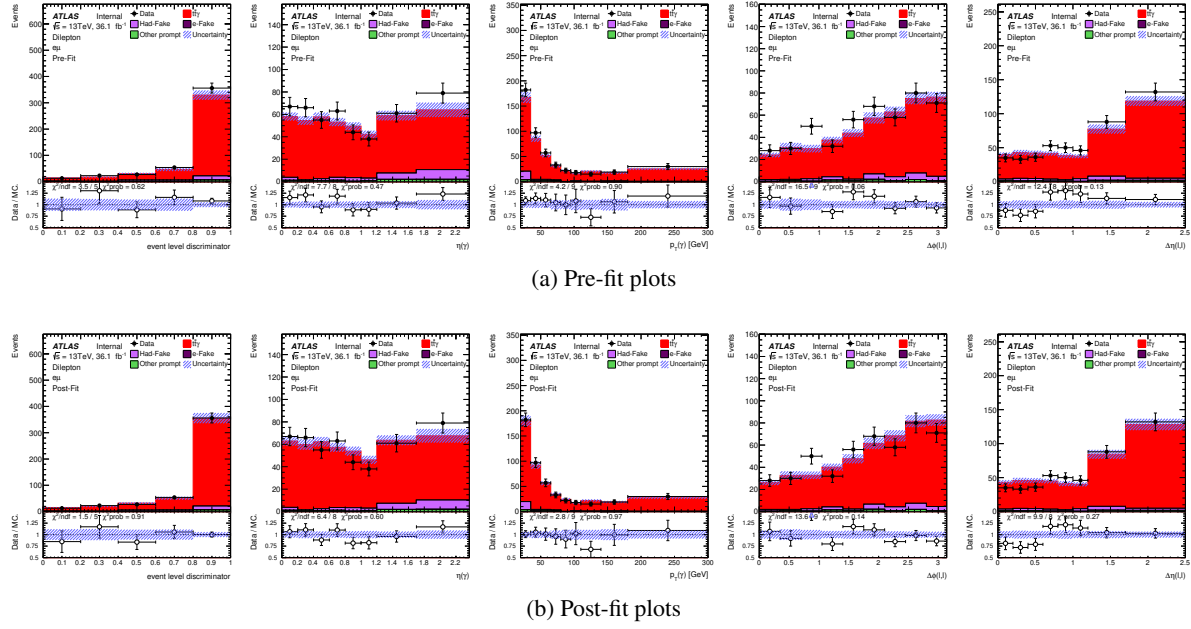


Figure 144: Pre- and post-fit plots for the ee channel where the ELD is used as the discriminating variable in the fit.

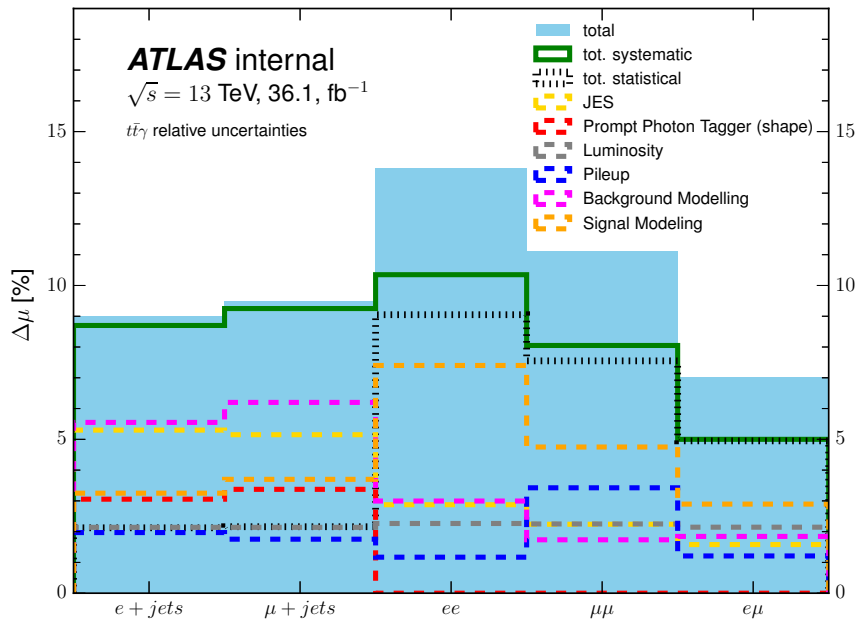


Figure 145: Grouped uncertainties for the individual channels relative to the signal strength.

Not reviewed, for internal circulation only

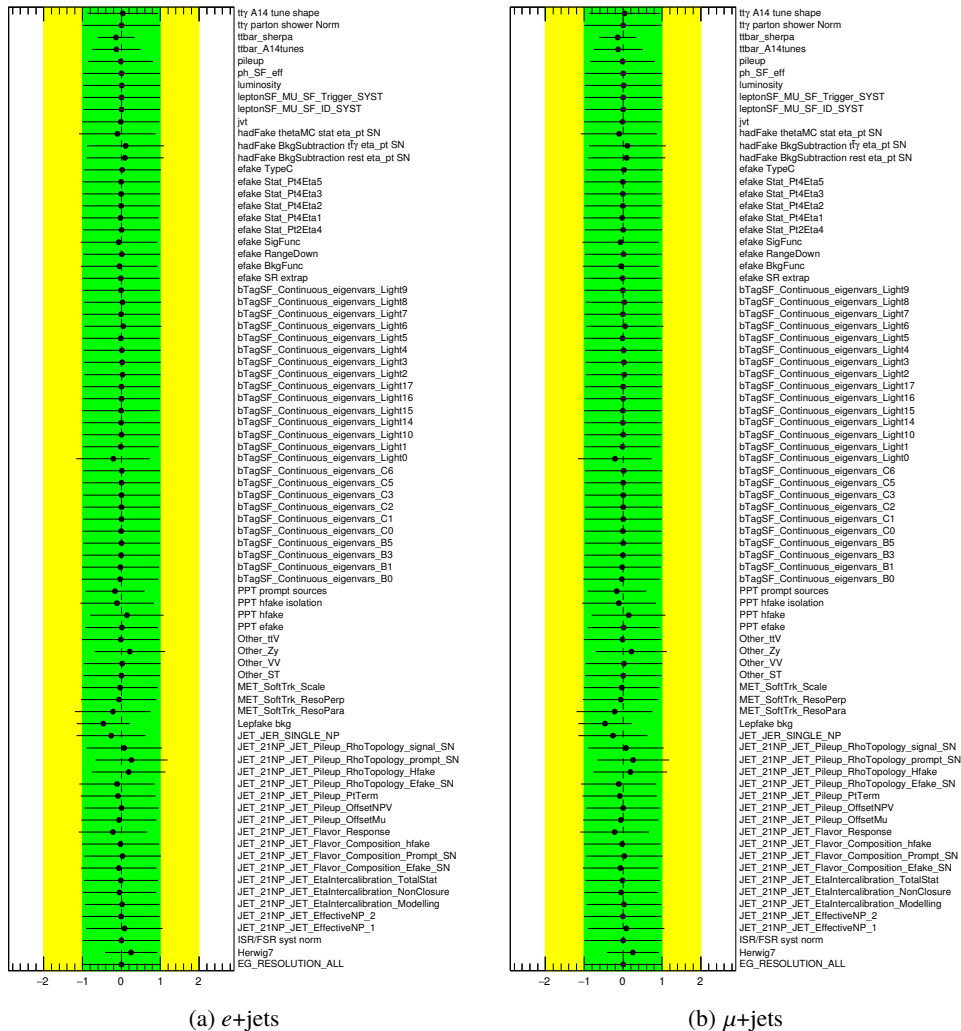


Figure 146: Pull plots for all nuisance parameters in the single lepton channels after a 0.7% pruning has been applied.

Table 44: 36.1 fb^{-1} Asimov fit results for each channel and a variety of scenarios. $V\gamma$ refers to $W\gamma$ for single lepton and $Z\gamma$ for dilepton. A dash infers that the $V\gamma$ background has been constrained with a systematic uncertainty of 50%, opposed to being left floating in the fit. Systematics described in 8 have been included in the fit with the exception of the PPT and $e \rightarrow \gamma$ fake systematics. Also included for these scenarios is the signal k-factor uncertainty.

channel	ELD template(s)	\pm error (μ)	\pm error ($V\gamma$)	S/B	$S/\sqrt{S+B}$
$e + jets$	≥ 1 btag	0.2693	-	1.36 ± 0.06	43.82 ± 2.09
	≥ 1 btag	0.2689	0.5680		
	$=1$ btag, ≥ 2 btag	0.2686	-		
	$=1$ btag, ≥ 2 btag	0.2691	0.3603		
$\mu + jets$	≥ 1 btag	0.2671	-	1.62 ± 0.07	44.11 ± 2.06
	≥ 1 btag	0.2684	0.2879		
	$=1$ btag, ≥ 2 btag	0.2688	-		
	$=1$ btag, ≥ 2 btag	0.2696	0.2435		
single lepton	≥ 1 btag	0.2633	-	1.47 ± 0.09	62.13 ± 4.09
	≥ 1 btag	0.2658	0.2714		
	$=1$ btag, ≥ 2 btag	0.2653	-		
	$=1$ btag, ≥ 2 btag	0.2659	0.2139		
ee	≥ 1 btag	0.3045	-	3.15 ± 0.41	10.24 ± 1.70
	≥ 1 btag	0.3054	0.3443		
	$=1$ btag, ≥ 2 btag	0.3025	-		
	$=1$ btag, ≥ 2 btag	0.3029	0.3495		
$\mu\mu$	≥ 1 btag	0.2987	-	1.93 ± 0.29	10.46 ± 1.67
	≥ 1 btag	0.2996	0.2915		
	$=1$ btag, ≥ 2 btag	0.2987	-		
	$=1$ btag, ≥ 2 btag	0.2998	0.2840		
$e\mu$	≥ 1 btag	0.2810	-	11.34 ± 0.87	18.71 ± 1.85
	$=1$ btag, ≥ 2 btag	0.2856	-		
dilepton	≥ 1 btag	0.2771	-	4.20 ± 0.50	23.53 ± 3.13
	≥ 1 btag	0.2779	0.2362		
	$=1$ btag, ≥ 2 btag	0.2767	-		
	$=1$ btag, ≥ 2 btag	0.2778	0.2337		

Not reviewed, for internal circulation only

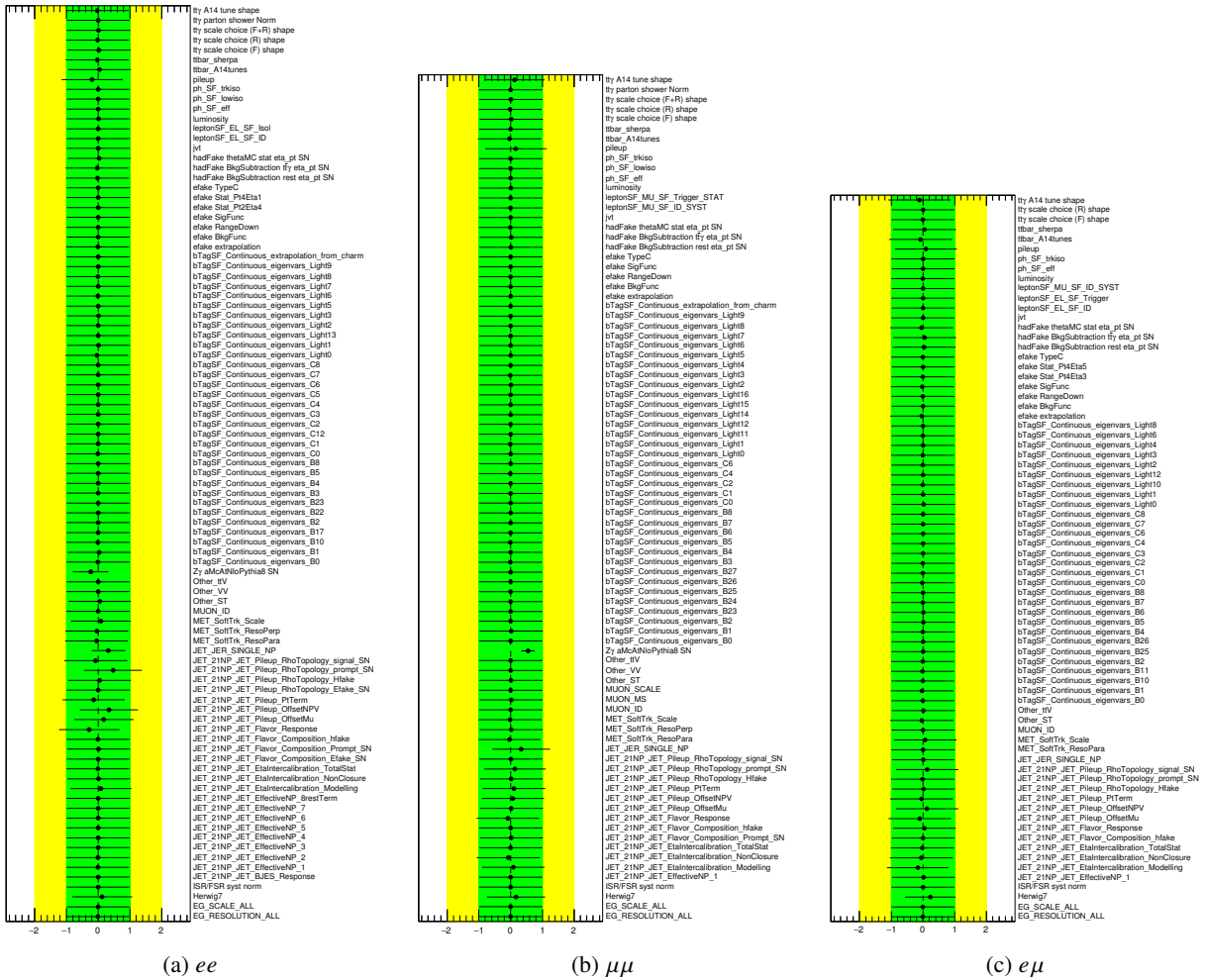


Figure 147: Pull plots for all nuisance parameters in the dilepton channels after a 0.7% pruning has been applied.

From the nuisance parameter plots we can see that in both the separated and combined single lepton cases the Lep fake background is constrained. The $W\gamma$ background, when not a floating parameter in the fit, is also constrained. Similarly for the separate and combined dilepton, there is tension for the $Z\gamma$ background when it is constrained in the fit, hinting that 50% assigned uncertainty is perhaps too conservative. These fits make use of the systematics defined in Section 8 with the exception of the PPT and $e \rightarrow \gamma$ fake systematics. The theoretical uncertainty on the k-factor is also included. Scale factors and uncertainties derived for the $e \rightarrow \gamma$ fake and hadronic fake background are also included.

K.2.2 Individual channel pull plots

The pull plots for individual channels are shown in Figure 150, 151, 152, 153 and 154.

Not reviewed, for internal circulation only

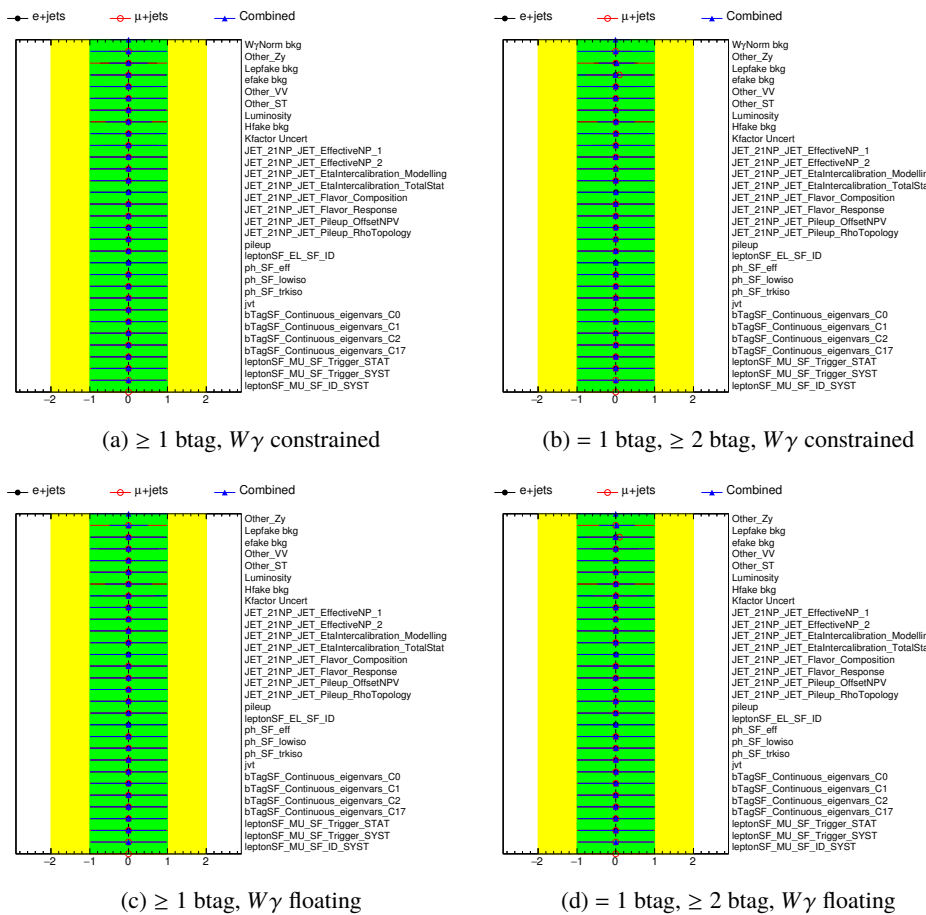


Figure 148: Pull plots for the combined single lepton channels showing $W\gamma$ constrained and floating. See Table 44 for reference. They are also shown for the case of splitting the signal region according to the number of b -jets.

Not reviewed, for internal circulation only

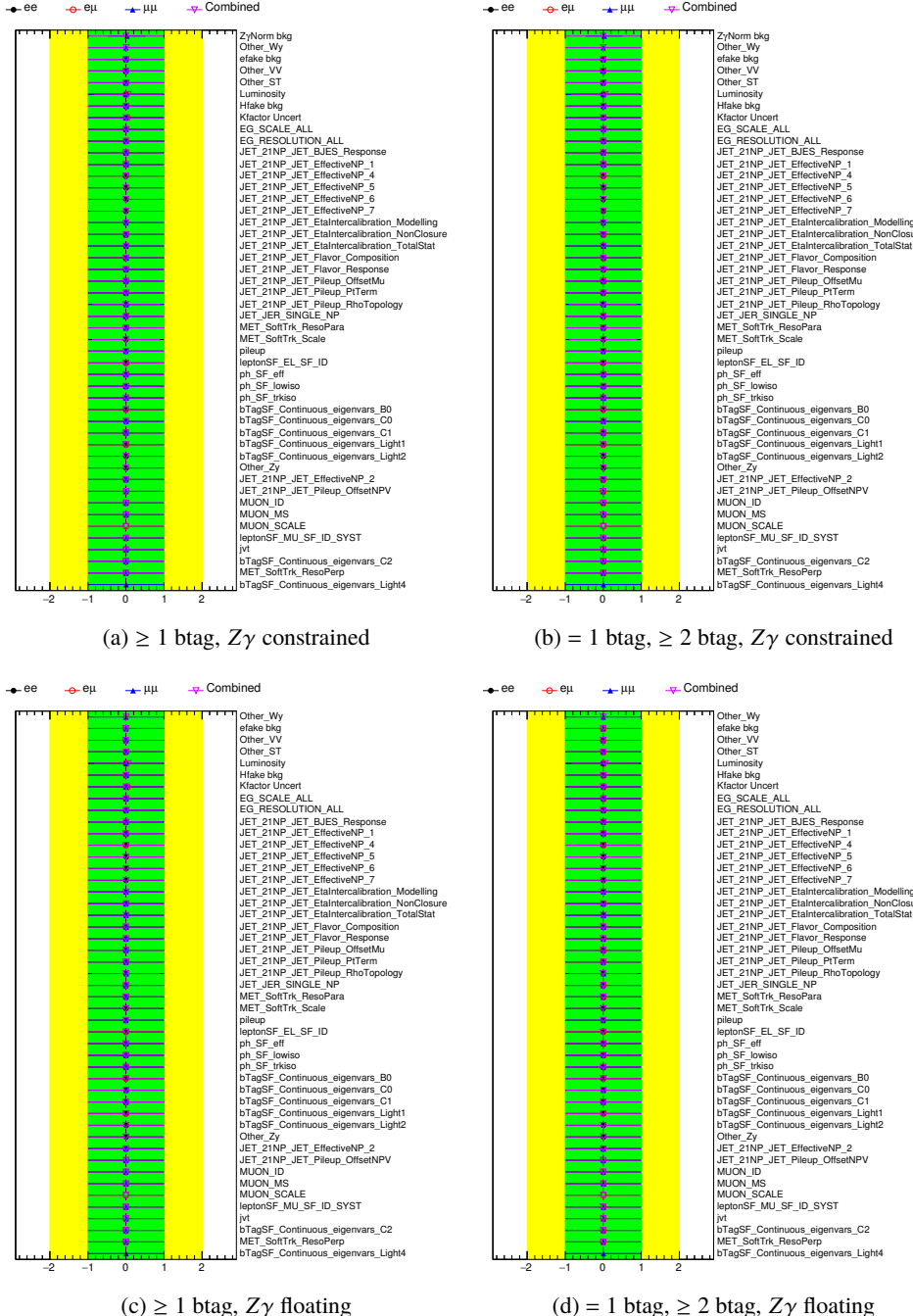


Figure 149: Pull plots for the combined dilepton channels showing $Z\gamma$ constrained and floating. See Table 44 for reference. They are also shown for the case of splitting the signal region according to the number of b -jets.

Not reviewed, for internal circulation only

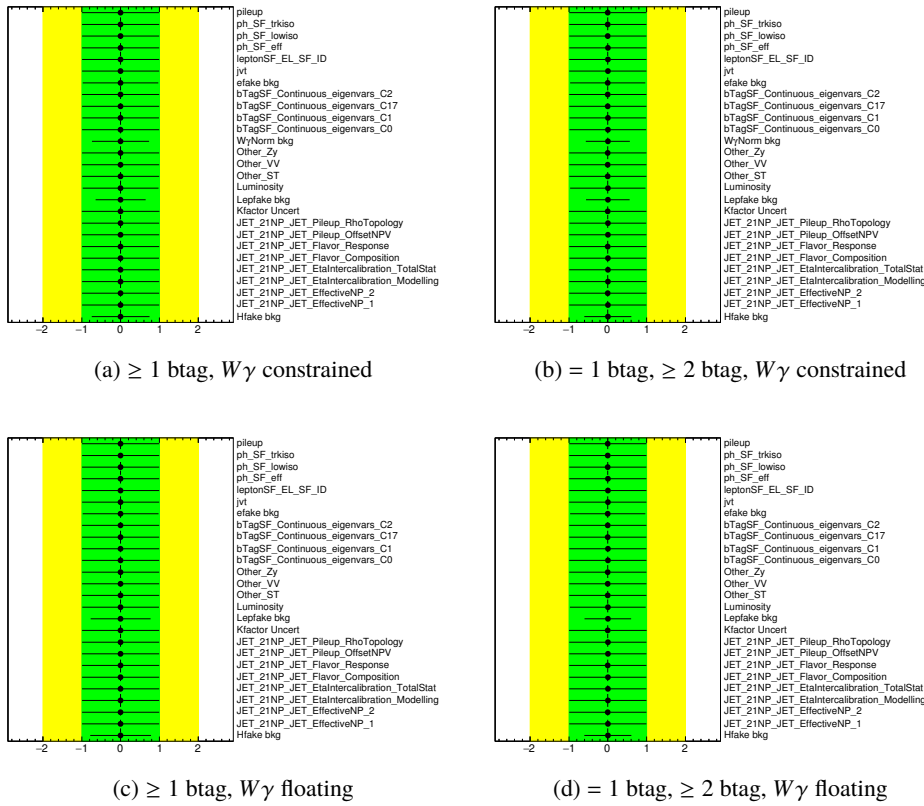


Figure 150: Pull plots for the $e+jets$ channels showing $W\gamma$ constrained and floating. See Table 44 for reference.

Not reviewed, for internal circulation only

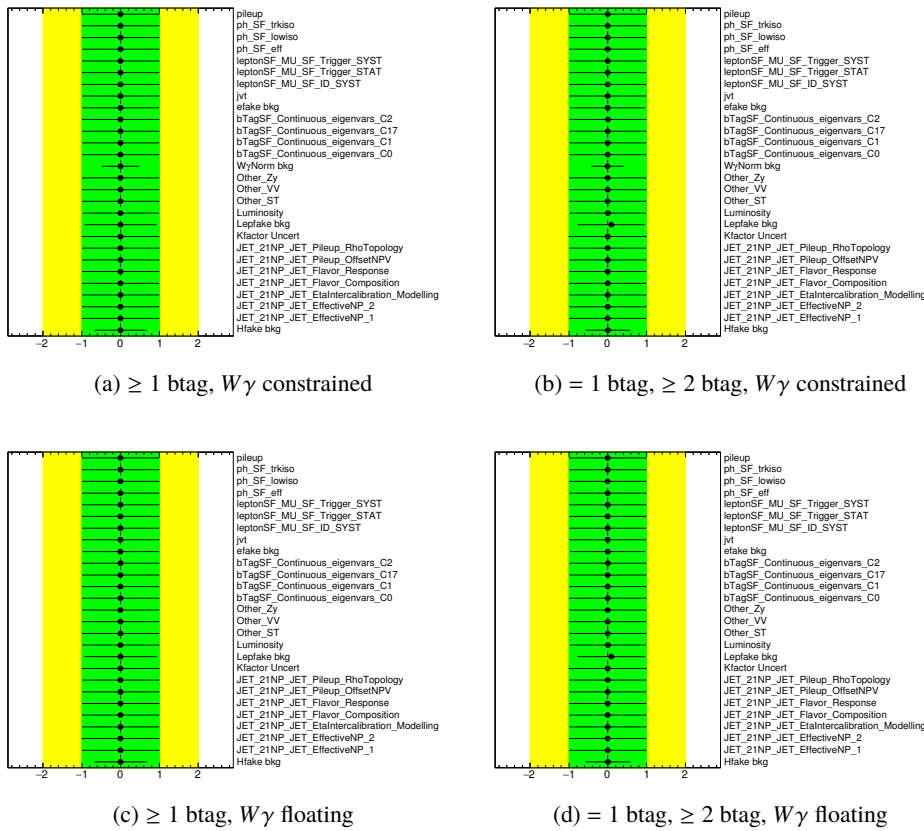


Figure 151: Pull plots for the μ +jets channels showing $W\gamma$ constrained and floating. See Table 44 for reference.

Not reviewed, for internal circulation only

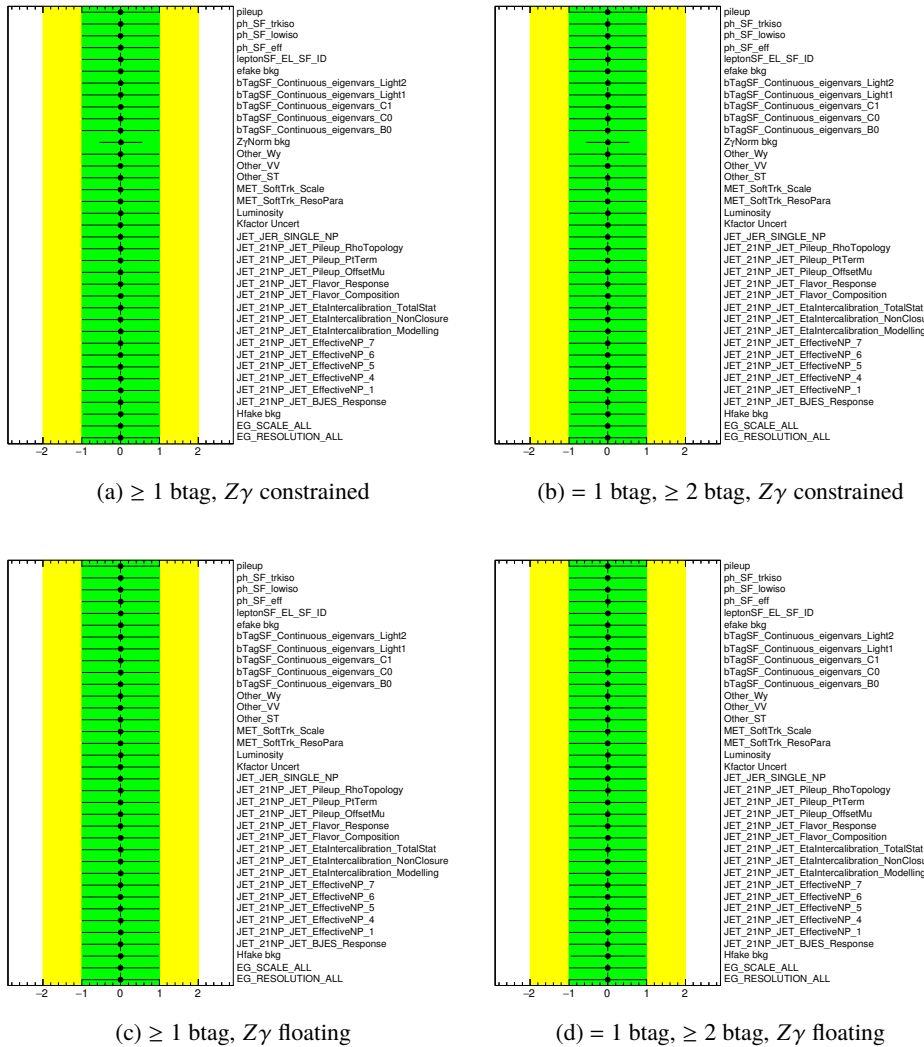


Figure 152: Pull plots for the ee channels showing $Z\gamma$ constrained and floating. See Table 44 for reference.

Not reviewed, for internal circulation only

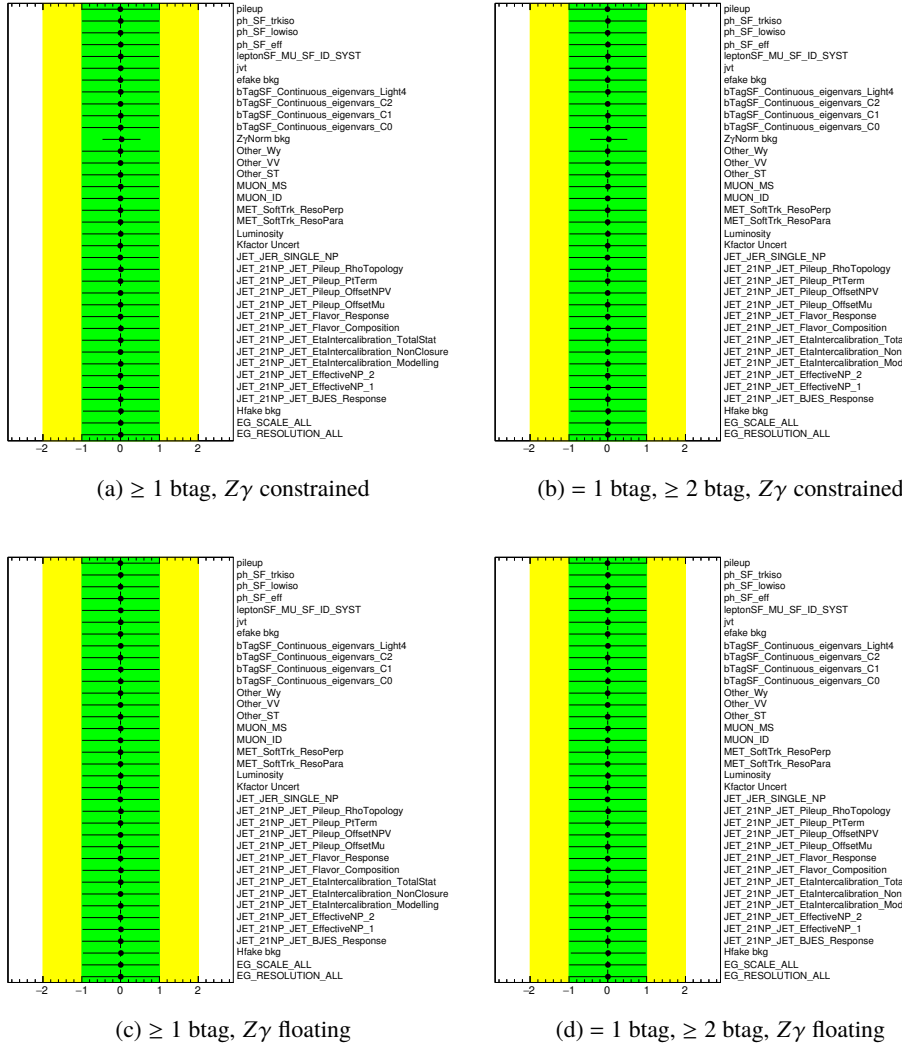


Figure 153: Pull plots for the $\mu\mu$ channels showing $Z\gamma$ constrained and floating. See Table 44 for reference.

Not reviewed, for internal circulation only

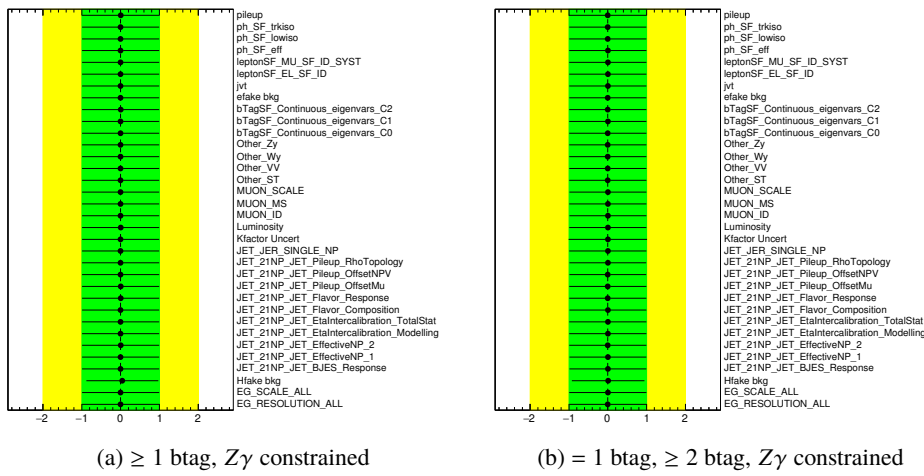


Figure 154: Pull plots for the $e\mu$ channels showing $Z\gamma$ constrained. See Table 44 for reference.

2147 L New physics observations using Effective Field Theory

2148 With the increase of signal events obtained at 100 fb^{-1} of integrated luminosity, possible deviations with
 2149 respect to the SM could become visible. The model-independent Effective Field Theory (EFT) approach
 2150 has been chosen in order to explore the possibility of observation of deviations with respect to the SM. In
 2151 this approach, any new model can be modeled by the addition of new higher-dimensional operators to the
 2152 SM Lagrangian, with corresponding coefficient. A study in the context of top quark pair production [6]
 2153 has shown that three operators can have a visible impact on the $t\bar{t}\gamma$ production: the dipole operators
 2154 O_{tB} , O_{tW} and O_{tG} , coupling to respectively weak hypercharge and isospin gauge bosons and gluons and
 2155 creating electroweak and chromomagnetic dipole moments. The operators are described by Equation 78
 2156 and shown in Figure 155.

$$\begin{aligned} O_{tW} &= y_t g_w (\bar{Q} \sigma^{\mu\nu} \tau^I t) \bar{\phi} W_{\mu\nu}^I, \\ O_{tB} &= y_t g_Y (\bar{Q} \sigma^{\mu\nu} t) \bar{\phi} B_{\mu\nu}, \\ O_{tG} &= y_t g_s (\bar{Q} \sigma^{\mu\nu} T^A t) \bar{\phi} G_{\mu\nu}^A, \end{aligned} \quad (78)$$

2157 where ϕ is the Higgs field, Q is the left-handed quark doublet of the third generation, g_w , g_t and g_s are
 2158 the SM coupling constants, and y_t is the top-Yukawa coupling constant.

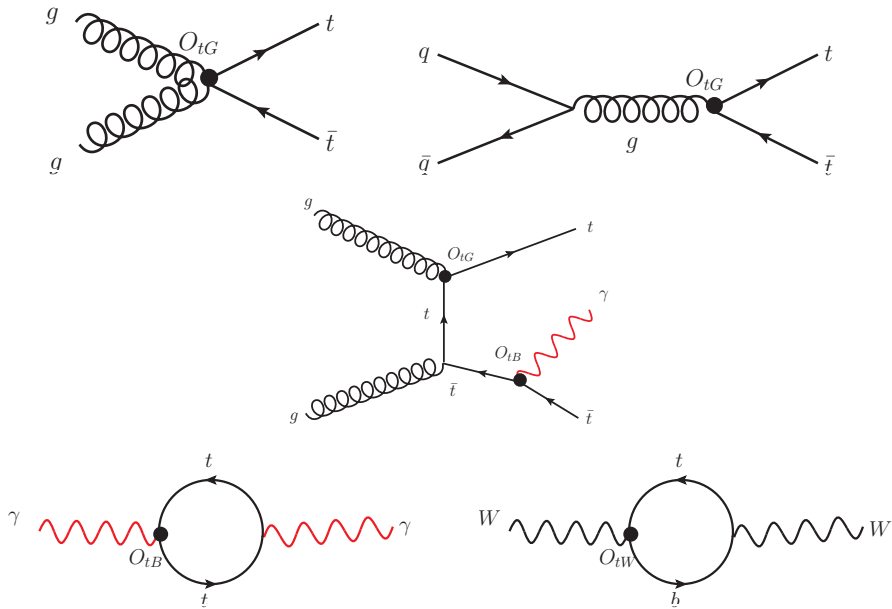


Figure 155: Feynman diagrams for the EFT vertices in top-quark production and decay.

2159 The effect of the above operators on the inclusive cross-section is given by:

$$\sigma = \sigma_{\text{SM}} + \frac{C_i}{\Lambda^2} \sigma_i^{(1)} + \frac{C_i^2}{\Lambda^4} \sigma_i^{(2)}, \quad (79)$$

2160 where σ_{SM} is the SM cross-section, $\sigma_i^{(1)}$ is the cross-section of the interference between diagrams with
 2161 operator O_i vertex and SM diagrams and $\sigma_i^{(2)}$ is the cross-section of the quadratic term of the operator
 2162 O_i . C_i is the coefficient associated to the operator O_i , and Λ is the cut-off in TeV units.

2163 **L.1 EFT samples**

2164 The chosen strategy is to generate several samples, using **MADGRAPH5_aMC@NLO** with a customized
 2165 Lagrangian as done in the reference paper[6], with all coefficients set to zero except one. The samples are
 2166 generated at the next-to-leading order and including only photons emitted from initial state or off-shell
 2167 top quark. For each operator, two samples are generated, with positive or negative coefficient value. The
 2168 list of those samples is given in Table 45. The positive and negative variations of the coefficients are used
 2169 to extract $\sigma_i^{(1)}$ and $\sigma_i^{(2)}$ in Equation 79.

2170 By considering only one operator at a time, this strategy neglects the possible cancellation from the
 2171 contributions of different EFT operators and the interferences between different EFT operators. The SM
 2172 sample is generated by setting all the coefficients very close to zero. The samples are generated using the
 2173 **MADGRAPH5_aMC@NLO**, and **PYTHIA** for parton showering. The selections at the generator level are
 2174 as the following, the leptons, photons, and jet transverse momenta are asked to be larger than 15 GeV and
 2175 $\eta < 5.0$. The NNPDF30 and the dynamic scale of the sum of transverse mass divided by two are used.
 2176 The cross section value for each coefficient variation is given in Table 45. $\sigma_i^{(1)}$ and $\sigma_i^{(2)}$ compared to the
 2177 SM cross section in Table 46. The validation of the generated samples is shown in the Appendix N.

Table 45: Expected NLO cross section for each different C_i generated at a time. Only statistical uncertainty is mentioned.

EFT operator	Cross section [pb]
σ_{SM}	2.652 ± 0.013
$C_{tB}/\Lambda^2 = +5$	3.005 ± 0.013
$C_{tB}/\Lambda^2 = -5$	2.807 ± 0.013
$C_{tG}/\Lambda^2 = +0.3$	2.914 ± 0.014
$C_{tG}/\Lambda^2 = -0.3$	2.469 ± 0.012
$C_{tW}/\Lambda^2 = +2$	2.757 ± 0.015
$C_{tW}/\Lambda^2 = -2$	2.670 ± 0.013

2178 **L.2 The study in the fiducial region**

2179 The same object definitions introduced in the fiducial region in Section 9.1.1 are implemented in rivet
 2180 routine and used for the study. The event level selections described in Section 5 are also applied. The
 2181 result of the inclusive cross sections are summarized in Table 47. The quadratic term has a larger impact
 2182 for the O_{tB} operator, while the interference term for the other two operators, O_{tG} and O_{tW} in both the
 2183 single lepton and dilepton channels. The differential cross sections in photon p_T , and the invariant mass
 2184 of the photon and the hardest jet, are compared to the SM cross section and shown in Figure 156 and
 2185 Figure 157, in the single lepton and dilepton channels respectively. The residual due to the O_{tB} operator is
 2186 increasing with higher photons p_T or higher values of the invariant mass variable, this is due to the amount

Table 46: The interference and quadratic cross section terms due to the new operators at the generator level in dilepton channel, the results are in pb.

Cross section/Operator	O_{tB}	O_{tG}	O_{tW}
σ_{SM}	2.652	2.652	2.652
$\sigma^{(1)}$	0.010	0.022	0.004
$\sigma^{(2)}$	0.025	0.004	0.006
$\sigma^{(1)}/\sigma_{SM}$	$< 10^{-3}$	10^{-3}	10^{-3}
$\sigma^{(2)}/\sigma_{SM}$	$< 10^{-3}$	10^{-3}	10^{-3}

of energy enters the EFT vertex, the behaviour is similar in both channels. However, for O_{tW} operator, the effect on the SM cross section is getting smaller with higher invariant mass values in the single lepton channel, while the interference and quadratic terms behave differently in the dilepton channel. For the photon p_T , it shows a similar behaviour as for the O_{tB} but with less impact on the SM cross section in both of the single lepton and dilepton channels. For the last operator, O_{tG} , the impact is stable over p_T and the invariant mass in the two channels.

Further variables have been checked in the Appendix M.3, since no visible effect of the operators has been observed for those variables, they will not be considered.

Table 47: The interference and quadratic cross section terms due to the new operators and their effect on the fiducial cross section in the single lepton and dilepton channels, the results are in pb.

Channel		O_{tB}	O_{tG}	O_{tW}
σ_{SM}	single lepton	0.286	0.286	0.286
	dilepton	0.059	0.059	0.059
$C\sigma^{(1)}$	single lepton	0.007	0.022	0.007
	dilepton	0.003	0.005	0.001
$C^2\sigma^{(2)}$	single lepton	0.036	0.007	0.001
	dilepton	0.007	0.001	0.001
$C\sigma^{(1)}/\sigma_{SM}$	single lepton	0.024	0.077	0.024
	dilepton	0.051	0.085	0.017
$C^2\sigma^{(2)}/\sigma_{SM}$	single lepton	0.126	0.024	$< 10^{-3}$
	dilepton	0.119	0.017	0.017

2195 L.2.1 The fit

2196 The SM cross section is fixed to the nominal one from the $t\bar{t}\gamma$ sample. The weights; $\sigma^{(1)}$ and $\sigma^{(2)}$, described
2197 in Table 47, are used as inputs to the fit (currently inclusive values, will be done later differentially).
2198 Table 48 shows a very preliminary Asimov fit results done in the single lepton and dilepton channels
2199 separately and also for their combinations. The results are in units of the corresponding coefficient for

Not reviewed, for internal circulation only

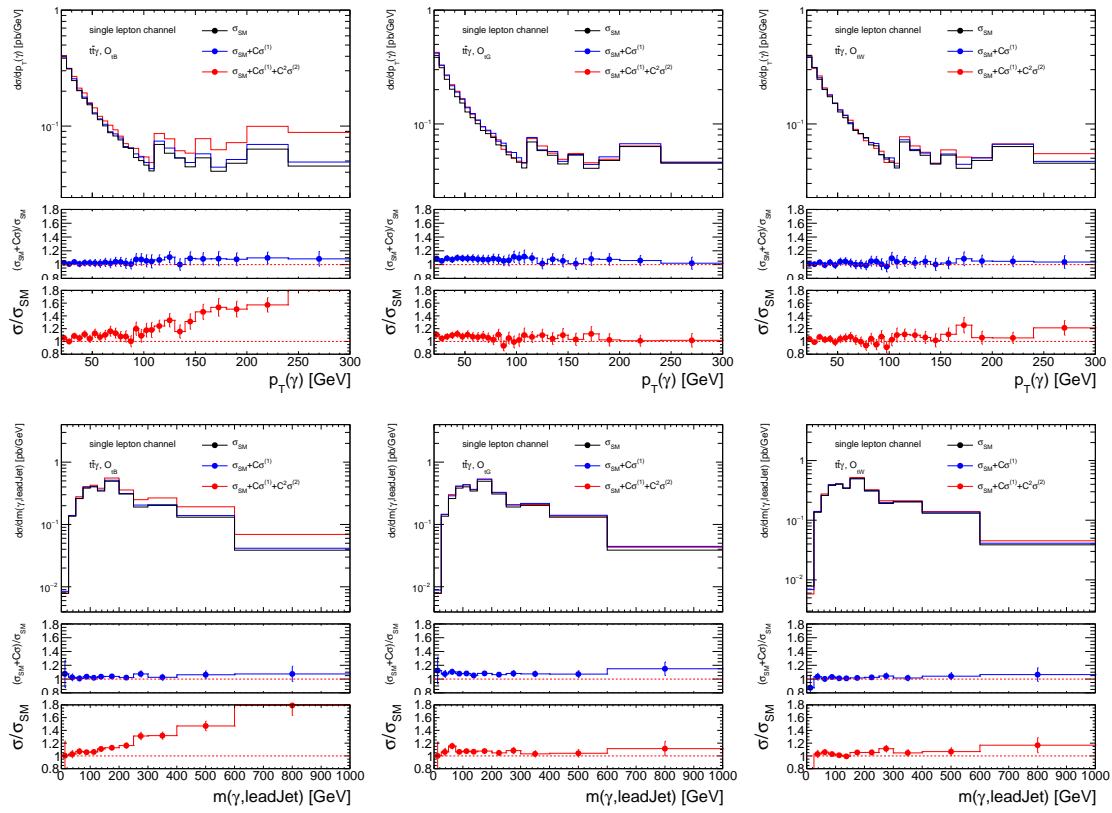


Figure 156: The effect of the operators O_{tB} (left) O_{tG} (right), and O_{tW} (middle) on the cross section as a function of the photon p_T (top) and invariant mass of the photon and the hardest jet (bottom), in the single channel, for the chosen value of $C_{tB} = \pm 5$, $C_{tG} = \pm 0.3$ and $C_{tW} = \pm 2$. The SM differential cross section in black, the effect of the interference term in blue, the effect of both interference and quadratic terms in red.

each operator ($C_{tB} = 5$, $C_{tG} = 0.3$ and $C_{tW} = 2$). It can be seen that the coefficient are not will constrained. The limits get improved by correcting the weights with fraction of photons from production to photons from decay, as shown in Table 49. The correction are predicted from theory at $\sqrt{s} = 14$ TeV [14]. A stronger constrain is observed in single lepton channel, and gets even stronger with the combination of the two channels.

Table 48: The constraints on the EFT coefficients by doing inclusive asimov fit in the single lepton and dilepton channels, and considering only photons from production.

		O_{tB}	O_{tG}	O_{tW}
Channel	single lepton	3.51754	1.19667	1.84423
	dilepton	5.33926	1.90162	1.89772
	combined	3.02848	1.01512	1.56445

Not reviewed, for internal circulation only

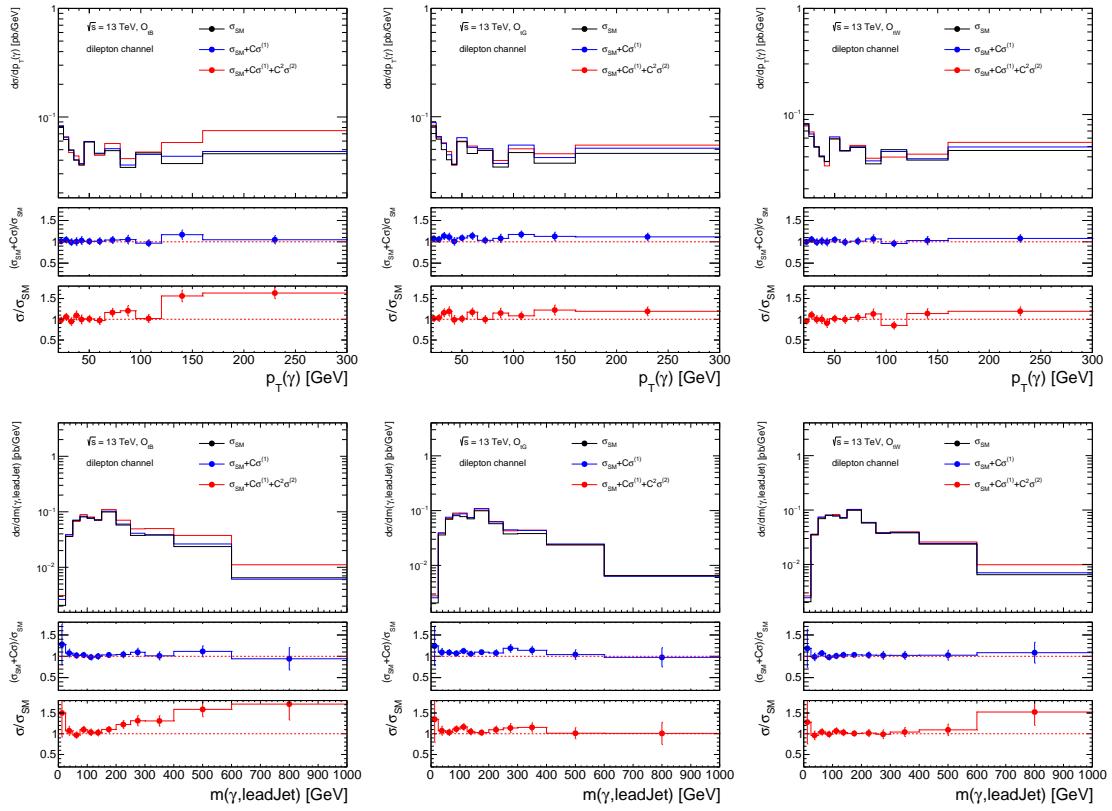


Figure 157: The effect of the operators O_{tB} (left) O_{tG} (right), and O_{tw} (middle) on the cross section as a function of the photon p_T (top) and invariant mass of the photon and the hardest jet (bottom), in the dilepton channel, for the chosen value of $C_{tB} = \pm 5$, $C_{tG} = \pm 0.3$ and $C_{tw} = \pm 2$. The SM differential cross section in black, the effect of the interference term in blue, the effect of both interference and quadratic terms in red.

Table 49: The constraints on the EFT coefficients by doing inclusive Asimov fit in the single lepton and dilepton channels, and considering photons from top production and decay. (Note: In this table small statistics is used.)

		O_{tB}	O_{tG}	O_{tw}
Channel	single lepton	2.55576	0.553034	7.05593
	dilepton	2.91095	0.837023	1.24251
	combined	1.89281	0.463836	1.09634

2205 M First look at EFT

2206 M.1 Cross check of first EFT results

2207 The results of the effect on the inclusive cross-section as a function of the photon transverse momentum
 2208 are shown in Figure 158 for the two operators O_{tG} and O_{tB} , the value of C_{tB} and C_{tG} are set to ± 4 and ± 1
 2209 respectively, the two values are chosen only to be compared to the results in [6]. The results are obtained
 2210 for all the decay modes of $t\bar{t}\gamma$, and with selections applied only at the generator level; the leptons and jet
 2211 transverse momenta should be greater than 15 GeV and $\eta < 5.0$. The photon p_T should be greater than 20
 2212 GeV. As shown in the figure, the squared term is increasing fast with the transverse momentum for the
 2213 O_{tB} while it is mostly constant for the O_{tG} , this is due to the amount of the momentum passing through
 2214 the EFT vertex.

Table 50: The interference and quadratic NLO cross section terms and their effect on the inclusive cross section, the results are in pb.

EFT operator	O_{tB}	O_{tG}	O_{tW}
σ_{SM}	2.668	2.668	2.668
$\sigma^{(1)}$	0.0135	0.833	0.007
$\sigma^{(2)}$	0.0077	0.289	0.002
$\sigma^{(1)}/\sigma_{SM}$	0.005	0.312	0.003
$\sigma^{(2)}/\sigma_{SM}$	0.003	0.108	0.0007
$\sigma^{(2)}/\sigma^{(1)}$	0.571	0.347	0.286

2215 M.2 The Monte Carlo study in the fiducial region in the single lepton channel

2216 A fiducial space region is defined in order to enhance the contributions from photons from production, and
 2217 also to focus on regions where the effect of the new EFT operators can be more visible. The event selections
 2218 used to define this region are originally optimised for the SM fiducial cross section measurement. In the
 2219 single lepton channel, the event is required to have exactly one lepton (either electron or muon), at least
 2220 for jets with a transverse momentum $p_T > 25$ GeV and $\eta < 2.5$, and at least one of them should be b -tagged
 2221 is also required. Exactly one photon of $p_T > 20$ GeV and $\eta < 2.37$ should exist, the distance between the
 2222 photon and the jet should be greater than 0.4, and the distance between the photon and the lepton should
 2223 be greater than 0.7.

2224 The results in Table 50 and Figure 158 are shown for all the decay modes of $t\bar{t}\gamma$, and with loose selections
 2225 applied at the generator level. The previous results can be compared to Table 51 and Figure 159 after
 2226 applying the fiducial selections in the single lepton channel. The results in the fiducial region shows that
 2227 the effect of quadratic term is further enhanced especially for the O_{tB} . Another interesting variable is the
 2228 invariant mass between the photon and the leading jet which shows a rising effect at high value of the
 2229 variable as shown in Figure 160. The results for separated single muon and single electron channels are
 2230 summarized in Table 52

Not reviewed, for internal circulation only

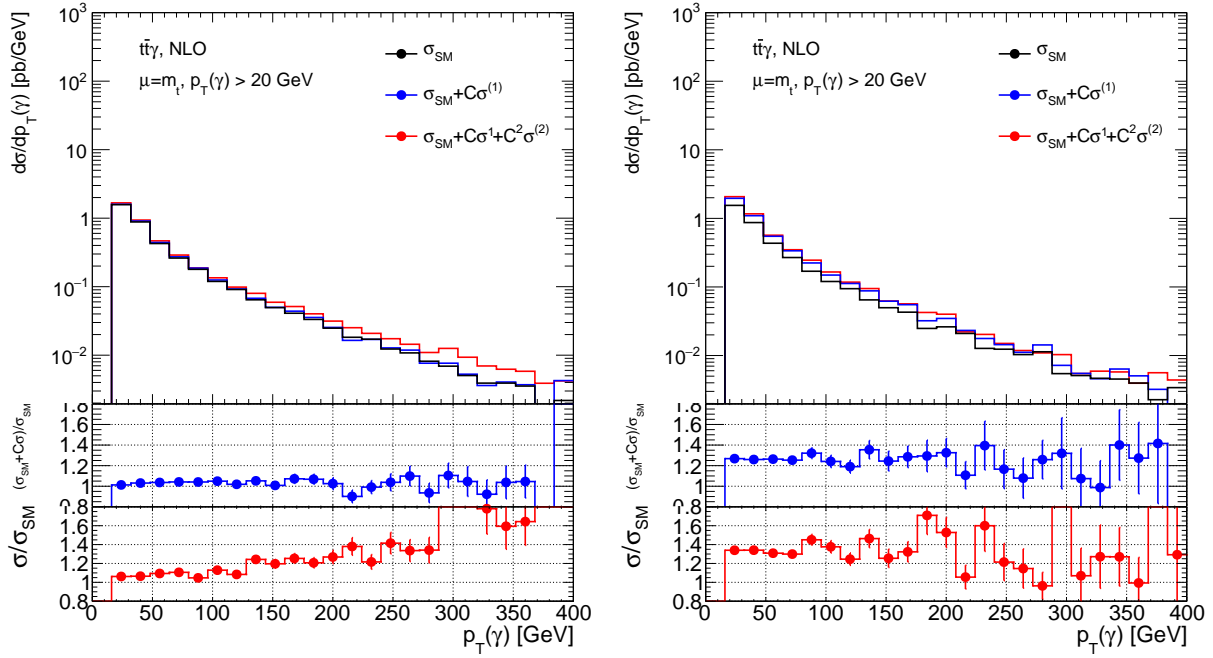


Figure 158: The effect of the operators O_{tB} (left) and O_{tG} (right) on the inclusive cross section as a function of the photon transverse momentum for the chosen value of $C_{tB} = \pm 4$ and $C_{tG} = \pm 1$. The SM differential cross section in black, the effect of the interference term in blue, the effect of both interference and quadratic terms in red. All decay channels are included.

Table 51: The interference and quadratic cross section terms due to the new operators and their effect on the fiducial cross section in the single lepton channel, the results are in pb.

EFT operator	O_{tB}	O_{tG}	O_{tW}
σ_{SM}	0.299	0.299	0.299
$\sigma^{(1)}$	0.002	0.078	0.003
$\sigma^{(2)}$	0.002	0.094	0.0006
$\sigma^{(1)}/\sigma_{SM}$	0.007	0.261	0.010
$\sigma^{(2)}/\sigma_{SM}$	0.007	0.314	0.002
$\sigma^{(2)}/\sigma^{(1)}$	1.	0.347	0.2

Not reviewed, for internal circulation only

Table 52: The interference and quadratic cross section terms due to the new operators and their effect on the fiducial cross section in the single muon and single electron channels, the results are in pb.

Channel		O_{tB}	O_{tG}	O_{tW}
σ_{SM}	μ -jets	0.156	0.156	0.156
	e -jets	0.159	0.159	0.159
$\sigma^{(1)}$	μ -jets	0.0012	0.0433	0.001
	e -jets	0.0011	0.0383	0.0025
$\sigma^{(2)}$	μ -jets	0.0007	0.0011	0
	e -jets	0.0007	0.0055	0.0012
$\sigma^{(1)}/\sigma_{SM}$	μ -jets	0.0075	0.2776	0.0064
	e -jets	0.0069	0.2408	0.0013
$\sigma^{(2)}/\sigma_{SM}$	μ -jets	0.0070	0.0047	0
	e -jets	0.0047	0.0353	0.0079
$\sigma^{(2)}/\sigma^{(1)}$	μ -jets	0.5833	0.0254	0
	e -jets	0.6727	0.1464	0.5

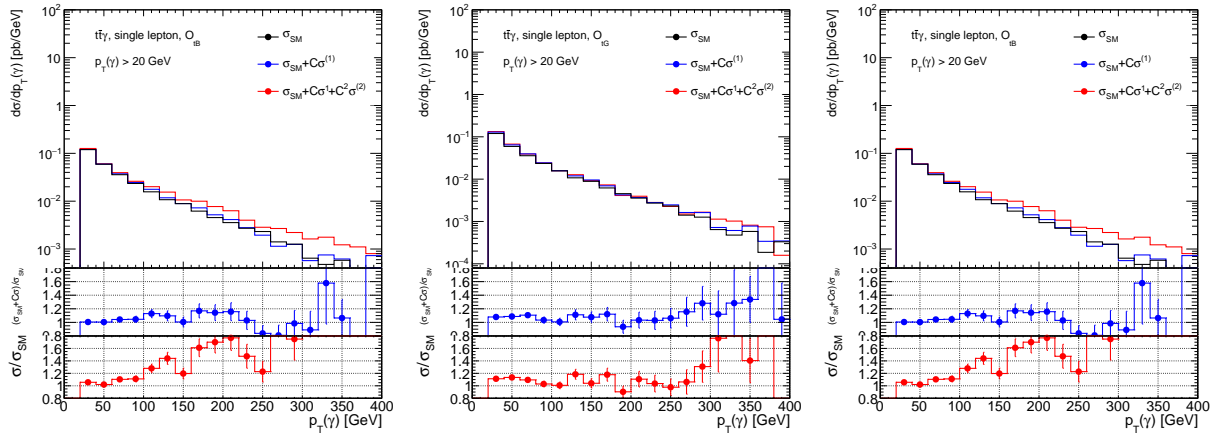


Figure 159: The effect of the operators O_{tB} (left) O_{tG} (right), and O_{tW} (middle) on the cross section as a function of the photon transverse momentum for the chosen value of $C_{tB} = \pm 5$, $C_{tG} = \pm 0.3$ and $C_{tW} = \pm 2$. The SM differential cross section in black, the effect of the interference term in blue, the effect of both interference and quadratic terms in red.

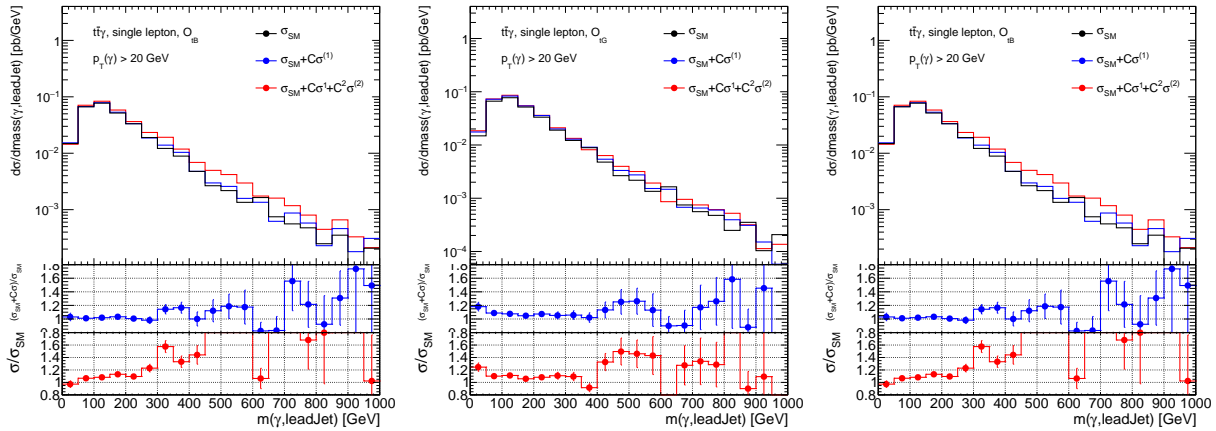


Figure 160: The effect of the operators O_{tB} (left) O_{tG} (right), and O_{tW} (middle) on the cross section as a function of invariant mass of the photon and the leading jet for the chosen value of $C_{tB} = \pm 5$, $C_{tG} = \pm 0.3$ and $C_{tW} = \pm 2$. The SM differential cross section in black, the effect of the interference term in blue, the effect of both interference and quadratic terms in red.

2231 **M.3 Further variables for the EFT in the fiducial region**

Not reviewed, for internal circulation only

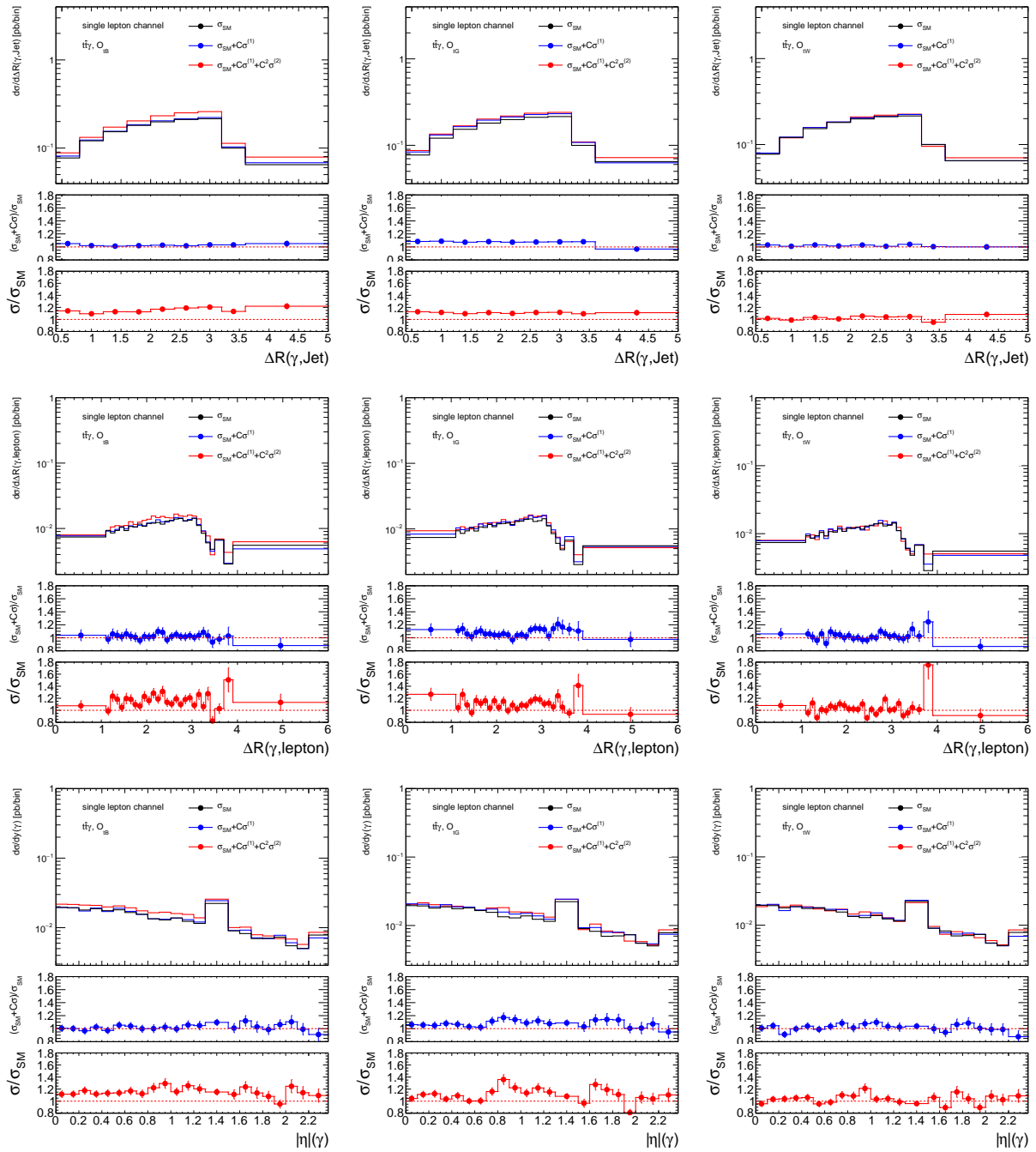


Figure 161: The effect of the operators O_{tB} (left) O_{tG} (right), and O_{tW} (middle) on the cross section as a function of the distance between the photon and the jet (top), between the photon and the lepton (middle), and the photon η (bottom), in the single lepton channel, for the chosen value of $C_{tB} = \pm 5$, $C_{tG} = \pm 0.3$ and $C_{tW} = \pm 2$. The SM differential cross section in black, the effect of the interference term in blue, the effect of both interference and quadratic terms in red.

Not reviewed, for internal circulation only

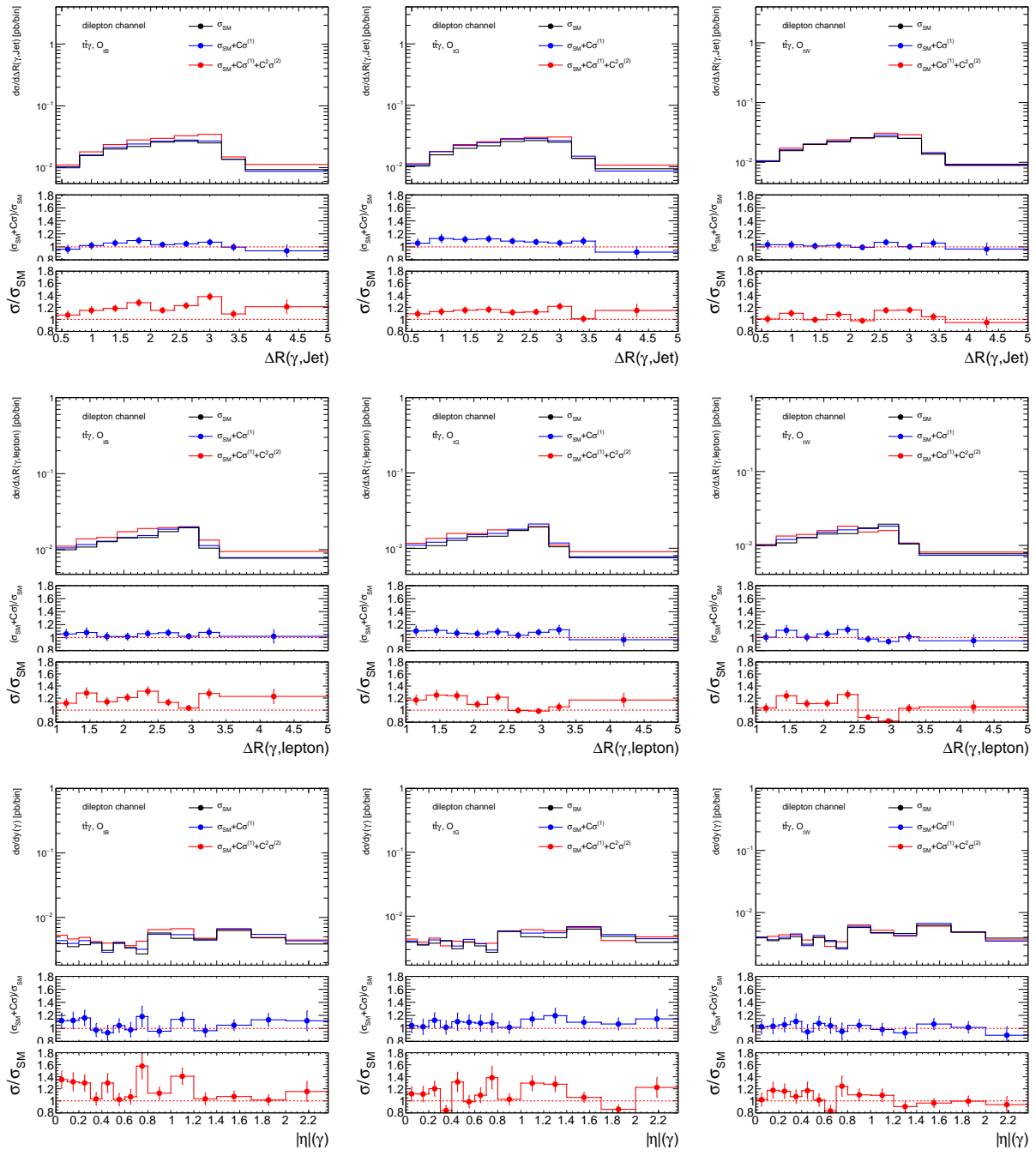


Figure 162: The effect of the operators O_{tB} (left) O_{tG} (right), and O_{tW} (middle) on the cross section as a function of the distance between the photon and the jet (top), between the photon and the lepton (middle), and the photon η (bottom), in the dilepton channel, for the chosen value of $C_{tB} = \pm 5$, $C_{tG} = \pm 0.3$ and $C_{tW} = \pm 2$. The SM differential cross section in black, the effect of the interference term in blue, the effect of both interference and quadratic terms in red.

2232 N EFT validation

2233 The validation is performed in order to confirm that the EFT model is performing similarly to the SM,
 2234 if the EFT coefficients are set very close to zero; in this case the process is referred as a SM-like. The
 2235 coefficients are not set exactly to zero to avoid possible divergences in the calculations of the amplitudes
 2236 in the EFT model. The validation is done by generating two samples, one is using the SM, and the other
 2237 is using the EFT model with coefficients ≈ 0 , both at LO and NLO. The differential cross section as a
 2238 function of the photon's observables are checked and found to behave very similarly in the two samples,
 2239 as and shown in Figure 163 for the LO process, and in Figure 164 for the NLO process.

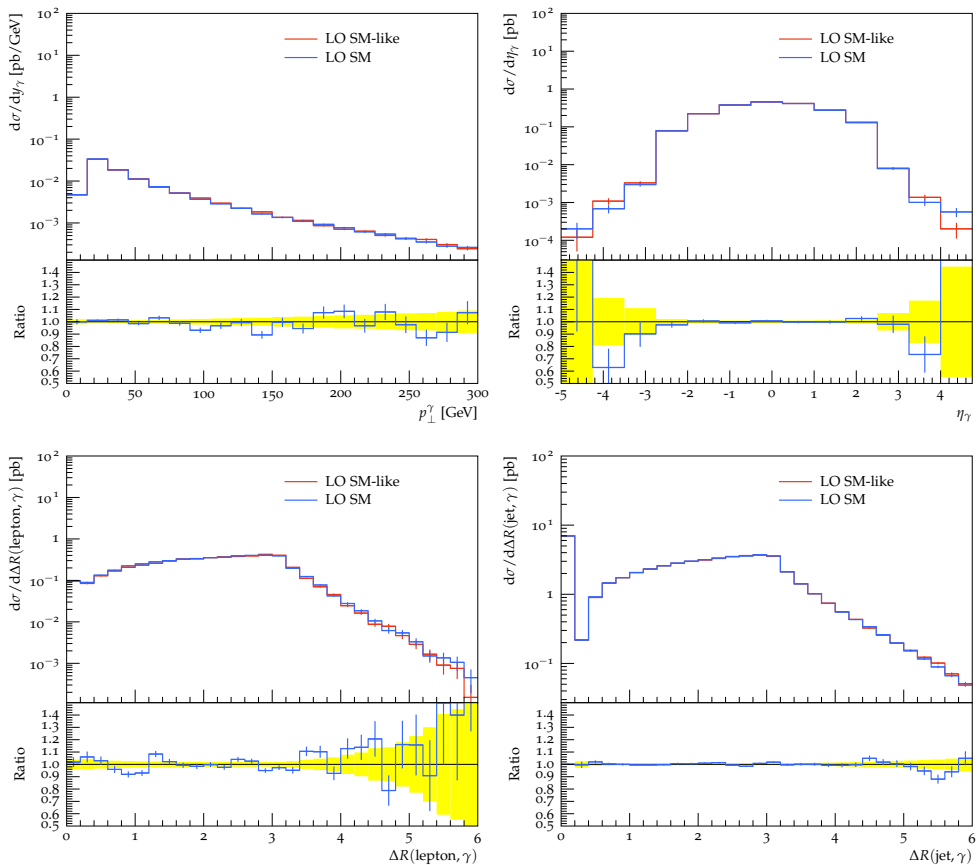


Figure 163: A comparison between generating a small sample using the SM, shown in blue, and using the EFT model and setting its coefficients very close to zero, and shown in red. Both are generated at LO

Not reviewed, for internal circulation only

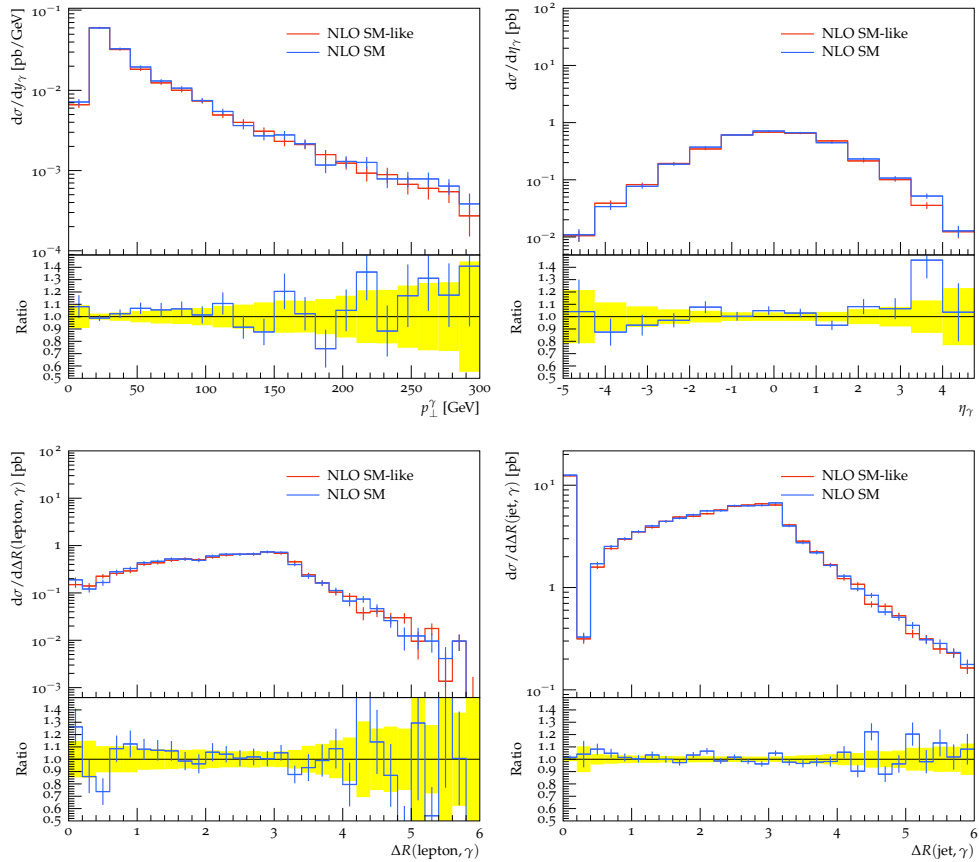


Figure 164: A comparison between generating a small sample using the SM, shown in blue, and using the EFT model and setting its coefficients very close to zero, and shown in red. Both are generated at NLO

2240 O Studying larger weights in the $W\gamma$ and $Z\gamma$ MC samples

2241 It is apparent (especially so in the dilepton channel) that some $V + \gamma$ samples have higher weights than
 2242 expected. This is shown by the large blue uncertainty band in the ELD distribution. Studies have been
 2243 made in both the single lepton and dilepton channels to determine the origin of these higher-than-normal
 2244 weights.

2245 Figure 165 shows the individual distributions for $weight_mc$ and $weight_pileup$ as well as the product of the
 2246 two versus the ELD for the $\mu^+\mu^-$ channel. Figure 166 shows the pileup dependence on the pileup weight.
 2247 Evidently, there is one. Figure 167 shows the product of the two weights versus the ELD distribution for
 2248 the $e+jets$ channel.

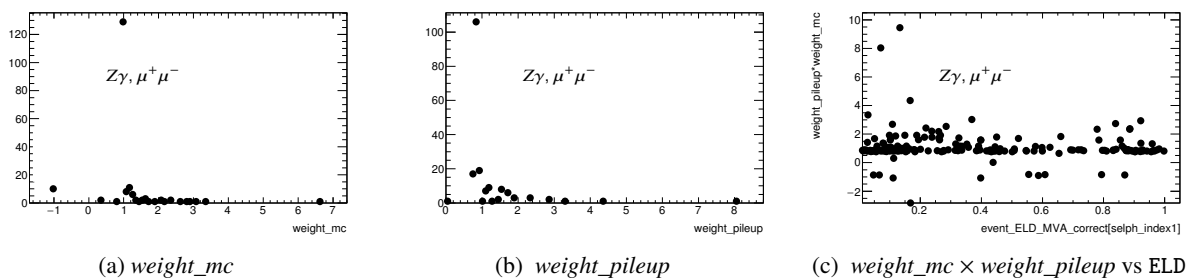


Figure 165: $weight_mc$ and $weight_pileup$ and the product of both versus the ELD for the $\mu^+\mu^-$ channel.

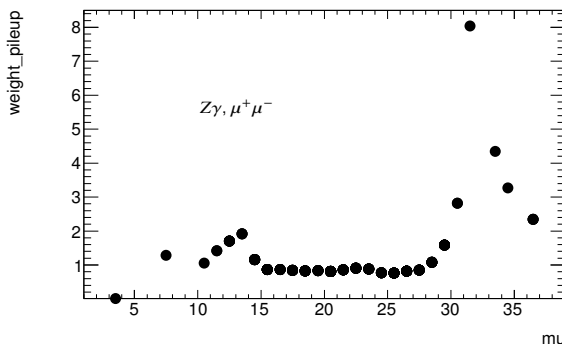


Figure 166: Pileup dependence of the weight for the $Z\gamma$ samples in the $\mu^+\mu^-$ channel. It was suggested if there was not a dependance we could drop this weight for these samples. This isn't the case.

2249 Various strategies have been discussed. One possibility is to place an arbitrary cut at some value of
 2250 $weight_mc \times weight_pileup$. While this solves the problem of these outlying large weights, it's quite hard
 2251 to justify since no weight is individually very large. Thus, a study is made to see if cutting these events
 2252 away or simply ignoring them actually changes our sensitivity.

2253 Three (two) Asimov tests are performed for the single lepton (dilepton) channel. In each channel, a fit
 2254 is performed without placing any cut on $weight_mc \times weight_pileup$ for the $V + \gamma$ samples. A second
 2255 fit is performed placing a cut at $weight_mc \times weight_pileup < 5$. For the single lepton channel a third fit
 2256 is performed with $weight_mc \times weight_pileup < 12$. The summary of the error in μ for each respective
 2257 fit is shown in Table 53. It's apparent that neglecting the larger weights in the $V + \gamma$ samples has a

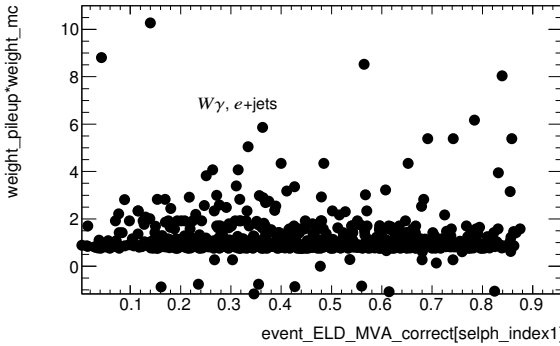


Figure 167: $weight_mc \times weight_pileup$ vs ELD for the $e+jets$ channel.

2258 negligible affect. For the single lepton channel a cut of < 5 is in any case too aggressive and so wouldn't
2259 be considered.

2260 Figure 168 shows the respective pull plots for the single lepton fits, while Figure 169 shows the same for
2261 the dilepton fits. Very little difference (if any) is seen between the different scenarios. For the single
2262 lepton channels the $W\gamma$ background is floating and so one can look at the associated errors in μ . These
2263 are 1 ± 0.43379 , 1 ± 0.42762 and 1 ± 0.40686 for no cut, <12 and < 5 , respectively. Thus, all acceptable
2264 for a floating background. For the dilepton channel, a 50% prior is placed on the $Z\gamma$ background since
2265 it is not floating. In both pull plots it can be seen to be constrained. This is because a cut at < 5 reduces
2266 weights which are uncommonly high, but this doesn't remove all of them. However, this is understood
2267 and so is acceptable.

Table 53: Summary of Asimov fits performed for different cuts on $weight_mc \times weight_pileup$.

channel	$weight_mc \times weight_pileup$ cut	$\pm \Delta\mu$
single lepton	no cut	+0.10357 -0.09558
	<12	+0.10280 -0.09504
	<5	+0.09967 -0.09234
dilepton	no cut	+0.07337 -0.06773
	< 5	+0.07361 -0.06806

2268 In summary, we abstain from cutting the few larger weights in the $V + \gamma$ SHERPA samples knowing that
2269 they will not drastically impact our final result.

Not reviewed, for internal circulation only

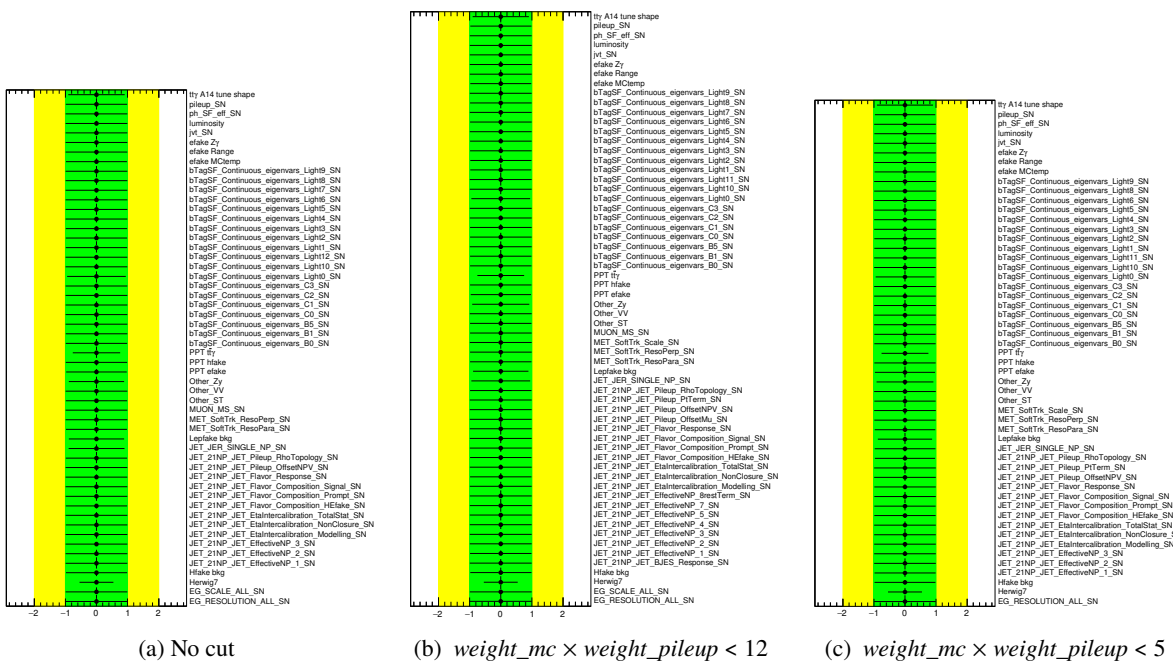


Figure 168: Pull plots for all nuisance parameters in the single lepton channel for various Asimov fits with or without cuts on $\text{weight}_{\text{mc}} \times \text{weight}_{\text{pileup}}$ for $V + \gamma$ samples.

Not reviewed, for internal circulation only

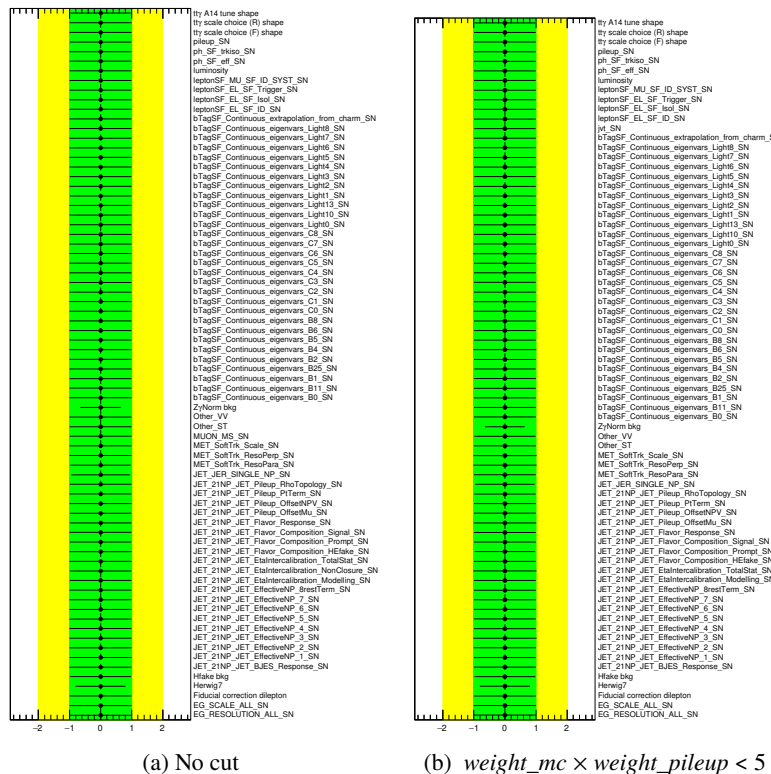


Figure 169: Pull plots for all nuisance parameters in the dilepton channel for various Asimov fits with or without cuts on $\text{weight}_{\text{mc}} \times \text{weight}_{\text{pileup}}$ for $V + \gamma$ samples.

2270 P Estimation of a possible mis-modelling of prompt photons from Pile-Up

2271 The possibility of mismodelling and under-estimating the presence of prompt photons due to a production
 2272 in pile-up events has been evaluated. To do so, the z position of the primary vertex of the event,
 2273 corresponding to the hard interaction producing the particles of the signal final state is compared to the z
 2274 position of the extrapolated vertex of the selected photon. If this photon is the result of pile-up activity,
 2275 this z position should be uncorrelated to the primary vertex z position. The extrapolated vertex of the
 2276 selected photon is obtained from the PhotonPointingTool tool from the PhotonVertexSelection package
 2277 provided by the EGamma group. For converted photons, this vertex z position is obtained from the vertex
 2278 of the conversion tracks. For unconverted photon, the z position is extrapolated from the shower shape
 2279 of the photon in the calorimeter. The discriminating variable is $(z(PV) - z(\gamma))/\Delta z(\gamma)$ where $z(PV)$
 2280 and $z(\gamma)$ is the z position of the primary vertex and the vertex of the selected photon respectively, and
 2281 $\Delta z(\gamma)$ is the uncertainty on the vertex position of the selected photon. In order to test if the simulation
 2282 is missing some pile-up prompt photon, three different distribution are created from the signal sample:
 2283 the nominal one and two where in a fraction of the events (10% and 30%) the z position of the selected
 2284 photon has been randomized. This randomization is done by taking the z position of the previous selected
 2285 event, and therefore correspond to a distribution corresponding to the typical expected z position. As
 2286 visible in Figure 170, the addition of randomized position will not affect significantly the bulk of the
 2287 event, but will have effects on the tails, as visible in the underflow and overflow bins. Comparing with the
 2288 data distribution, we can conclude that there is no need to add a percentage of randomized photon vertex
 2289 position, and therefore that the simulation accounts correctly for the prompt photon not associated to the
 2290 primary vertex. Those distributions are normalized to unity, and done for the dilepton channels after the
 2291 full signal selection. The distributions of the single variables ($z(PV)$, $z(\gamma)$ and $\Delta z(\gamma)$) also show a good
 2292 shape agreement between data and simulation.

Not reviewed, for internal circulation only

[Not reviewed, for internal circulation only]

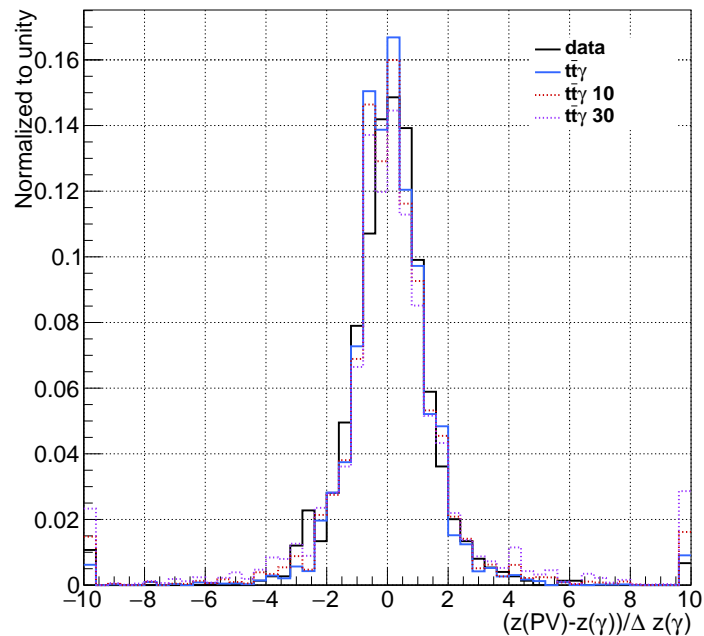


Figure 170: Distribution of The bin-by-bin migration matrix of (a) the photon p_T and (b) the photon $|\eta|$ in the dilepton channel.

2293 **Q Monte Carlo Samples**

2294 **Q.1 Nominal samples**

Table 54: Nominal MC samples.

DSID	explanation	nevents	genName	genTune	Sample Lumi [fb-1]	AMIXsec [pb]	K-factor	FiltEff	$\sigma \times Kfactors \times FiltEff$ [pb]
<i>tty MC15c</i>									
410389	MadGraphPythia8EvtGen A14NNPDF23 ttgamma nonallhadronic	4926000	MadGraph +Pythia8 +EvtGen	A14 NNPDF23LO	1065.47271429	4.6233	1.7	1.0	7.860
<i>t̄t MC15c</i>									
410501	PowhegPythia8EvtGen A14 hdamp258p75 ttbar nonallhad	58439000	Powheg +Pythia8 +EvtGen	A14 NNPDF23LO	147.178260062	730.19	1.1390	0.54378	452.25443603
<i>Zγ MC15c</i>									
364500	Sherpa 222 NNPDF30NNLO eegamma_pty_7_15	3968000	Sherpa	NNPDF3.0 NNLO	68.8243660457	57.654	1.0	1.0	57.654
364501	Sherpa 222 NNPDF30NNLO eegamma_pty_15_35	2950000	Sherpa	NNPDF3.0 NNLO	85.3390418885	34.568	1.0	1.0	34.568
364502	Sherpa 222 NNPDF30NNLO eegamma_pty_35_70	989000	Sherpa	NNPDF3.0 NNLO	157.148759017	6.2934	1.0	1.0	6.2934
364503	Sherpa 222 NNPDF30NNLO eegamma_pty_70_140	484000	Sherpa	NNPDF3.0 NNLO	984.560304319	0.49159	1.0	1.0	0.49159
364504	Sherpa 222 NNPDF30NNLO eegamma_pty_140_E_CMS	99000	Sherpa	NNPDF3.0 NNLO	1570.13258897	0.063052	1.0	1.0	0.063052
364505	Sherpa 222 NNPDF30NNLO mumugamma_pty_7_15	3954000	Sherpa	NNPDF3.0 NNLO	68.530426192	57.697	1.0	1.0	57.697
364506	Sherpa 222 NNPDF30NNLO mumugamma_pty_15_35	2957000	Sherpa	NNPDF3.0 NNLO	85.4500794683	34.605	1.0	1.0	34.605
364507	Sherpa 222 NNPDF30NNLO mumugamma_pty_35_70	992000	Sherpa	NNPDF3.0 NNLO	157.790927022	6.2868	1.0	1.0	6.2868
364508	Sherpa 222 NNPDF30NNLO mumugamma_pty_70_140	489500	Sherpa	NNPDF3.0 NNLO	991.231800417	0.49383	1.0	1.0	0.49383
364509	Sherpa 222 NNPDF30NNLO mumugamma_pty_140_E_CMS	100000	Sherpa	NNPDF3.0 NNLO	1587.10005079	0.063008	1.0	1.0	0.063008
364510	Sherpa 222 NNPDF30NNLO tautaugamma_pty_7_15	3957000	Sherpa	NNPDF3.0 NNLO	68.6335726923	57.654	1.0	1.0	57.654
364511	Sherpa 222 NNPDF30NNLO tautaugamma_pty_15_35	2958000	Sherpa	NNPDF3.0 NNLO	85.3802857555	34.645	1.0	1.0	34.645
364512	Sherpa 222 NNPDF30NNLO tautaugamma_pty_35_70	980000	Sherpa	NNPDF3.0 NNLO	155.523463412	6.3013	1.0	1.0	6.3013
364514	Sherpa 222 NNPDF30NNLO tautaugamma_pty_140_E_CMS	98000	Sherpa	NNPDF3.0 NNLO	1555.0865612	0.063019	1.0	1.0	0.063019
<i>Wγ MC15c</i>									
364521	Sherpa 222 NNPDF30NNLO enugamma_pty_7_15	12374000	Sherpa	NNPDF3.0 NNLO	62.0748469951	199.34	1.0	1.0	199.34
364522	Sherpa 222 NNPDF30NNLO enugamma_pty_15_35	12855000	Sherpa	NNPDF3.0 NNLO	95.6402053419	134.41	1.0	1.0	134.41
364523	Sherpa 222 NNPDF30NNLO enugamma_pty_35_70	1992000	Sherpa	NNPDF3.0 NNLO	104.424407633	19.076	1.0	1.0	19.076
364524	Sherpa 222 NNPDF30NNLO enugamma_pty_70_140	248000	Sherpa	NNPDF3.0 NNLO	128.817785165	1.9252	1.0	1.0	1.9252
364525	Sherpa 222 NNPDF30NNLO enugamma_pty_140_E_CMS	97500	Sherpa	NNPDF3.0 NNLO	325.347036839	0.29968	1.0	1.0	0.29968
364526	Sherpa 222 NNPDF30NNLO munugamma_pty_7_15	12386000	Sherpa	NNPDF3.0 NNLO	62.0852130326	199.5	1.0	1.0	199.5
364527	Sherpa 222 NNPDF30NNLO munugamma_pty_15_35	12853000	Sherpa	NNPDF3.0 NNLO	95.56133829	134.5	1.0	1.0	134.5
364528	Sherpa 222 NNPDF30NNLO munugamma_pty_35_70	1986000	Sherpa	NNPDF3.0 NNLO	103.664265581	19.158	1.0	1.0	19.158
364529	Sherpa 222 NNPDF30NNLO munugamma_pty_70_140	248000	Sherpa	NNPDF3.0 NNLO	129.362057274	1.9171	1.0	1.0	1.9171
364530	Sherpa 222 NNPDF30NNLO munugamma_pty_140_E_CMS	97500	Sherpa	NNPDF3.0 NNLO	330.284552846	0.2952	1.0	1.0	0.2952
364531	Sherpa 222 NNPDF30NNLO taunugamma_pty_7_15	12352000	Sherpa	NNPDF3.0 NNLO	61.9489442801	199.39	1.0	1.0	199.39
364532	Sherpa 222 NNPDF30NNLO taunugamma_pty_15_35	12841000	Sherpa	NNPDF3.0 NNLO	95.4721189591	134.5	1.0	1.0	134.5
364533	Sherpa 222 NNPDF30NNLO taunugamma_pty_35_70	1987000	Sherpa	NNPDF3.0 NNLO	103.928029709	19.119	1.0	1.0	19.119
364534	Sherpa 222 NNPDF30NNLO taunugamma_pty_70_140	2455000	Sherpa	NNPDF3.0 NNLO	126.748928701	1.9369	1.0	1.0	1.9369
364535	Sherpa 222 NNPDF30NNLO taunugamma_pty_140_E_CMS	99500	Sherpa	NNPDF3.0 NNLO	331.854717673	0.29983	1.0	1.0	0.29983
<i>ST + γ MC15c</i>									
DSID	explanation	nevents	genName	genTune	Sample Lumi [fb-1]	AMIXsec [pb]	K-factor	FiltEff	$\sigma \times Kfactors \times FiltEff$ [pb]

Not reviewed, for internal circulation only

Table 54: Nominal MC samples.

DSID	explanation	nevents	genName	genTune	Sample Lumi [fb-1]	AMIXsec [pb]	K-factor	FiltEff	$\sigma \times K \text{factor} \times \text{FiltEff}$ [pb]
410011	PowhegPythiaEvtGen P2012 singletop_tchan_lept_top	4986200	Powheg +Pythia +EvtGen	Perugia2012	113.998948307	43.739	1.0094	1.0	44.1501466
410012	PowhegPythiaEvtGen P2012 singletop_tchan_lept_antitop	4989800	Powheg +Pythia +EvtGen	Perugia2012	193.568158895	25.778	1.0193	1.0	26.2755154
410013	PowhegPythiaEvtGen P2012 Wt_inclusive_top	4985800	Powheg +Pythia +EvtGen	Perugia2012	146.602369961	34.009	1.054	1.0	35.845486
410014	PowhegPythiaEvtGen P2012 Wt_inclusive_antitop	4985600	Powheg +Pythia +EvtGen	Perugia2012	146.682750302	33.989	1.054	1.0	35.824406
410025	PowhegPythiaEvtGen P2012 SingleTopSchan_noAllHad_top	997800	Powheg +Pythia +EvtGen	Perugia2012	486.328410586	2.0517	1.005	1.0	2.0619585
410026	PowhegPythiaEvtGen P2012 SingleTopSchan_noAllHad_antitop	995400	Powheg +Pythia +EvtGen	Perugia2012	789.060642093	1.2615	1.022	1.0	1.289253
$VV + \gamma$ MC15c									
DSID	explanation	nevents	genName	genTune	Sample Lumi [fb-1]	AMIXsec [pb]	K-factor	FiltEff	$\sigma \times K \text{factor} \times \text{FiltEff}$ [pb]
361063	Sherpa CT10 llll	2964000	Sherpa	CT10	230.679430306	12.849	0.91	1.0	11.69259
361064	Sherpa CT10 llvSFMinus	448800	Sherpa	CT10	243.357553411	1.8442	0.91	1.0	1.678222
361065	Sherpa CT10 llvOFMinus	898000	Sherpa	CT10	247.69680587	3.6254	0.91	1.0	3.299114
361066	Sherpa CT10 llvSFPlus	596600	Sherpa	CT10	232.88312905	2.5618	0.91	1.0	2.331238
361067	Sherpa CT10 llvOFplus	1197000	Sherpa	CT10	238.218436555	5.0248	0.91	1.0	4.572568
361068	Sherpa CT10 llvv	5929600	Sherpa	CT10	423.542857143	14.0	0.91	1.0	12.74
361070	Sherpa CT10 llvjj ss EW6	10000	Sherpa	CT10	232.536508232	0.043004	0.91	1.0	0.03913364
361071	Sherpa CT10 llvjjj EW6	9800	Sherpa	CT10	233.238927101	0.042017	0.91	1.0	0.03823547
361072	Sherpa CT10 llllijj EW6	60000	Sherpa	CT10	1905.00381001	0.031496	0.91	1.0	0.02866136
361077	Sherpa CT10 ggllvv	6289000	Sherpa	CT10	7364.08238779	0.85401	0.91	1.0	0.7771491
361091	Sherpa CT10 WplWmqq SHv21 improved	3993900	Sherpa	CT10	160.494273659	24.885	0.91	1.0	22.64535
361092	Sherpa CT10 WpqWmlv SHv21 improved	3993700	Sherpa	CT10	160.667015328	24.857	0.91	1.0	22.61987
361093	Sherpa CT10 WlvZqq SHv21 improved	3993600	Sherpa	CT10	347.450843919	11.494	0.91	1.0	10.45954
361094	Sherpa CT10 WqqZll SHv21 improved	3990500	Sherpa	CT10	1165.65402816	3.4234	0.91	1.0	3.115294
361095	Sherpa CT10 WqqZvv SHv21 improved	4962400	Sherpa	CT10	732.241404751	6.777	0.91	1.0	6.16707
361096	Sherpa CT10 ZqqZll SHv21 improved	3988900	Sherpa	CT10	1690.07837686	16.445	0.91	0.14352	2.147769624
361097	Sherpa CT10 ZqqZvv SHv21 improved	4483500	Sherpa	CT10	966.017888751	16.432	0.91	0.28245	4.223508744
$Z + jets$ MC15c									
DSID	explanation	nevents	genName	genTune	Sample Lumi [fb-1]	AMIXsec [pb]	K-factor	FiltEff	$\sigma \times K \text{factor} \times \text{FiltEff}$ [pb]
364100	Sherpa 221 NNPDF30NNLO Zmmumu MAXHPTV0_70 CVetoBVeto	7891000	Sherpa	NNPDF3.0 NNLO	4.84043821455	1983.0	0.9751	0.8221	1589.63171493
364101	Sherpa 221 NNPDF30NNLO Zmmumu MAXHPTV0_70 CFilterBVeto	4917000	Sherpa	NNPDF3.0 NNLO	21.9786141692	1978.4	0.9751	0.11308	218.146906947
364102	Sherpa 221 NNPDF30NNLO Zmmumu MAXHPTV0_70 BFilter	7902000	Sherpa	NNPDF3.0 NNLO	62.1324429023	1982.2	0.9751	0.064161	124.013153838
364103	Sherpa 221 NNPDF30NNLO Zmmumu MAXHPTV70_140 CVetoBVeto	5917000	Sherpa	NNPDF3.0 NNLO	78.8760104787	108.92	0.9751	0.68873	73.1485614572
364104	Sherpa 221 NNPDF30NNLO Zmmumu MAXHPTV70_140 CFilterBVeto	1969800	Sherpa	NNPDF3.0 NNLO	96.8068045993	109.42	0.9751	0.18596	19.8410843943
364105	Sherpa 221 NNPDF30NNLO Zmmumu MAXHPTV70_140 BFilter	5900600	Sherpa	NNPDF3.0 NNLO	476.29608478	108.91	0.9751	0.11375	12.0800385388
364106	Sherpa 221 NNPDF30NNLO Zmmumu MAXHPTV140_280 CVetoBVeto	4943000	Sherpa	NNPDF3.0 NNLO	203.538739262	39.878	0.9751	0.60899	23.6805991698
364107	Sherpa 221 NNPDF30NNLO Zmmumu MAXHPTV140_280 CFilterBVeto	2954400	Sherpa	NNPDF3.0 NNLO	318.519317285	39.795	0.9751	0.23308	9.04446067686
364108	Sherpa 221 NNPDF30NNLO Zmmumu MAXHPTV140_280 BFilter	12339300	Sherpa	NNPDF3.0 NNLO	1932.72316485	43.675	0.9751	0.14618	6.22543965365

Not reviewed, for internal circulation only

Table 54: Nominal MC samples.

DSID	explanation	nevents	genName	genTune	Sample Lumi [fb-1]	AMIXsec [pb]	K-factor	FiltEff	$\sigma \times K\text{factor} \times \text{FiltEff}$ [pb]
364109	Sherpa 221 NNPDF30NNLO Zmumu MAXHTPTV280 500 CVetoBVeto	1973000	Sherpa	NNPDF3.0 NNLO	413.369042021	8.5375	0.9751	0.55906	4.65412767872
364110	Sherpa 221 NNPDF30NNLO Zmumu MAXHTPTV280 500 CFilterBVeto	986000	Sherpa	NNPDF3.0 NNLO	435.210414507	8.5403	0.9751	0.26528	2.20915807148
364111	Sherpa 221 NNPDF30NNLO Zmumu MAXHTPTV280 500 BFilter	1971400	Sherpa	NNPDF3.0 NNLO	1321.91527905	8.4932	0.9751	0.17559	1.4541870954
364112	Sherpa 221 NNPDF30NNLO Zmumu MAXHTPTV500 1000	2960500	Sherpa	NNPDF3.0 NNLO	1655.66802752	1.7881	0.9751	1.0	1.74357631
364113	Sherpa 221 NNPDF30NNLO Zmumu MAXHTPTV1000 E CMS	988000	Sherpa	NNPDF3.0 NNLO	6689.68785971	0.14769	0.9751	1.0	0.144012519
364114	Sherpa 221 NNPDF30NNLO Zee MAXHTPTV0 70 CVeto-BVeto	7900000	Sherpa	NNPDF3.0 NNLO	4.8550350808	1981.8	0.9751	0.82106	1586.66000797
364115	Sherpa 221 NNPDF30NNLO Zee MAXHTPTV0 70 CFilter-BVeto	4940500	Sherpa	NNPDF3.0 NNLO	22.0822865422	1980.8	0.9751	0.11295	218.160449136
364116	Sherpa 221 NNPDF30NNLO Zee MAXHTPTV0 70 BFilter	7883600	Sherpa	NNPDF3.0 NNLO	62.3454455468	1981.7	0.9751	0.063809	123.301682947
364117	Sherpa 221 NNPDF30NNLO Zee MAXHTPTV70 140 CVetoBVeto	5925000	Sherpa	NNPDF3.0 NNLO	77.6616159528	110.5	0.9751	0.69043	74.3928313765
364118	Sherpa 221 NNPDF30NNLO Zee MAXHTPTV70 140 CFilter-BVeto	1972600	Sherpa	NNPDF3.0 NNLO	97.0003619098	110.63	0.9751	0.18382	19.8296400357
364119	Sherpa 221 NNPDF30NNLO Zee MAXHTPTV70 140 BFilter	5855000	Sherpa	NNPDF3.0 NNLO	463.844185493	110.31	0.9751	0.11443	12.3084662448
364120	Sherpa 221 NNPDF30NNLO Zee MAXHTPTV140 280 CVetoBVeto	4949000	Sherpa	NNPDF3.0 NNLO	197.722621181	40.731	0.9751	0.61452	24.4067667684
364121	Sherpa 221 NNPDF30NNLO Zee MAXHTPTV140 280 CFilterBVeto	2962600	Sherpa	NNPDF3.0 NNLO	316.111997843	40.67	0.9751	0.23044	9.13863212948
364122	Sherpa 221 NNPDF30NNLO Zee MAXHTPTV140 280 BFilter	12330900	Sherpa	NNPDF3.0 NNLO	2032.5277594	40.643	0.9751	0.14927	5.91571777281
364123	Sherpa 221 NNPDF30NNLO Zee MAXHTPTV280 500 CVetoBVeto	1932800	Sherpa	NNPDF3.0 NNLO	396.941483556	8.6743	0.9751	0.56134	4.74798769611
364124	Sherpa 221 NNPDF30NNLO Zee MAXHTPTV280 500 CFilterBVeto	988900	Sherpa	NNPDF3.0 NNLO	433.732058608	8.6711	0.9751	0.26294	2.22320755605
364125	Sherpa 221 NNPDF30NNLO Zee MAXHTPTV280 500 BFilter	1976850	Sherpa	NNPDF3.0 NNLO	1322.86442976	8.6766	0.9751	0.17223	1.45716098463
364126	Sherpa 221 NNPDF30NNLO Zee MAXHTPTV500 1000	2973000	Sherpa	NNPDF3.0 NNLO	1644.26746308	1.8081	0.9751	1.0	1.76307831
364127	Sherpa 221 NNPDF30NNLO Zee MAXHTPTV1000 E CMS	988000	Sherpa	NNPDF3.0 NNLO	6650.06394292	0.14857	0.9751	1.0	0.144870607
364128	Sherpa 221 NNPDF30NNLO Ztautau MAXHTPTV0 70 CVetoBVeto	7907000	Sherpa	NNPDF3.0 NNLO	4.85769756199	1981.6	0.9751	0.82142	1587.19549779
364129	Sherpa 221 NNPDF30NNLO Ztautau MAXHTPTV0 70 CFilterBVeto	4941000	Sherpa	NNPDF3.0 NNLO	22.0697176888	1978.8	0.9751	0.11314	218.306784343
364130	Sherpa 221 NNPDF30NNLO Ztautau MAXHTPTV0 70 BFilter	7890600	Sherpa	NNPDF3.0 NNLO	61.7741911262	1981.8	0.9751	0.064453	124.552404811
364131	Sherpa 221 NNPDF30NNLO Ztautau MAXHTPTV70 140 CVetoBVeto	5935500	Sherpa	NNPDF3.0 NNLO	78.0718037803	110.37	0.9751	0.68883	74.1331155392
364132	Sherpa 221 NNPDF30NNLO Ztautau MAXHTPTV70 140 CFilterBVeto	1961200	Sherpa	NNPDF3.0 NNLO	97.0301270827	110.51	0.9751	0.1829	19.7089932529
364133	Sherpa 221 NNPDF30NNLO Ztautau MAXHTPTV70 140 BFilter	5912550	Sherpa	NNPDF3.0 NNLO	480.932428087	110.87	0.9751	0.110886	11.9878119426
364134	Sherpa 221 NNPDF30NNLO Ztautau MAXHTPTV140 280 CVetoBVeto	4956000	Sherpa	NNPDF3.0 NNLO	199.81121944	40.781	0.9751	0.60821	24.185807051
364135	Sherpa 221 NNPDF30NNLO Ztautau MAXHTPTV140 280 CFilterBVeto	2973000	Sherpa	NNPDF3.0 NNLO	318.709713854	40.74	0.9751	0.22897	9.09596467878
364136	Sherpa 221 NNPDF30NNLO Ztautau MAXHTPTV140 280 BFilter	4932950	Sherpa	NNPDF3.0 NNLO	900.322268996	40.761	0.9751	0.13442	5.34266418886
364137	Sherpa 221 NNPDF30NNLO Ztautau MAXHTPTV280 500 CVetoBVeto	1973000	Sherpa	NNPDF3.0 NNLO	411.797480449	8.5502	0.9751	0.56036	4.67188943921

Not reviewed, for internal circulation only

Table 54: Nominal MC samples.

DSID	explanation	nevents	genName	genTune	Sample Lumi [fb-1]	AMIXsec [pb]	K-factor	FiltEff	$\sigma \times K\text{factor} \times \text{FiltEff}$ [pb]
364138	Sherpa 221 NNPDF30NNLO Ztautau MAXHTPTV280 500 CFilterBVeto	986000	Sherpa	NNPDF3.0 NNLO	433.287517426	8.6707	0.9751	0.26245	2.21896214715
364139	Sherpa 221 NNPDF30NNLO Ztautau MAXHTPTV280 500 BFilter	1974950	Sherpa	NNPDF3.0 NNLO	1314.14727158	8.6804	0.9751	0.17313	1.46541699447
364140	Sherpa 221 NNPDF30NNLO Ztautau MAXHTPTV500 1000	2944800	Sherpa	NNPDF3.0 NNLO	1627.32095491	1.8096	0.9751	1.0	1.76454096
364141	Sherpa 221 NNPDF30NNLO Ztautau MAXHTPTV1000 E CMS	980000	Sherpa	NNPDF3.0 NNLO	6606.44465417	0.14834	0.9751	1.0	0.144646334
<i>W + jets MC15c</i>									
DSID	explanation	nevents	genName	genTune	Sample Lumi [fb-1]	AMIXsec [pb]	K-factor	FiltEff	$\sigma \times K\text{factor} \times \text{FiltEff}$ [pb]
364156	Sherpa 221 NNPDF30NNLO Wmumu MAXHTPTV0 70 CVetoBVeto	24723000	Sherpa	NNPDF3.0 NNLO	1.56772318768	19143.0	0.9702	0.8238	15300.0572987
364157	Sherpa 221 NNPDF30NNLO Wmumu MAXHTPTV0 70 CFilterBVeto	9847000	Sherpa	NNPDF3.0 NNLO	3.94926016845	19121.0	0.9702	0.1304	2419.07572368
364158	Sherpa 221 NNPDF30NNLO Wmumu MAXHTPTV0 70 BFilter	17226200	Sherpa	NNPDF3.0 NNLO	20.405404216	19135.0	0.9702	0.044118	819.040831686
364159	Sherpa 221 NNPDF30NNLO Wmumu MAXHTPTV70 140 CVetoBVeto	14788000	Sherpa	NNPDF3.0 NNLO	23.1996228452	944.85	0.9702	0.67463	618.428915666
364160	Sherpa 221 NNPDF30NNLO Wmumu MAXHTPTV70 140 CFilterBVeto	9853800	Sherpa	NNPDF3.0 NNLO	44.7969889819	937.78	0.9702	0.23456	213.410699631
364161	Sherpa 221 NNPDF30NNLO Wmumu MAXHTPTV70 140 BFilter	19639000	Sherpa	NNPDF3.0 NNLO	274.827498956	944.63	0.9702	0.075648	69.3298810068
364162	Sherpa 221 NNPDF30NNLO Wmumu MAXHTPTV140 280 CVetoBVeto	9882000	Sherpa	NNPDF3.0 NNLO	46.4914010851	339.54	0.9702	0.62601	206.221283425
364163	Sherpa 221 NNPDF30NNLO Wmumu MAXHTPTV140 280 CFilterBVeto	7408000	Sherpa	NNPDF3.0 NNLO	75.2561266792	340.06	0.9702	0.28947	95.5037405876
364164	Sherpa 221 NNPDF30NNLO Wmumu MAXHTPTV140 280 BFilter	9826000	Sherpa	NNPDF3.0 NNLO	28.9391529717	339.54	0.9702	0.11229	36.9147888
364165	Sherpa 221 NNPDF30NNLO Wmumu MAXHTPTV280 500 CVetoBVeto	4940000	Sherpa	NNPDF3.0 NNLO	125.436572946	72.067	0.9702	0.54647	38.208856376
364166	Sherpa 221 NNPDF30NNLO Wmumu MAXHTPTV280 500 CFilterBVeto	2958000	Sherpa	NNPDF3.0 NNLO	129.0699178	72.198	0.9702	0.31743	22.234860368
364167	Sherpa 221 NNPDF30NNLO Wmumu MAXHTPTV280 500 BFilter	2959500	Sherpa	NNPDF3.0 NNLO	308.003993468	72.045	0.9702	0.13337	9.32230412883
364168	Sherpa 221 NNPDF30NNLO Wmumu MAXHTPTV500 1000	5910500	Sherpa	NNPDF3.0 NNLO	393.770819454	15.01	0.9702	1.0	14.562702
364169	Sherpa 221 NNPDF30NNLO Wmumu MAXHTPTV1000 E CMS	3959000	Sherpa	NNPDF3.0 NNLO	3207.22618276	1.2344	0.9702	1.0	1.19761488
364170	Sherpa 221 NNPDF30NNLO Wenu MAXHTPTV0 70 CVetoBVeto	24740000	Sherpa	NNPDF3.0 NNLO	1.56883756535	19127.0	0.9702	0.82447	15299.7024868
364171	Sherpa 221 NNPDF30NNLO Wenu MAXHTPTV0 70 CFilterBVeto	9853500	Sherpa	NNPDF3.0 NNLO	3.953039329	19130.0	0.9702	0.1303	2418.3583578
364172	Sherpa 221 NNPDF30NNLO Wenu MAXHTPTV0 70 BFilter	17242400	Sherpa	NNPDF3.0 NNLO	20.4139516402	19135.0	0.9702	0.044141	819.467821557
364173	Sherpa 221 NNPDF30NNLO Wenu MAXHTPTV70 140 CVetoBVeto	14660500	Sherpa	NNPDF3.0 NNLO	23.2587435151	942.58	0.9702	0.66872	611.538499092
364174	Sherpa 221 NNPDF30NNLO Wenu MAXHTPTV70 140 CFilterBVeto	9818400	Sherpa	NNPDF3.0 NNLO	45.5631726263	945.67	0.9702	0.22787	209.068226178
364175	Sherpa 221 NNPDF30NNLO Wenu MAXHTPTV70 140 BFilter	9801900	Sherpa	NNPDF3.0 NNLO	100.28754283	945.15	0.9702	0.10341	94.8253702473
364176	Sherpa 221 NNPDF30NNLO Wenu MAXHTPTV140 280 CVetoBVeto	9879000	Sherpa	NNPDF3.0 NNLO	48.7043751025	339.81	0.9702	0.59691	196.791474684
364177	Sherpa 221 NNPDF30NNLO Wenu MAXHTPTV140 280 CFilterBVeto	7410000	Sherpa	NNPDF3.0 NNLO	75.2717206264	339.87	0.9702	0.28965	95.5097338041
364178	Sherpa 221 NNPDF30NNLO Wenu MAXHTPTV140 280 BFilter	9880900	Sherpa	NNPDF3.0 NNLO	29.1059856251	339.48	0.9702	0.11229	36.9965304

Not reviewed, for internal circulation only

Table 54: Nominal MC samples.

DSID	explanation	nevents	genName	genTune	Sample Lumi [fb-1]	AMIXsec [pb]	K-factor	FiltEff	$\sigma \times K \text{factor} \times \text{FiltEff}$ [pb]
364179	Sherpa 221 NNPDF30NNLO Wenu MAXHTPTV280 500 CVetoBveto	4923800	Sherpa	NNPDF3.0 NNLO	125.468709773	72.084	0.9702	0.54441	38.0738015769
364180	Sherpa 221 NNPDF30NNLO Wenu MAXHTPTV280 500 CFilterBveto	2963400	Sherpa	NNPDF3.0 NNLO	129.708896015	72.128	0.9702	0.31675	22.1657169888
364181	Sherpa 221 NNPDF30NNLO Wenu MAXHTPTV280 500 BFilter	2958000	Sherpa	NNPDF3.0 NNLO	306.317350162	72.113	0.9702	0.13391	9.36888360547
364182	Sherpa 221 NNPDF30NNLO Wenu MAXHTPTV500 1000	5916800	Sherpa	NNPDF3.0 NNLO	388.649500788	15.224	0.9702	1.0	14.7703248
364183	Sherpa 221 NNPDF30NNLO Wenu MAXHTPTV1000 E CMS	3947000	Sherpa	NNPDF3.0 NNLO	3200.09729204	1.2334	0.9702	1.0	1.19664468
364184	Sherpa 221 NNPDF30NNLO Wtaunu MAXHTPTV0 70 CVetoBveto	24784000	Sherpa	NNPDF3.0 NNLO	1.56866295484	19152.0	0.9702	0.82495	15328.6190165
364185	Sherpa 221 NNPDF30NNLO Wtaunu MAXHTPTV0 70 CFilterBveto	9865600	Sherpa	NNPDF3.0 NNLO	3.98248214869	19153.0	0.9702	0.12934	2403.4269992
364186	Sherpa 221 NNPDF30NNLO Wtaunu MAXHTPTV0 70 BFilter	17273200	Sherpa	NNPDF3.0 NNLO	20.2130975747	19163.0	0.9702	0.044594	829.089088304
364187	Sherpa 221 NNPDF30NNLO Wtaunu MAXHTPTV70 140 CVetoBveto	14808500	Sherpa	NNPDF3.0 NNLO	23.1909855548	947.65	0.9702	0.67382	619.516866415
364188	Sherpa 221 NNPDF30NNLO Wtaunu MAXHTPTV70 140 CFilterBveto	9860000	Sherpa	NNPDF3.0 NNLO	46.86705154	946.73	0.9702	0.22222	204.11294685
364189	Sherpa 221 NNPDF30NNLO Wtaunu MAXHTPTV70 140 BFilter	9857000	Sherpa	NNPDF3.0 NNLO	100.562851001	943.3	0.9702	0.10391	95.0973575706
364190	Sherpa 221 NNPDF30NNLO Wtaunu MAXHTPTV140 280 CVetoBveto	9899000	Sherpa	NNPDF3.0 NNLO	48.9242450604	339.36	0.9702	0.59622	196.303689268
364191	Sherpa 221 NNPDF30NNLO Wtaunu MAXHTPTV140 280 CFilterBveto	7365000	Sherpa	NNPDF3.0 NNLO	74.7127079545	339.63	0.9702	0.29025	95.6399947965
364192	Sherpa 221 NNPDF30NNLO Wtaunu MAXHTPTV140 280 BFilter	9834000	Sherpa	NNPDF3.0 NNLO	257.927814235	339.54	0.9702	0.11229	36.9907635913
364193	Sherpa 221 NNPDF30NNLO Wtaunu MAXHTPTV280 500 CVetoBveto	4931200	Sherpa	NNPDF3.0 NNLO	125.39558066	72.065	0.9702	0.54569	38.1532603845
364194	Sherpa 221 NNPDF30NNLO Wtaunu MAXHTPTV280 500 CFilterBveto	2956400	Sherpa	NNPDF3.0 NNLO	129.786408974	71.976	0.9702	0.31648	22.1001513385
364195	Sherpa 221 NNPDF30NNLO Wtaunu MAXHTPTV280 500 BFilter	2954100	Sherpa	NNPDF3.0 NNLO	305.484551818	72.026	0.9702	0.13426	9.38203847935
364196	Sherpa 221 NNPDF30NNLO Wtaunu MAXHTPTV500 1000	5945000	Sherpa	NNPDF3.0 NNLO	395.121627011	15.046	0.9702	1.0	14.5976292
364197	Sherpa 221 NNPDF30NNLO Wtaunu MAXHTPTV1000 E CMS	3946000	Sherpa	NNPDF3.0 NNLO	3197.99011265	1.2339	0.9702	1.0	1.19712978

2295 Q.2 Samples for estimation of systematic uncertainties

Table 55: MC samples used for modelling systematics.

DSID	explanation	nevents	genName	genTune	Sample Lumi [fb-1]	AMIXsec [pb]	K-factor	FiltEff	$\sigma \times K \text{factor} \times \text{FiltEff}$ [pb]
<i>t̄tγ MC15c</i>									
DSID	explanation	nevents	genName	genTune	Sample Lumi [fb-1]	AMIXsec [pb]	K-factor	FiltEff	$\sigma \times K \text{factor} \times \text{FiltEff}$ [pb]
410404	MadGraphPythia8EvtGen A14NNPDF23Var3cUp ttgamma nonallhad	4899000	MadGraph +Pythia8 +EvtGen	A14 NNPDF23LO	1059.632729868	4.6233	1.0	1.0	4.6233
410405	MadGraphPythia8EvtGen A14NNPDF23Var3cDown ttgamma nonallhad	4927000	MadGraph +Pythia8 +EvtGen	A14 NNPDF23LO	1065.689010014	4.6233	1.0	1.0	4.6233
410395	MGH7EG H7UE ttgamma nonallhadronic	4804000	MadGraph +Herwig7 +EvtGen	MMHT2014	1039.084636515	4.6233	1.0	1.0	4.6233
<i>t̄t MC15c</i>									
DSID	explanation	nevents	genName	genTune	Sample Lumi [fb-1]	AMIXsec [pb]	K-factor	FiltEff	$\sigma \times K \text{factor} \times \text{FiltEff}$ [pb]
410250	Sherpa 221 NNPDF30NNLO t̄bar SingleLeptonP MEPS NLO	13587000	Sherpa	NNPDF3.0NNLO	85.582010582	158.760	1.1484	1.0	182.319984

Table 55: MC samples used for modelling systematics.

DSID	explanation	nevents	genName	genTune	Sample Lumi [fb-1]	AMIXsec [pb]	K-factor	FiltEff	$\sigma \times K\text{factor} \times \text{FiltEff}$ [pb]
410251	Sherpa 221 NNPDF30NNLO ttbar SingleLeptonM MEPS NLO	14923000	Sherpa	NNPDF3.0NNLO	93.87305781	158.970	1.1484	1.0	182.561148
410252	Sherpa 221 NNPDF30NNLO ttbar dilepton MEPS NLO	9944000	Sherpa	NNPDF3.0NNLO	130.36695203	76.277	1.1484	1.0	87.596507
410511	PowhegPythia8EvtGen A14v3cUp hdamp517p5 ttbar nonallhad		Powheg +Pythia8 +EvtGen	A14 NNPDF23LO		824.51	1.0088	0.54383	452.339134105
410512	PowhegPythia8EvtGen A14v3cDo hdamp258p75 ttbar nonallhad		Powheg +Pythia8 +EvtGen	A14 NNPDF23LO		640.4	1.2988	0.54388	452.377629

$Z\gamma$ MC15c									
DSID	explanation	nevents	genName	genTune	Sample Lumi [fb-1]	AMIXsec [pb]	K-factor	FiltEff	$\sigma \times K\text{factor} \times \text{FiltEff}$ [pb]
345775	aMcAtNloPythia8 NNPDF30NLO FxFx ee-gamma HT0 125	1948000	aMcAtNlo Pythia8	A14 NNPDF23LO	93.187906621	20.904	1.0	1.0	20.904
345777	aMcAtNloPythia8 NNPDF30NLO FxFx ee-gamma HTGT125 MjjLT500	391000	aMcAtNlo Pythia8	A14 NNPDF23LO	332.241609497	10.176	1.0	0.11565	1.1768544
345778	aMcAtNloPythia8 NNPDF30NLO FxFx ee-gamma HTGT125 MjjGT500	99000	aMcAtNlo Pythia8	A14 NNPDF23LO	749.068567285	10.179	1.0	0.012984	0.132164136
345779	aMcAtNloPythia8 NNPDF30NLO FxFx mu-mugamma HT0 125	1953000	aMcAtNlo Pythia8	A14 NNPDF23LO	93.213058419	20.952	1.0	1.0	20.952
345781	aMcAtNloPythia8 NNPDF30NLO FxFx mumugamma HTGT125 MjjLT500	393000	aMcAtNlo Pythia8	A14 NNPDF23LO	328.843168141	10.191	1.0	0.11727	1.19509857
345782	aMcAtNloPythia8 NNPDF30NLO FxFx mumugamma HTGT125 MjjGT500	96000	aMcAtNlo Pythia8	A14 NNPDF23LO	730.468599335	10.187	1.0	0.012901	0.131422487
345783	aMcAtNloPythia8 NNPDF30NLO FxFx taugaugamma pty 10	2244000	aMcAtNlo Pythia8	A14 NNPDF23LO	80.360979802	27.924	1.0	1.0	27.924

Not reviewed, for internal circulation only